



Deliverable D1.2

Initial channel models based on measurements

Project Number:	ICT-317669
Project Name:	Mobile and wireless communications Enablers for the Twenty-twenty Information Society

Document Number:	ICT-317669-METIS/D1.2
Document Title:	Initial channel models based on measurements
Editor(s):	Tommi Jämsä (Anite), Pekka Kyösti (Anite), Katsutoshi Kusume (DOCOMO),
Author(s):	Vuokko Nurmela (Nokia), Aki Karttunen (Aalto), Antti Roivainen (UOulu), Leszek Raschkowski (Fraunhofer HHI), Tetsuro Imai (NTT DOCOMO), Jan Järveläinen (AALTO), Jonas Medbo (Ericsson), Jaakko Viirialä (NSN), Juha Meinilä (EB), Jukka Kyröläinen (Anite), Katsuyuki Haneda (AALTO), Veikko Hovinen (UOulu), Juha Ylitalo (EB), Nobutaka Omaki (NTT DOCOMO), Veli-Matti Kolmonen (Nokia), Katsutoshi Kusume (DOCOMO), Pekka Kyösti (Anite), Tommi Jämsä (Anite).
Dissemination Level:	PU (indicate the dissemination level)
Contractual Date of Delivery:	30/04/2014
Status:	Final
Version:	1.0
File Name:	METIS_D1.2_v1.0

Abstract:

In this report, the results of the measurement campaigns are provided based on the propagation scenarios defined in METIS project. Channel modelling approaches are discussed and the Initial METIS Channel Model is described in detail. The initial METIS channel model includes both stochastic (generic) and map-based (site-specific) models. Moreover, the initial modelling results are reported via the measurement data analysis and characterisation in order to parameterise the generic models. The output of this document will be used for the performance evaluation in other WPs.

Keywords:

channel model, propagation, propagation scenarios, channel measurements, test cases, D2D, backhaul, BS-UE, mmW, 5G



Executive summary

METIS' vision is a future where access to information and sharing of data is available anywhere and anytime to anyone and anything. The future information society will be provided with a wide variety of applications and services including completely new industrial and professional applications with a wide range of requirements. As a consequence, the METIS overall technical goal provides a system concept that, relative to today, supports, e.g., 1000 times higher mobile data volume per area, 10 to 100 times higher number of connected devices, 10 to 100 times higher user data rate, and 5 times reduced end-to-end latency, at a similar cost and energy dissipation as today.

To meet these requirements, new scenarios and use cases from the end user perspective and respective technology components are envisaged. These factors set new challenges for the propagation modelling.

The main objective of this document is to provide the Initial METIS Channel Models and the results of the measurement campaigns conducted by the METIS partners. The output of this document will be utilized for the performance evaluation in other work packages within the METIS project.

We took the following approaches to achieve the main objective. The scenarios and test cases that have been identified in the early stage of the METIS project from the end user perspective are mapped to the propagation scenarios. Then, some of the propagation scenarios are closely focused through the discussions with other technical activities within METIS. Those propagation scenarios have been investigated by searching the literature, conducting measurement campaigns, and exploring several new modelling approaches.

This document reports the following results. The 5G challenges and requirements for the propagation modelling are identified. These requirements include, e.g., spatial consistency for supporting highly dense scenarios and coexistence of different types of links in same area such as cellular links with different cell sizes and device-to-device (D2D) connections, dual link mobility for supporting D2D and vehicular-to-vehicle (V2V) connections as well as moving base stations, high spatial resolution and spherical waves for supporting very large antenna arrays and beamforming, elevation extension for supporting 3D models, higher frequencies up to 86 GHz for sufficiently wide spectrum to achieve high bitrates, and specular scattering characteristics especially for high frequencies. Several new promising channel modelling approaches to fulfil some of the 5G requirements are proposed. It was recognised that none of the proposed approach fulfils all the requirements at the same time. Therefore, four different approaches are proposed in this deliverable, and two of them are taken into account in the Initial METIS Channel Models. They are geometry-based stochastic channel model (GSCM based on WINNER/IMT-Advanced/3GPP) and map-based models (deterministic environment based models). These models are described more in details in this deliverable. The results of the measurement campaigns conducted by the METIS partners are used in parametrisation of the models and the detailed measurement reports are also provided.

As the next steps, the initial modelling results of this document will be updated by investigating the different channel model approaches and also by addressing corrections and additions based on the feedback received from other activities during the progress of the METIS project. Besides, complementary propagation measurements are planned in order to understand better the frequency dependency of propagation parameters and other phenomena towards the final channel modelling. The final METIS channel models will be published in the deliverable D1.4 in February 2015.

Contents

1	Introduction	1
1.1	Objective of document.....	2
1.2	Structure of document.....	2
2	5G Channel Model Requirements	3
2.1	Spatial consistency and mobility.....	3
2.2	Diffuse versus specular scattering.....	3
2.3	Very large antenna arrays	4
2.4	Frequency range.....	4
2.5	Complexity vs. Accuracy	4
2.6	Applicability of the existing and proposed models on the 5G requirements	5
3	METIS Propagation Scenarios	6
3.1	Test cases and propagation scenarios	6
4	Literature Review	8
4.1	Available channel models.....	8
4.1.1	WINNER / IMT-Advanced	8
4.1.2	COST 2100	8
4.1.3	IEEE 802.11 for 60 GHz.....	8
4.2	Model deficiencies.....	9
4.3	Frequency dependency of propagation effects.....	10
5	Channel Measurements	11
5.1	Channel measurements at 2.3 GHz and 5.25 GHz in Oulu downtown.....	12
5.2	Channel measurement in crowded areas	13
5.3	26 GHz path loss measurement in urban area	14
5.4	60 GHz channel measurements in an indoor office	15
5.5	60 GHz channel measurements in a shopping mall.....	16
5.6	Utilization of measurement results	17
6	Channel Modelling Approaches.....	18
6.1	Map based (simplified ray-tracing) modelling approach.....	19
6.1.1	LOS and diffracted pathways	19
6.1.2	Determination of pathways.....	20
6.1.3	Example of RX route	21
6.1.4	Shadowing objects	22
6.1.5	Scattering objects.....	24
6.1.6	Specular paths	27
6.1.7	Diffuse paths	30
6.1.8	Diffraction.....	31
6.1.9	Penetration path.....	34
6.1.10	Analysis	37
6.2	Visibility region based modelling approach.....	38
6.3	Grid-based GSCM (GGSCM) modelling approach	40
6.3.1	Single bounce vs. multiple bounce clusters.....	41
6.3.2	Physical locations of clusters	41
6.3.3	LOS probability	41
6.3.4	Interpolation of parameters between grid points	42
6.3.5	Shadowing and path loss	42
6.3.6	Example of a cluster drop.....	42
6.3.7	Analysis	43
6.4	Comparison of Approaches.....	44
7	Initial METIS Channel Model	45
7.1	Antenna modelling	45
7.1.1	Spherical coordinate system	45
7.1.2	Vector field rotation / mechanical tilting	46
7.1.3	Polarization transfer matrix.....	47

7.1.4	LOS depolarization.....	47
7.1.5	NLOS depolarization	48
7.2	Map-based model	48
7.2.1	Outdoor-to-Indoor channel model.....	52
7.3	Geometry-based stochastic model	55
7.3.1	Choose the system centre frequency f_c	57
7.3.2	Choose one of the scenarios (3D-UMa, 3D-UMi)	57
7.3.3	Choose the number of BSs and UEs.....	57
7.3.4	Choose BS and UE antenna field patterns	57
7.3.5	Generate BS locations	57
7.3.6	Generate UE locations	57
7.3.7	Generate BS antenna orientations	57
7.3.8	Generate UE antenna orientations	57
7.3.9	Generate UE velocity vectors	57
7.3.10	Determine LOS/NLOS links.....	57
7.3.11	Generate large-scale parameters.....	59
7.3.12	Generate path delays.....	60
7.3.13	Generate cluster powers	60
7.3.14	Generate arrival and departure directions	61
7.3.15	Coupling of angles	64
7.3.16	Generate cross polarization ratios.....	64
7.3.17	Draw random phases	65
7.3.18	Generate channel coefficients	65
7.3.19	Apply pathloss and shadowing	66
7.3.20	Parameterisation (based on measurement / literature)	68
7.4	Output	68
8	Conclusion and future work	69
Appendix A	Propagation scenarios sets	70
A.1	Virtual reality office propagation scenario set (for TC1)	70
A.1.1	Basic propagation environment and link topology.....	71
A.2	Dense urban propagation scenario set (for TC2).....	71
A.2.1	Basic propagation environment and link topology.....	72
A.2.2	Link topology specific characteristics.....	72
A.2.3	Frequency regions	73
A.3	Shopping mall propagation scenario set (for TC3).....	73
A.3.1	Basic propagation environment and link topology.....	73
A.3.2	Propagation scenarios	74
A.3.3	Frequency ranges	74
A.4	Stadium propagation scenario set (for TC4)	75
A.4.1	Basic propagation environment and link topology.....	75
A.4.2	Frequency ranges	76
A.4.3	Propagation scenarios	76
A.5	Smart energy distribution grid propagation scenario set (for TC5)	76
A.5.1	Propagation scenarios	77
A.6	Traffic jam propagation scenario set (for TC6)	77
A.6.1	Propagation scenarios	78
A.7	Blind spots propagation scenario set (for TC7).....	78
A.7.1	Propagation scenarios	79
A.8	Remote computing propagation scenario set (for TC8)	79
A.8.1	Propagation scenarios	80
A.9	Open air festival propagation scenario set (for TC9)	80
A.9.1	Frequency ranges	81
A.9.2	Propagation scenarios	81
A.10	Emergency propagation scenario set (for TC10).....	82
A.10.1	Propagation scenarios	83



A.11	Massive sensor and actuator propagation scenario set (for TC11)	83
A.11.1	Propagation scenarios	84
A.12	Traffic safety propagation scenario set (for TC12)	84
A.12.1	General requirements for the TC12 D2D channel models	84
A.12.2	Propagation scenarios	85
Appendix B	Detailed measurement reports.....	86
B.1	Channel measurements at 2.3 GHz and 5.25 GHz in Oulu downtown.....	86
B.1.1	Measurement equipment and antennas	87
B.1.2	Measurement scenarios.....	93
B.1.3	Measurement results.....	105
B.2	Channel measurement in crowded areas	109
B.2.1	Measurement system.....	109
B.2.2	Measurement environment.....	110
B.2.3	Measurement results.....	111
B.3	26 GHz band path loss measurement in urban area	114
B.3.1	Measurement system.....	114
B.3.2	Measurement environment.....	114
B.3.3	Measurement results.....	116
B.4	60 GHz indoor office measurements	118
B.4.1	Overview	118
B.4.2	Measurement setup	119
B.4.3	Body blocking scenario	120
B.4.4	Office medium range measurements.....	120
B.4.5	Office corridor long range measurements	121
B.5	60 GHz channel measurements in a shopping mall.....	123
B.5.1	Overview	123
B.5.2	Measurement system and sounder configuration	124
B.5.3	Measurement scenario.....	125
B.5.4	Post-processing and results	128
Appendix C	Early simulation channel models	134
Appendix D	Details of METIS initial model.....	135
D.1	LOS path antenna rotations	135
References.....		137

List of Figures

Figure 2-1: Scenario using very large wall mounted antenna arrays.....	4
Figure 3-1: Mapping of the five scenarios and the twelve test cases [MET 13-D11].	6
Figure 5-1: Measurement setup for UMi O2I (left) and UMa O2I (right)	13
Figure 5-2: Measurement environment during day- (left) and night-time (right).....	13
Figure 5-3: Measurement environment for 26.4 GHz measurements in Nihonbashi.	15
Figure 5-4: Measurement set-up and floor plan of measurement environment.	16
Figure 5-5: Signal strength relative to free space at 1 m distance for isotropic antennas measured and modelled at 2.4 GHz and 60 GHz in a corridor of an indoor office scenario. ...	16
Figure 5-6: Photographs of the measurement site of the 60 GHz channel measurements in a shopping mall.	17
Figure 6-1: Selection of Channel Modelling Approach.	19
Figure 6-2: Example of a street corner acting as a node (left). Manhattan map (middle). Topological example with four nodes (right).	20
Figure 6-3: Determination of pathways.	21
Figure 6-4: Diffracted paths between TX and RX (left) and relative power over the RX route	21
Figure 6-5: Received power over the RX route for isotropic antennas and 0 dBm transmit power.	22
Figure 6-6: Path angles and propagation distances at RX along the route for direct paths only. The power scale is relative to the strongest path for each RX location.	22
Figure 6-7: Shadowing screen model.	23
Figure 6-8: Diffracted paths between TX and RX (left), and, relative power over the RX route (right). Obstructing objects are shown with black dots.	23
Figure 6-9: Body blocking loss for a LOS link (4 m distance) at 60 GHz. The signal strength was measured as one person was walking back and forth crossing the LOS link. A model screen width of 30 cm is used to approximate the width of the person.	24
Figure 6-10: Received power at 2 GHz over the RX route for isotropic antennas and 0 dBm transmit power for 1.5 m RX height. The upper curve (blue) corresponds to the case with no obstructing objects and the middle curve (red) to the case with obstructing objects when the TX is at 10 m height and the lower curve (green) to the case when TX is at 1.5 m height.	24
Figure 6-11: Schematic drawing of the scattering model.	25
Figure 6-12: Paths between TX and scatterers around one RX location (upper left) and paths between one RX location and scatterers around TX (upper right), and, relative power over the RX route due to scatterers around RX (lower left) and scatterers around TX (lower right).	26
Figure 6-13: Distributions of path angles (left) and propagation distances (right) at RX for paths between TX and scatterers around RX (lower) and paths between RX and scatterers around TX (upper). The power is relative to the strongest path (LOS or diffracted) shown in Figure 6-6.....	27
Figure 6-14: Specular path along the RX route.....	28
Figure 6-15: Reflection on a wall.	29
Figure 6-16: Random point sources approximating a rough surface.....	31
Figure 6-17: Model for canonical problem of diffraction	32

Figure 6-18: Basic analysis model.....	34
Figure 6-19: Analysis model.....	35
Figure 6-20: Measured path loss for V2V measured in Oulu (left) and map based model with shadowing objects along the streets (right). The details of the measurement campaign are described in Section B.1.3.1 and of the shadowing model in Section 6.1.4.	37
Figure 6-21: Measured Doppler spectrum along a street in Kista Stockholm (upper graphs) and modelled spectrum as described in Section 6.1.5 (lower graphs). The scatterers and measurement routes are indicated in the leftmost figures.....	38
Figure 6-22: Basic components of the visibility region based modelling approach.....	40
Figure 6-23: Grid Points (GPs) separated by ΔGP in the xy plane.....	41
Figure 6-24: Propagation parameter drifting due to small movement of the UE.....	41
Figure 6-25: Advanced birth-death process.....	42
Figure 6-26: Simulation of GGSCM (WINNER C1 NLOS).	43
Figure 7-1: Spherical coordinate system.	46
Figure 7-2: Deterministic LOS depolarization.	48
Figure 7-3: Concept of proposed O2I channel model.	53
Figure 7-4: Setting of apertures.....	53
Figure 7-5: Ray-tracing procedure.....	54
Figure 7-6: Calculation results.....	55
Figure 7-7: Channel coefficient generation procedure [3GPP14-36873].	56
Figure 7-8: 2D and 3D distances for outdoor (left) and indoor (right) UEs [3GPP14-36873]..	59
Figure A-1: Virtual reality office environmental reference model.....	71
Figure A-2: Conceptual image of TC2 environment.....	71
Figure A-3: Overview on the Madrid grid model.....	72
Figure A-4: Plan of the reference shopping mall [MET13-D61].	74
Figure A-5: Reference stadium environment [METISD61].	75
Figure A-6: An example of stadium sector as an elementary block of the test case.....	76
Figure A-7: Overview of smart energy distribution grid.	77
Figure A-8: Conceptual overview of traffic jam test case environment.....	78
Figure A-9: Propagation scenarios for TC7 Blind Spots. Two conditions shown: The vehicle out of the ordinary coverage area (upper) and the vehicle in the ordinary coverage area (lower) of the BS.	79
Figure A-10: Propagation scenario for TC8 [MET13-D11].	80
Figure A-11: Conceptual overview of TC9 Open Air Festival.	82
Figure A-12: Overview of TC environment and NW deployment / user distribution.....	82
Figure A-13: Data from several sensors is received by a data collecting device, which transmits it further to the network.	83
Figure A-14: Overview of TC12 traffic safety environment.....	84
Figure B-1: PropSound system architecture.	87

Figure B-2: TX ULA antenna for ME3, ME4 and ME5 scenarios at 2.3 GHz (left) and 5.25 GHz (right).....	88
Figure B-3: RX antenna for 2.3 GHz.....	89
Figure B-4: RX antenna for 5.25 GHz.....	89
Figure B-5: Measurement setup for ME1.....	93
Figure B-6: TX leading and RX follows, vehicles move in the same directions.	94
Figure B-7: RX leading and TX follows, vehicles move to the same directions.	94
Figure B-8: TX (blue line) and RX (red line) routes moves to the opposite directions.	94
Figure B-9: TX/RX (blue/red dot) stationary position and RX/TX (red/blue line) moves on the cross street.....	95
Figure B-10: TX antennas: 5.25 GHz dipole (SIMO) and 2.3 GHz ULA (MIMO).	95
Figure B-11: RX measurement routes 1 and 2.	96
Figure B-12: RX measurement routes 3 and 4.	96
Figure B-13: RX measurement routes 5 and 6.	96
Figure B-14: RX (red line) measurement route 7.	97
Figure B-15: TX antenna on the top of building.	97
Figure B-16: Measurement spots inside the hotel room for ME3 scenario.	98
Figure B-17: The floorplan of the hotel with measurement spots in the corridors on floors 3 to 5.	99
Figure B-18: Magnified floorplan of the hotel corridors on floors 3 to 5.	100
Figure B-19: Measurement example, TX was located on the roof of neighbouring building. 100	100
Figure B-20: Views from the TX site towards the target building Left: from position 2, Right: From position 1.	101
Figure B-21: The hotel layout and measurement spots on the corridor of 2 nd floor.....	101
Figure B-22: The hotel layout and measurement spots in the corridor of 6 th floor.	102
Figure B-23: Measurement spots in the hotel room and in the end of corridor at 2.3 GHz and 5.25 GHz.....	103
Figure B-24: TX antenna distances at different heights in room measurements.	103
Figure B-25: The TX mounted on an articulated crane at a height of 5 m (left) and 15 m (right).	104
Figure B-26: TX antenna distances at different heights in corridor measurements.	104
Figure B-27: Measurement spots on the hotel corridor for ME4 at 2.3 GHz and 5.25 GHz. ..	104
Figure B-28: Measurement routes for ME5 at 2.3 GHz and 5.25 GHz.	105
Figure B-29: Measurement equipment: transmitter (left) and receiver (right).	109
Figure B-30: Measurement environment in front of Shibuya station.....	110
Figure B-31: Measurement results	112
Figure B-32: Path loss measurement system at 26.35 GHz.	114
Figure B-33: Map of Nihonbashi in Tokyo (typical Manhattan grid layout environment).	115
Figure B-34: Photographs of the measurement environment.....	116

Figure B-35: The frequency dependence of the path loss; (a) Path loss at 2.2 GHz (b) Path loss at 4.7 GHz (c) Path loss at 26.35 GHz.....	117
Figure B-36: TX antenna height dependency of the path loss. (a) TX antenna height is 1.5 m. (b) TX antenna height is 6 m. (c) TX antenna height is 10 m.....	117
Figure B-37: Measurement antenna patterns.....	119
Figure B-38: Measurement Set-Up.....	120
Figure B-39: Human body shadowing: Measurements vs. model at 60 GHz.....	120
Figure B-40: Measurement locations for medium range measurement.....	121
Figure B-41: Measured loss through door and window.....	121
Figure B-42: Measurement locations for long range corridor measurement.....	122
Figure B-43: Relative RX power measured and modelled at 2.4 GHz and 60 GHz for the long range corridor measurement.....	122
Figure B-44: Measurement system and sounder configuration.....	124
Figure B-45: Tx (left) and Rx (right) antennas.....	125
Figure B-46: Photographs of the measurement sites of the 60 GHz channel measurements at the first and third floors of the Sello shopping mall.....	125
Figure B-47: Floor plan of the 1 st floor of the Sello shopping mall with Tx and Rx locations.	126
Figure B-48: Floor plan of the 3 rd floor of the Sello shopping mall with Tx and Rx locations.	127
Figure B-49: Number of measurements as a function of the Tx-Rx distance.....	127
Figure B-50: Path loss and shadow fading when the Tx is aligned for maximum received power.....	128
Figure B-51: Path loss and shadow fading with the 360° rotation of the Tx.....	129
Figure B-52: Examples of LOS and NLOS PDP's: third floor measurement locations Rx1Tx2 and Rx1Tx3.....	129
Figure B-53: Angular spread as a function of the Tx-Rx distance and cumulative distribution functions with fitted normal distributions $N(\mu, \sigma^2)$	130
Figure B-54: Examples of LOS and NLOS PDP's: third floor measurement locations Rx1Tx2 and Rx1Tx3.....	130
Figure B-55: Delay spread as a function of the Tx-Rx distance and cumulative distribution functions with fitted normal distributions $N(\mu, \sigma^2)$	131
Figure B-56: Examples of LOS and NLOS PDP's with the detected peaks: third floor measurement locations Rx1Tx2 and Rx1Tx3.....	132
Figure B-57: CDF of the number of detected peaks 3 dB or more above noise level and of the number of relatively strong peaks (upper 20 dB of PDP).....	132
Figure B-58: Narrowband Ricean K-factor as a function of the Tx-Rx distance and cumulative distribution functions with fitted normal distributions $N(\mu, \sigma^2)$	133

List of Tables

Table 3-1: Propagation scenarios	7
Table 3-2: Mapping of propagation scenarios on test cases	7
Table 5-1: Overview of completed measurement campaigns within METIS	11
Table 5-2: Preliminary results of O2O measurements	12
Table 5-3: Measurement results in the Tokyo downtown crowded area for UMi and D2D scenarios.....	14
Table 7-1: Parameter table for the map based model.....	49
Table 7-2: Recommended PL and fading models for each propagation scenario	56
Table 7-3: 3D-UMi LOS link probabilities [3GPP14-36873].....	58
Table 7-4: 3D-UMa LOS link probabilities [3GPP14-36873]	58
Table 7-5: Scaling factors for AOA, AOD generation	61
Table 7-6: Ray offset angles within a cluster, given for 1 RMS angle spread [WIN08-D112] .	61
Table 7-7: Scaling factors for ZOA, ZOD Generation.....	62
Table 7-8: 3D-UMa ZSD and ZoD offset parameters [3GPP14-36873].....	63
Table 7-9: 3D-UMi ZSD and ZoD offset parameters [3GPP14-36873].....	64
Table 7-10: Sub-cluster information for intra cluster delay spread clusters	65
Table 7-11: 3D-UMi pathloss models [3GPP14-36873]	66
Table 7-12: 3D-UMa pathloss models [3GPP14-36873]	67
Table 7-13: Parameterisation [3GPP14-36873]	68
Table A-1: METIS test cases	70
Table B-1: The summary of the measurement environments at 2.3 and 5.25 GHz in Oulu downtown	86
Table B-2: TX antenna properties.....	88
Table B-3: RX antenna properties	88
Table B-4: Settings for measurements at 2.3 GHz	90
Table B-5: Settings for measurements at 5.2 GHz	91
Table B-6: V2V measurement results (ME1)	105
Table B-7: The summary of UMi O2I room results at 2.3 GHz (ME4)	106
Table B-8: The summary of UMi O2I corridor results at 2.3 GHz (ME4)	106
Table B-9: The summary of UMa O2I corridor results at 2.3 GHz (ME3)	107
Table B-10: The summary of O2O results at 2.3 GHz	108
Table B-11: Measurement parameters.	109
Table B-12: Large scale parameters of measured data	113
Table B-13: Street widths of the routes.....	115
Table B-14: The median, standard deviation and RMS of the differences due to the frequency	117



Document: FP7-ICT-317669-METIS/D1.2

Date: 29/04/2014

Security: Public

Status: Final

Version: 1.0

Table B-15: The median, standard deviation and RMS of the differences due to the frequency	117
Table B-16: Measurement campaign overview.....	118
Table B-17: Tx and Rx antennas	119
Table B-18: Measurement campaign overview.....	123
Table B-19: Tx and Rx antennas	123
Table B-20: Parameters	133
Table C-1: Early simulation channel models for METIS project	134



List of Abbreviations, Acronyms, and Definitions

Abbreviations

AoA	Azimuth angle of Arrival	M2M	Machine to Machine
AoD	Azimuth angle of Departure	MU-MIMO	Multi User MIMO
ASA	Azimuth angle Spread of Arrival	O2I	Outdoor to Indoor
ASD	Azimuth angle Spread of Departure	O2O	Outdoor to Outdoor
BS	Base Station	PAS	Power Angular Spectrum
BH	Back Haul	PHY	Physical layer
CO	Confidential	PL	Path Loss
C2X	Car-to-Anything	PS	Propagation Scenario
CW	Continuous Wave	PU	Public
D	Deliverables	RF	Radio Frequency
DL	Downlink	RMS(E)	Root mean square (Error)
DoA	Direction of Arrival (space angle)	RX	Receiver
DoD	Direction of Departure (space angle)	SAGE	Space-Alternating Generalized Expectation-maximization
D2D	Device to Device	SCM	Spatial Channel Model
EHF	Extremely High Frequency	SHF	Super High Frequency
EMF	Electro Magnetic Field	SIMO	Single-Input Multiple Output
EM	Electro Magnetic	SS	Small Scale
EoA	Elevation angle of Arrival	T	Task
EoD	Elevation angle of Departure	TDD	Time Division Duplex
ESA	Elevation angle Spread of Arrival	TC	Test Case
ESD	Elevation angle Spread of Departure	TL	Task Leader
E2E	End-to-End	TRX	Transceiver
FBC	First Bounce Cluster	TX	Transmitter
FDD	Frequency Division Duplex	UE	User Equipment
GCS	Global Coordinate System	UHF	Ultra High Frequency
GGSCM	Grid-based GSCM	UL	Uplink
GP	Grid Point	ULA	Uniformly spaced Linear Antenna array
GSCM	Geometry-based Stochastic Channel Model	UMa	Urban Macrocell
HT	Horizontal Topics	UMi	Urban Microcell
I2I	Indoor to Indoor	UTD	Uniform geometrical Theory of Diffraction
IEEE	Institute of Electrical and Electronics Engineers	V2V	Vehicle to Vehicle
IMT	International Mobile Communications	V-V	Vertical to Vertical
IR	Internal Report	VR	Visibility Region
ISIS	Initialization and Search Improved SAGE	VRBM	Visibility Region Based Model
ITU	International Telecommunication Union	WLAN	Wireless Local Area Network
ITU-R	ITU Radiocommunication sector	WP	Work Package
LAN	Local Area Network	WRC	World Radiocommunication Conference
LBC	Last Bounce Cluster	XPD	Cross Polarization Discrimination
LCS	Local Coordinate System	XPR	Cross Polarization Ratio
LS	Large Scale	ZoA	Zenith angle of Arrival
LTE	Long Term Evolution	ZoD	Zenith angle of Departure
LTE-A	Long Term Evolution-Advanced	ZSA	Zenith angle Spread of Arrival
MIMO	Multiple-Input Multiple-Output	ZSD	Zenith angle Spread of Departure
MMC	Massive Machine Communication		
mmW	Millimetre Waves		

Definitions

Early Simulation Models

Channel models selected from literature for early simulations in the beginning of METIS project. The models are not intended to be used after the final METIS model is specified.

Final METIS Channel Models

Final METIS channel models to be specified in D1.4 in February 2015.

Initial METIS Channel Models

Initial METIS channel models described in Section 7.

1 Introduction

The overall goal of the METIS (Mobile and wireless communications Enablers for the Twenty-twenty Information Society) project is to lay the foundation of the fifth generation (5G) mobile and wireless communication systems, targeting beyond 2020, by providing the technical enablers needed to address the requirements foreseen for this time frame [MET12].

METIS' vision is a future where access to information and sharing of data is available anywhere and anytime to anyone and anything. The future information society of private and professional users will be provided with a wide variety of applications and services, ranging from infotainment services, through increased safety and efficient usage of transportation, to completely new industrial and professional applications [MET13-D11]. Realizing this vision calls for solutions to challenges such as the provisioning of very high data rates, and the handling of very dense user crowds, with higher requirements on the end-to-end performance and user-experience. Other challenges that arise from new application areas are the requirement on very low latency, very low energy consumption, hence cost, as well as the support of a massive number of devices. As a consequence, the METIS overall technical goal provides a system concept that, relative to today, supports [MET13-D11]:

- 1000 times higher mobile data volume per area,
- 10 to 100 times higher number of connected devices,
- 10 to 100 times higher user data rate,
- 10 times longer battery life for low power massive machine communication (MMC),
- 5 times reduced end-to-end latency, at a similar cost and energy dissipation as today.

To meet these demands, today's spectrum can be used more efficiently, e.g. through higher spectral efficiency in bits/s/Hz and increased spectrum utilization through dynamic spectrum access, or by operating in new frequency bands. Furthermore, system capacity and coverage can be improved via new network topologies and technologies such as moving networks, multi-hop communications, self-configuration networks, and direct device-to-device (D2D) communications [OBB+14]. All these aspects set new requirements for radio channel and propagation modelling. Currently recognized and widely used channel models, e.g. 3GPP/3GPP2 Spatial Channel Model (SCM) [3GPP03-25996], WINNER [WIN08-D112, WIN10-D53], and ITU-R IMT-Advanced [ITU09-2135], were found to be inadequate for 5G requirements [MBH+14]. Therefore, the available models will be extended and modified for each selected propagation scenario.

While common channel models such as SCM, WINNER, and IMT-Advanced were designed for frequencies of up to 6 GHz, there are also other models available such as IEEE 802.11ad that focus on the 60 GHz band. Whereas those models are only applicable for a specific frequency range, the final METIS channel model shall cover the full frequency range from cellular bands of below 6 GHz up to 86 GHz [MET13-D51], which sets additional challenges to the propagation modelling.

The channel model investigation in METIS project comprises the analysis of propagation measurements conducted by some of the METIS partners, extensive literature reviews, and ray tracing simulations. The objective of the propagation research in METIS project is to ensure the availability of relevant propagation models, especially for the new scenarios defined in METIS. The radio channel and path loss models should have the appropriate level of detail based on the new scenarios defined in [MET13-D11] and meet the purpose of performance evaluation of the technology components of respective HTs and system concepts in the other WPs. Some of the models will be derived from propagation measurements that will be conducted for relevant scenarios.

Based on the literature review, ray tracing simulations, propagation measurements and theoretical studies on channel models, the Initial METIS Channel Models are proposed in this deliverable. The channel models described in the METIS project are physical, geometry-based



models and provide separate modelling of antennas and propagation, thus enabling optimization of different multi-antenna designs.

1.1 Objective of document

In this deliverable, the results of the measurement campaigns from METIS project are provided based on the propagation scenarios derived from the new scenarios in [MET13-D11] that are summarized in Section 3. Moreover, the initial modelling results are reported via the measurement data analysis and characterisation in order to parameterise the generic models. The output of this document will be used for the performance evaluation in other WPs and HTs within the METIS project. The initial modelling results will be updated by addressing corrections and additions based on the feedback received from other activities during the progress of the METIS project and will be reported in D1.4 in February 2015.

1.2 Structure of document

The remainder of the document is organized as follows:

- Section 2 provides the 5G challenges and requirements for the propagation modelling that are derived from the end user scenario perspective and the envisaged technology components foreseen to meet the METIS overall technical goal.
- Section 3 gives a summary of the METIS propagation scenarios that are mapped from the end user scenarios and test cases, which have been identified in the early stage of the METIS project. The detailed analysis is described in Appendix A.
- Section 4 provides the literature review results of the existing radio channel models along with some important features that are missing in the literature regarding the 5G channel modelling requirements in Section 2.
- Section 5 gives an overview of the measurement campaigns that were conducted by the METIS partners. And the detailed technical measurement reports are provided in Appendix B.
- Section 6 introduces the new alternative channel modelling approaches to fulfil the 5G channel modelling requirements in Section 2, and also gives the background for the Initial METIS Channel Model in Section 7.
- Section 7 describes the Initial METIS Channel Models; either stochastic or map-based models, depending on the propagation scenarios.
- Section 8 draws conclusions and describes the future work towards the final METIS channel models to be published in D1.4 in February 2015.

2 5G Channel Model Requirements

There are two main factors determining requirements on the propagation modelling. The first is the scenarios from the environment and user perspective and the second is the technology components envisaged to provide the required end user services. The usage scenarios include new aspects compared to 3G/4G, ultra-dense networks, car safety, and emergency scenarios, for instance. A detailed description of the propagation scenarios is given in Section 3. From a technology perspective, the propagation challenge is mainly higher frequencies and wider bandwidths, together with much larger antenna arrays in terms of number of elements and in terms of physical size with respect to the wavelength. Combining these two factors the following main challenges have been identified.

2.1 Spatial consistency and mobility

The 5G communication system is going to consist of various link types. An important aspect is the expected decrease of cell sizes from traditional macro- and microcells to pico- and femtocells, and, future movable nomadic base stations and direct device-to-device (D2D) connections between user terminals. These various types of links will co-exist in the same area. The traditional models with one end of the link fixed and only one end at an arbitrary location are not applicable in the case where both ends of the link are moving, and hence can be at arbitrary locations. Also the density of the links is expected to grow tremendously. All these set new requirements to channel modelling.

The current most commonly used channel models [ITU09-2135, WIN08-D112] are drop based, meaning that the scattering environment is randomly created for each link. The corresponding performance of spatial techniques like MU-MIMO is exaggerated, because the model assumes independent scatterers also in the case of nearby mobiles, which is not the case in reality. As the importance of spatial transmission techniques, as well as the density of links is expected to increase, it is even more important to model these links in a consistent manner. A spatially consistent model can also inherently support mobility of users.

To create a consistent model, geometric locations of the scatterers of the first and last hop of each path (transmitter-to-scatterer and scatterer-to-receiver) have to be defined. Moreover, a death and birth process of rays has to be defined according to the visibility of the scatterers. Dual mobility in the D2D case causes different Doppler model, different spatial correlation of LS and SS parameters than in the conventional cellular case. Additionally consistency between D2D and cellular case is not available with the current models.

2.2 Diffuse versus specular scattering

Due to the higher bandwidth and higher number of antennas, both delay and spatial resolution of the receiver increases. Visibility based channel models (e.g. COST 2100 [VZ12]) assume scattering by geographically fixed clusters. On the contrary, GSCM based model assumes fixed AoA/AoD with certain angular spread. In both cases, specular propagation is ignored. It is necessary to clarify the dominant propagation effects and differentiate between diffuse and specular scattering. Literature [MAB+12] and measurements performed in METIS (Figure B-52) indicate, however, that specular paths may dominate in many scenarios especially in higher frequencies. The characteristics of specular paths are very different from diffuse paths regarding apparent scatterer locations which are not fixed for specular propagation. As 5G transmission schemes are expected to utilize steerable highly directive and/or very large MIMO antennas the channel modelling should take into account realistic modelling of specular paths. The power ratio between specular and diffuse scattering may be frequency and receiver resolution dependent.

2.3 Very large antenna arrays

Current channel models [ITU09-2135, WIN08-D112] assume plane wave propagation (far field) and that the size of an antenna array is small (i.e. the propagation characteristics are similar at both ends of the antenna array). Only phase difference is caused due to different locations of antenna elements and direction of arrival/departure. An important technology component of 5G mobile communications is the use of very large antenna arrays (which even may extend over large scale fading regions) for e.g. massive MIMO and pencil beamforming as illustrated in Figure 2-1. For these highly directive antennas or large antenna arrays substantially non-realistic performance will be achieved using present modelling. Current channel models needs to be improved in angular resolution as well as sub-path (ray) amplitude distribution. Furthermore, these large arrays require spherical wave modelling replacing the commonly used plane wave approximation.

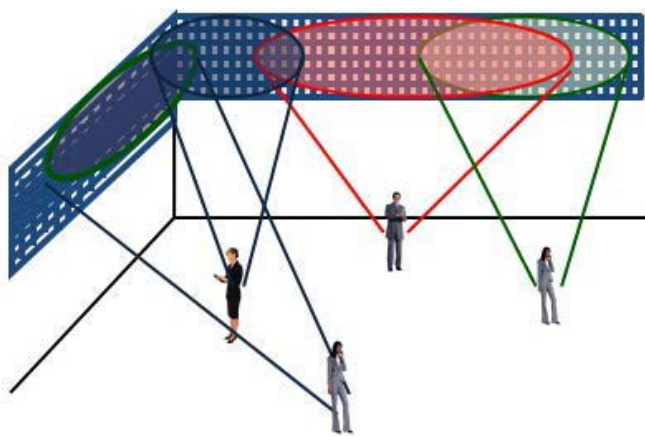


Figure 2-1: Scenario using very large wall mounted antenna arrays.

2.4 Frequency range

METIS Project has defined prioritized frequency bands from current cellular spectrum up to 86 GHz. The medium and high priority bands are 10 GHz, 28 – 29 GHz, 32 – 33 GHz, 43 GHz, 46 – 50 GHz, 56 – 76 GHz, and 81 – 86 GHz [METIS-D51]. Other bands have also been proposed.

The millimetre wave frequencies have very promising prospects of providing substantial additional amount of both spectrum and spatial multiplexing capacity. Although millimetre wave propagation has been investigated quite extensively, particularly at 60 GHz, crucial characteristics such as highly resolved angular properties and NLOS path loss are not well known.

The ultimate goal for 5G channel model is to define continuous functions for all channel model parameters and propagation effects for the full frequency range from 350 MHz up to 100 GHz.

2.5 Complexity vs. Accuracy

Simulations of wide range of propagation scenarios and network topologies (from stationary to very high speed, from single antenna to massive arrays, from single link to massive Mesh etc.) set different requirements to model accuracy and complexity. For example, a massive sensor network may be based on very simple transceivers with one antenna each. For that case, the model can be simplified in angular domain. On the contrary, angular information is crucial in Massive-MIMO simulations, but the number of massive arrays in one simulation is usually low. Therefore, different simplifications may be considered depending on the simulation requirements or test case.



2.6 Applicability of the existing and proposed models on the 5G requirements

All the stochastic model (GSCM, VRB) ignore the specular reflection. The Map-based model provides a solution for that. The VRB and map-based models provide spatial consistency better than the GSCM. The Map-based model is site specific, but the stochastic models try to create virtually any kind of environment. The frequency dependency of propagation parameters is still a challenge due to the lack of measurement data. The applicability of the models in network simulation will be increased by the simplifications provided later.

3 METIS Propagation Scenarios

In order to classify the propagation scenarios (PS) a number of basic propagation environments, link types and topologies are defined. Basic propagation environments in METIS are: dense urban, urban, rural, indoor, (office and shopping mall) and highway. More exceptional environments are: stadium, outdoor festival and rubble. In METIS three link types are used: cellular BS-UE link, backhaul BS-BS link and D2D link. Basic link topologies are: outdoor to outdoor (O2O), outdoor to indoor (O2I) and indoor to indoor (I2I) link.

Propagation scenario means here the propagation environment with the following parameters defined:

- Cell type, e.g. micro-cell, macro-cell, indoor, outdoor-to-indoor, and so on,
- BS location(s) and antenna height(s) in relation to the local roof-top heights (outdoor), and corresponding indoor parameters in relation to the building dimensions,
- UE antenna height and location range(s) within the environment and UE velocity range(s).

The requirements for the PSs are based on the requirements for the corresponding Test cases (TC1 – TC12) stated in [MET13-D11]. The usage of the test cases and PSs has been expressed in detail in [MET13-D61]. The text in this section has been aligned with these documents.

3.1 Test cases and propagation scenarios

Test cases (TCs) specified in [MET13-D11] are the baseline for simulations. Figure 3-1 shows the twelve TCs and their relation to the five METIS scenarios.

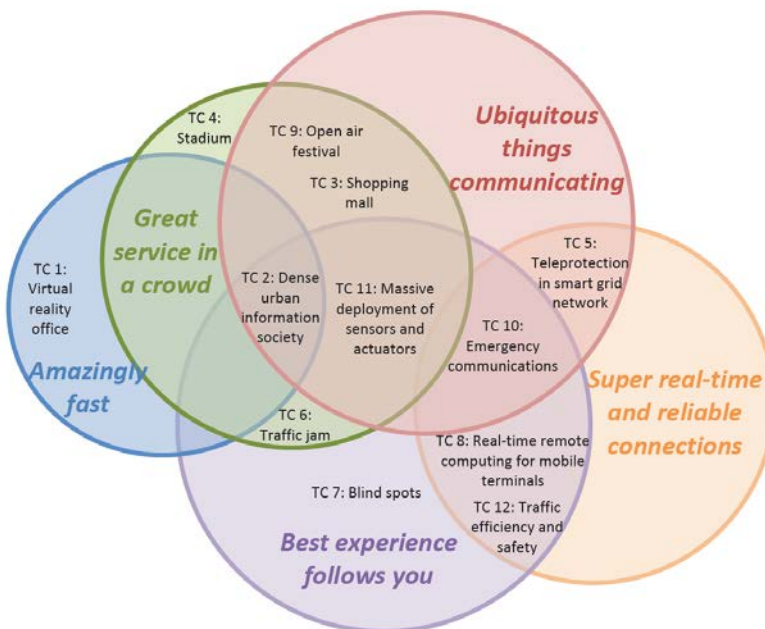


Figure 3-1: Mapping of the five scenarios and the twelve test cases [MET 13-D11].

One TC can cover one or more PSs. This fact can be tackled by specifying the concept of propagation scenario set. It means defining the set of all the needed propagation scenarios to cover a specific test case. Usually one to three propagation scenarios are used in the simulations. The selection of those propagation scenarios in METIS has been performed in accordance with [MET13-D61].



Proposed propagation scenarios (PS) with early simulation models and initial METIS models are listed in Table 3-1 while the mapping between propagation scenarios and test cases is shown in Table 3-2. Lower case 'x' means that the PS is for below 6 GHz frequencies. Capital 'X' means that the PS is for both below and over 6 GHz. For brevity the backhaul link type is not shown. When needed the same PS can usually be used as in the corresponding BS-UE links. The difference in the PSs is then only in the Tx and/or Rx antenna heights. The mapping in Table 3-2 is based on discussions and common understanding in T1.2.

Table 3-1: Propagation scenarios

Propagation Scenario		Initial METIS Model			
#	Name	Map-based Model (recommended in 5G simulations)	Supported link types	Model description	Supported link types
1	Urban Micro O2O, O2I	Madrid Grid specified in Section 7.2	any	Section 7.3	BS-UE, D2D/V2V
2	Urban Macro O2O, O2I	Madrid Grid specified in Section 7.2	any	Section 7.3	BS-UE, BH
3	Rural Macro O2O, O2I			Section 7.3	BS-UE, D2D/V2V, BH
4	Indoor Office	Section 7.2	any	Section 7.3	BS-UE
5	Indoor Shopping mall	Section 7.2	any	Section 7.3	BS-UE
6	Highway			Section 7.3	BS-UE, V2V
7	Open Air Festival O2O			Section 7.3	BS-UE, BH, D2D, BH
8	Stadium O2O	Section 7.2	any		

Table 3-2: Mapping of propagation scenarios on test cases

Link	Propagation Scenario	Test Case											
		1	2	3	4	5	6	7	8	9	10	11	12
BS-UE	Urban Micro O2O		X		X	x	x	x	x	X		X	x
	Urban Micro O2I	x	x									x	
	Urban Macro O2O		x		X	x	x	x	x	X	x	x	x
	Urban Macro O2I	x	x	x							x		
	Rural O2O					x	x	x	x	X	x		
	Rural O2I												
	Indoor Office	X	X									x	
	Indoor Shopping mall			X								X	
	Open Air Festival									x			
D2D	Stadium				x								
	Urban O2O (also V2V)		x			x	x	x	x		x	x	x
	Urban O2I	x	x								x		
	Rural O2O									x	x	x	
	Rural O2I												
	Indoor Office	X	X										
	Indoor Shopping mall			X								x	
	Highway V2V					x							x
	Open Air Festival									x			
	Stadium				x								

4 Literature Review

This section discusses available channel models with respect to the 5G channel model requirements as described in Section 2. Available models like WINNER / IMT-Advanced, COST 2100, and IEEE 802.11 are first discussed. Then the shortcomings of the available models are emphasized. Finally, a general overview on the frequency dependency of propagation parameters is given.

4.1 Available channel models

4.1.1 WINNER / IMT-Advanced

The radio channel models specified in [ITU09-2135], [WIN08-D112] and [WIN10-D53] describe various environments, outdoor, indoor and outdoor-to-indoor. The models are parameterized using results from an extensive set of measurement campaigns, and they are widely used and accepted.

The WINNER family is a set of geometry-based stochastic channel models. The channel parameters are determined stochastically, based on statistical distributions extracted from channel measurements. There are several randomized values, e.g. delay spread, delay values, angle spread, shadow fading, and cross-polarization ratio. For each channel snapshot the channel parameters are calculated according to the distributions. Channel realizations are generated by summing up contributions of rays with specific properties like delay, power, angle-of-arrival and angle-of-departure. Different propagation scenarios are modelled by using the same approach, but with different parameters. Although the WINNER models were originally designed for 2D propagation, further development has led to extensions like WINNER+ [WIN10-D53] and QuaDRiGa ([JRB+14a], [JRB+14b]), which handle radio propagation in 3D.

As the models are designed for cellular communication between a fixed base station and a mobile user terminal, they are not as such applicable to situations where both link ends can be at arbitrary locations, like D2D or in case of moving base station, or even ultra-dense deployment, where closely located BSs see partly the same environment. Another known defect of the WINNER approach is the lack of support for spherical waves and consistent modelling of closely located users. These things are discussed in more detail in Section **Error! Reference source not found..**

4.1.2 COST 2100

Unlike in WINNER / IMT-Advanced models, in COST 2100 model (see [VZ12]) the clusters (i.e. scattering objects) are defined as being present in the environment and are not specific to one single link. Each cluster has a visibility region, and is visible to the UEs located inside its visibility region. This enables closely located users to see partly similar environments. Also spherical waves and smooth time evolution of the channel is supported because the clusters have their fixed (x,y) coordinates.

Like the WINNER family, the COST 2100 model is also designed for cases where one end of the link is fixed, and thus is not adequate for all 5G propagation scenarios defined in Section 3. Furthermore the parameterizing the COST 2100 model to different environments is challenging, because the cluster characteristics cannot be easily extracted from propagation measurements.

4.1.3 IEEE 802.11 for 60 GHz

The IEEE 802.11ad channel model is intended for 60 GHz Wireless Local Area Networks (WLANs), where very high data rates are required [MEP10]. The model is cluster-based and describes the channel by providing accurate space-time characteristics including polarization and supports non-stationary characteristics of the channel. The paths considered by the model include the line-of-sight and first and second order reflections. As a result of



experimental measurements and ray tracing simulations, the model is parameterized for three indoor scenarios, namely a conference room, a cubicle and a living room. Since the model parameters are created deterministically, the parameterization for each scenario is site-specific and may not be valid for other similar environments.

4.1.1 Ray tracing

Ray tracing is a method for approximating the propagation of a wave in some environment using discrete rays. The discrete rays are launched to different directions and their propagation within the environment is traced by calculating the interactions of the rays, such as reflections, with the surrounding objects as they propagate in the environment. For accurate simulation results multiple rays need to be launched from the transmitter using a dense angular grid.

As such, ray tracing requires knowledge of the environment as well as knowledge on the material parameters of the objects. As the simulation approach relies on the environmental knowledge, this approach is inherently environment specific and as such deterministic. The approach supports different transmitter and receiver locations, i.e., macro-, microcellular, or D2D and it is spatially consistent.

Although ray tracing is very accurate way of simulating radiowave propagation, it suffers from mainly two aspects; 1) knowledge of the environment is required, and 2) the computational burden is high.

4.2 Model deficiencies

Regarding to the 5G channel modelling requirements discussed in Section 2, some important features are lacking from the existing models. In the future various types of links (e.g. traditional cellular, D2D, movable base stations, etc.) will co-exist in the same area, and they need to be described in a consistent manner.

A traditional model with base stations at fixed locations is not necessarily always adequate. When both ends of each link can be at arbitrary locations, consistent modelling is difficult to achieve with the existing models discussed in Sections 4.1.1 and 4.1.2. In WINNER and IMT-Advanced channel models good correlation properties of large scale (LS) parameters are achieved by pre-calculating a map for each location (x, y) of the simulated world. If both TX and RX can be at any location, the required map would be 4-dimensional ($x_{TX}, y_{TX}, x_{RX}, y_{RX}$), or even 6-dimensional, if height is also included. For a typical size of the simulated world (few hundred meters to kilometres) and typical required resolution of the LS parameter map (few meters to tens of meters), the size of this table grows too large and is not computationally feasible in practice, and thus a different approach is needed. Anyhow, ignoring the correlation of LS parameters, especially shadowing, can lead to incorrect conclusions, as demonstrated in [AP09].

For some applications the current modelling of small scale parameters is also inadequate, as explained in Section 2. A spatially consistent model is required to describe time evolution of the channel in dynamic simulations. It is also required to describe close-by links in a realistic manner, because if two radios are located close to each other, they should see similar scattering environment, and thus have similar directions of arrival (DoA) and departure (DoD). Ignoring this can overestimate the performance of spatial multi-antenna techniques.

In the future new frequency bands will be utilized for radio communications. Existing models cannot adequately describe propagation at frequencies beyond the current cellular bands. Most radio propagation measurements have been concentrating on frequencies below 6 GHz, and especially between 6 GHz and 60 GHz the available results are few and far between. Based on literature, a short summary of the frequency dependency of propagation is presented in Section 4.3 below.

4.3 Frequency dependency of propagation effects

Frequency dependency of propagation parameters in the frequency range from cellular frequencies up to millimetre waves is discussed, e.g., in [ITU12-1238], [ITU12-1410], [ITU12-1411].

It is often claimed that free space propagation loss is directly proportional to the square of the frequency (Friis transmission equation, [FR45]). The Friis's equation is based on an assumption that the antenna has an identical electric size over the frequency, and hence, has a smaller physical size as the frequency is higher. Similarly, most of the standardized path loss models include this frequency-squared phenomenon [ITU14-2135], [3GPP14-36873]. However, the propagation itself is frequency independent. If the device/antenna physical size is constant, we can ignore the frequency effect – or even make path loss lower in high frequency (by using a dish antenna as a result of gain focusing [Jac08]). To be more precise, at higher frequency it is possible to implement more directive antenna in the same physical volume and then compensate the path loss effect.

Another misunderstanding is often based on the famous curve on attenuation caused by water vapour and oxygen. This curve shows very high attenuation peaks around 22 and 60 GHz. However, these peaks show attenuations of 0.2 dB/km and 15 dB/km, respectively ([ITU13-676], Figure 5 on page 16). The former is clearly small in short-range communications and the latter is also insignificant when the distance between the transmitter and receiver is less than 100 m. On the contrary, high path loss (attenuation of signal level) is generally good for reducing the interference level.

The Fresnel zone is narrower in higher frequency, which makes the definition of LOS more obvious in millimetre waves than at current cellular frequencies. Smooth surfaces at 800 MHz radio frequency such as building walls composed of bricks may be rough at 5 GHz radio frequency because the wavelength becomes comparable to the roughness of the surface. When the radio frequency is further increased to 60 GHz, a scale of the surface roughness may be much larger than the wavelength, and therefore, waves may see the rough surface rather smooth, i.e. specular scattering exists (see measurement results in Section 5.4 "60 GHz channel measurements in an indoor office") . The surface roughness is quantified by the Rayleigh criterion and affects dominance of wave scattering. Whether scattering is dominant or not strongly depends also on the environment and materials. The ratio between specular scattering and diffuse scattering is one of the key research questions in 5G channel modelling.

Absorption of electromagnetic (EM) radiation is caused due to the effect that the energy of the radiation is transformed into internal energy of the matter, for example thermal energy. The amount of the energy loss of the EM radiation depends on the material permittivity and permeability, and it increases along frequency. It makes millimetre wave communication more isolated in the case of, e.g. buildings with concrete walls. Due to the absorption, also shadowing is higher in millimetre waves than cellular frequencies.

Diffraction happens in all frequencies (Huygens principle), but the spatial transition from the LOS to the shadowed regions attenuates higher frequencies more than lower ones because the attenuation of diffracted waves is increases as a function of frequency.

5 Channel Measurements

The channel measurements that have been conducted by the METIS partners are summarized in Table 5-1. This section provides an overview of the measurement campaigns and the detailed technical measurement reports are provided in Appendix B. Measurement campaigns have mainly focused on Test case 2 (see Section 3), including measurements at 2.3, 5.25 and 26 GHz for the link types vehicle-to-vehicle (V2V) and device-to-device (D2D), and link topologies outdoor to indoor (O2I) and outdoor to outdoor (O2O). In addition, 60 GHz indoor measurements have been done in an office (TC1) and a shopping mall (TC3).

Table 5-1: Overview of completed measurement campaigns within METIS

Partner	Frequency / bandwidth	Environment/ Test case	Antenna setup ($N_t \times N_r$)	Short description
UOulu	2.3 GHz / 100 MHz	Outdoor V2V/ TC2	1 x 56	Antennas on the roof of two cars. Tx and Rx move simultaneously
	2.3 GHz / 100 MHz	UMi O2I/ TC2	30 x 56	Tx and Rx stationary, Tx antenna heights: 5 m, 10 m and 15 m, Rx on the different floors of a building
	2.3 GHz / 100 MHz	UMi O2O/ TC2	30 x 16	Tx stationary, Rx stationary, Tx antenna heights 5 m, 10 m, LOS/NLOS
	2.3 GHz / 100 MHz	UMa O2I/ TC2	30 x 56	Tx on the roof of a building, Rx on the different floors of another building
	2.3 GHz / 100 MHz	UMa O2O/ TC2	1 x 56	Tx stationary, Rx mobile, LOS/NLOS
	2.3 GHz / 100 MHz	UMa O2O/ TC2	30 x 16	Tx stationary, Rx stationary, LOS/NLOS
	5.25 GHz / 200 MHz	Outdoor V2V/ TC2	1 x 50	Antennas on the roof of two cars. Tx and Rx move simultaneously
	5.25 GHz / 200 MHz	UMi O2I/ TC2	30 x 50	Tx and Rx stationary, Tx antenna heights: 5 m, 10 m and 15 m, Rx on the different floors of a building
	5.25 GHz / 200 MHz	UMi O2O/ TC2	30 x 18	Tx stationary, Rx stationary, Tx antenna heights 5 m, 10 m, LOS/NLOS
	5.25 GHz / 200 MHz	UMa O2O/ TC2	1 x 50	Tx stationary, Rx mobile, LOS/NLOS
DOCOMO	2.225 GHz / 50 MHz	Outdoor/ TC2 UMi D2D	1 x 198	Tx stationary, Rx mobile, Tx antenna heights 1.5 m, 3 m, Rx antenna height 1.5 m, LOS/NLOS
	26 GHz / < 10 Hz	Outdoor/ TC2 UMi D2D	1 x 1	Tx stationary, Rx mobile, Tx antenna heights 1.5 m, 6 m, 10 m, Rx antenna heights 1.5 m, 2.5 m, LOS/NLOS

Ericsson	58.68 GHz / 2 GHz	Indoor/ TC1 office	1 x 1	LOS and NLOS
Aalto	63 GHz / 4 GHz	Indoor/ TC3 shopping mall	1 x 1	LOS / NLOS, angular properties by rotation

5.1 Channel measurements at 2.3 GHz and 5.25 GHz in Oulu downtown

The wideband radio channel measurements were performed in Oulu downtown area for METIS Test Case 2 (TC2) considering dense urban information society. The measurements were conducted by EB PropSound channel sounder [Ele04] at 2.3 GHz and 5.25 GHz centre frequency for several measurement scenarios. Bandwidths of 100 MHz and 200 MHz were used at 2.3 GHz and 5.25 GHz, respectively. Urban V2V measurements were performed for single-input multiple-output (SIMO) antenna setup whereas urban macrocell (UMa) O2O, urban microcell (UMi) O2O, UMa O2I and UMi O2I were performed for multiple-input multiple-output (MIMO) antenna setup. The measurement setup for UMi and UMa O2O are presented in Figure 5-1. An omnidirectional vertically oriented dipole antenna was used as Tx antenna for the V2V scenario whereas uniformly spaced linear antenna arrays (ULAs) were used as Tx antennas for the other scenarios. The ULAs consist of 15 dual polarized elements (30 feeds) in both frequencies. Uniform cylindrical arrays (omnidirectional array ODA) were used as Rx antennas for all scenarios. The ODAs consist of 28 (56 feeds) and 25 (50 feeds) dual polarized elements in 2.3 GHz and 5.25 GHz, respectively.

The Tx and Rx antennas were placed on the rooftop of two cars in V2V measurements and both cars were moving during the measurements. In the other measurement scenarios, Tx and Rx were stationary. The Tx antenna was placed on an articulated crane for UMi measurements and on top of a building for UMa measurements. The heights of Tx antenna were 5 m, 10 m and 15 m for UMi measurements and 18 m for UMa measurements. In O2I measurements, the Rx was located 1.6 meters above floor level on the different floors of Hotel Scandic Oulu.

The transition between LOS and NLOS state was of particular interest in V2V and O2O scenarios whereas the statistics of elevation angles provided by Initialization and Search Improved SAGE (ISIS) [SJ03] super resolution algorithm was the main interest of the O2I measurements. Table 5-2 presents the preliminary results of O2O measurements at 2.3 GHz. In UMa O2O, the mean value of elevation angle spread of departure (ESD) is smaller in comparison to [3GPP14-36873], which is caused by a lower height of Tx antenna. On the other hand, an accurate vertical resolution indicates larger ESD in UMi O2O and a larger standard deviation of ESD in measurements in comparison to [3GPP14-36873].

Table 5-2: Preliminary results of O2O measurements

Parameter		UMa O2O	UMa O2O, [3GPP14-36873]		UMi O2O, Tx 10 m		UMi O2O,[3GPP14-36873]	
		All	LOS	NLOS	LOS	NLOS	LOS	NLOS
ESD* log10(degrees)	μ_{ESD}	0.5	0.7	0.9	0.71	0.88	0.4	0.6
	σ_{ESD}	0.35	0.2	0.2	0.54	0.32	0.2	0.2
ESA** log10(degrees)	μ_{ESA}	1.04	0.95	1.26	0.92	1.03	0.6	0.88
	σ_{ESA}	0.38	0.16	0.16	0.36	0.23	0.16	0.16
Cross-Correlations***	ESD vs ASD	0.57	0.5	0.5	0.61	0.15	0.5	0.5
	ESD vs ASA	-0.06	-0.3	0	0.06	-0.37	0	0
	ESD vs ESA	0.12	0	0	0	0	0	0
	ESD vs DS	-0.1	-0.2	-0.5	0.04	0.18	0	-0.5

Distance dependency	ESD	UMa O2O	UMi O2O,Tx 10 m	
		$ESD(d) = 8.9 \cdot e^{(-0.01 \cdot d)}$	LOS: $ESD(d) = 20.17 \cdot e^{(-0.01 \cdot d)}$ NLOS: $ESD(d) = 31.11 - 0.38 \cdot (d)$	
* ESD = Elevation angle spread of departure [3GPP03-25996]				
**ESA = Elevation angle spread of arrival [3GPP03-25996]				
*** Calculated according to [WIN08-D112]				



Figure 5-1: Measurement setup for UMi O2I (left) and UMa O2I (right)

5.2 Channel measurement in crowded areas

The wideband radio channel measurements were performed in the Tokyo downtown crowded area (vicinities of Shibuya railway station) for METIS' dense urban test case (TC2). Here, in order to analyse influence of shadowing of pedestrians, the measurements were performed in daytime and midnight-time as shown in Figure 5-2. In the investigated area, there were few pedestrians in midnight-time. The measurements were conducted by DOCOMO channel sounder [KSO+09] at 2.225 GHz centre frequency for urban microcell (UMi) and D2D scenarios. The user equipment (UE) antenna height was set to 1.5 m and the base station (BS) antenna heights for UMi and D2D scenarios were set to 3 and 1.5 m, respectively. A sleeve antenna and a slotted cylinder antenna were used to transmit vertically and horizontally polarized wave, respectively. Here, these antennas were manually switched. The signal was received by cylindrical array antenna, which has 96 dual-polarized patch antenna elements (192 feeds). The spatial distribution properties at UE side and BS side were measured by reversing the Tx and Rx location. In data processing, SAGE algorithm was applied to extraction of paths.

In both UMi and D2D scenarios, the average received power in daytime is about 5 dB lower than that in midnight-time (here, Tx and Rx polarizations are vertical). In UMi scenario in daytime, the median XPR from V-pol. to H-pol. was 8 dB, and the median XPR from H-pol. to V-pol. was 5 dB. The other obtained results are shown in Table 5-3.



Figure 5-2: Measurement environment during day- (left) and night-time (right).

Table 5-3: Measurement results in the Tokyo downtown crowded area for UMi and D2D scenarios

Scenario		ITU-R M2135 UMi (LoS)	SmallCell (LoS, Daytime)	SmallCell (LoS, Midnight)	D2D (LoS, Daytime)	D2D (LoS, Midnight)
Polarization			V-V	H-H	V-V	V-V
Delay spread (DS) log10(sec)	μ_{DS}	-7.19	-7.42	-7.24	-7.29	-7.59
	σ_{DS}	0.4	0.18	0.41	0.17	0.21
AoD azimuth spread (ASD) log10(deg)	μ_{ASD}	1.2	1.86	1.86	1.85	
	σ_{ASD}	0.43	0.08	0.08	0.08	
AoD elevation spread (ESD) log10(deg)	μ_{ESD}		0.90	0.90	0.88	
	σ_{ESD}		0.30	0.22	0.25	
AoA azimuth spread (ASA) log10(deg)	μ_{ASA}	1.75	1.70	1.65	1.73	1.61
	σ_{ASA}	0.19	0.16	0.16	0.16	0.17
AoA elevation spread (ESA) log10(deg)	μ_{ESA}		1.00	1.02	0.91	1.16
	σ_{ESA}		0.31	0.28	0.32	0.31
Cross correlation	ASD vs DS	0.5	0.07	0.23	0.27	
	ASA vs DS	0.8	0.21	0.52	0.46	0.41
Cluster ASD		3	5.56	5.14	5.99	
Cluster ESD			3.64	3.53	3.42	
Cluster ASA		17	5.91	6.63	6.04	5.26
Cluster ESA			4.50	4.57	3.72	6.08
						4.85

5.3 26 GHz path loss measurement in urban area

The path loss measurements at 26.4 GHz were performed in the Tokyo downtown area (Nihonbashi) for METIS' dense urban test case TC2 by DOCOMO, as shown in Figure 5-3. The measurements were conducted by continuous wave (CW) for urban microcell (UMi) and D2D scenarios. Here, the path losses of 4.7 and 2.2 GHz were also measured simultaneously, in order to confirm frequency characteristics. The user equipment (UE) antenna heights were set to 2.5, 1.5 m, and the BS antenna heights were set to 10, 6, and 1.5 m. Sleeve antennas were used as Tx and Rx antennas.

As expected, when the frequency is higher, the path loss increases. In data analysis, the measurement results were compared with the predicted path loss by the ITU-R M.2135 path loss equation (for UMi scenario) [ITU09-2135]. Note that the frequency of 26.4 GHz is beyond the application range of the equation. The predicted results for 4.7 and 2.2 GHz agree with the measurement results well. On the other hand, at 26.4 GHz, the difference between prediction and measurement for NLOS situation is very large, RMSE is over 10 dB. In order to determine the path loss distance dependency, a multi-regression analysis was performed for all

measurement data. Here, the function form and parameters are the same as that of the equation of ITU-R M.2135. The obtained result is as follows:

for LOS

$$PL_{\text{LOS}} = \begin{cases} 34.5 \log_{10} \frac{d_1}{[m]} + 1.7 + 23.4 \log_{10} \frac{f_c}{[\text{GHz}]} & \text{for } d_1 \leq d'_{BP} \\ 42.1 \log_{10} \frac{d_1}{[m]} - 6.8 - 7.6 \left(\log_{10} \frac{h'_{BS}}{[m]} + \log_{10} \frac{h'_{UE}}{[m]} \right) + 15.8 \log_{10} \frac{f_c}{[\text{GHz}]} & \text{else} \end{cases} \quad (5-1)$$

for NLOS

$$PL_{\text{NLOS}}(d_1, d_2) = PL_{\text{LOS}}(d_1) + 1.1 - 13.7 n_j + 11.5 n_j \log_{10} \frac{d_2}{[m]} + 6.1 \log_{10} \frac{f_c}{[\text{GHz}]} \quad (5-2)$$

The RMSE of this equation is 6.6 dB which indicates the potential of the M.2135 path loss model.



Figure 5-3: Measurement environment for 26.4 GHz measurements in Nihonbashi.

5.4 60 GHz channel measurements in an indoor office

A measurement campaign has been performed in an indoor office environment in the Kista area of Stockholm, Sweden by Ericsson. A vector network analyser (VNA) operating in the 2-4 GHz range was used in combination with up- and down converters providing 58.68 GHz centre radio frequency over the air. Optical fibres were used to feed the RF signal between the VNA and the up-converter and the local oscillator for synchronization of both converters. This method enables long range measurements of up to several hundred meters. Horn antennas with about 10 dBi gain were used at both ends of the link.

Figure 5-5 shows the path loss along the corridor shown in the floor plan in Figure 5-4. The signal strength in the LOS part of the corridor is in agreement with free space propagation. In the NLOS region after the corner the excess loss (relative to free space loss) is substantial. There is also a clear frequency dependency as the excess loss is about 15 dB larger at 60 GHz than at 2.4 GHz. The body blocking measurement results are shown in Figure 6-9 in Section 6.1.4. Here a blocking loss of about 20 dB was measured for an indoor LOS link of 4 m distance. Both results confirm the proposed METIS modelling in Sections 6.1 and 7.2.

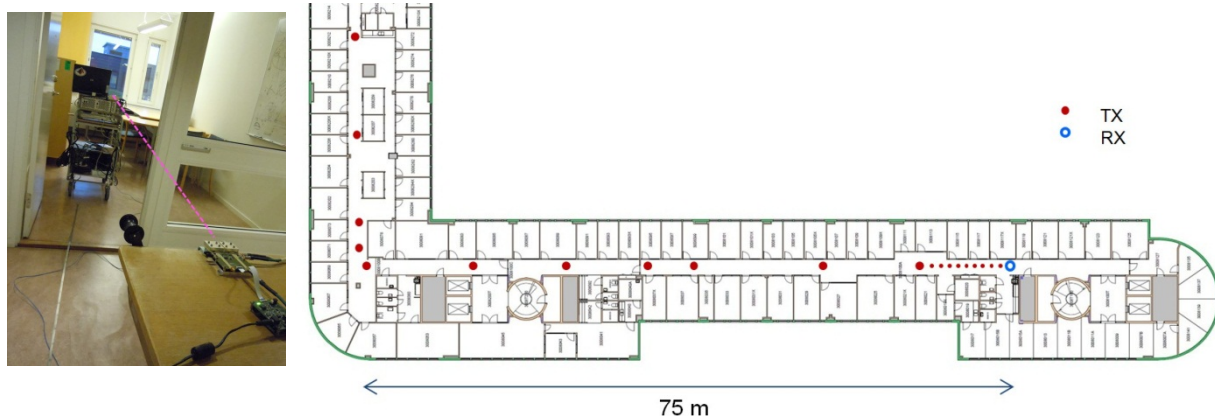


Figure 5-4: Measurement set-up and floor plan of measurement environment.

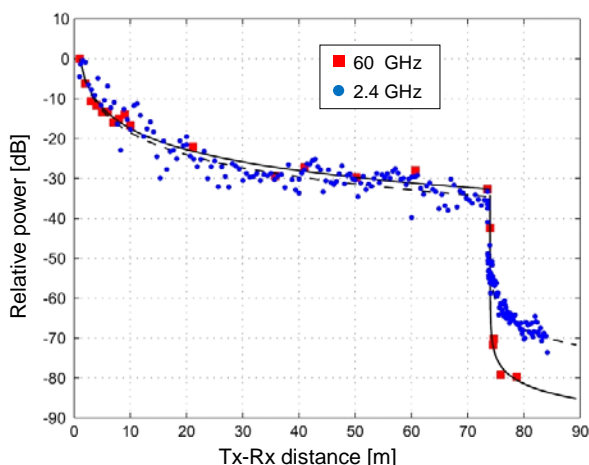


Figure 5-5: Signal strength relative to free space at 1 m distance for isotropic antennas measured and modelled at 2.4 GHz and 60 GHz in a corridor of an indoor office scenario.

5.5 60 GHz channel measurements in a shopping mall

Channel measurements were performed in a shopping mall illustrated in Figure 5-6 at the 61 - 65 GHz frequency range by Aalto University. These measurements were done with a VNA, up-/down converters, an omnidirectional Rx antenna and a standard gain horn at the Tx. The 20 dBi horn antenna was rotated in the azimuth direction providing good angular resolution, and the 4 GHz bandwidth provides a good delay resolution. In total 41 LOS and 14 NLOS measurements were conducted. The results (cf. Section B.5 in the Appendix) show that the 60 GHz propagation channel in an indoor shopping mall is dominated by specular paths, i.e., sharp peaks in the power delay profile.



Figure 5-6: Photographs of the measurement site of the 60 GHz channel measurements in a shopping mall.

5.6 Utilization of measurement results

Preliminary analysis from the measurements conducted so far shows generally a good agreement between measurement results and existing models. In the V2V measurements reported in Section 5.1 it is found that due to dual mobility, low antenna heights and many moving scatterers in the propagation environment, the decorrelation distance was shorter compared to existing results for the BS-UE propagation scenario. In the 60 GHz shopping mall measurements it was found that specular propagation mechanisms are clearly dominant compared to diffuse components.

The measurement campaigns were conducted in order to discover radio channel characteristics of the different TC's for the METIS channel model development. The measurement results will mainly be used for parameterization of the model, but observations drawn from the measurements can also be used to modify the channel modelling approach.

6 Channel Modelling Approaches

The purpose of this section is to describe alternative approaches to fulfil the 5G channel modelling requirements presented in Section 2 and also to give background for the initial METIS channel model defined as step by step instructions in Section 7. Three alternatives are presented, all utilizing 3D coordinates of the interacting objects to enable spatial consistency and support for spherical waves:

1. Map-based model: a simplified map to determine propagation paths including LOS, reflection, diffraction, in addition random scattering components (Step-by-step instructions of the map-based model is described in Section 7.2)
2. Visibility region-based model: stochastic 3D spatial distribution of clusters with corresponding visibility regions (VR) and couplings of clusters
3. WINNER-based model, 3D coordinates of clusters determined to grid points from random (angular) parameter distributions of WINNER model

Typically fast fading and time evolution of small scale propagation parameters (e.g. path lengths and directions) is related to motion of either or both of the link ends. There are two options to model motion with any of the introduced channel modelling approaches. The first one is the *true motion (Dynamic Mobility)* where trajectories are defined for one or two link ends and all parameters are determined and continuously updated based on locations of TX, RX and interacting objects along spatially sampled routes. For example propagation delay, phases of path components and the resulting fast fading are calculated for each time instant, i.e. each location assuming constant velocity, based on true spatial locations in a coordinate system.

The second option is the *virtual motion (Quasi Static)*, which is similar to the drop or channel segment concepts of IMT-Advanced [ITU09-2135] and WINNER [WIN08-D112] channel models. In this option the TX and the RX are not described by their continuous routes through the environment, but instead by discrete locations and velocity vectors. The channel is wide sense stationary (WSS) over time during the channel segment. The fast fading is modelled by a phase rotation of path components defined by Doppler shifts. Doppler shift may result from (virtual) motion of TX, RX or an interacting object, e.g., a car.

A hybrid of the two mentioned options would be to model true motion of TX and RX, but to model motion of interacting objects just by Doppler shift on path components affected by the moving objects.

Figure 6-1 shows the selection of channel modelling approach. If a map-based model is available for the desired scenario, the user should use it. Otherwise, the user should use a stochastic model in which the first selection is done between virtual motion (quasi-static) and true motion (dynamic). If single antennas or small sized multi antenna designs (i.e. plane wave assumption is valid) are used, quasi-static simulations with only virtual motion can be done with the legacy geometry based stochastic models as specified in Section 7.3. The true motion model can be fully mobile, i.e. supporting dual-mobility in which all propagation parameters are spatially consistent. The partial mobility model on the other hand supports spherical waves, time evolution of spatial parameters, and it is more suitable for cellular networks than D2D. Currently, there are two models available, i.e. a map-based model and a GSCM (both described in Section 7). The visibility region based model (VRBM) and the grid based GSCM (GGSCM) are still under investigation. They are introduced in Sections 6.2 and 6.3, respectively.

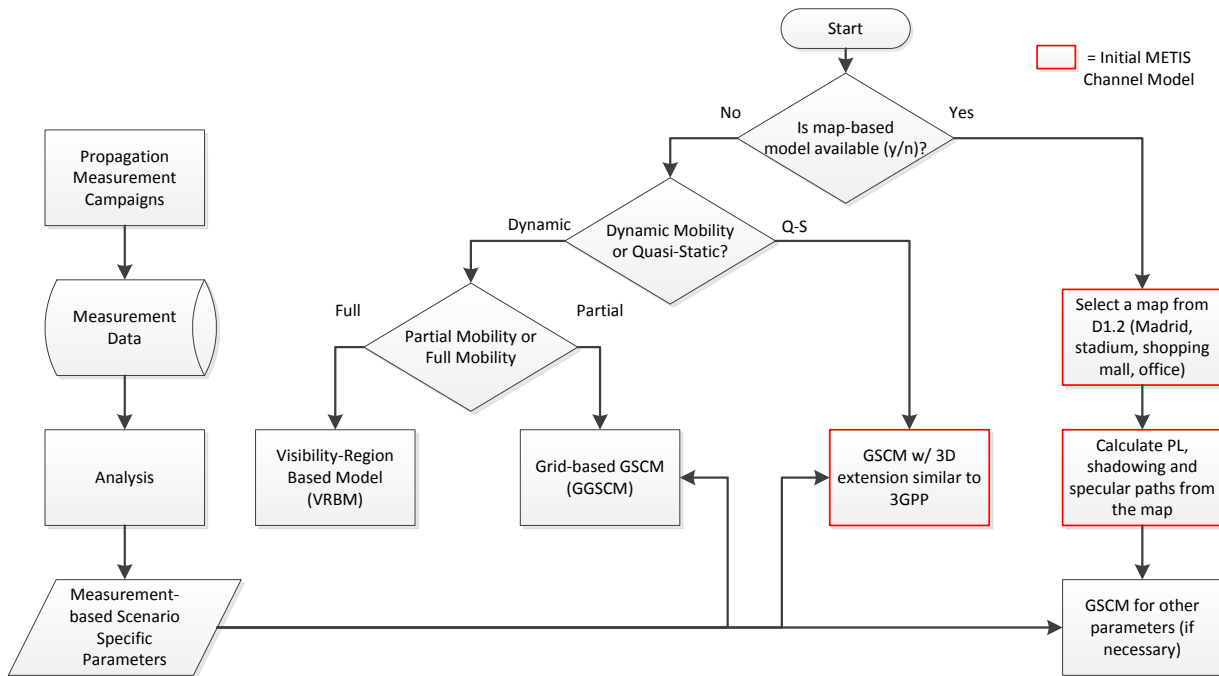


Figure 6-1: Selection of Channel Modelling Approach.

6.1 Map based (simplified ray-tracing) modelling approach

A map based channel model, based on simplified ray-tracing, is appealing in the sense that it makes the provisioning of realistic propagation modelling possible at a fairly low complexity, especially in case of a simple and systematic map like the Manhattan grid. The basic idea is to utilize main features of full blown ray-tracing techniques but with substantially reduced complexity. Regarding computational complexity the aim is to keep it at a similar as for the GSCM approach. In order to achieve this goal the geometrical environment description as well as the modelling of propagation mechanisms is kept simple. This modelling approach is based on a simple geometrical description of the radio environment by means of geographical maps or 3D indoor models. Figure 6-2 (middle) illustrates a Manhattan-like grid with a defined TX location and RX route. For each TX and RX location there are different possible pathways along the different streets.

The basic per path modelling of attenuation, delay and DoA & DoD is described in Sections 6.1.1 and 6.1.4 - 6.1.7. In the outdoor-to-indoor case the penetration effect is defined in Section 6.1.9. If polarized TX and RX arrays are considered the reflection and diffraction coefficients have to be calculated as described in Sections 6.1.6.1 and 6.1.8.4.

6.1.1 LOS and diffracted pathways

The LOS and diffracted pathways are described by the Berg recursive model [Ber95]. This is a semi-empirical model designed for signal strength prediction along streets in an urban environment. It is semi-empirical in the sense that it reflects physical propagation mechanisms without being strictly based on electromagnetics theory. It is based on the assumption that a street corner appears like a source of its own when a propagating radio wave turns around it. The corners of buildings and the antennas represent nodes (See Figure 6-2 left).

Any two subsequent nodes must be in LOS with respect to each other. Moreover, for any three subsequent nodes the middle node is blocking LOS between the first and the third node. Along a propagation path each node contributes a loss which depends on the change in direction θ . The total loss at a specific node n is given by the well-known expression for free space loss between isotropic antennas where a fictitious distance d_n is used, i.e.

$$L_n|_{dB} = 20 \log_{10} \left(\frac{4\pi d_n}{\lambda} \right) \quad (6-1)$$

where λ is the wave length. It should be noted that the fictitious distance corresponds to the real distance but multiplied by a factor at each diffraction node. The result is that the fictitious distance d_n becomes longer than the real distance meaning that it accounts for diffraction loss when used in the free space loss, cf. Equation (6-1). An example with four nodes is shown in Figure 6-2 (right). At each node, the fictitious distance is given by the following recursive expression

$$d_j = k_j s_{j-1} + d_{j-1} \quad (6-2)$$

with

$$k_j = k_{j-1} + d_{j-1} q_{j-1} \quad (6-3)$$

where s_j is the real distance between node j and its following node $(j+1)$, q_j is a function of θ_j (See Figure 6-2 middle). The initial values are $d_0 = 0$ and $k_0 = 1$.

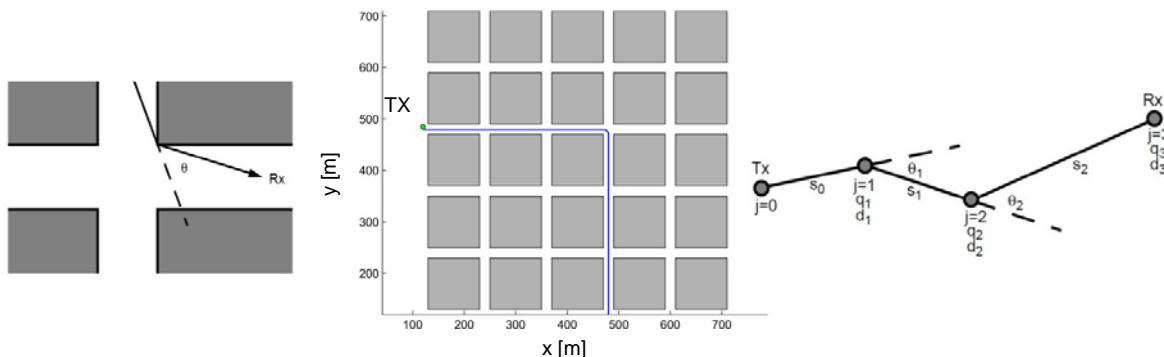


Figure 6-2: Example of a street corner acting as a node (left). Manhattan map (middle). Topological example with four nodes (right).

The angle dependence is given by the following expression

$$q_j = q_{90} \left(\frac{\theta_j}{90^\circ} \right)^\nu \quad (6-4)$$

where q_{90} and ν are parameters determined by fitting the model to measurement data. The parameter q_{90} accounts for the amount off diffraction loss caused by each node. A larger value results in larger diffraction loss. The parameter ν accounts for how fast the loss changes in the transition zone between LOS and NLOS. These two parameters are known for frequencies below 6 GHz but need calibration by measurements for higher frequencies. Further, there is a corresponding polarimetric matrix for these parameters expressed in terms of horizontal and vertical polarizations as described in Section 6.1.8.4.

6.1.2 Determination of pathways

For a Manhattan type of topology (e.g. the METIS Madrid topology) the significant pathways are determined for maximum 2 intermediate nodes. The corresponding building blocks are identified by drawing perpendicular lines parallel to the streets through the RX and the TX nodes as shown in Figure 6-3. Those building blocks which are fully or partly inside the corresponding rectangle are selected. The corners of the selected building blocks which are in LOS to either RX or TX are connected to corresponding RX or TX. The next step is to connect all intermediate nodes which are in LOS relative to each other. Nodes which are not blocking intermediate paths are disregarded.

For more complex street layouts the determination of pathways is more complex. The basic principle is always to find pathways with least number of nodes and shortest propagation distance.

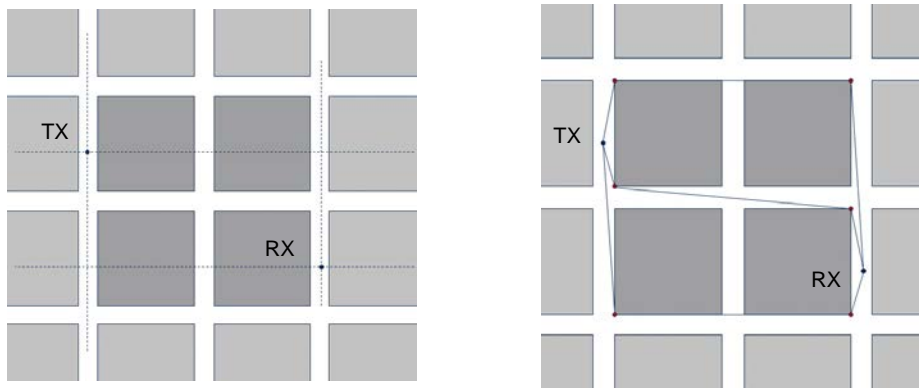


Figure 6-3: Determination of pathways.

6.1.3 Example of RX route

Figure 6-4 shows one example of pathways between a transmitter (TX) and a receiver (RX) along the RX route and the corresponding relative signal strength (relative to maximum power over the RX route) over the full route. Here $f_c = 2$ GHz, $q_{90} = 0.5$ and $\nu = 3.5$ (recommended values for V-V polarized antennas) have been used. Figure 6-5 shows the corresponding received signal (assuming isotropic antennas and 0 dBm transmit power) versus TX-RX distance. Figure 6-6 shows the distributions of RX propagation path angles and distances along the route. In LOS only the LOS path contributes (all paths with power 40 dB below the strongest path are disregarded). In NLOS there are several paths which contribute to the received power (cf. Figure 6-4).

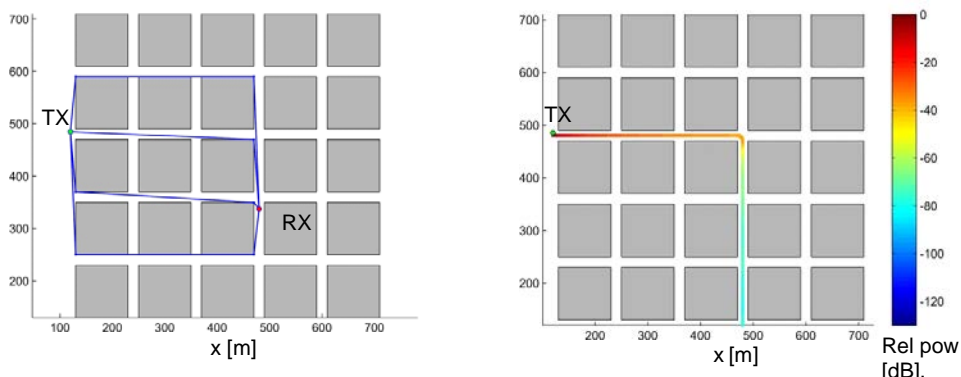


Figure 6-4: Diffracted paths between TX and RX (left) and relative power over the RX route (right).

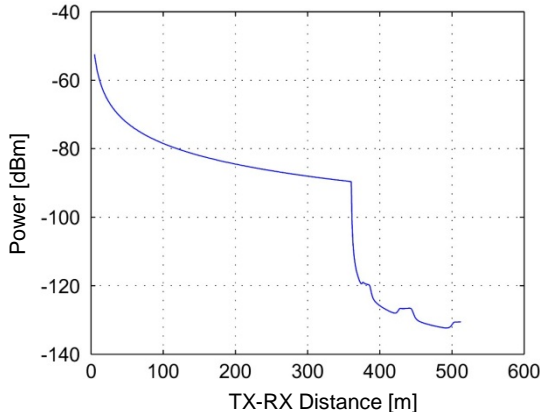
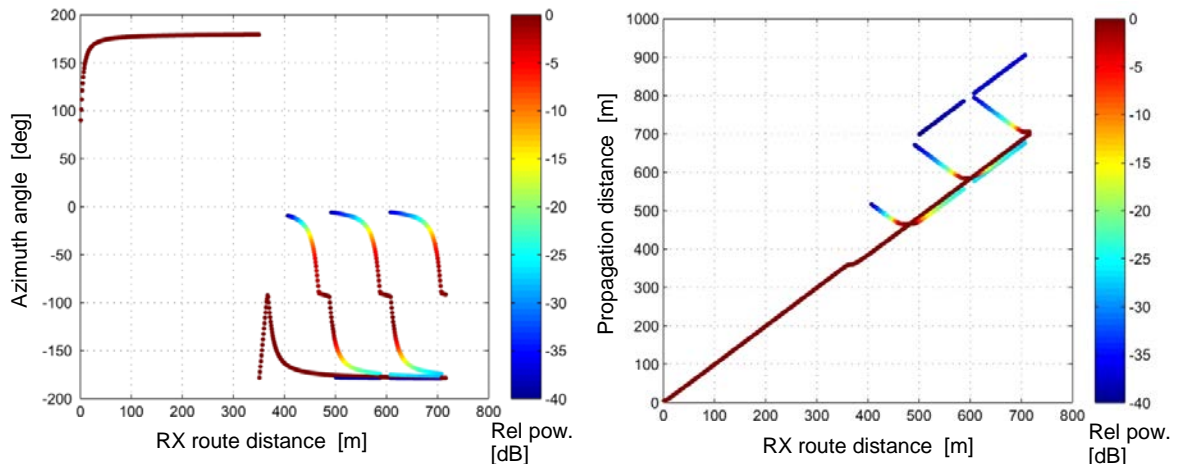


Figure 6-5: Received power over the RX route for isotropic antennas and 0 dBm transmit power.



**Figure 6-6: Path angles and propagation distances at RX along the route for direct paths only.
The power scale is relative to the strongest path for each RX location.**

6.1.4 Shadowing objects

Each path may be obstructed by e.g. humans and vehicles. The effect of this blocking may be substantial, particularly for higher frequencies in the millimetre range. This effect is accounted for using a simplified blocking model [MH13]. Each blocking object is approximated by a rectangular screen as illustrated in Figure 6-7. The screen is vertical and perpendicularly oriented with respect to the line connecting the two nodes of the link in the projection from above. This means that as either node is moving the screen turns around a vertical line through the centre of the screen so that it is always perpendicular to the line connecting TX and RX. The corresponding shadowing loss is modelled using a simple knife edge diffraction model for the four edges of the screen as

$$L_{Shad}|_{dB} = -20 \log_{10}(1 - (F_{h1} + F_{h2})(F_{w1} + F_{w2})) \quad (6-5)$$

where F_{h1}, F_{h2} and F_{w1}, F_{w2} account for knife edge diffraction at the four edges corresponding to the height, h , and width, w , of the screen (See Figure 6-7). The shadowing for a single edge is given by

$$F = \frac{\text{atan}\left(\pm\frac{\pi}{2}\sqrt{\frac{\pi}{\lambda}(D_1+D_2-r)}\right)}{\pi} \quad (6-6)$$

where λ is the wave length, D_1 and D_2 are the projected distances (according to the projections from side and from above in Figure 6-7) between the nodes and the edges of the screen and r is the projected distance between the nodes. The plus sign refers to the shadow zone for each projection (i.e. it is possible that one projection is in LOS and the other in NLOS). When the link is in NLOS the plus sign apply to both edges. For LOS conditions the edge farthest from the link is in the shadow zone (plus sign) and the other in the LOS zone (minus sign). Figure 6-9 shows a comparison of the model with measurements at 60 GHz.

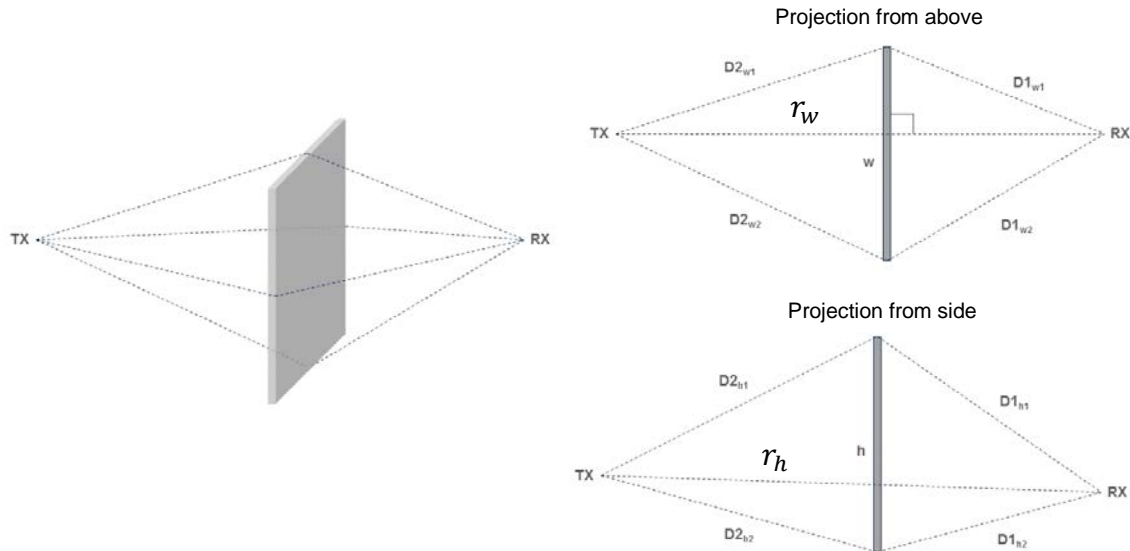


Figure 6-7: Shadowing screen model.

A random distribution of shadowing objects has been introduced along the streets as shown in Figure 6-8. In this case all blocking objects have a height of 2.5 m and a width of 3 m. The shadowing model is applied between all pairs of connected nodes and for all screens. Figure 6-10 shows the corresponding result on the received power for two different TX heights of 1.5 m and 10 m. For the 10 m TX height the impact of shadowing objects is relatively small. For the lower TX height of 1.5 m however the impact of shadowing is significant (about 7 dB loss). It should be noted that the severe shadowing loss shown in Figure 6-9 is due to high frequency (60 GHz) and that the blocking object is close to the antenna. The results shown in Figure 6-10 are for 2 GHz and in average considerable longer distances to the blocking objects.

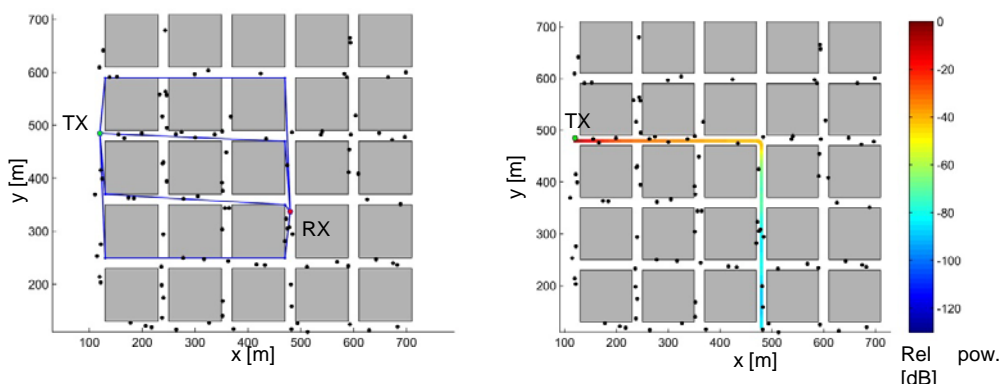


Figure 6-8: Diffracted paths between TX and RX (left), and, relative power over the RX route (right). Obstructing objects are shown with black dots.

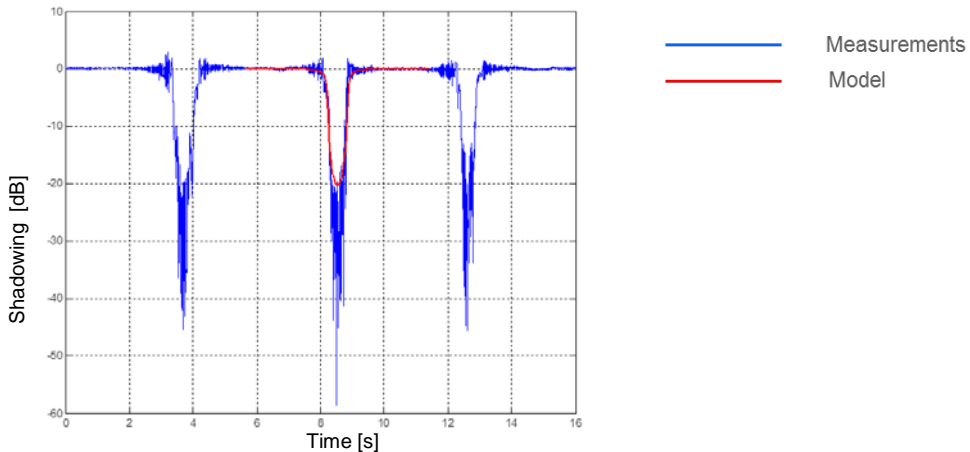


Figure 6-9: Body blocking loss for a LOS link (4 m distance) at 60 GHz. The signal strength was measured as one person was walking back and forth crossing the LOS link. A model screen width of 30 cm is used to approximate the width of the person.

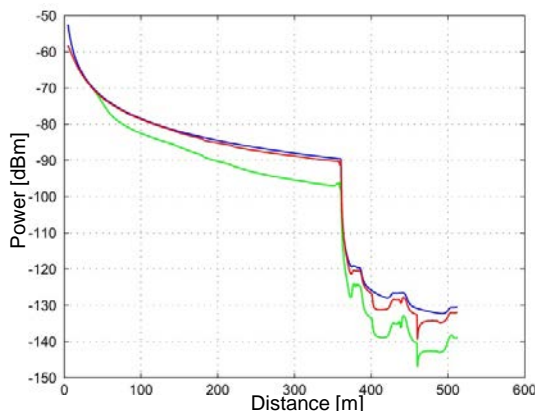


Figure 6-10: Received power at 2 GHz over the RX route for isotropic antennas and 0 dBm transmit power for 1.5 m RX height. The upper curve (blue) corresponds to the case with no obstructing objects and the middle curve (red) to the case with obstructing objects when the TX is at 10 m height and the lower curve (green) to the case when TX is at 1.5 m height.

6.1.5 Scattering objects

Each path may be scattered, as well as shadowed, by object like humans and vehicles. The effect of such scatterers is significant when they are located close to either end of the link (TX or RX antennas). The scattering is accounted for using the same model as for the shadowing [MH13]. The power of the scattered wave is modelled based on the scattering cross section for a perfectly conducting sphere as

$$RCS = \pi R^2. \quad (6-7)$$

Further, it is assumed that the scattered power is also shadowed i.e. it is reduced according to the shadowing model. The corresponding scattered power is given by

$$P_{scat} = P_{source} (1 - \alpha) \left(\frac{\lambda R}{8\pi R_1 R_2} \right)^2 \left(1 - (F_{h1} + F_{h2})(F_{w1} + F_{w2}) \right)^2 \quad (6-8)$$

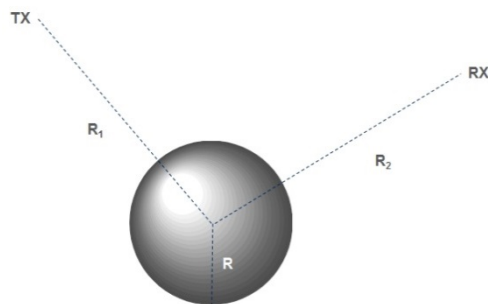


Figure 6-11: Schematic drawing of the scattering model.

where P_{source} is the channel power at the source node (TX) of Figure 6-11 and α is the absorption coefficient of the scatterer. In order to match the size of the screen with the cross section of the sphere the radius is set to

$$R = \sqrt{\frac{w h}{\pi}} . \quad (6-9)$$

Figure 6-12 shows the pathways between TX and significant scatterers around RX, and, RX and significant scatterers around TX. The corresponding distributions of path angles and path propagation distances are shown in Figure 6-13.

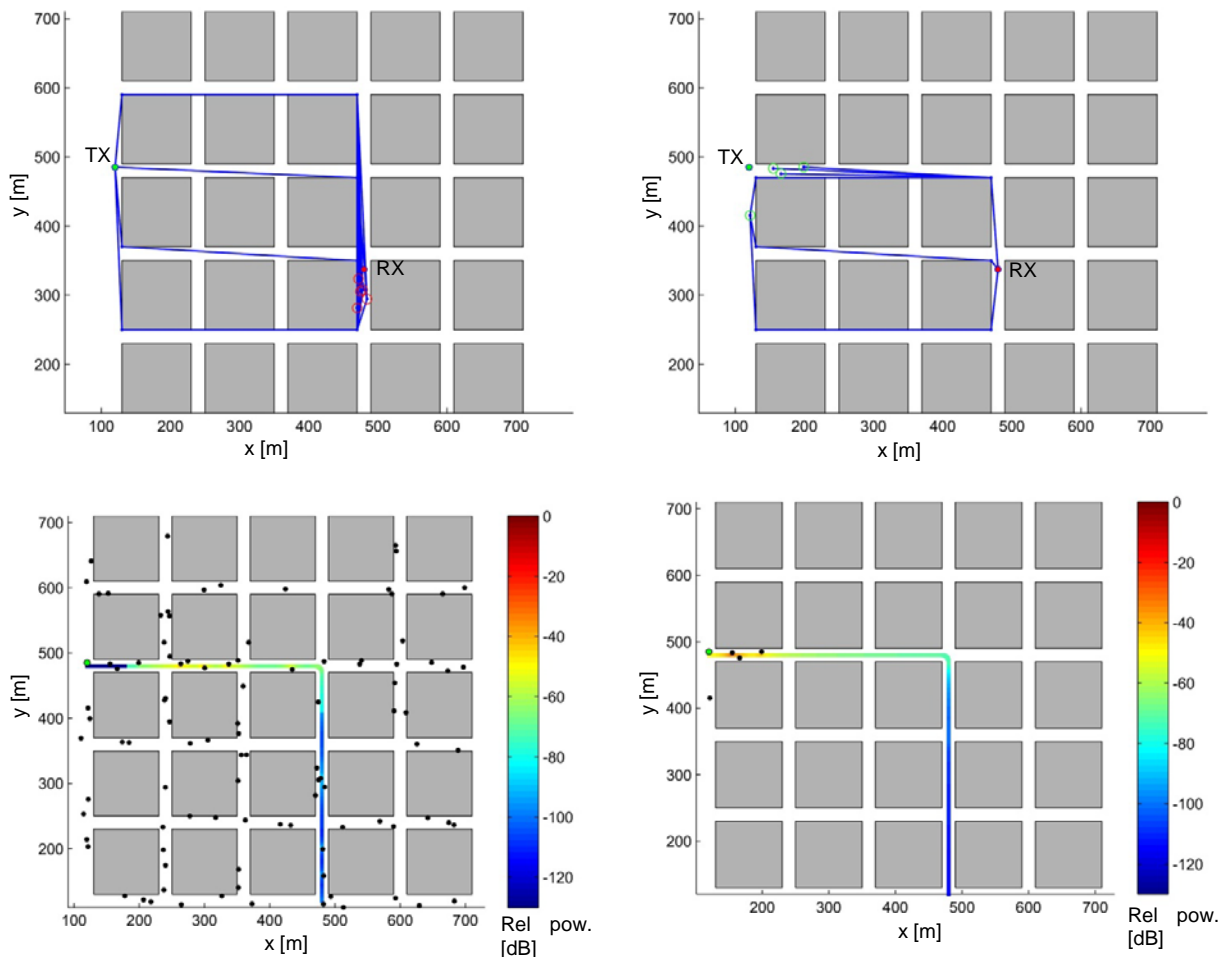


Figure 6-12: Paths between TX and scatterers around one RX location (upper left) and paths between one RX location and scatterers around TX (upper right), and, relative power over the RX route due to scatterers around RX (lower left) and scatterers around TX (lower right).

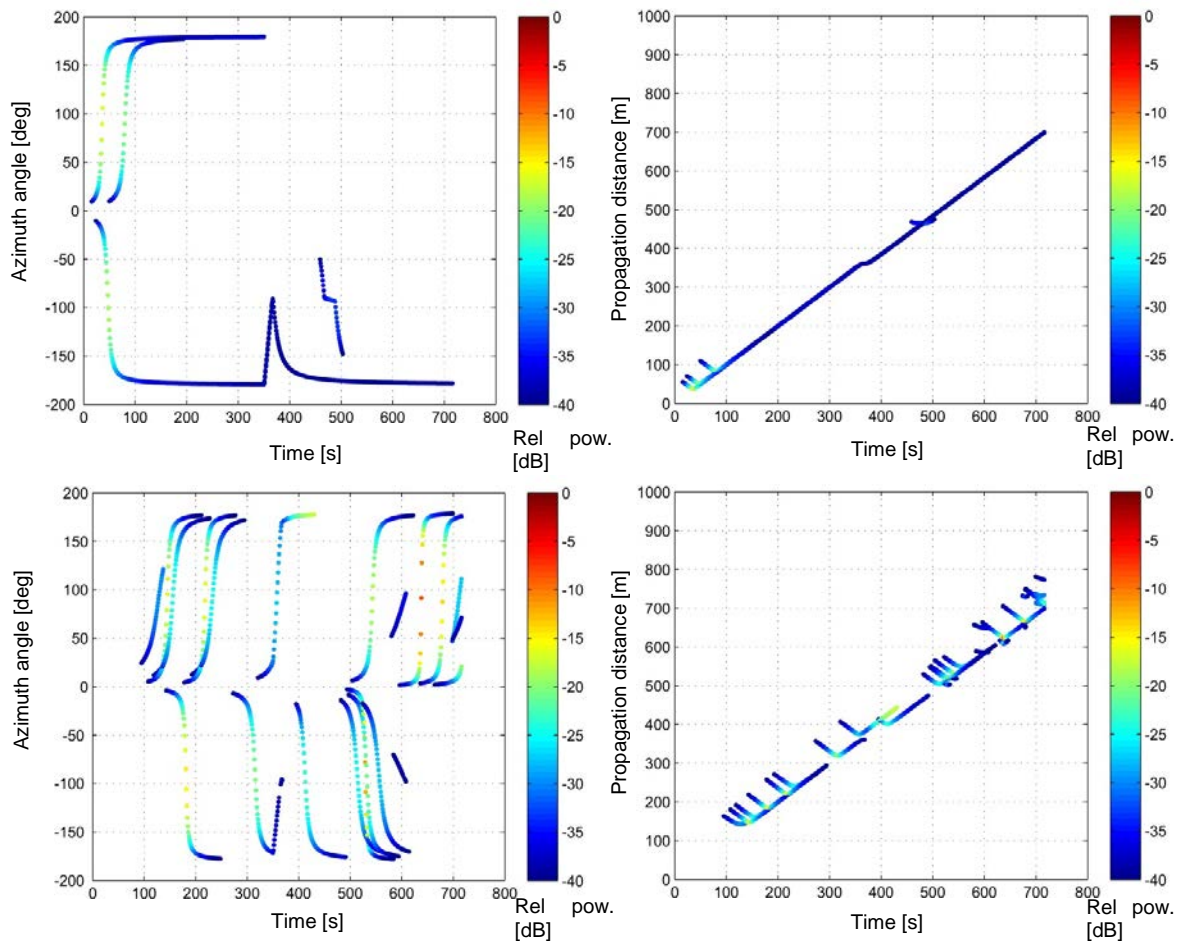


Figure 6-13: Distributions of path angles (left) and propagation distances (right) at RX for paths between TX and scatterers around RX (lower) and paths between RX and scatterers around TX (upper). The power is relative to the strongest path (LOS or diffracted) shown in Figure 6-6.

Only scatterers which are in LOS to either TX and/or RX or in LOS to the first and the last of three consecutive nodes are selected. Moreover, the power of the scattered wave should be more than -40 dB relative to the strongest path.

6.1.6 Specular paths

Specular propagation paths between TX and RX may result from specular reflection on walls and ground in an urban environment and on walls, floor, and ceiling in an indoor environment. From ray optics we know that in specular reflection the incidence and reflected angles are equal. In order to model specular paths the existence and locations of reflection points have to be determined based on TX and RX locations and the layout of walls. Path lengths (propagation delay) and directions of arrival and departure can be determined knowing the reflection points. Finally 2x2 coefficients for specular reflections are calculated with some material constants assuming, e.g., concrete walls. Surfaces are assumed smooth and straight, the roughness is accounted by diffuse scattering introduced in Section 6.1.7. Specular paths may be diffracted/shadowed similarly as the LOS and diffracted paths described in Section 6.1.2. This is illustrated in Figure 6-14 where the angle θ_j in Equation (6-3) is shown for the case of a specular diffracted path. There is a LOS RX route along the street. There are corresponding specular image routes for the RX as shown in the figure. For these routes the street openings act as blocking objects. In the upper graph the specular path is in the LOS region and in the lower graph the specular path in the NLOS region. The corresponding loss is

given by the recursive expressions (6-2) and (6-4) using the corresponding θ_j as indicated in the figure.

The specular paths are based on a layout defined by a global xyz Cartesian co-ordinate system, where x-axis points to “East”, y to “North” and z to “up”. Each wall is defined by its start and end points xy co-ordinates and a height.

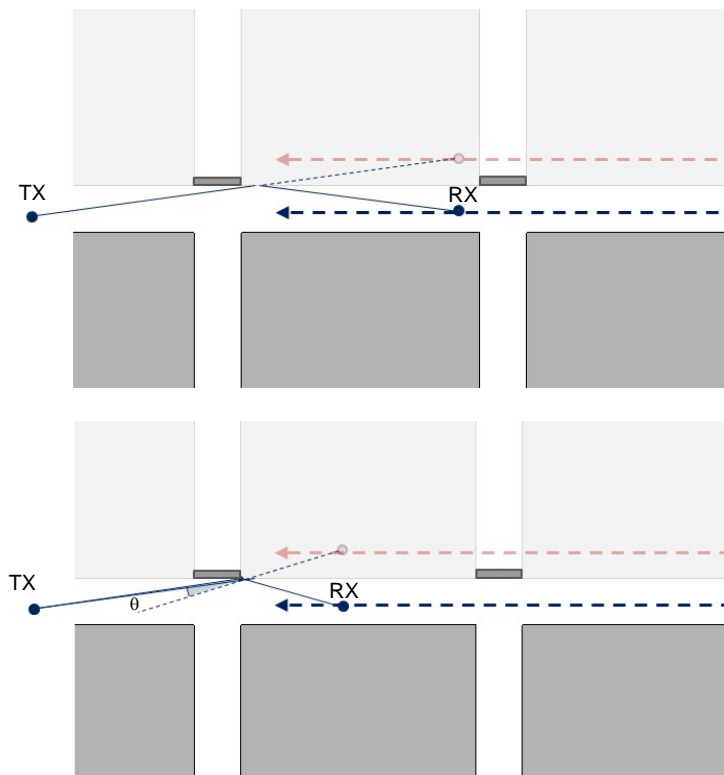


Figure 6-14: Specular path along the RX route.

The reflection point can be determined by mirroring a node, e.g., RX with respect to the reflecting surface and defining the crossing point of the surface and a line defined by the TX node and image of the RX node. A ground/floor/ceiling path exists only if both ends of the paths are in line-of-sight. For wall reflections a reflection point can be determined for each wall. Then a path between TX node, reflection point and RX node is composed. As a next step the existence of a path is found by checking if the composed path is blocked by any wall.

Figure 6-14 depicts an exemplary specular path along an RX route through a Manhattan-like grid. The corresponding route of the specular image of the RX is inside the building blocks. The path between TX and the specular image of RX is blocked by the street openings as indicated in the figure. This blocking results in corresponding diffraction nodes as indicated in the lower graph where the diffraction angle θ is indicated.

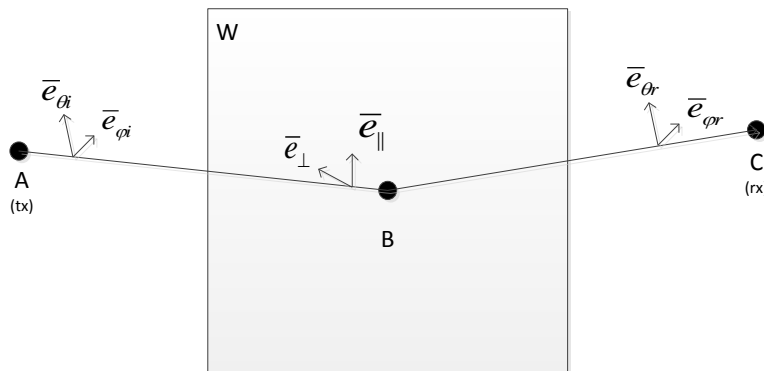


Figure 6-15: Reflection on a wall.

6.1.6.1 Calculation of reflection

This sub-section describes in details how to determine polarimetric reflection coefficients. In Figure 6-15: point A is a transmitter, B is a reflection point on a surface (plane W), and C is a receiver. Vector \overrightarrow{AB} is the direction of incidence ray (DoD) and vector \overrightarrow{BC} is the direction of reflected ray (DoA). The path length is $\|\overrightarrow{AB}\| + \|\overrightarrow{BC}\|$. Angles of arrival and departure are azimuth and elevation directions of vectors \overrightarrow{AB} and \overrightarrow{BC} . Matrix format polarimetric reflection coefficient

$$\mathbf{A} = \begin{bmatrix} \alpha_{\varphi\varphi} & \alpha_{\varphi\theta} \\ \alpha_{\theta\varphi} & \alpha_{\theta\theta} \end{bmatrix} \quad (6-10)$$

defines relation between the incidence and reflected electric field components as follows

$$\begin{bmatrix} E_{\varphi r} \\ E_{\theta r} \end{bmatrix} = \mathbf{A} \begin{bmatrix} E_{\varphi i} \\ E_{\theta i} \end{bmatrix} \quad (6-11)$$

Entries of matrix \mathbf{A} are calculated as

$$\begin{cases} \alpha_{\varphi\varphi} = (\bar{e}_{\varphi r} \cdot \bar{e}_{\perp i})(\bar{e}_{\varphi i} \cdot \bar{e}_{\perp i} R_{\perp}) + (\bar{e}_{\varphi r} \cdot \bar{e}_{\parallel i})(\bar{e}_{\varphi i} \cdot \bar{e}_{\parallel i} R_{\parallel}) \\ \alpha_{\theta\varphi} = (\bar{e}_{\theta r} \cdot \bar{e}_{\perp i})(\bar{e}_{\varphi i} \cdot \bar{e}_{\perp i} R_{\perp}) + (\bar{e}_{\theta r} \cdot \bar{e}_{\parallel i})(\bar{e}_{\varphi i} \cdot \bar{e}_{\parallel i} R_{\parallel}) \\ \alpha_{\varphi\theta} = (\bar{e}_{\varphi r} \cdot \bar{e}_{\perp i})(\bar{e}_{\theta i} \cdot \bar{e}_{\perp i} R_{\perp}) + (\bar{e}_{\varphi r} \cdot \bar{e}_{\parallel i})(\bar{e}_{\theta i} \cdot \bar{e}_{\parallel i} R_{\parallel}) \\ \alpha_{\theta\theta} = (\bar{e}_{\theta r} \cdot \bar{e}_{\perp i})(\bar{e}_{\theta i} \cdot \bar{e}_{\perp i} R_{\perp}) + (\bar{e}_{\theta r} \cdot \bar{e}_{\parallel i})(\bar{e}_{\theta i} \cdot \bar{e}_{\parallel i} R_{\parallel}) \end{cases} \quad (6-12)$$

where the unit vectors and Fresnel reflection coefficient are defined as listed here

- $\bar{s}_i = \begin{bmatrix} x_i \\ y_i \\ z_i \end{bmatrix}$ is the unit vector in the direction of the incidence ray ($\bar{s}_i \parallel \overrightarrow{AB}$)
- $\bar{s}_r = \begin{bmatrix} x_r \\ y_r \\ z_r \end{bmatrix}$ is the unit vector in the direction of the reflected ray ($\bar{s}_r \parallel \overrightarrow{BC}$)
- $\bar{n} = \begin{bmatrix} x_{end} - x_{begin} \\ y_{end} - y_{begin} \\ 0 \end{bmatrix} \times \begin{bmatrix} 0 \\ 0 \\ 1 \end{bmatrix} / \left\| \begin{bmatrix} x_{end} - x_{begin} \\ y_{end} - y_{begin} \\ 0 \end{bmatrix} \times \begin{bmatrix} 0 \\ 0 \\ 1 \end{bmatrix} \right\|$ is the unit normal vector of the surface to direction of the incidence plane

- $\bar{e}_{\varphi i} = \begin{bmatrix} -y_i \\ \sqrt{x_i^2+y_i^2} \\ x_i \\ \sqrt{x_i^2+y_i^2} \\ 0 \end{bmatrix}$ and $\bar{e}_{\theta i} = \bar{s}_i \times \bar{e}_{\varphi i}$ are unit vectors to directions of incidence polarization components $E_{\varphi i}$ and $E_{\theta i}$ in the reflection point B
- $\bar{e}_{\perp i} = \bar{s}_i \times \bar{e}_{\parallel i}$ and $\bar{e}_{\parallel i} = \frac{\bar{s}_i \times (\bar{n} \times \bar{s}_i)}{\|\bar{s}_i \times (\bar{n} \times \bar{s}_i)\|}$ are incidence rays unit vectors to directions perpendicular and parallel to the plane ABC
- $\bar{e}_{\parallel r} = \frac{\bar{s}_r \times (\bar{n} \times \bar{s}_r)}{\|\bar{s}_r \times (\bar{n} \times \bar{s}_r)\|}$ and $\bar{e}_{\perp r} = \bar{s}_r \times \bar{e}_{\parallel r}$ are reflected rays unit vectors to directions parallel and perpendicular to the plane ABC
- $\bar{e}_{\varphi r} = \begin{bmatrix} -y_r \\ \sqrt{x_r^2+y_r^2} \\ x_r \\ \sqrt{x_r^2+y_r^2} \\ 0 \end{bmatrix}$ and $\bar{e}_{\theta r} = \bar{s}_r \times \bar{e}_{\varphi r}$ are unit vectors to directions of reflected polarization components $E_{\varphi r}$ and $E_{\theta r}$ in the reflection point B
- $R_{\parallel} = \frac{\epsilon_r \sin \psi - \sqrt{\epsilon_r - \cos^2 \psi}}{\epsilon_r \sin \psi + \sqrt{\epsilon_r - \cos^2 \psi}}$ where ψ is the grazing angle, i.e. the angle between the surface and the incidence ray and ϵ_r is the relative permittivity (e.g. for concrete $\epsilon_r = 4.5$) [VA03]
- $R_{\perp} = \frac{\sin \psi - \sqrt{\epsilon_r - \cos^2 \psi}}{\sin \psi + \sqrt{\epsilon_r - \cos^2 \psi}}$ [VA03]

6.1.7 Diffuse paths

In addition to the specular paths a set of random point sources can be introduced over the surfaces of the exterior walls accounting for the surface roughness. Here it is important to conserve the power. According to [DGM04] the power scattered by a surface may be expressed in a similar way as for the spherical scatterer (6-8) i.e. as

$$P_{scat} = P_{source} \Delta S (1 - \beta) \pi^{-3} \left(\frac{\lambda}{4R_1 R_2} \right)^2 \cos(\theta_i) \cos(\theta_s), \quad (6-13)$$

where ΔS the size of a fraction of the surface area corresponding to the point source, β is the relative amount of specular power and θ_i and θ_s are the angles of the incoming and scattered paths relative to the normal of the surface (See Figure 6-16). A uniform distribution of point sources may be used. Moreover the distribution should be as sparse as possible in order reduce the model complexity. Typically the density of the point sources should not be higher than what can be resolved by the antennas used in the simulation.

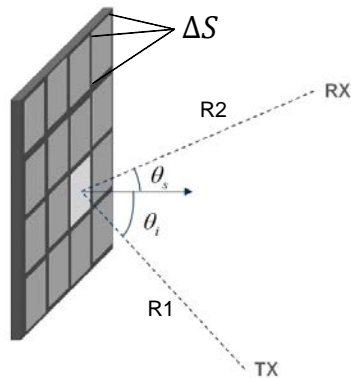


Figure 6-16: Random point sources approximating a rough surface.

6.1.8 Diffraction

6.1.8.1 Calculation of electric field with ray-method

When the ray interacts N times (such as reflection, transmission and diffraction) between source and observation points, let \bar{W}_n ($n = 1 \sim N$) be a dyadic coefficient which accommodates the ray interactions, in general, the electric field of the i^{th} ray can be derived as

$$E_i = \sqrt{\frac{P_t}{4\pi}} \frac{e^{-jkr_i}}{r_0} \mathbf{F}_t(\theta_i^{(t)}, \phi_i^{(t)}) \prod_{n=1}^N \bar{W}_n. \quad (6-14)$$

Where, P_t is transmitted power, k is wavenumber ($k = 2\pi/\lambda$), r_i is total path length, r_0 is path length between source and a first diffraction point and $(\theta_i^{(t)}, \phi_i^{(t)})$ are the angles of the launched ray from the source to the first diffraction point. The antenna pattern of transmitter \mathbf{F}_t is introduced with gain pattern G_θ and G_ϕ as

$$\mathbf{F}_t(\theta, \phi) = \sqrt{G_\theta(\theta, \phi)} \hat{\mathbf{u}}_\theta^t + \sqrt{G_\phi(\theta, \phi)} \hat{\mathbf{u}}_\phi^t. \quad (6-15)$$

Here $\hat{\mathbf{u}}_\theta^t$, $\hat{\mathbf{u}}_\phi^t$ are unit vectors with the origin at the source point. In this section, calculation of diffraction is of interest and the concept of UTD (Uniform Geometrical Theory of Diffraction) is focused.

6.1.8.2 Propagation of diffraction

Figure 6-17: illustrates canonical model for wedge diffraction where the spread angle of the wedge is $(2 - n)\pi$ with the incident ray impinges at skew angle. Unit vector $\hat{\mathbf{l}}$ parallel to the direction of the wedge is also defined as shown. Unit vectors $\hat{\mathbf{r}}_{\text{in}}$ and $\hat{\mathbf{r}}_D$ indicate direction of propagation for the incident ray and the diffracted ray with respect to diffraction point D, respectively.

These unit vectors are related based on the Fermat principle;

$$(\hat{\mathbf{r}}_{\text{in}} - \hat{\mathbf{r}}_D) \hat{\mathbf{l}} = 0. \quad (6-16)$$

Equation (6-16) indicates the extended Snell's law of $\beta_D = \beta_{\text{in}}$. The diffracted ray should be defined within a cone of the spread angle β_D with an apex at D: the diffracted ray propagates with arbitrary angles in a xy -plane. Hence the unit vector of direction of propagation for diffracted ray can be determined by

$$\hat{\mathbf{r}}_D = \begin{pmatrix} \sin \beta_{in} \cos \phi_D \\ \sin \beta_{in} \sin \phi_D \\ -\cos \beta_{in} \end{pmatrix}. \quad (6-17)$$

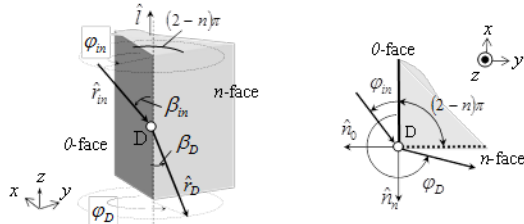


Figure 6-17: Model for canonical problem of diffraction

6.1.8.3 Calculation of diffraction

In order to consider diffraction, the dyadic coefficient \bar{W}_n is replaced with dyadic diffraction coefficient \bar{D} as

$$\bar{W}_n = \bar{D} A(r_{in}, r_D), \quad (6-18)$$

where $A(r_{in}, r_D)$ is so-called the spreading factor. For example, when the incident is spherical wave, the spreading factor is defined as

$$A(r_{in}, r_D) = \sqrt{\frac{r_{in}}{(r_{in} + r_D) r_D}}. \quad (6-19)$$

Here the path length between a source point (or a former diffraction point when multiple diffractions are considered) and a diffraction point is r_{in} . The path length between the diffraction point to an observation point (or a latter diffraction point when multiple diffractions are considered) is r_D . The dyadic diffraction coefficient \bar{D} is expressed with scalar diffraction coefficient

$$\bar{D} = (\hat{u}_{\beta}^{in} \quad \hat{u}_{\phi}^{in}) \begin{pmatrix} D_a & D_b \\ D_c & D_d \end{pmatrix} \begin{pmatrix} \hat{u}_{\beta}^D \\ \hat{u}_{\phi}^D \end{pmatrix} \quad (6-20)$$

Here, \hat{u}_{β}^{in} , \hat{u}_{ϕ}^{in} , \hat{u}_{β}^D , and \hat{u}_{ϕ}^D are defined as

$$\hat{u}_{\beta}^{in} = \frac{\hat{l} - \hat{r}_{in} \cos \beta_{in}}{\sin \beta_{in}} \quad (6-21)$$

$$\hat{u}_{\phi}^{in} = \frac{\hat{r}_{in} \times \hat{l}}{\sin \beta_{in}} \quad (6-22)$$

$$\hat{u}_{\beta}^D = \frac{\hat{l} - \hat{r}_D \cos \beta_D}{\sin \beta_D} \quad (6-23)$$

$$\hat{u}_{\phi}^D = \frac{\hat{r}_D \times \hat{l}}{\sin \beta_D} \quad (6-24)$$

There are various expressions of the scalar diffraction coefficient. Especially UTD is well-known method formulated by R. G. Kouyoumjian and P. H. Pathak [KP74] where the wedge is considered to be conductor. In this section, one of the practical methods by Luebbers [Lue84] is described. His expression of diffraction coefficient accounts for finite conductive wedge

which extended the capability of UTD for more practical use. When the wedge is long enough compared to wavelength, the diffraction coefficient in Figure 6-17 of the canonical problem is defined

$$\begin{pmatrix} D_a & D_b \\ D_c & D_d \end{pmatrix} = I_{2 \times 2} (D^+(\phi_D - \phi_{in}) + D^-(\phi_D - \phi_{in})) + R_0 D^-(\phi_D + \phi_{in}) + R_n D^+(\phi_D + \phi_{in}) \quad (6-25)$$

with

$$D^+(\phi) = \frac{-e^{-j\frac{\pi}{4}}}{2n\sqrt{2\pi k} \sin \beta_{in}} \cot\left(\frac{\pi+(\phi)}{2n}\right) F(kL a^+(\phi)), \quad (6-26)$$

$$D^-(\phi) = \frac{-e^{-j\frac{\pi}{4}}}{2n\sqrt{2\pi k} \sin \beta_{in}} \cot\left(\frac{\pi+(\phi)}{2n}\right) F(kL a^-(\phi)). \quad (6-27)$$

Here $I_{2 \times 2}$ is the 2x2 identity matrix and R_0 and R_n are matrices of reflection coefficient for “0” face and “n” face respectively as stated earlier (note: the matrix is expressed as matrix A in 6.1.6.1). The $F(x)$ is the Fresnel integral

$$F(x) = 2j\sqrt{x} e^{jx} \int_{\sqrt{x}}^{+\infty} e^{-j\tau^2} d\tau \quad (6-28)$$

where L and a^\pm are also defined:

$$L = \frac{r_D r_{in}}{r_D + r_{in}} \sin^2 \beta_{in}, \quad (6-29)$$

$$a^\pm(\mu) = 2 \cos^2\left(\frac{2n\pi N^\pm - \mu}{2}\right). \quad (6-30)$$

Here $\mu = \phi \pm \phi'$ and N^\pm is also given as:

$$2n\pi N^\pm - \mu = \pm\pi. \quad (6-31)$$

Here the closest integer value satisfying the equation is chosen. For further explanations, the terms in (6-26) – (6-31) and their formulations can be also found in [Bal89].

When multiple ray interactions (e.g. reflection, transmission and diffraction) are occurred N times, the dyadic coefficients $\bar{W}_{1 \sim N}$ should be defined respectively. After all, the coefficients are multiplied by inner product as (6-14) in order to derive electric field at an observation point.

6.1.8.4 Simple polarization model

In order to provide low complexity modelling of polarization the following approach is proposed. The parameters of the Berg recursive model [Ber95] are generalized to account for polarization by providing a polarization matrix for q_{90} i.e.

$$\mathbf{Q}_{90} = \begin{bmatrix} q_{90}^{VV} & q_{90}^{VH} \\ q_{90}^{HV} & q_{90}^{HH} \end{bmatrix}. \quad (6-32)$$

Each element accounts for the polarization coupling between horizontal (H) and vertical (V) polarized TX and RX antennas. If the propagation path is elevated the V-polarization is in the direction perpendicular to the path and the horizontal direction (H). The parameter v is

assumed to be independent of polarization. Literature indicates cross polarization discrimination (XPD) values in the range 10-20 dB. For diffraction it is assumed that the XPD is large. Lower XPD values are most likely caused by diffuse scattering and specular reflection resulting in paths having significant elevation angles. For the METIS model

$$\mathbf{Q}_{90} = q_{90} \begin{bmatrix} 1 & \infty \\ \infty & \gamma \end{bmatrix} \quad (6-33)$$

is proposed where q_{90} is the corresponding vertically co-polarized (VV) value defined in Section 6.1.1 and γ is the horizontally co-polarized (HH) value. The γ value is probably lower than 1, but this has to be calibrated by measurements. It is assumed that the XPD is very large which is obtained by selecting $q_{90}^{VH} = \infty$ and $q_{90}^{HV} = \infty$.

6.1.9 Penetration path

As outdoor-to-indoor paths, the paths through windows may be dominant. In this case, we know that waves passing through a window undergo diffraction, and electric field at arbitrary observation point can be calculated based on Kirchhoff's solution which is one of the methods in physical optics as follows [FE08].

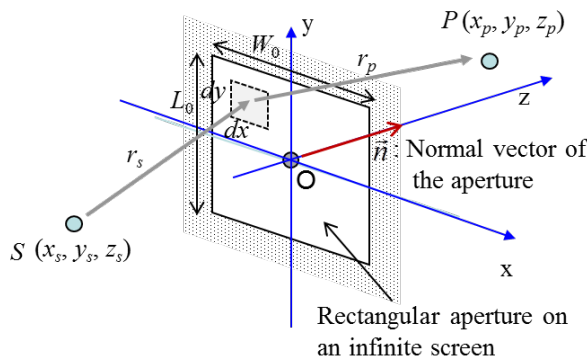


Figure 6-18: Basic analysis model.

Now, we assume an infinite screen with rectangular aperture between radiation source, S , and observation point, P , as shown in the Figure 6-18. When applying Kirchhoff's solution to this problem, electric field at P is given by

$$E = \frac{E_0}{\lambda} \int_{-\frac{L_0}{2}}^{\frac{L_0}{2}} \int_{-\frac{W_0}{2}}^{\frac{W_0}{2}} \frac{Q e^{-jk(r_s+r_p)}}{r_s r_p} dx dy. \quad (6-34)$$

Here, E_0 is constant depending on the transmitted power and antenna gain, λ and k are wave length and wave number, respectively. And also Q is the so-called inclination factor that is defined by

$$Q = \frac{\cos(\mathbf{r}_s, \mathbf{n}) + \cos(\mathbf{r}_p, \mathbf{n})}{2}. \quad (6-35)$$

Note that $\cos(\cdot, \cdot)$ is an operator defined by

$$\cos(\mathbf{x}, \mathbf{y}) = \frac{\mathbf{x}^T \mathbf{y}}{|\mathbf{x}| |\mathbf{y}|}. \quad (6-36)$$

Calculation of (6-34) may take a lot of time due to including integration operation. So, we propose an effective approximation method as follows.

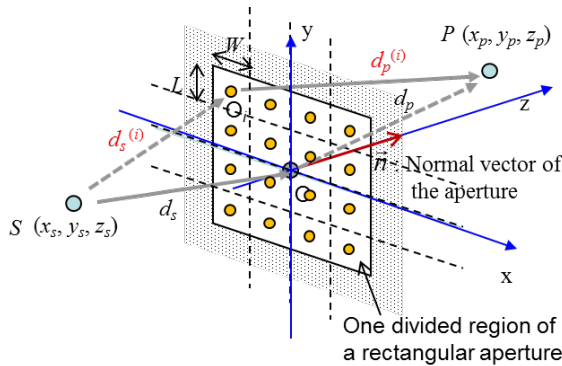


Figure 6-19: Analysis model.

Figure 6-19 shows an analysis model for approximation. When the aperture is equally divided into some regions, the electric field at P is expressed by

$$E = \frac{E_0}{\lambda} \sum_i \int_{y_i - \frac{L_0}{2}}^{y_i + \frac{L_0}{2}} \int_{x_i - \frac{W_0}{2}}^{x_i + \frac{W_0}{2}} \frac{Q e^{-jk(r_s+r_p)}}{r_s r_p} dx dy. \quad (6-37)$$

Here, $(x_i, y_i, 0)$ is coordinates of the centre of i^{th} region, O_i . Let the distances of SO_i and O_iP be $d_s^{(i)}$ and $d_p^{(i)}$, respectively. When the size of the divided regions satisfies the condition

$$\min(d_s^{(i)}, d_p^{(i)}) \geq 0.62 \sqrt{\frac{(\min(W, L))^3}{\lambda}}, \quad (6-38)$$

the so-called Fresnel approximation can be applied to (6-37), and electric field at P is approximated by

$$E = \frac{E_0}{\lambda} \sum_i \int_{y_i - \frac{L_0}{2}}^{y_i + \frac{L_0}{2}} \int_{x_i - \frac{W_0}{2}}^{x_i + \frac{W_0}{2}} \frac{Q e^{-jk(r_s+r_p)}}{r_s r_p} dx dy \approx \sum_i E_{s,i} U_i \Delta E_{p,i} \quad (6-39)$$

where

$$E_{s,i} = \frac{E_0 e^{-jkd_s^{(i)}}}{d_s^{(i)}} \quad (6-40)$$

$$\Delta E_{p,i} = \frac{e^{-jkd_p^{(i)}}}{d_p^{(i)}} \quad (6-41)$$

$E_{s,i}$ and $\Delta E_{p,i}$ represent electric field at the centre of the region and relative electric field from the centre of the region at P , respectively. The parameter U_i represents effect of the region, expressed by

$$U_i = Q e^{j \left(k \left(\frac{K}{2} (A^2 + B^2) - C_s - C_p \right) + \frac{\pi}{2} \right) \frac{(F(S_1) + F(S_2))(F(S_3) + F(S_4))}{2K}} \quad (6-42)$$

where Q and $F(\cdot)$ are inclination factor and Fresnel integral, defined by

$$Q \approx \frac{\cos(d_s^{(i)}, \mathbf{n}) + \cos(d_p^{(i)}, \mathbf{n})}{2}, \quad (6-43)$$

$$F(s) = \int_0^s e^{-j\frac{\pi}{2}t^2} dt, \quad (6-44)$$

respectively. The other parameters in (6-42) are given by

$$K = \frac{d_s^{(i)} + d_p^{(i)}}{d_s^{(i)} d_p^{(i)}}. \quad (6-45)$$

$$A = \frac{d_p^{(i)} x_s + d_s^{(i)} x_p}{d_s^{(i)} + d_p^{(i)}}. \quad (6-46)$$

$$B = \frac{d_p^{(i)} y_s + d_s^{(i)} y_p}{d_s^{(i)} + d_p^{(i)}}. \quad (6-47)$$

$$C_s = \frac{2x_s x_i - x_i^2 + 2y_s y_i - y_i^2}{2d_s^{(i)}}. \quad (6-48)$$

$$C_p = \frac{2x_p x_i - x_i^2 + 2y_p y_i - y_i^2}{2d_p^{(i)}}. \quad (6-49)$$

$$S_1 = \sqrt{\frac{2K}{\lambda}} \left(\frac{W}{2} - A + x_i \right). \quad (6-50)$$

$$S_2 = \sqrt{\frac{2K}{\lambda}} \left(\frac{W}{2} + A - x_i \right). \quad (6-51)$$

$$S_3 = \sqrt{\frac{2K}{\lambda}} \left(\frac{L}{2} - B + y_i \right). \quad (6-52)$$

$$S_4 = \sqrt{\frac{2K}{\lambda}} \left(\frac{L}{2} + B - y_i \right). \quad (6-53)$$

Hereafter, U_i is called aperture contribution factor in this document.

Although (6-42) includes Fresnel integral, same approximation method exists. Therefore, the calculation time of (6-39) is much less than that of (6-34). In addition, the calculation time becomes shorter under following conditions.

When the length of d_s is equal to or larger than the value of $0.62 \sqrt{(\min(W_0, L_0))^3 / \lambda}$, $d_s^{(i)}$ in Equations (6-40) to (6-49) can be replace to d_s , and also C_s become zero. In the same way, when the length of d_p is equal to or larger than the value of $0.62 \sqrt{(\min(W_0, L_0))^3 / \lambda}$, $d_p^{(i)}$ can be replaced by d_p , and also C_p become zero. Therefore, electric field at P is given by

$$E = \begin{cases} E_s U \Delta E_p & \text{for } \min(d_s, d_p) \geq 0.62 \sqrt{(\min(W_0, L_0))^3 / \lambda} \\ E_s \sum_i U_i \Delta E_{p,i} & \text{for } d_s \geq 0.62 \sqrt{(\min(W_0, L_0))^3 / \lambda} > d_p \\ \Delta E_p \sum_i E_{s,i} U_i & \text{for } d_p \geq 0.62 \sqrt{(\min(W_0, L_0))^3 / \lambda} > d_s \end{cases}. \quad (6-54)$$

By comparing with (6-35), we understand that the procedure for the calculation is reduced in (6-40).

6.1.9.1 Simple outdoor to indoor model

A simplified method to model outdoor to indoor is to make use of the shadowing model described in Section 6.1.4. By Babinet's principle the shadowing properties of a window is complementary to the screen i.e.

$$L_{Window}|_{dB} = -20 \log_{10}((F_{h1} + F_{h2})(F_{w1} + F_{w2})) \quad (6-55)$$

where F_{h1}, F_{h2} and F_{w1}, F_{w2} are defined according to Equation (6-6) and Figure 6-7.

6.1.10 Analysis

The map based model provides an alternative to performing extensive measurement campaigns to parameterize GSCM type of models. As the model is kept at a simple level it does not suffer from the corresponding complexity of full blown ray tracing. The required effort lies mainly in providing a map and/or geometric description of the propagation environment. An important advantage is that this modelling provides realistic and accurate spatial channel characteristics required for advanced antennas like massive MIMO. A drawback is that the complexity might be unnecessary high when simple antennas are studied. However, for the case of e.g. D2D a lower complexity level may be chosen using only LOS and diffracted paths in combination with the shadowing model i.e. neglecting scatterers and specular paths.

In Figure 6-20 the V2V measured path loss is compared with that of the map model. Very similar behaviour is observed resulting in average shadowing loss around 7 dB supporting that the model provides realistic results. Further in Figure 6-21 the Doppler spectrum caused by waves propagation along a street which are scattered by objects along the street is compared for measurements [MSK+09] and the map based model. The results are very similar suggesting that the modelling approach provides realistic results.

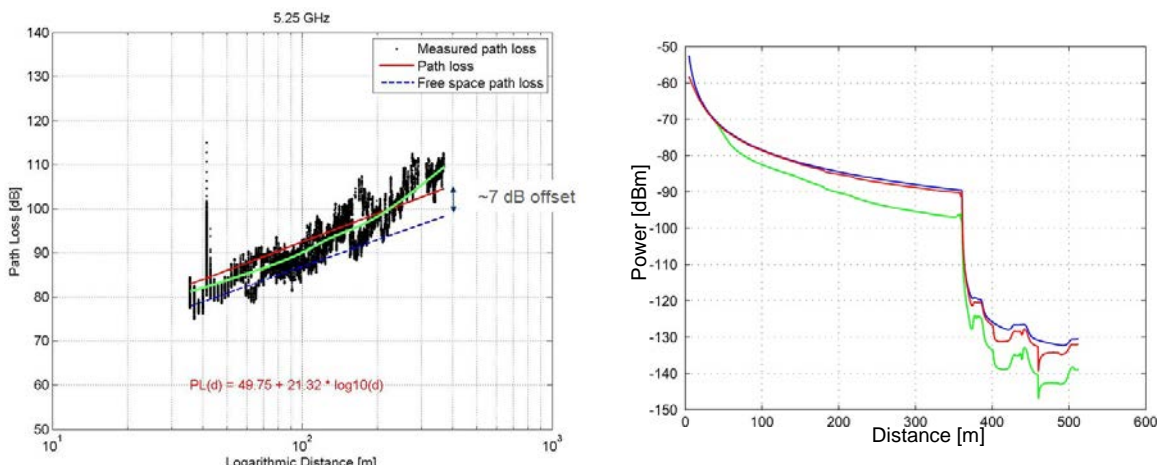


Figure 6-20: Measured path loss for V2V measured in Oulu (left) and map based model with shadowing objects along the streets (right). The details of the measurement campaign are described in Section B.1.3.1 and of the shadowing model in Section 6.1.4.

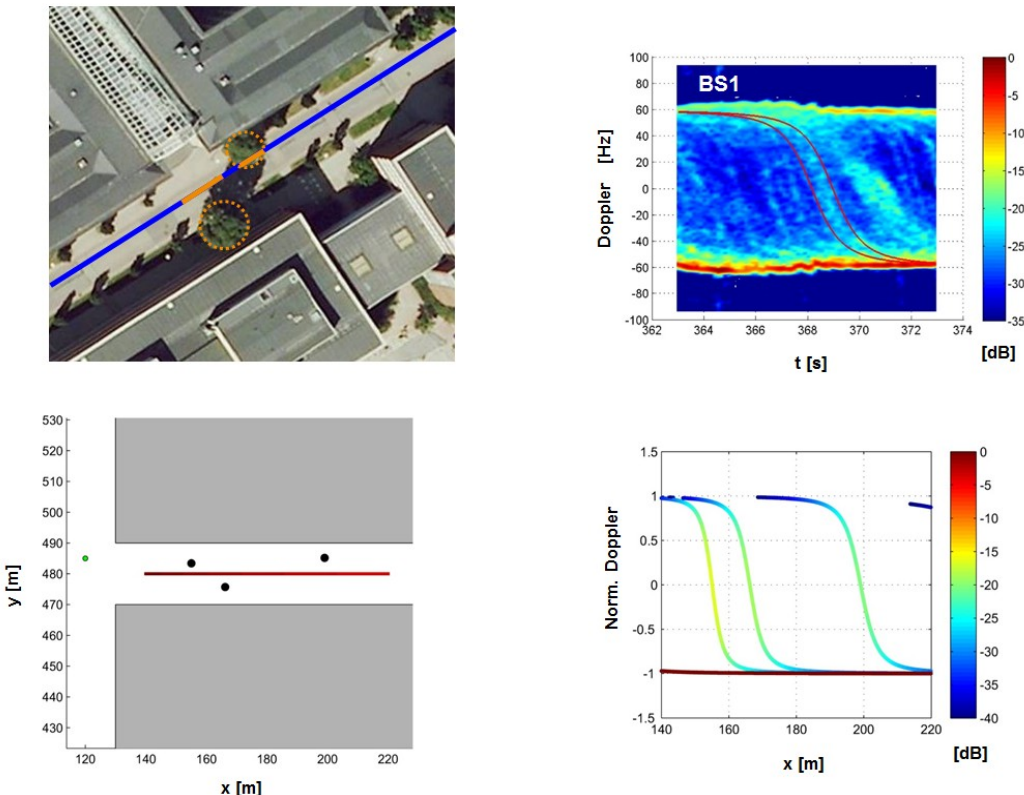


Figure 6-21: Measured Doppler spectrum along a street in Kista Stockholm (upper graphs) and modelled spectrum as described in Section 6.1.5 (lower graphs). The scatterers and measurement routes are indicated in the leftmost figures.

6.2 Visibility region based modelling approach

The visibility region based modelling framework has its origin in the COST 2100 model [VZ12]. In COST 2100 the scattering clusters exist in the environment, and are not specific to a certain link. In the beginning of a simulation the environment is created in a stochastic manner. After that the radios (transmitter and receiver nodes) are placed at their locations and the propagation between them is calculated. After the stochastic definition of the environment, the calculation of the propagation is deterministic, i.e. it only depends on the locations of the two radios. This is like simplified ray tracing, even simpler than in the map-based model. Instead of a real map, an artificial “map” of randomly drawn clusters is used. Like in actual ray tracing, also large scale parameters including the total power of the link are composed by adding up the contributions of propagation paths.

Like in the original COST 2100 model, each cluster has its visibility region. Furthermore the clusters have fixed geographic coordinates, and the channel evolves smoothly when the mobile moves. When two mobiles are located close to each other, they see partly same clusters, and thus have a similar propagation environment, including angular characteristics hence maintaining spatial consistency.

One shortcoming with the original COST 2100 model is the base station centric approach. The COST 2100 model describes, which clusters are visible to a certain mobile location with a given base station location. This does not directly support D2D communication, where the communication cannot be assumed to happen between one static and one moving radio, but both ends of the link can be at arbitrary locations, and can be moving. To obtain this, the COST 2100 model was modified. The basic structure of the model is explained below.

6.2.1 Scattering clusters

In the beginning of a simulation the environment is created by dropping clusters to random locations according to a pre-defined distribution. If the environment has not any pre-defined structure the distribution is uniform, but the distribution could also be selected such that it includes structure models like buildings or streets. The spatial distribution of clusters can also be 3D and thus enabling the 3 dimensional propagation characteristics to be used.

6.2.2 Visibility regions

Like in COST 2100 every cluster has a visibility region. The shapes and sizes of the visibility regions are model parameters. Typically a radio can see several clusters at the same time, thus multiple visibility regions intersect in all possible locations. The visibility regions may be defined in 3D in order to create a height-dependency of the propagation parameters. Visibility regions are expected to grow with increasing height.

6.2.3 Coupling between clusters

To allow also dual bounce propagation paths, the coupling between clusters needs to be defined. This is new compared to the present COST models. Note that in the proposed model links longer than the visibility region size would not exist without the coupling between clusters. Two clusters may or may not be coupled. The probability of coupling decreases as a function of distance between the clusters.

LOS/NLOS condition is determined by defining some clusters as “LOS coupled”. This approach enables consistent modelling of the LOS condition, since the LOS probability of closely located links is not independent.

6.2.4 Radio link

A radio link can consist of three different types of paths:

- 1) *Line-of-sight path* exists between two radios that are located in visibility regions of LOS coupled clusters.
- 2) *First order interaction* exists if two radios are in the visibility region of the same cluster.
- 3) *Second order interaction* exists if the first radio is within the VR of the first cluster, the second radio is within the VR of the second cluster, and the two clusters are coupled. Even remote radios with a long link distance may be connected by coupled clusters

The radio link is calculated by adding up all paths between the RX and TX. The propagation delay is calculated directly from the path length, and the angles of arrival and departure are based on the locations of the TX/RX and the locations of the first/last interacting clusters.

Neither path loss nor shadowing is modelled explicitly with any empirical path loss model or distribution of shadow fading. Instead, they both result from the composition of path gains. Those gains are calculated as free space path loss, adding a cluster-specific random attenuation at each interaction. Different types of interactions can be assumed at clusters, and it has an impact on how much loss there is at each interaction.

6.2.5 Analysis

This modelling framework can fulfil all the requirements for the 5G channel model listed in Section 2. It can describe consistently both large and small scale as well as 3D characteristics of the channel. It also enables fair comparison between different types of links, because e.g. cellular and D2D propagation is calculated from the same model, only with different height. Because of the implicit modelling of the link gain, it even solves the challenging problem of creating realistic large scale correlation properties for dual mobility case (see Section 2.1). Basic components of the modelling approach are illustrated in Figure 6-22.

As with the other modelling approaches, this approach should be verified against measurements. The COST2100 model has been parameterized to large extent already within the COST community. However, the modifications introduced in this section have not been verified.

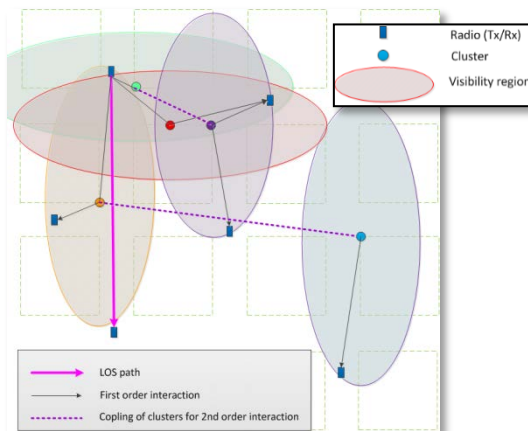


Figure 6-22: Basic components of the visibility region based modelling approach.

6.3 Grid-based GSCM (GGSCM) modelling approach

The initial *stochastic* channel models described in Section 7 of this document are based on WINNER II, WINNER+ and IMT-Advanced. They all follow the same principles, but there are some differences in path loss models, parameter values, availability of elevation parameters, etc. According to the drop concept, the UEs are located randomly and the propagation parameters are randomly drawn from the pre-defined probability distributions. The channel is assumed to be stationary along a short distance (segment), but this assumption does not hold for longer distances, therefore the parameters need to be re-calculated. This approach is called as block-stationary modelling in which large scale (LS) and small scale (SS) parameters are fixed during the segment and fully different between the segments. To improve the reality and time evolution, it is possible to interpolate between the segments/drops. However, it is difficult to ensure spatial consistency especially between nearby users in multi-user case. Therefore, a new method is proposed and drafted in the following.

In contrary to WINNER II/WINNER+/IMT-Advanced (Legacy GSCM) model, in the GGSCM approach a discrete two-dimensional map of possible UE locations is defined. Instead of drawing LS and SS cluster parameters for the actual user locations, the cluster parameters are drawn for every grid point. Then the cluster parameters for the actual UE locations are interpolated between four nearest grid points. Figure 6-23: shows the location of grid points (GPs), which are separated by a constant spacing ΔGP .

The grid can be intuitively understood as a drop in which the distance between two adjacent users is constant in x and y dimensions. The drops are independent between the GPs, i.e., LS and SS parameters are randomly drawn from the pre-defined distributions (similar to the legacy GSCM). ΔGP can be either a) longer than the correlation distance, making the LS parameters fully independent between GPs, which makes implementation easier, or b) shorter than the correlation distance, which means we have to ensure the correlation between GPs.

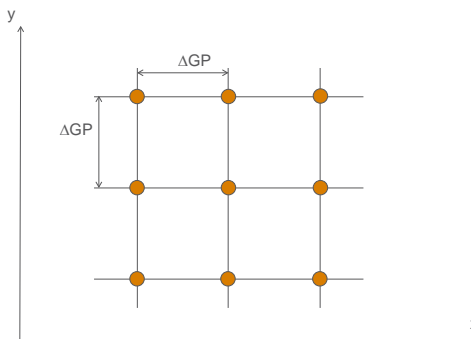


Figure 6-23: Grid Points (GPs) separated by ΔGP in the xy plane.

6.3.1 Single bounce vs. multiple bounce clusters

In addition to the legacy GSCM, also single bounce clusters are defined in the proposed GGSCM. In case of a single bounce cluster, AoA, AoD, and delay are coupled. However, in case of multiple bounces, the connection between first and last clusters is unknown. The number of single bounce clusters may be either a parameter or a random variable.

6.3.2 Physical locations of clusters

For the simulation of very large arrays a modelling of spherical waves is required, thus it is necessary to define physical locations (x,y,z coordinates) of clusters. In case of a single bounce cluster (SBC) the modelling is straightforward. The SBC clusters can be calculated directly based on the drawn cluster parameters in each GP. These parameters are delay and DoD (or DoA). Then the direction at the other end is calculated by matching DoA (or DoD) with DoD (or DoA) and delay. In this case half of the SBC clusters may be (randomly) chosen to be calculated based on the TX-side cluster parameters and half based on the RX-side cluster parameters and the originally drawn cluster delays and also powers and cluster indexing are kept.

In case of multiple bounces, DoAs, DoDs, and delays are defined based on the legacy GSCM principle. The cluster locations are defined based on DoA, DoD, and delay. The physical distances of the first bounce cluster (FBC) and the last bounce cluster (LBC) are randomly drawn with the limitation of total distance from TX to RX via FBC and LBC is adjusted according to the delay.

After fixing the physical locations, drifting of LS and SS parameters is enabled for a short distance movement as illustrated in Figure 6-24. Implementation of the drifting is straightforward and is fully based on the geometry (for each impulse response, phase, delay, and angle of arrival is recalculated).

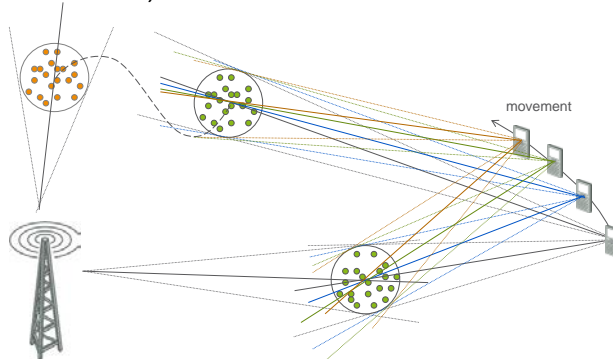


Figure 6-24: Propagation parameter drifting due to small movement of the UE.

6.3.3 LOS probability

The method to model LOS/NLOS condition is as follows. LOS component, i.e. a specular path with the shortest delay, is always present, but in the NLOS condition the Ricean K factor is set

to zero (linear) value for simplicity. (This approach ignores specular reflection, which is for future study.) The benefit is that the same parameter tables for both LOS and NLOS cases can be used. LOS probability (p_{LOS}) is a parameter in the table. The K factor has a pre-defined probability distribution function. In the case of NLOS, the K factor is zero.

6.3.4 Interpolation of parameters between grid points

The interpolation can be done via an advanced birth-death process in which physical location of the clusters is fixed, and DoA/DoD, delay, Doppler etc. are dynamic.

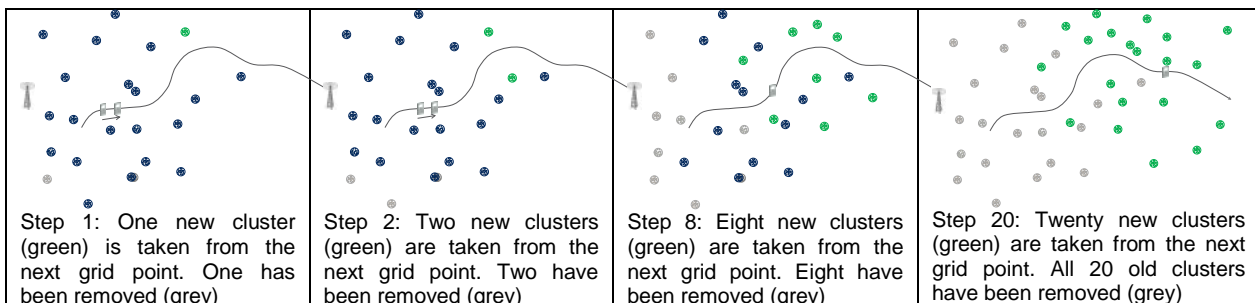


Figure 6-25: Advanced birth-death process.

The clusters are calculated only for the grid points and on the need basis to avoid excessive use of memory. A smooth birth-death process of clusters can be realized by weighting the cluster powers in each grid point based on the distance from UE. All clusters of the four closest grid points are active and the powers are weighted by a UE location dependent function

$$P_{GP} = \frac{1/D_{GP}}{\sum_{i=1}^4 (1/D_i)}, \quad (6-56)$$

where D_i denotes the distance between GP i and the user and D_{GP} is the distance between GPs. Figure 6-25 shows a simplified example how UE sees different clusters from two adjacent GPs. When the UE is close to the first GP, it sees mostly the clusters related to that GP. Along the route, it will see more and more clusters from the next GP. Steps 1, 2, 8, and 20 are example steps along the route. The number {1, 2, 8, 20} refers to how many clusters are changed. For simplicity, ΔGP was selected as the distance of the first zero of the LS correlation.

6.3.5 Shadowing and path loss

Path loss is calculated from the distance between TX and RX. It is possible to partly utilize path loss equations from Legacy GSCM. Shadowing map for cellular case it is quite straightforward but it will be more complicated for D2D case in which x_1, y_1 coordinates are defined for UE1 and x_2, y_2 coordinates for UE2. Since all combinations of (x_1, y_1, x_2, y_2) need to be modelled, it may lead to a 4-dimensional map. For reducing the complexity, shadowing for only the four nearest grid points around each transmitter and receiver location is calculated. The final shadowing value at UE location is interpolated from the four values.

6.3.6 Example of a cluster drop

Figure 6-26 shows an initial simulation result of cluster locations in macro-cell case (WINNER C1 NLOS). Grid spacing is 50 m and the single bounce and multi-bounce clusters are defined per grid. The x, y coordinates denote location in metres, rotated squares with different colours depict grid points and the circles with the same colour the related cluster locations. Dark circle means BS location. If the UE is located exactly at a GP, it will see the cluster denoted with the same colour. As can be seen from the Figure 6-26, there are no common clusters for different GPs. However, movement from between the grids should lead to smooth change of delay, angle of arrival/departure, Doppler etc. based on the interpolation method described above. The statistics of the LS and SS parameters between the GPs is for future study.

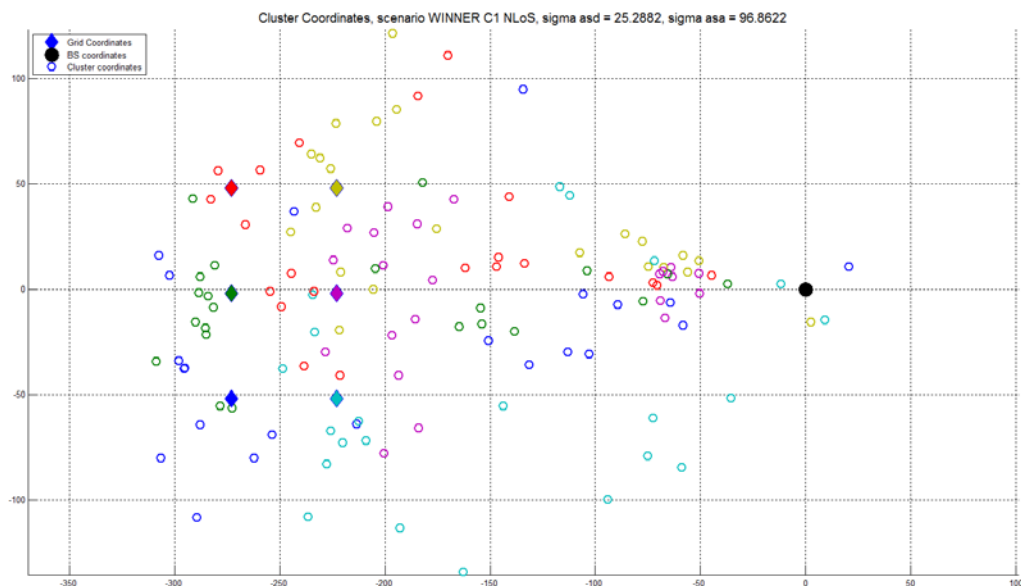


Figure 6-26: Simulation of GGSCM (WINNER C1 NLOS).

6.3.7 Analysis

Four requirements for 5G channel modelling were identified in Section 2. The legacy GCSM approach is appropriate for higher frequencies with a proper parameterization, but fails in the other three requirements. The proposed grid based GSCM supports spherical waves and should enable consistent modelling of LS & SS parameters when one link end is spatially distributed, e.g. with very large arrays on base station side or with longer continuous route of a mobile terminal. The grid based GSCM proposal does not support full spatial consistency with both link ends moving arbitrarily. The above introduction of the GGSCM is 2D for simplicity, and 3D extension including elevation parameters of propagation as well as UE height dependency is for future study.

6.4 Comparison of Approaches

The four approaches (existing GSCM and three new approaches introduced above) are briefly compared in the table below. This is a high level comparison and several details are left out from the comparison due to the incompleteness of the new approaches.

Feature	VRBM	GGSCM	METIS Initial Models	
			GSCM	Map-based
Path Loss	implicit	separate, empirical	separate, empirical	implicit
Shadowing	implicit	separate	separate	implicit
Explicit building model / generic	generic	generic	generic	explicit
Parametrization by measurements	hard	easy	easy	easy
Support spherical waves	yes	yes	no	yes
Support extremely large arrays beyond coherence distance	yes	no	no	yes
Support dual mobility	yes	no	no	yes
Support 3D	yes	yes	yes	yes
Support mmW	yes	yes	yes	yes
Dynamic modelling	yes	yes	no	yes
Polarization modelling	XPR	XPR	XPR	Ray-based
Maturity	low	low	high	medium
Complexity in terms of definition	low	medium	medium	medium-high*
Complexity in terms of calculation of channel realizations	medium	medium	medium	medium-high*
Public implementation available	no	no	partly	no

* much simpler than full-blown ray tracing. Further simplification will be done by D1.4.

7 Initial METIS Channel Model

This section describes the Initial METIS Channel Models. Depending on the test case or rather the propagation scenario, either a stochastic or a deterministic model shall be applied. More precisely, two approaches were selected to serve as initial channel models, i.e. the Geometry-based Stochastic Channel Model (GSCM) further developed from WINNER/3GPP, and the map-based model introduced in Section 6.1. The selection of these two approaches shall not be restrictive, i.e. other channel model approaches (e.g., the visibility region based approach) are not excluded from further development and may therefore be included in the final METIS channel models.

Within METIS a multitude of channel models per propagation scenario was proposed. A coarse classification of the proposed channel models can be done by their requirement for explicit building/scene models. In case explicit building/scene models are available it is possible to calculate propagation paths based on this deterministic environment and to add some random elements on top of it. Without these building/scene models propagation paths need to be generated fully stochastically. In both cases it shall be possible to apply various antenna models; the channel models are therefore independent of the antennas. Section 7.1 gives some basic information about antenna modelling, especially on how to correctly deal with 3D antenna patterns.

Section 7.2 gives the steps needed for the channel model with available building/scene models, while Section 7.3 exemplifies the WINNER based channel model approach including new findings from 3GPP's study items on 3D channel modelling and D2D, as well as further investigations in METIS.

Output of the channel model shall be complex MIMO channel impulse responses per user link depending on the user location. In some evaluations it may be adequate to investigate only the path loss and shadowing effect. In these cases, the channel model output is the sum effect of path loss and shadowing which can be determined by PL & SF models of WINNER based approach or by a sum of path attenuations of the map based model, without considering polarizations or antenna models. For some cases the time evolution of the channel is of importance, therefore it has to be clarified whether the users are mobile or stationary. In case of mobile users, user routes need to be defined in terms of time and space.

7.1 Antenna modelling

The influence of the antenna is typically modelled by its radiation field pattern \underline{F} or radiation power pattern P . These metrics depend on the direction (θ, ϕ) of the incoming or outgoing wave. Whereas P is a scalar quantity, \underline{F} is a vector quantity that gives information about the directivity (complex gain to/from certain direction) given a certain polarization.

$$\underline{F}(\theta, \phi) = \left. \frac{\underline{E}(r, \theta, \phi) e^{jk_0 r}}{|\underline{E}(r, \theta, \phi)|_{\max}} \right|_{r=\text{const} \rightarrow +\infty} = \begin{pmatrix} F_\theta(\theta, \phi) \\ F_\phi(\theta, \phi) \end{pmatrix} \quad (7-1)$$

The radiation power pattern $P(\theta, \phi)$ in linear scale is defined as

$$P(\theta, \phi) = |F_\theta(\theta, \phi)|^2 + |F_\phi(\theta, \phi)|^2 \quad (7-2)$$

7.1.1 Spherical coordinate system

In the past there has been a lot of confusion since different coordinate systems were used to define propagation and antenna characteristics. This problem has already been acknowledged in WINNER+ [WIN10-D53]. Harmonizing the coordinate systems, i.e. using only one coordinate system for propagation and antenna characteristics, is therefore a crucial point. The spherical coordinate system as specified in the ISO 31-11 standard was selected as the one that should be used from now on and is thus given in the following.

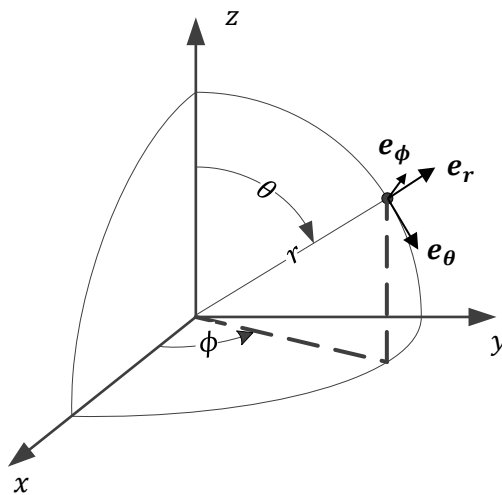


Figure 7-1: Spherical coordinate system.

The spherical coordinate system as depicted in Figure 7-1 defines $\theta \in [0^\circ; +180^\circ]$ as the zenith / inclination angle and $\phi \in [-180^\circ; +180^\circ]$ as the azimuth angle. $e_r(\theta, \phi)$, $e_\theta(\theta, \phi)$ and $e_\phi(\theta, \phi)$ denote the orthonormal basis vectors of the coordinate system.

$$e_r(\theta, \phi) = \begin{pmatrix} \sin \theta \cos \phi \\ \sin \theta \sin \phi \\ \cos \theta \end{pmatrix} \quad e_\theta(\theta, \phi) = \begin{pmatrix} \cos \theta \cos \phi \\ \cos \theta \sin \phi \\ -\sin \theta \end{pmatrix} \quad e_\phi(\theta, \phi) = \begin{pmatrix} -\sin \phi \\ \cos \phi \\ 0 \end{pmatrix} \quad (7-3)$$

Given a position vector $\mathbf{r} = (x \ y \ z)^T = r e_r(\theta, \phi)$, the angles θ and ϕ can be determined by

$$\theta = \arccos \left\{ \begin{pmatrix} 0 \\ 0 \\ 1 \end{pmatrix}^T e_r(\theta, \phi) \right\} \quad (7-4)$$

and

$$\phi = \arg \left\{ \begin{pmatrix} 1 \\ j \\ 0 \end{pmatrix}^T e_r(\theta, \phi) \right\}. \quad (7-5)$$

7.1.2 Vector field rotation / mechanical tilting

When an antenna is rotated around its principal axes the radiation field is rotated likewise. Since this vector field rotation is not too trivial we will discuss it in the following. We define a global coordinate system (GCS) with coordinates (θ, ϕ) and a local coordinate system (LCS) with coordinates (θ', ϕ') . With $\mathbf{R} \in \mathbb{R}^{3 \times 3}$ being an arbitrary rotation between those two coordinate systems with

$$e_{r,GCS}(\theta, \phi) = \mathbf{R} e_{r,LCS}(\theta', \phi') \quad (7-6)$$

$$e_{r,LCS}(\theta', \phi') = \mathbf{R}^T e_{r,GCS}(\theta, \phi). \quad (7-7)$$

Note that this relationship does not apply for the other two basis vectors e_θ and e_ϕ .

From (7-7) and (7-4) it follows

$$\theta' = \arccos \left\{ \begin{pmatrix} 0 \\ 0 \\ 1 \end{pmatrix}^T \mathbf{R}^T e_{r,GCS}(\theta, \phi) \right\}. \quad (7-8)$$

From (7-7) and (7-5) it follows

$$\phi' = \arg \left\{ \begin{pmatrix} 1 \\ j \\ 0 \end{pmatrix}^T \mathbf{R}^T \mathbf{e}_{r,GCS}(\theta, \phi) \right\} \quad (7-9)$$

The radiation field pattern as given in the LCS is defined as

$$\begin{aligned} \mathbf{F}_{LCS}(\theta', \phi') &= \begin{pmatrix} F_{\theta,LCS}(\theta', \phi') \\ F_{\phi,LCS}(\theta', \phi') \end{pmatrix} \\ &= F_{\theta,LCS}(\theta', \phi') \mathbf{e}_{\theta,LCS}(\theta', \phi') + F_{\phi,LCS}(\theta', \phi') \mathbf{e}_{\phi,LCS}(\theta', \phi') \end{aligned} \quad (7-10)$$

Since the basis vectors $\mathbf{e}_\theta(\theta, \phi)$ and $\mathbf{e}_\phi(\theta, \phi)$ are different in both coordinate systems, there has to be a transformation from LCS to GCS:

$$\mathbf{F}_{GCS}(\theta, \phi) = \begin{pmatrix} \cos \psi & -\sin \psi \\ \sin \psi & \cos \psi \end{pmatrix} \begin{pmatrix} F_{\theta,LCS}(\theta', \phi') \\ F_{\phi,LCS}(\theta', \phi') \end{pmatrix} \quad (7-11)$$

With the system transformation from above it follows

$$\cos \psi = \mathbf{e}_{\theta,GCS}(\theta, \phi)^T \mathbf{R} \mathbf{e}_{\theta,LCS}(\theta', \phi') \quad (7-12)$$

$$\sin \psi = \mathbf{e}_{\phi,GCS}(\theta, \phi)^T \mathbf{R} \mathbf{e}_{\theta,LCS}(\theta', \phi') \quad (7-13)$$

7.1.3 Polarization transfer matrix

The polarization transfer matrix \mathbf{M} describes the change in polarization of a single electromagnetic wave departing from a transmitting antenna in direction (θ^d, ϕ^d) and arriving at a receiving antenna at (θ^a, ϕ^a) . With the antenna gains at transmitter and receiver the overall transfer function can be described by

$$\mathbf{F}_{GCS,rx}(\theta^a, \phi^a)^T \mathbf{M} \mathbf{F}_{GCS,tx}(\theta^d, \phi^d) \quad (7-14)$$

Note that although the antenna patterns are both given in their GCSs, they still differ for the given angles.

7.1.4 LOS depolarization

In case there is a line-of-sight (LOS) connection between transmitting and receiving antenna the polarization transfer matrix can be determined geometrically, since in this case it is just a coordinate transformation. For parallel coordinate systems at transmitter and receiver $\theta^a + \theta^d = 180^\circ$ and $\phi^a = \phi^d + 180^\circ$ and \mathbf{M} results to

$$\mathbf{M}_{LOS} = \begin{pmatrix} 1 & 0 \\ 0 & -1 \end{pmatrix} \quad (7-15)$$

The factor -1 is due to the opposing directions of $\mathbf{e}_{\phi,tx}$ and $\mathbf{e}_{\phi,rx}$ as can be seen in Figure 7-2:.

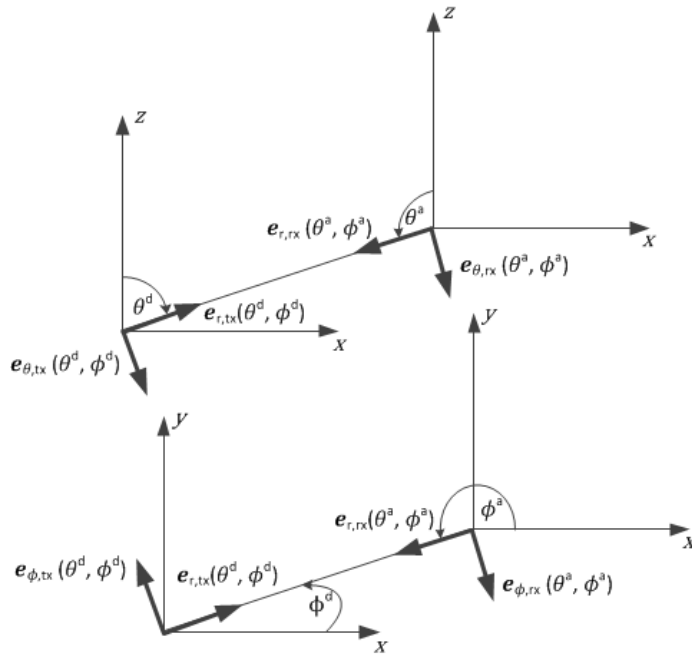


Figure 7-2: Deterministic LOS depolarization.

Due to LOS time delay there is a deterministic phase Φ_{LOS} which needs to be applied, resulting in the following expression for the LOS component:

$$\begin{pmatrix} F_{\theta,\text{GCS},\text{rx}}(\theta^a, \phi^a) \\ F_{\phi,\text{GCS},\text{rx}}(\theta^a, \phi^a) \end{pmatrix}^T \begin{pmatrix} +\exp(j\Phi_{\text{LOS}}) & 0 \\ 0 & -\exp(j\Phi_{\text{LOS}}) \end{pmatrix} \begin{pmatrix} F_{\theta,\text{GCS},\text{tx}}(\theta^d, \phi^d) \\ F_{\phi,\text{GCS},\text{tx}}(\theta^d, \phi^d) \end{pmatrix}. \quad (7-16)$$

Note that this is different to WINNER II, in which a random phase offset between vertical-to-vertical (VV) and horizontal-to-horizontal (HH) polarization is introduced to the LOS path.

7.1.5 NLOS depolarization

In case of NLOS \mathbf{M} is the product of various polarization filters and coordinate transformations according to the incident planes of passed interactions.

$$\begin{pmatrix} F_{\theta,\text{GCS},\text{rx}}(\theta^a, \phi^a) \\ F_{\phi,\text{GCS},\text{rx}}(\theta^a, \phi^a) \end{pmatrix}^T \begin{pmatrix} m_{\theta\theta} & m_{\theta\phi} \\ m_{\phi\theta} & m_{\phi\phi} \end{pmatrix} \begin{pmatrix} F_{\theta,\text{GCS},\text{tx}}(\theta^d, \phi^d) \\ F_{\phi,\text{GCS},\text{tx}}(\theta^d, \phi^d) \end{pmatrix} \quad (7-17)$$

With $m_{\theta\theta}$, $m_{\theta\phi}$, $m_{\phi\theta}$, $m_{\phi\phi}$ being the NLOS depolarization coefficients. These coefficients can only be determined if there is additional data available about the interactions. Such data includes electromagnetic properties of the scatterer material, their locations as well as their plane normals. With the geometry-based stochastic channel model approach this is not the case, therefore a stochastic approach is used to randomly generate the depolarization coefficients. With the map based model the depolarization coefficients can be determined by calculating the reflection and diffraction coefficients as described in Sections 6.1.6.1 and 6.1.8.

7.2 Map-based model

This model is based on a specified geometrical environment. The model applies to those propagation scenarios that provide the necessary geometry data.

These include:

- PS1: Urban Microcell
- PS2: Urban Macrocell
- PS4: Indoor Office
- PS5: Indoor Shopping Mall
- PS6: Highway
- PS7: Festival (open air)
- PS8: Stadium

Table 7-1: Parameter table for the map based model

Parameter	Symbol [unit]	Propagation scenario						
		PS1	PS2	PS4	PS5	PS6	PS7	PS8
Object density	$D [1/m^2]$	0.1	0.1 (traffic jam)	0.05	0.05	0.1 (traffic jam)	4	4
Object height	$h [m]$	1.5/4	1.5/4	1.5	1.5	1.5/4	1.5	1.5
Object width	$w [m]$	0.5/3	0.5/3	0.5	0.5	3	0.5	0.5

Creation of the environment:

Step 1: Define the map in global xyz coordinate system. Give each wall start and end xy coordinates and a height (z coordinate). For simplicity assume the map spans an area on the positive x and y quarter, i.e. the origin is in the lower left corner of the map. For METIS scenarios Madrid (PS1&2), virtual reality office (PS4), and shopping mall (PS5) the wall layouts are defined in the Appendix 1. For the open air festival and stadium scenarios (PS7, PS8) no walls are modelled. For the highway scenario (PS6) a simplified wall layout based on Figure A-8 in Appendix A can be sketched.

Step 2: Draw randomly shadowing/scattering objects to the map from uniform distribution

$$o_n(x, y, z) = (X_n, Y_n, Z_n) \quad (7-18)$$

where $X_n \sim U(0, X_{max})$, $Y_n \sim U(0, Y_{max})$, $Z_n = 0$, $n = 1, \dots, (X_{max}Y_{max}D)$, X_{max} and Y_{max} are the edges of the map on x and y axis, respectively. Different distribution densities are used for streets (Madrid grid), indoor office, shopping mall, stadium and outdoor festival. The shadowing screen sizes (*object height & width*) according to (6-5) and (6-8) for different objects i.e. humans, vehicles, trees, lamp posts etc. are given in Table 7-1. This and the previous step are performed only once. After this step the procedure is fully deterministic.

TX and RX locations:

Step 3: Define a single transmitter location or a trajectory and a single receiver location or a trajectory in xyz co-ordinates. The roles of TX and RX are interchangeable, but for simplicity we use terms TX and RX throughout this description. Multiple radio links can be modelled consistently to the environment specified by Steps 1 and 2 by repeating Steps from 3 to 16. To simplify the notation the following steps are described for a single radio link only.

Define position vectors for receiver antenna elements u and transmitter antenna elements v

$$\begin{cases} \mathbf{r}_u^{rx} = [x_u \ y_u \ z_u]^T \\ \mathbf{r}_v^{tx} = [x_v \ y_v \ z_v]^T \end{cases} \quad (7-19)$$

where $u = 1, \dots, U$ and $v = 1, \dots, V$. U and V denote the total number of antenna elements at receiver and transmitter, respectively.

Note that if the antenna arrays are small and the radiation patterns are defined with a common phase centre it is adequate to specify only locations of TX and RX antenna phase centres, not locations of individual elements. In this case antenna indices u and v can be dropped from location vectors and the path coefficients defined in the coming steps. Finally the spatial separation of antennas is taken into account in Step 16.

Determination of propagation paths:

Step 4: Determine possible pathways i.e. LOS and diffracted pathways according to environment description (Madrid/Manhattan map or indoor/stadium geometry). In Manhattan case use method described in Section 6.1.2.

Step 5: Similarly to Step 4 determine specular paths as described in Section 6.1.6. These paths are equivalent to the “direct paths” using apparent TX and RX nodes. Use single order reflection of TX and RX. All surfaces seen by either RX or TX will result in respective mirror images.. The number of combinations is equal to $(N_{\text{imTX}} + 1) \times (N_{\text{imRX}} + 1)$, with N_{imTX} and N_{imRX} being the number of images of a single transmitter and a single receiver, respectively. For all these combinations determine pathways according to Step 4.

Step 6: For diffuse scattering determine point source distributions over planar surfaces i.e. exterior and indoor walls, floors, ground etc. as described in Section 6.1.7. These distributions should be as dense as required by the angular resolution (aperture) of the antenna used in the simulations. For low resolution a tile size of 10 m x 10 m is used and for high resolution a tile size of 5 m x 5 m is used.

Step 7: For each segment of all direct and specular paths determine the shadowing loss L_{shad} according to Section 6.1.4. Each shadowing object may result a loss for that specific path. The total shadowing loss for a specific path is the sum of the losses from all shadowing objects, in dB units, along that specific pathway. The loss for a specific shadowing object is determined for all path segments in the vicinity (on the same street) of the object.

Step 8: For each path determine diffraction loss according to Equations (6-1)-(6-4) in Section 6.1.1.

Step 9: Determine scatterers (both on wall surfaces and other objects) which are in LOS and near to either TX or RX end. Determine paths according to Steps 4 and 5 between either TX and scatterer close to RX or RX and scatterer close to TX according to Section 6.1.5. For these paths determine the signal strength according to Steps 4-8. For the last path segment between the scatterer and either TX or RX use cross-sections as defined by Equations (6-8) and (6-14). Discard weak scatterers i.e. those for which

$$20 \log_{10} \left(\frac{R d_{\text{direct}}}{2d_1 d_2} \right) < -30 \text{ dB} \quad (7-20)$$

where R is the radius of the scatterer, d_{direct} is the distance for the direct path between the last corner and either TX or RX and, d_1 and d_2 are the distances for the two path segments between last corner and either TX or RX via the scatterer.

Step 10: Determine scatterers which are in LOS with respect to two nodes (TX, RX or building corner) which in turn are in NLOS with respect to each other. For these paths determine the signal strength according to Steps 4-8. For the last path segment between the scatterer and either TX or RX use cross-sections as defined by Equations (6-8) and (6-14).

Determination of channel coefficient matrices:

Step 11: For LOS paths the 2x2 polarization transfer matrix is given by

$$\mathbf{h}_{u,v}^{\text{LOS}} = \begin{bmatrix} 1 & 0 \\ 0 & -1 \end{bmatrix} \frac{\exp(j2\pi d_{u,v}/\lambda)}{4\pi d_{u,v}/\lambda} \quad (7-21)$$

Determine delay $\tau_{u,v}^{\text{LOS}} = d_{u,v}/c$ and wave vectors $\mathbf{k}_{u,v}^{\text{rx,LOS}}$ and $\mathbf{k}_{u,v}^{\text{tx,LOS}}$ from the geometry.

Step 12: Determine path parameters for $k = 1, \dots, K$ specular reflected paths. Calculate path lengths $d_{k,u,v}$ from the geometry. Calculate 2x2 propagation matrices for reflected paths with matrix \mathbf{A} as defined in Section 6.1.6.

$$\mathbf{h}_{k,u,v}^{\text{ref}} = \mathbf{A}_{k,u,v}^{\text{ref}} \frac{\exp(j2\pi d_{k,u,v}/\lambda)}{4\pi d_{k,u,v}/\lambda} \quad (7-22)$$

Determine delay $\tau_{k,u,v}^{\text{ref}}$ and wave vectors $\mathbf{k}_{k,u,v}^{\text{rx,ref}}$ and $\mathbf{k}_{k,u,v}^{\text{tx,ref}}$ from the geometry.

Step 13: Determine path parameters for $k = 1, \dots, K'$ diffracted paths. Calculate path lengths $d_{k,u,v}$ from the geometry. Calculate 2x2 propagation matrices for diffracted paths either with simplified method as defined in Section 6.1.1 and 6.1.8.4

$$\mathbf{h}_{k,u,v}^{\text{dif}} = \begin{bmatrix} L_n^{\theta\theta} e^{j\Phi_k^{\theta\theta}} & L_n^{\theta\phi} e^{j\Phi_k^{\theta\phi}} \\ L_n^{\phi\theta} e^{j\Phi_k^{\phi\theta}} & L_n^{\phi\phi} e^{j\Phi_k^{\phi\phi}} \end{bmatrix}, \quad (7-23)$$

where terms L_n are defined in Equation (6-1) and i.i.d. random phases Φ follow uniform distribution in range $[0, 2\pi]$, or with diffraction formulas as defined in Section 6.1.8

$$\mathbf{h}_{k,u,v}^{\text{dif}} = \mathbf{A}_{k,u,v}^{\text{dif}} \frac{\exp(j2\pi d_{k,u,v}/\lambda)}{4\pi d_{k,u,v}/\lambda} \quad (7-24)$$

Determine delay $\tau_{k,u,v}^{\text{dif}}$ and wave vectors $\mathbf{k}_{k,u,v}^{\text{rx,dif}}$ and $\mathbf{k}_{k,u,v}^{\text{tx,dif}}$ from the geometry.

Step 14: Determine parameters for $k = 1, \dots, K''$ paths resulting from scattering objects and diffuse scattering. Calculate path lengths $d_{k,u,v}$ from the geometry. Calculate 2x2 propagation matrices for scattered paths as follows

$$\mathbf{h}_{k,u,v}^{\text{sca}} = \sqrt{P_{k,u,v}^{\text{scat}}} \mathbf{A}_{k,u,v}^{\text{sca}} = \sqrt{P_{k,u,v}^{\text{scat}}} \begin{bmatrix} e^{j\Phi_k^{\theta\theta}} & e^{j\Phi_k^{\theta\phi}} \\ e^{j\Phi_k^{\phi\theta}} & e^{j\Phi_k^{\phi\phi}} \end{bmatrix} \quad (7-25)$$

where the scattered power $P_{k,u,v}^{\text{scat}}$ is calculated from Equations (6-8) and (6-13) for the scattering objects and the diffuse scattering, respectively. Parameter value $\alpha = 0$ and $\beta = 0.5$ are used in Equations (6-8) and (6-13), respectively. Entries of $\mathbf{A}_{k,u,v}^{\text{sca}}$ have random phases Φ following uniform distribution in range $[0, 2\pi]$. Determine delay $\tau_{k,u,v}^{\text{sca}}$ and wave vectors $\mathbf{k}_{k,u,v}^{\text{rx,sca}}$ and $\mathbf{k}_{k,u,v}^{\text{tx,sca}}$ from the geometry.

Calculation of the radio channel transfer function:

Step 15: Normalize the propagation path coefficients \mathbf{h} in order to apply the path loss L_{tot} . Calculate a normalization factor as a sum of Frobenius norms of matrix coefficients of all paths, i.e. LOS, reflected diffracted, scattered, etc. over all path indices k ,

$$C_{u,v} = \sum \|\mathbf{h}_{u,v}\|_F \quad (7-26)$$

Step 16: Finally the complex impulse response between RX antenna element u and TX antenna elements v with a *true motion* of transceivers is given by

$$H_{u,v}(t, \tau) = \sqrt{\frac{L_{tot}}{C_{u,v}}} \left(\mathbf{g}_u^{\text{rx}} \left(-\mathbf{k}_{u,v}^{\text{rx,LOS}}(t) \right)^T \mathbf{h}_{u,v}^{\text{LOS}}(t) \mathbf{g}_v^{\text{tx}} \left(\mathbf{k}_{u,v}^{\text{tx,LOS}}(t) \right) \delta(\tau - \tau_{u,v}^{\text{LOS}}(t)) + \right.$$

$$\begin{aligned} \sum_{k=1}^K \mathbf{g}_u^{\text{rx}}(-\mathbf{k}_{k,u,v}^{\text{rx,ref}}(t))^T \mathbf{h}_{k,u,v}^{\text{ref}}(t) \mathbf{g}_v^{\text{tx}}(\mathbf{k}_{k,u,v}^{\text{tx,ref}}(t)) \delta(\tau - \tau_{k,u,v}^{\text{ref}}(t)) + \\ \sum_{k=1}^{K'} \mathbf{g}_u^{\text{rx}}(-\mathbf{k}_{k,u,v}^{\text{rx,dif}}(t))^T \mathbf{h}_{k,u,v}^{\text{dif}}(t) \mathbf{g}_v^{\text{tx}}(\mathbf{k}_{k,u,v}^{\text{tx,dif}}(t)) \delta(\tau - \tau_{k,u,v}^{\text{dif}}(t)) + \\ \sum_{k=1}^{K''} \mathbf{g}_u^{\text{rx}}(-\mathbf{k}_{k,u,v}^{\text{rx,sca}}(t))^T \mathbf{h}_{k,u,v}^{\text{sca}}(t) \mathbf{g}_v^{\text{tx}}(\mathbf{k}_{k,u,v}^{\text{tx,sca}}(t)) \delta(\tau - \tau_{k,u,v}^{\text{sca}}(t)), \end{aligned} \quad (7-27)$$

where \mathbf{g}_u^{rx} and \mathbf{g}_v^{tx} are the complex polarimetric antenna pattern vectors, of RX element u and TX element v , for the direction and frequency of corresponding wave vectors. Above the time parameter t is interchangeable to a parameter indicating TX and RX locations. Except if moving scattering objects are introduced having time dependent channel coefficients with temporal variation independent on TX and RX locations.

With the virtual motion (as defined in Section 6), assuming there is no time evolution of propagation parameters and that each element experiences the same Doppler shift per path, the complex impulse response is given by

$$\begin{aligned} H_{u,v}(t, \tau) = \\ \sqrt{\frac{L_{tot}}{C_{u,v}}} \left(\mathbf{g}_u^{\text{rx}}(-\mathbf{k}_{u,v}^{\text{rx,LOS}})^T \mathbf{h}_{u,v}^{\text{LOS}} \mathbf{g}_v^{\text{tx}}(\mathbf{k}_{u,v}^{\text{tx,LOS}}) e^{it\omega^D,LOS} \delta(\tau - \tau_{u,v}^{\text{LOS}}) + \right. \\ \sum_{k=1}^K \mathbf{g}_u^{\text{rx}}(-\mathbf{k}_{k,u,v}^{\text{rx,ref}})^T \mathbf{h}_{k,u,v}^{\text{ref}} \mathbf{g}_v^{\text{tx}}(\mathbf{k}_{k,u,v}^{\text{tx,ref}}) e^{it\omega_k^D,\text{ref}} \delta(\tau - \tau_{k,u,v}^{\text{ref}}) + \\ \sum_{k=1}^{K'} \mathbf{g}_u^{\text{rx}}(-\mathbf{k}_{k,u,v}^{\text{rx,dif}})^T \mathbf{h}_{k,u,v}^{\text{dif}} \mathbf{g}_v^{\text{tx}}(\mathbf{k}_{k,u,v}^{\text{tx,dif}}) e^{it\omega_k^D,\text{dif}} \delta(\tau - \tau_{k,u,v}^{\text{dif}}) + \\ \left. \sum_{k=1}^{K''} \mathbf{g}_u^{\text{rx}}(-\mathbf{k}_{k,u,v}^{\text{rx,sca}})^T \mathbf{h}_{k,u,v}^{\text{sca}} \mathbf{g}_v^{\text{tx}}(\mathbf{k}_{k,u,v}^{\text{tx,sca}}) e^{it\omega_k^D,\text{sca}} \delta(\tau - \tau_{k,u,v}^{\text{sca}}) \right), \end{aligned} \quad (7-28)$$

where ω^D is the Doppler frequency in rad/s. If both antenna arrays are small in size the equation can be further simplified by approximation

$$\begin{aligned} H_{u,v}(t, \tau) = \\ \sqrt{\frac{L_{tot}}{C}} \left(\mathbf{g}_u^{\text{rx}}(-\mathbf{k}_{u,v}^{\text{rx,LOS}})^T \mathbf{h}^{\text{LOS}} \mathbf{g}_v^{\text{tx}}(\mathbf{k}_{u,v}^{\text{tx,LOS}}) e^{it\omega^D,LOS} \delta(\tau - \tau^{\text{LOS}}) + \right. \\ \sum_{k=1}^K \mathbf{g}_u^{\text{rx}}(-\mathbf{k}_{k,u,v}^{\text{rx,ref}})^T \mathbf{h}_k^{\text{ref}} \mathbf{g}_v^{\text{tx}}(\mathbf{k}_{k,u,v}^{\text{tx,ref}}) e^{it\omega_k^D,\text{ref}} \delta(\tau - \tau_k^{\text{ref}}) + \\ \sum_{k=1}^{K'} \mathbf{g}_u^{\text{rx}}(-\mathbf{k}_{k,u,v}^{\text{rx,dif}})^T \mathbf{h}_k^{\text{dif}} \mathbf{g}_v^{\text{tx}}(\mathbf{k}_{k,u,v}^{\text{tx,dif}}) e^{it\omega_k^D,\text{dif}} \delta(\tau - \tau_k^{\text{dif}}) + \\ \left. \sum_{k=1}^{K'''} \mathbf{g}_u^{\text{rx}}(-\mathbf{k}_{k,u,v}^{\text{rx,sca}})^T \mathbf{h}_k^{\text{dif}} \mathbf{g}_v^{\text{tx}}(\mathbf{k}_{k,u,v}^{\text{tx,sca}}) e^{it\omega_k^D,\text{sca}} \delta(\tau - \tau_k^{\text{sca}}) \right), \end{aligned} \quad (7-29)$$

where propagation matrices are determined to centre points of TX and RX arrays and antenna indices u and v can be dropped.

7.2.1 Outdoor-to-Indoor channel model

The outdoor-to-indoor (or O2I) channel model described here is based on ray tracing in outdoors and indoors, and the penetration path model based on physical optics in Section 6.1.9. Concept of this model is as follows. As shown in the Figure 7-3, first, outdoor ray-tracing between outdoor BS and windows and indoor ray-tracing between the windows and indoor UE are performed. Next, outdoor-to-indoor rays (or O2I rays) are obtained by combining outdoor rays with indoor rays, and then, the electric field strength of each O2I ray is calculated taking the aperture effect of the window into consideration. Detailed procedures in this model are described below.

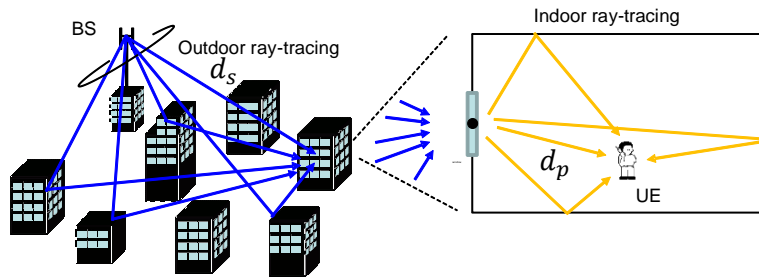


Figure 7-3: Concept of proposed O2I channel model.

At first, some apertures are equally set as shown in the Figure 7-4. Let the size of the window be $\tilde{W}_0 \times \tilde{L}_0$. Condition of the size of aperture, $W_0 \times L_0$, is given by

$$W_0 = \frac{\tilde{W}_0}{N_{W_0}} \leq \left(\left(\frac{d_s}{0.62} \right)^2 \lambda \right)^{1/3} \quad (7-30)$$

$$L_0 = \frac{\tilde{L}_0}{N_{L_0}} \leq \left(\left(\frac{d_s}{0.62} \right)^2 \lambda \right)^{1/3} \quad (7-31)$$

Here, N_{W_0} and N_{L_0} are the number of tiles within the window in horizontal and vertical direction, respectively. And then, each aperture is divided into $N_W \times N_L$ regions as shown in Figure 7-4 (or Figure 6-19). Condition of the size of each region, $W \times L$, is given by

$$W = \frac{W_0}{N_W} \leq \left(\left(\frac{d_p^{(i)}}{0.62} \right)^2 \lambda \right)^{1/3}, \quad (7-32)$$

and

$$L = \frac{L_0}{N_L} \leq \left(\left(\frac{d_p^{(i)}}{0.62} \right)^2 \lambda \right)^{1/3}. \quad (7-33)$$

In (7-32), $d_p^{(i)}$ is the distance between the centre of region i and the UE as described in Section 6.1.9.

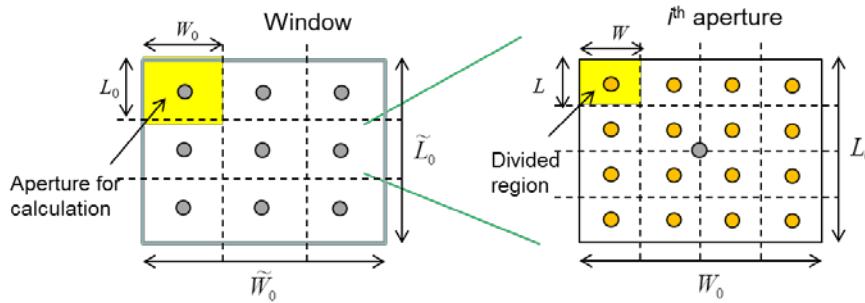


Figure 7-4: Setting of apertures

Next, channels between BS and UE are obtained by the following procedure.

1. Trace outdoor-rays between BS and each centre of the aperture in outdoor, and calculate electric field, $E_i^{(m)}$ (m : outdoor-ray number, i : aperture number), cf. Figure 7-5.

2. Trace indoor-rays between centre of each divided region and UE in indoor, and calculate relative electric field, $\Delta E_{i,j}^{(n)}$ (n : indoor ray number, j : divided region number), cf. Figure 7-5.
3. Combine the outdoor-ray and the indoor-ray, and calculate the contribution factor of region, $U_{i,j}^{(m,n)}$, based on Equation (6-42).
4. Calculate the electric field of each combined ray (O2I ray) between BS and UE as follows.

$$E_{i,j}^{(m,n)} = E_i^{(m)} U_{i,j}^{(m,n)} \Delta E_{i,j}^{(n)} \quad (7-34)$$

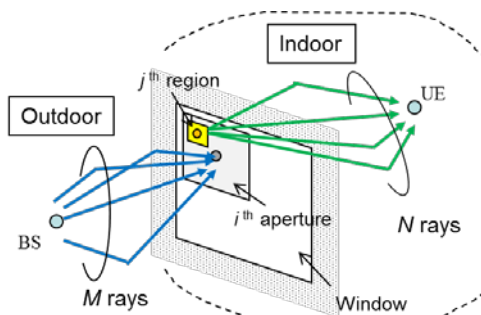


Figure 7-5: Ray-tracing procedure.

In this model, the total number of O2I paths between BS and UE is $I \times J \times M \times N$ with I being the number of apertures and J being the number of divided regions. Finally the total electric field is given by

$$E = \sum_{i=1}^I \sum_{m=1}^M E_i^{(m)} \sum_{j=1}^J \sum_{n=1}^N U_{i,j}^{(m,n)} \Delta E_{i,j}^{(n)}. \quad (7-35)$$

Note that, when the loss that is caused by the material of the window cannot be ignored, we should add the related loss to the equation (7-34). This model is basically applied to each window when there are plural windows in the room.

Examples of calculation based on this model are shown in Figure 7-6. Calculation conditions are frequency of 2 GHz, BS antenna height of 10 m, UE antenna height of 1.5 m, ceiling height of 3 m and material of walls (ceiling, floor) of concrete. While the maximum number of reflections indoors is set to 7, for the outdoor part only the direct ray is taken into account. In Figure 7-6, the thick blue line represents a window.

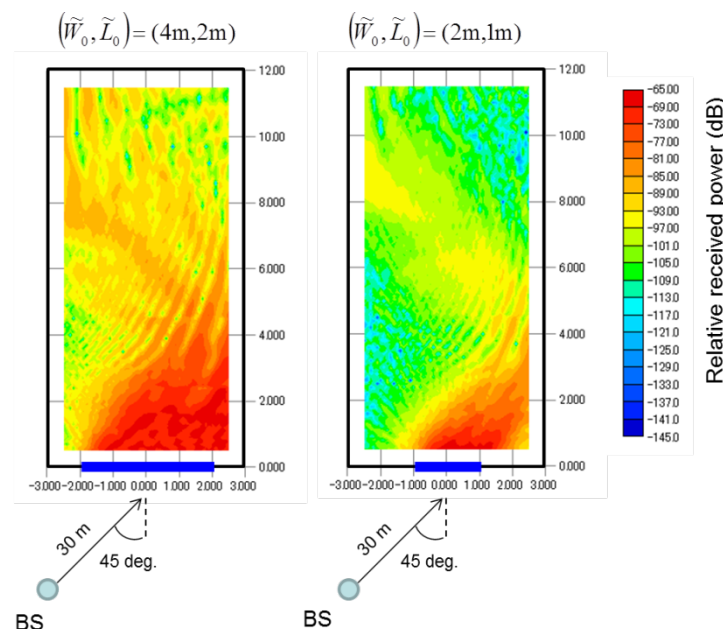


Figure 7-6: Calculation results.

7.3 Geometry-based stochastic model

The geometry-based stochastic model described in this section follows the WINNER approach as depicted in Figure 7-7. For Urban Micro-cell and Urban Macro-cell scenarios it is extended to 3D propagation based on the latest findings in 3GPP, cf. [3GPP14-36873]. Since the study item within 3GPP is not yet finished, the current status is included within this section, including some clarifying changes and extensions.

The model shall be applicable to the METIS propagation scenarios without predefined building structure geometries, i.e.

- Urban Micro-cell O2O, O2I
- Urban Macro-cell O2O, O2I
- Rural Macro
- Indoor Office
- Highway
- Open Air Festival

Please note that the parameterisation currently only encompasses UMi and UMa scenarios. The parameterisation of the other scenarios has to be further investigated and verified. The D2D scenarios depict another difficulty, since it is not yet clear how to take the dual mobility into account except for the additional Doppler shift at the transmitter. Due to these shortcomings alternative stochastic models for each propagation scenario are given in Table 7-2. The following instructions are to a large amount based on [3GPP14-36873].

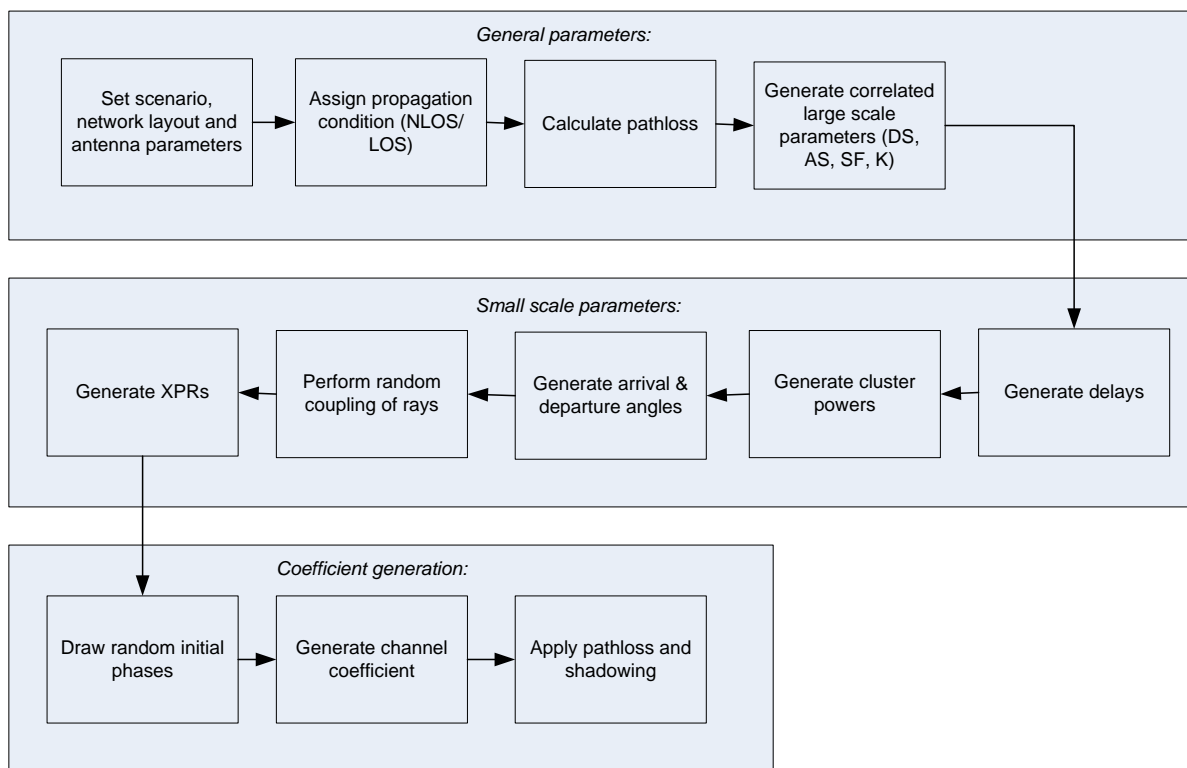


Figure 7-7: Channel coefficient generation procedure [3GPP14-36873].

Table 7-2: Recommended PL and fading models for each propagation scenario

#	Propagation Scenario	In/Out	Link types for stochastic model	Path Loss Model	Fading Channel Model
1	Urban Micro	O2O	BS-UE	3GPP 3D-UMi LOS/NLOS	
			D2D/V2V	WINNER+ B1, Manhattan layout with 10 dB extra loss, page 74-75, Table 4-1 [WIN10-D53]	IMT-Advanced-UMi [ITU09-2135], AoA / ASA at both link ends, dual mobility – or Shibuya D2D Table 5-3
		O2I	BS-UE	3GPP 3D-UMi O-to-I	
2	Urban Macro	O2O	BS-UE	3GPP 3D-UMa LOS/NLOS	
			BH	IMT-Advanced UMa [ITU09-2135] (hBS =25 m, hUE=10 m)	IMT-Advanced UMa [ITU09-2135]
		O2I	BS-UE	3GPP 3D-UMa O-to-I	
3	Rural Macro	O2O	BS-UE	IMT-Advanced-RMa [ITU09-2135]	
			D2D/V2V	WINNER+ C2 [WIN10-D53] (hBS =1.5 m, hUE=1.5 m)	WINNER+ C2 [WIN10-D53] AoA / ASA at both link ends, dual mobility
			BH	IMT-Advanced RMa [ITU09-2135]	
		O2I	BS-UE	IMT-Advanced RMa-O2I [ITU09-2135] -Outdoor PL from O2O-R	IMT-Advanced RMa-O2I [ITU09-2135] Angle spreads: BS: O2O-RMa, UE: O2I-UMa
			D2D/V2V	WINNER+ C4 [WIN10-D53], page 75, Table 4-1	IMT-Advanced-UMa (O2I) [ITU09-2135]
4	Indoor Office	I2I	BS-UE	WINNER II -A1-rr (room-to-room) [WIN08-D112]	
5	Indoor Shopping mall	I2I	BS-UE	WINNER II -A1-cc (corridor-to- corridor) WINNER II -A1-cr WINNER II -A1-rr [WIN08-D112]	
6	Highway	O2O	BS-UE	IMT-Advanced-RMa [ITU09-2135]	
			V2V	Karedal [KTC+09]	
		O2O	BS-UE	IMT-Advanced-RMa [ITU09-2135]	
7	Open Air Festival	O2O	D2D	WINNER+ C2 [WIN10-D53] (hBS =1.5 m, hUE=1.5 m)	WINNER+ C2 [WIN10-D53] Angle params at BS: Update to UE params.
			BH	IMT-Advanced RMa [ITU09-2135]	

7.3.1 Choose the system centre frequency f_c

A common default value is 2 GHz.

7.3.2 Choose one of the scenarios (3D-UMa, 3D-UMi)

7.3.3 Choose the number of BSs and UEs

Please note that in the following BSs refer to transmitters (TXs) and UEs refer to receivers (RXs) since we are only considering the user downlink.

7.3.4 Choose BS and UE antenna field patterns

$F_{rx}(\theta, \phi)$ and $F_{tx}(\theta, \phi)$ need to be given in the global coordinate system as defined in Section 7.1.1.

7.3.5 Generate BS locations

The 2D coordinates of the BSs in the horizontal plane can be extracted from the commonly used hexagonal grid network layout as given in [ITU09-2135]. Intersite distances (ISDs) of 200 m and 500 m for 3D-UMi and 3D-UMa respectively are common default values, cf. [ITU09-2135]. Common values for the BS heights are 10 m (3D-UMi) and 25 m (3D-UMa).

7.3.6 Generate UE locations

The 2D coordinates of the UEs in the horizontal plane may be uniformly distributed over the whole network layout area, while the heights depend on whether the users are located indoors or outdoors. In [3GPP14-36873] it is assumed that 80 % of the users are located indoors. The outdoor users are assumed to be located at the same height, i.e. 1.5 m above the ground. For the two scenarios 3D-UMa and 3D-UMi the environment height is assumed to be flat, i.e. $h_E = 0$ m. The indoor users on the other hand may be located on different floors inside a building. In [3GPP14-36873], the number of floors per building is equally distributed between 4 and 8 floors, i.e. $N_{floors} \sim U[4, 8]$. The UE height is then given by $h_{UE} = 3(n_{floor} - 1) + 1.5$ with $n_{floor} \sim U[1, N_{floor}]$. Obviously the LOS direction of departure ($\theta_{LOS}^d, \phi_{LOS}^d$) and arrival ($\theta_{LOS}^a, \phi_{LOS}^a$) result directly from the generated BS and UE locations.

7.3.7 Generate BS antenna orientations

The BS antenna orientations are defined by three angles $\Omega_{BS,\alpha}$ (BS bearing angle), $\Omega_{BS,\beta}$ (BS downtilt angle) and $\Omega_{BS,\gamma}$ (BS slant angle). The bearing angles may be derived from the hexagonal grid network layout in [ITU09-2135], while the mechanical downtilt angles are commonly assumed to be around 12 degrees. The slant angles are usually zero degrees.

7.3.8 Generate UE antenna orientations

The UE antenna orientations are defined by three angles $\Omega_{UE,\alpha}$ (UE bearing angle), $\Omega_{UE,\beta}$ (UE downtilt angle) and $\Omega_{UE,\gamma}$ (UE slant angle). The orientation may be completely randomly generated or based on more realistic distributions.

7.3.9 Generate UE velocity vectors

The direction of motion of the receiver v_{rx} in the global coordinate system may be chosen uniformly at random in the horizontal plane. A typical value for the magnitude is 3 km/h. Besides the fixed velocity case the magnitude could also be generated at random according to a more realistic distribution.

7.3.10 Determine LOS/NLOS links

Assign propagation conditions (LOS/NLOS) according to Table 7-3 and Table 7-4. The given probabilities for outdoor UEs are based on [ITU09-2135], while the probabilities for indoor users were developed in [3GPP14-36873]. The different distances used are defined in Figure 7-8 and in Equation (7-36).

Table 7-3: 3D-UMi LOS link probabilities [3GPP14-36873]

$$\text{Prob(LOS|outdoor UE)} = \begin{cases} \frac{1}{d_{2D}} + \left(1 - \frac{1}{d_{2D}}\right) \exp\left(-\frac{d_{2D}}{36}\right) & d_{2D} \leq 18 \text{ m} \\ \text{else} \end{cases}$$

Note that $d_{2D} \geq d_{2D,\min}$ with $d_{2D,\min} = 10 \text{ m}$

$$\text{Prob(LOS|indoor UE)} = \begin{cases} \frac{1}{d_{2D-out}} + \left(1 - \frac{1}{d_{2D-out}}\right) \exp\left(-\frac{d_{2D-out}}{36}\right) & d_{2D-out} \leq 18 \text{ m} \\ \text{else} \end{cases}$$

Note that $d_{2D-out} \geq d_{2D,\min}$ with $d_{2D,\min} = 10 \text{ m}$

Table 7-4: 3D-UMa LOS link probabilities [3GPP14-36873]

$$\text{Prob(LOS|outdoor UE)} = \begin{cases} \frac{1}{d_{2D}} + \left(1 - \frac{1}{d_{2D}}\right) \exp\left(-\frac{d_{2D}}{63}\right) & d_{2D} \leq 18 \text{ m} \\ \text{else} \end{cases}$$

Assuming that $h_{UT} < 13 \text{ m}$.

Note that $d_{2D} \geq d_{2D,\min}$ with $d_{2D,\min} = 35 \text{ m}$

$\text{Prob}(\text{LOS}|\text{indoor UE})$

$$= \begin{cases} 1 & d_{2D-\text{out}} \leq 18 \text{ m} \\ \left(\frac{18 \text{ m}}{d_{2D-\text{out}}} + \left(1 - \frac{18 \text{ m}}{d_{2D-\text{out}}}\right) \exp\left(-\frac{d_{2D-\text{out}}}{63 \text{ m}}\right) \right) (1 + C(d_{2D-\text{out}}, h_{UT})) & \text{else} \end{cases}$$

where

$$C(d_{2D-\text{out}}, h_{UE}) = \begin{cases} 0 & h_{UE} < 13 \text{ m} \\ \left(\frac{h_{UE} - 13 \text{ m}}{10 \text{ m}} \right)^{1.5} g(d_{2D-\text{out}}) & 13 \text{ m} \leq h_{UE} \leq 23 \text{ m} \end{cases}$$

and

$$g(d_{2D-\text{out}}) = (1.25e - 6) \left(\frac{d_{2D-\text{out}}}{1 \text{ m}} \right)^3 \exp\left(-\frac{d_{2D-\text{out}}}{150 \text{ m}}\right)$$

Note that $d_{2D-\text{out}} \geq d_{2D,\text{min}}$ with $d_{2D,\text{min}} = 35 \text{ m}$

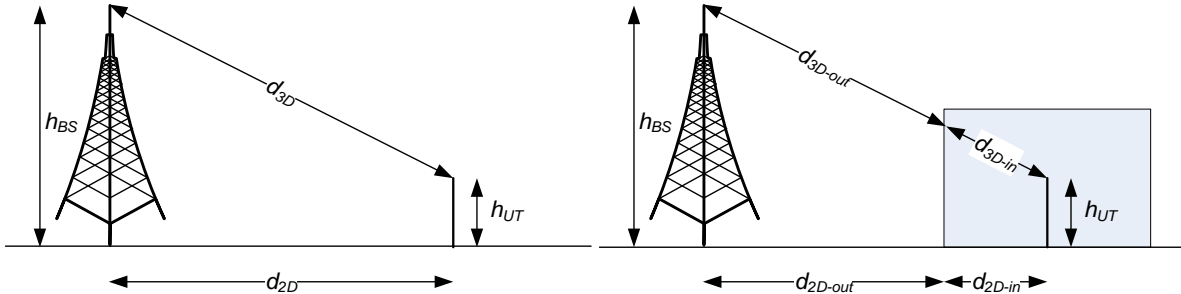


Figure 7-8: 2D and 3D distances for outdoor (left) and indoor (right) UEs [3GPP14-36873].

$$d_{3D-\text{out}} + d_{3D-\text{in}} = \sqrt{(d_{2D-\text{out}} + d_{2D-\text{in}})^2 + (h_{BS} - h_{UE})^2} \quad (7-36)$$

7.3.11 Generate large-scale parameters

Generate the large scale parameters (LSPs), i.e. delay spread, angular spreads, Ricean K factor and shadow fading taking into account cross correlation according to Table 7-13. The definitions of the LSPs are given in [3GPP03-25996]. In order to account for the spatial correlation between different UEs the LSPs are based on so-called LSP maps. Spatial-, cross- and intersite correlation can be incorporated as well. The spatial correlation is assumed to follow a decaying exponential function

$$R(\Delta x) = e^{-\frac{|\Delta x|}{d_{cor}}}, \quad (7-37)$$

with the decorrelation distance d_{cor} being dependent on the environment.

Furthermore the azimuthal spreads of arrival and departure are limited to 104 degrees, i.e., $\sigma'_{ASA} = \min(\sigma'_{ASA}, 104^\circ)$, $\sigma'_{ASD} = \min(\sigma'_{ASD}, 104^\circ)$, while the zenith spreads of arrival and departure are limited to 52 degrees, i.e., $\sigma'_{ZSA} = \min(\sigma'_{ZSA}, 52^\circ)$, $\sigma'_{ZSD} = \min(\sigma'_{ZSD}, 52^\circ)$. The dashed values denote the randomly generated spread values.

7.3.12 Generate path delays

Delays are drawn randomly from the delay distribution defined in Table 7-13. With exponential delay distribution calculate

$$\tau'_n = -r_\tau \sigma_\tau \ln(X_n), \quad (7-38)$$

where σ_τ is the RMS delay spread, r_τ the delay distribution proportionality factor, $X_n \sim U(0,1)$, and cluster index $n \in [1, N]$. With uniform delay distribution the delay values τ'_n are drawn from the corresponding range. Normalise the delays by subtracting the minimum delay and sort the normalised delays to descending order:

$$\tau_n = \text{sort}(\tau'_n - \min(\{\tau'_i\}_{i=1}^N)). \quad (7-39)$$

In the case of LOS condition, additional scaling of delays is required to compensate for the effect of LOS peak addition to the delay spread.

$$\tau_n^{LOS} = \frac{\tau_n}{C_{DS}}. \quad (7-40)$$

The heuristically determined scaling constant C_{DS} depends on the Ricean K-factor and is defined as

$$C_{DS} = 0.7705 - 0.0433 \left(\frac{K}{dB} \right) + 0.0002 \left(\frac{K}{dB} \right)^2 + 0.000017 \left(\frac{K}{dB} \right)^3, \quad (7-41)$$

with K being the Ricean K-factor in dB scale defined in Table 7-13. The scaled delays are not to be used in cluster power generation.

7.3.13 Generate cluster powers

Cluster powers are calculated assuming a single slope exponential power delay profile. Power assignment depends on the delay distribution. With exponential delay distribution the cluster powers are determined by

$$P'_n = 10^{\frac{-Z_n}{10}} \exp\left(-\tau_n \frac{r_\tau - 1}{r_\tau \sigma_\tau}\right), \quad (7-42)$$

where $Z_n \sim N(0, \zeta^2)$ is the per cluster shadowing term in [dB]. Average the power so that the sum power of all cluster powers is equal to one, i.e.,

$$P_n = \frac{P'_n}{\sum_{i=1}^N P'_i}. \quad (7-43)$$

In the case of LOS condition an additional specular component is added to the first cluster. The power of the LOS component is given by

$$P_{1,LOS} = \frac{K}{K+1}, \quad (7-44)$$

whereas the cluster powers are not as in (7-43), but

$$P_n = \frac{1}{K+1} \frac{P'_n}{\sum_{i=1}^N P'_i} + \delta(n-1)P_{1,LOS}, \quad (7-45)$$

where $\delta(n)$ is Dirac's delta function and K is the Ricean K-factor defined in Table 7-13 converted to linear scale. These power values are used *only* in (7-44) and (7-51), but not in (7-59).

Assign the power of each ray m within a cluster n is given by



$$P_{n,m} = \frac{P_n}{M}, \quad (7-46)$$

where M is the number of rays per cluster.

Remove clusters with less than -25 dB power compared to the maximum cluster power.

7.3.14 Generate arrival and departure directions

7.3.14.1 Generate azimuth angles of arrival

The composite power angular spectrum (PAS) in azimuth of all clusters is modelled as wrapped Gaussian (cf. Table 7-13). The azimuth angles of arrival are determined by applying the inverse Gaussian function (7-47) with input parameters P_n and RMS angle spread σ_{ASA}

$$\hat{\phi}_n^a = \frac{\sigma_{ASA}}{0.7 C_{AS}} \sqrt{-\ln\left(\frac{P_n}{\max(\{P_i\}_{i=1}^N)}\right)}, \quad (7-47)$$

where σ_{ASA} denotes the azimuthal spread of arrival as generated in Section 7.3.11.

In (7-47) the constant C_{AS} is a scaling factor related to the total number of clusters N and is given in Table 7-5.

Table 7-5: Scaling factors for AOA, AOD generation

N	4	5	8	10	11	12	14	15	16	19	20
C_{AS}	0.779	0.860	1.018	1.090	1.123	1.146	1.190	1.211	1.226	1.273	1.289

In the LOS case, constant C_{AS} is also dependent on the Ricean K-factor. Constant C_{AS} in Equation (7-47) is substituted by C_{AS}^{LOS} . An additional scaling of the angles is required in order to compensate for the effect of the additional LOS. The heuristically determined Ricean K-factor dependent scaling constant is given by

$$C_{AS}^{LOS} = C_{AS} \left(1.1035 - 0.028 \left(\frac{K}{dB} \right) - 0.002 \left(\frac{K}{dB} \right)^2 + 0.0001 \left(\frac{K}{dB} \right)^3 \right), \quad (7-48)$$

where K is the Ricean K-factor in dB scale as given in Table 7-13. More details on the derivation of C_{AS} and C_{AS}^{LOS} can be found in [QC13].

Finally the azimuth angles of arrival are given by

$$\phi_n^a = \begin{cases} X_n \hat{\phi}_n^a + Y_n + \phi_{LOS}^a & \text{for NLOS links} \\ X_n \hat{\phi}_n^a + Y_n - X_1 \hat{\phi}_1^a - Y_1 + \phi_{LOS}^a & \text{for LOS links} \end{cases}, \quad (7-49)$$

with $X_n \in \{-1, +1\}$ being a uniformly distributed random variable and $Y_n \sim N\left(0, \left(\frac{\sigma_{ASA}}{7}\right)^2\right)$. ϕ_{LOS}^a is the LOS direction defined in the network layout description, cf. Section 7.3.6.

Finally add offset angles α_m from Table 7-6 to the cluster angles

$$\phi_{n,m}^a = \phi_n^a + \sigma_{CASA} \alpha_m, \quad (7-50)$$

where σ_{CASA} is the cluster-wise RMS azimuth spread of arrival angles (cluster ASA) as given in Table 7-13.

Table 7-6: Ray offset angles within a cluster, given for 1 RMS angle spread [WIN08-D112]

Ray number m	Offset angles α_m
1,2	± 0.0447
3,4	± 0.1413
5,6	± 0.2492
7,8	± 0.3715
9,10	± 0.5129
11,12	± 0.6797
13,14	± 0.8844

15,16	± 1.1481
17,18	± 1.5195
19,20	± 2.1551

7.3.14.2 Generate azimuth angles of departure

The generation of the azimuth angles of departure $\phi_{n,m}^d$ follows a similar procedure as the one presented in Section 7.3.14.1.

7.3.14.3 Generate zenith angles of arrival

The generation of zenith angles of arrival (ZOAs) assumes that the composite PAS in the zenith dimension of all clusters is Laplacian (see Table 7-13). The ZOAs are determined by applying the inverse Laplacian function (7-51) with input parameters P_n and RMS angle spread σ_{ZSA} .

$$\hat{\theta}_n^a = -\frac{\sigma_{ZSA}}{C_{ZS}} \ln \left(\frac{P_n}{\max(\{P_i\}_{i=1}^N)} \right), \quad (7-51)$$

where σ_{ZSA} denotes the zenith spread of arrival as generated in Section 7.3.11.

In (7-51) the constant C_{ZS} is a scaling factor related to the total number of clusters N and is given in Table 7-7. More details on the derivation of C_{ZS} and C_{ZS}^{LOS} can be found in [QC13].

Table 7-7: Scaling factors for ZOA, ZOD Generation

N	12	19	20
C_{ZS}	1.104	1.184	1.178

In the LOS case, constant C_{ZS} in (7-51) is substituted by C_{ZS}^{LOS} given by:

$$C_{ZS}^{LOS} = C_{ZS} \left(1.3086 + 0.0339 \left(\frac{K}{dB} \right) - 0.0077 \left(\frac{K}{dB} \right)^2 + 0.0002 \left(\frac{K}{dB} \right)^3 \right) \quad (7-52)$$

where K is the Ricean K-factor in dB scale defined in Table 7-13.

Finally the zenith angles of arrival are given by

$$\theta_n^a = \begin{cases} X_n \hat{\theta}_n^a + Y_n + \bar{\theta}^a & \text{for NLOS links} \\ X_n \hat{\theta}_n^a + Y_n - X_1 \hat{\theta}_1^a - Y_1 + \bar{\theta}^a & \text{for LOS links} \end{cases}, \quad (7-53)$$

with $X_n \in \{-1, +1\}$ being a uniformly distributed random variable and $Y_n \sim N \left(0, \left(\frac{\sigma_{ZSA}}{7} \right)^2 \right)$.

Furthermore

$$\bar{\theta}^a = \begin{cases} 90^\circ & \text{for indoor users} \\ \theta_{LOS}^a & \text{for outdoor users} \end{cases}. \quad (7-54)$$

The LOS direction θ_{LOS}^a is defined by the BS and UE location, cf. Section 7.3.6.

Finally add offset angles α_m from Table 7-6 to the cluster angles

$$\theta_{n,m}^a = \theta_n^a + \sigma_{CZSA} \alpha_m, \quad (7-55)$$

where σ_{CZSA} is the cluster-wise RMS zenith angular spread of arrival (cluster ZSA) in Table 7-13. Assuming that $\theta_{n,m}^a$ is wrapped within $[0^\circ, 360^\circ]$, if $\theta_{n,m}^a \in [180^\circ, 360^\circ]$, then $\theta_{n,m}^a$ is set to $(360^\circ - \theta_{n,m}^a)$.

7.3.14.4 Generate zenith angles of departure

The generation of zenith angles of departure $\theta_{n,m}^d$ follows a similar procedure as the one presented in Section 7.3.14.3 except for (7-53) which should be replaced by (7-56)

$$\theta_n^d = \begin{cases} X_n \hat{\theta}_n^d + Y_n + \mu_{\text{offsetZOD}} + \theta_{LOS}^d & \text{for NLOS links} \\ X_n \hat{\theta}_n^d + Y_n - X_1 \hat{\theta}_1^d - Y_1 + \theta_{LOS}^d & \text{for LOS links} \end{cases}, \quad (7-56)$$

with $X_n \in \{-1, +1\}$ being a uniformly distributed random variable and $Y_n \sim N\left(0, \left(\frac{\sigma_{ZSD}}{7}\right)^2\right)$, where σ_{ZSD} denotes the zenith spread of departure as generated in Section 7.3.11. Furthermore $\mu_{\text{offsetZOD}}$ is a function of distance and receiver height and is given in Table 7-8, and Table 7-9. In addition (7-55) should be replaced by (7-57)

$$\theta_{n,m}^d = \theta_n^d + \frac{3}{8} \alpha_m 10^{\mu_{ZSD}} \quad (7-57)$$

where μ_{ZSD} is the mean of the ZSD log-normal distribution and also a function of distance and receiver height, cf. Table 7-8, Table 7-9.

Table 7-8: 3D-UMa ZSD and ZoD offset parameters [3GPP14-36873]

The zenith spread of departure ZSD in [log10(deg)] is given by

$$\sigma_{ZSD} \sim N(\mu_{ZSD}, \epsilon_{ZSD}^2)$$

with

$$\mu_{ZSD} = \begin{cases} \max\left(-0.5, -2.1\left(\frac{d_{2D}}{1 \text{ km}}\right) - 0.01\left(\frac{h_{\text{UE}}}{1 \text{ m}}\right) + 0.765\right) & \text{for LOS links} \\ \max\left(-0.5, -2.1\left(\frac{d_{2D}}{1 \text{ km}}\right) - 0.01\left(\frac{h_{\text{UE}}}{1 \text{ m}}\right) + 0.915\right) & \text{for NLOS links} \end{cases}$$

$$\epsilon_{ZSD} = \begin{cases} 0.4 & \text{for LOS links} \\ 0.49 & \text{for NLOS links} \end{cases}$$

$$\mu_{\text{offset-ZOD}} = \begin{cases} 0 & \text{for LOS links} \\ -10^{-0.62 \log_{10}(\max(10, \frac{d_{2D}}{1 \text{ m}})) + 2.035 - 0.07(\frac{h_{\text{UE}}}{1 \text{ m}})} & \text{for NLOS links} \end{cases}$$

Note that the proposed average ZSD is smaller compared to WINNER+.

Note that the parameters are the same for indoor and outdoor UEs in case of O2I.

Table 7-9: 3D-UMi ZSD and ZoD offset parameters [3GPP14-36873]

The zenith spread of departure ZSD in [log10(deg)] is given by

$$\sigma_{ZSD} \sim N(\mu_{ZSD}, \epsilon_{ZSD}^2)$$

with

$$\mu_{ZSD} = \begin{cases} \max\left(-0.5, -2.1\left(\frac{d_{2D}}{1 \text{ km}}\right) + 0.01 \left|\frac{h_{UE} - h_{BS}}{1 \text{ m}}\right| + 0.75\right) & \text{for LOS links} \\ \max\left(-0.5, -2.1\left(\frac{d_{2D}}{1 \text{ km}}\right) + 0.01 \max\left(\frac{h_{UE} - h_{BS}}{1 \text{ m}}, 0\right) + 0.9\right) & \text{for NLOS links} \end{cases}$$

$$\epsilon_{ZSD} = \begin{cases} 0.4 & \text{for LOS links} \\ 0.6 & \text{for NLOS links} \end{cases}$$

$$\mu_{\text{offset-ZOD}} = \begin{cases} 0 & \text{for LOS links} \\ -10^{-0.55 \log_{10}(\max(10, \frac{d_{2D}}{1 \text{ m}})) + 1.6} & \text{for NLOS links} \end{cases}$$

Note that the proposed average ZSD is smaller compared to WINNER+.

Note that the parameters are same for indoor and outdoor UEs in case of O2I.

The height dependence of the ZOD offset was investigated by means of ray-tracing simulations. It was not showing a common and strong trend and is therefore neglected.

7.3.15 Coupling of angles

- Couple randomly the azimuth angles of departure $\phi_{n,m}^d$ and arrival $\phi_{n,m}^a$ within a cluster n , or within a sub-cluster in the case of two strongest clusters (Section 7.3.18 and Table 7-10).
- Couple randomly the zenith angles of departure $\theta_{n,m}^d$ and arrival $\theta_{n,m}^a$ using the same procedure.
- Couple randomly the azimuth angles of departure $\phi_{n,m}^d$ with the zenith angles of departure $\theta_{n,m}^d$ within a cluster n or within a sub-cluster in the case of two strongest clusters (Section 7.3.18 and Table 7-10).

7.3.16 Generate cross polarization ratios

The XPR in dB ($X_{n,m}$) is assumed to be a normally distributed random variable with $X_{n,m} \sim N(\mu_{XPR}, \sigma_{XPR}^2)$ where μ_{XPR} and σ_{XPR} are given in Table 7-13. The XPRs in linear scale ($\kappa_{n,m}$) are therefore given by

$$\kappa_{n,m} = 10^{\frac{X_{n,m}}{10}}, \quad (7-58)$$

7.3.17 Draw random phases

Draw randomly the phases $\Phi_{n,m}^{\theta\theta}$, $\Phi_{n,m}^{\theta\phi}$, $\Phi_{n,m}^{\phi\theta}$, $\Phi_{n,m}^{\phi\phi}$ for each ray m and each cluster n . The phases are assumed to be uniformly distributed within $[0, 2\pi)$. In the LOS case, draw also a random phase Φ_{LOS} . It should be noted that there these random phases are same for multiple antenna array elements of a single user.

7.3.18 Generate channel coefficients

Generate channel coefficients for each cluster n and each receiver and transmitter element pair u, s .

For the $N - 2$ weakest clusters, say $n = 3, 4, \dots, N$, the channel coefficients are given by:

$$H_{u,s,n}^{N\text{LOS}}(t) = \sqrt{\frac{P_n}{M}} \sum_{m=1}^M \begin{pmatrix} F_{\theta,\text{GCS},rx,u}(\theta_{n,m}^a, \phi_{n,m}^a) \\ F_{\phi,\text{GCS},rx,u}(\theta_{n,m}^a, \phi_{n,m}^a) \end{pmatrix}^T \begin{pmatrix} \exp(j\Phi_{n,m}^{\theta\theta}) & \frac{\exp(j\Phi_{n,m}^{\theta\phi})}{\sqrt{\kappa_{n,m}}} \\ \frac{\exp(j\Phi_{n,m}^{\phi\theta})}{\sqrt{\kappa_{n,m}}} & \exp(j\Phi_{n,m}^{\phi\phi}) \end{pmatrix} \begin{pmatrix} F_{\theta,\text{GCS},tx,s}(\theta_{n,m}^d, \phi_{n,m}^d) \\ F_{\phi,\text{GCS},tx,s}(\theta_{n,m}^d, \phi_{n,m}^d) \end{pmatrix} \exp\left(j\frac{2\pi}{\lambda_c}(\mathbf{e}_r(\theta_{n,m}^a, \phi_{n,m}^a)^T \mathbf{d}_{rx,u})\right) \exp\left(j\frac{2\pi}{\lambda_c}(\mathbf{e}_r(\theta_{n,m}^d, \phi_{n,m}^d)^T \mathbf{d}_{tx,s})\right) \exp\left(j\frac{2\pi}{\lambda_c}(\mathbf{e}_r(\theta_{n,m}^a, \phi_{n,m}^a)^T \mathbf{v}_{rx,t})\right) \quad (7-59)$$

where $F_{\theta,\text{GCS},rx,u}$ and $F_{\phi,\text{GCS},rx,u}$ are the radiation field patterns in the direction of the spherical basis vectors, \mathbf{e}_θ and \mathbf{e}_ϕ respectively of receive antenna element u , while $F_{\theta,\text{GCS},tx,s}$ and $F_{\phi,\text{GCS},tx,s}$ are the radiation field patterns in the direction of the spherical basis vectors, \mathbf{e}_θ and \mathbf{e}_ϕ respectively of transmit antenna element s . \mathbf{e}_r is the spherical unit vector defined in Section 7.1.1. $\mathbf{d}_{rx,u}$ and $\mathbf{d}_{tx,s}$ are the position vectors of the receive antenna element u and transmit antenna element s , given in GCS. λ_c is the wavelength of the carrier frequency. The Doppler component in (7-59) is calculated by using the velocity vector \mathbf{v}_{rx} , which describes the RX's direction of movement in GCS as well as its magnitude in velocity.

For the two strongest clusters, say $n = 1$ and 2 , rays are spread in delay to three sub-clusters (per cluster), with fixed delay offset $\{0, 5, 10 \text{ ns}\}$ (see Table 7-5). The delays of the sub-clusters are

$$\begin{aligned} \tau_{n,1} &= \tau_n + 0 \text{ ns} \\ \tau_{n,2} &= \tau_n + 5 \text{ ns} \\ \tau_{n,3} &= \tau_n + 10 \text{ ns} \end{aligned} \quad (7-60)$$

Twenty rays of a cluster are mapped to sub-clusters as presented in Table 7-10 below. The corresponding offset angles are taken from Table 7-6 with mapping of Table 7-10.

Table 7-10: Sub-cluster information for intra cluster delay spread clusters

sub-cluster #	mapping to rays	power	delay offset
1	1,2,3,4,5,6,7,8,19,20	10/20	0 ns
2	9,10,11,12,17,18	6/20	5 ns
3	13,14,15,16	4/20	10 ns

In the LOS case, determine the channel coefficients by adding a single line-of-sight ray and scaling down the other channel coefficients generated in (7-59). The channel coefficients are given by

$$\begin{aligned}
& H_{u,s,n}^{LOS}(t) = \\
& \sqrt{\frac{1}{K+1}} H_{u,s,n}^{NLOS}(t) + \\
& \left(\begin{array}{c} F_{\theta,GCS,rx,u}(\theta_{LOS}^a, \phi_{LOS}^a) \\ F_{\phi,GCS,rx,u}(\theta_{LOS}^a, \phi_{LOS}^a) \end{array} \right)^T \begin{pmatrix} \exp(j\Phi_{LOS}) & 0 \\ 0 & -\exp(j\Phi_{LOS}) \end{pmatrix} \\
& \delta(n-1) \sqrt{\frac{K}{K+1}} \left(\begin{array}{c} F_{\theta,GCS,tx,s}(\theta_{LOS}^d, \phi_{LOS}^d) \\ F_{\phi,GCS,tx,s}(\theta_{LOS}^d, \phi_{LOS}^d) \end{array} \right) \exp \left(j \frac{2\pi}{\lambda_c} (\mathbf{e}_r(\theta_{LOS}^a, \phi_{LOS}^a)^T \mathbf{d}_{rx,u}) \right) , \\
& \exp \left(j \frac{2\pi}{\lambda_c} (\mathbf{e}_r(\theta_{LOS}^d, \phi_{LOS}^d)^T \mathbf{d}_{tx,s}) \right) \exp \left(j \frac{2\pi}{\lambda_c} (\mathbf{e}_r(\theta_{LOS}^a, \phi_{LOS}^a)^T \mathbf{v}_{rx,t}) \right)
\end{aligned} \quad (7-61)$$

where $\delta(n)$ is the Dirac's delta function and K is the Ricean K-factor defined in Table 7-13 in linear scale.

Note that $\mathbf{e}_r(\theta_{LOS}^d, \phi_{LOS}^d) = -\mathbf{e}_r(\theta_{LOS}^a, \phi_{LOS}^a)$.

7.3.19 Apply pathloss and shadowing

Calculate pathloss according to Table 7-11 and Table 7-12 and scale the channel coefficients accordingly.

Table 7-11: 3D-UMi pathloss models [3GPP14-36873]

$PL_{LOS} _{dB} = 22 \log_{10} \left(\frac{d_{3D}}{1 \text{ m}} \right) + 28 + 20 \log_{10} \left(\frac{f_c}{1 \text{ GHz}} \right) + APL_{LOS} _{dB}$ <p>Additional pathloss</p> $APL_{LOS} _{dB} = \begin{cases} 0 & 10 \text{ m} < d_{2D} < d'_{BP} \\ -9 \log_{10} \left(\left(\frac{d'_{BP}}{1 \text{ m}} \right)^2 + \left(\frac{h_{BS} - h_{UE}}{1 \text{ m}} \right)^2 \right) & d'_{BP} < d_{2D} < 5 \text{ km} \end{cases}$ <p>with $d'_{BP} = 4(h_{BS} - 1 \text{ m})(h_{UE} - 1 \text{ m}) \frac{f_c}{c}$, c denotes the speed of light.</p> <p>Shadow fading std in [dB] is assumed to be $\sigma_{SF} = 3$ according to [3GPP10-36814]</p>	Applicability range $10 \text{ m} < d_{2D} < 5 \text{ km}$ default antenna heights $h_{BS} = 10 \text{ m}$ $1.5 \text{ m} \leq h_{UE} \leq 22.5 \text{ m}$
For hexagonal cell layout: $PL_{NLOS} _{dB} = \max(PL_{LOS} _{dB}, PL_A _{dB})$ <p>with</p> $PL_A _{dB} = 36.7 \log_{10} \left(\frac{d_{3D}}{1 \text{ m}} \right) + 23.15 + 26 \log_{10} \left(\frac{f_c}{1 \text{ GHz}} \right) - 0.3 \left(\frac{h_{UE}}{1 \text{ m}} \right)$ <p>Shadow fading std in [dB] is assumed to be $\sigma_{SF} = 4$ according to [3GPP10-36814]</p>	Applicability range $10 \text{ m} < d_{2D} < 2 \text{ km}$ default antenna heights $h_{BS} = 10 \text{ m}$ $1.5 \text{ m} \leq h_{UE} \leq 22.5 \text{ m}$

$PL_{O2I} _{dB} = PL_{LOS/NLOS} _{dB}(d_{3D-out} + d_{3D-in}) + 20 + 0.5 \left(\frac{d_{2D-in}}{1 \text{ m}} \right)$ <p>d_{2D-in} is assumed to be uniformly distributed between 0 and 25 m. Shadow fading std in [dB] is assumed to be $\sigma_{SF} = 7$ according to [3GPP10-36814]</p>	Applicability range $10 \text{ m} < d_{2D-out} + d_{2D-in} < 1 \text{ km}$ $0 \text{ m} < d_{2D-in} < 25 \text{ m}$ default antenna heights $h_{BS} = 10 \text{ m}$ $1.5 \text{ m} \leq h_{UE} \leq 22.5 \text{ m}$
---	---

Table 7-12: 3D-UMa pathloss models [3GPP14-36873]

$PL_{LOS} _{dB} = 22 \log_{10} \left(\frac{d_{3D}}{1 \text{ m}} \right) + 28 + 20 \log_{10} \left(\frac{f_c}{1 \text{ GHz}} \right) + APL_{LOS} _{dB}$ <p>Additional pathloss</p> $APL_{LOS} _{dB} = \begin{cases} 0 & 10 \text{ m} < d_{2D} < d'_{BP} \\ -9 \log_{10} \left(\left(\frac{d'_{BP}}{1 \text{ m}} \right)^2 + \left(\frac{h_{BS} - h_{UE}}{1 \text{ m}} \right)^2 \right) & d'_{BP} < d_{2D} < 5 \text{ km} \end{cases}$ <p>with $d'_{BP} = 4(h_{BS} - h_E)(h_{UE} - h_E) \frac{f_c}{c}$, where c denotes the speed of light.</p> <p>In the event that the link is determined to be LOS, $h_E = 1 \text{ m}$ with a probability equal to $1 / (1 + C(d_{2D}, h_{UE}))$ and chosen from a discrete uniform distribution uniform(12,15,...,($h_{UE} - 1.5$)) otherwise. The function $C(d_{2D}, h_{UE})$ is defined in Table 7-4.</p> <p>Shadow fading std in [dB] is assumed to be $\sigma_{SF} = 4$ according to [3GPP10-36814]</p>	Applicability range $10 \text{ m} < d_{2D} < 5 \text{ km}$ default antenna heights $h_{BS} = 25 \text{ m}$, $1.5 \text{ m} \leq h_{UE} \leq 22.5 \text{ m}$
$PL_{NLOS} _{dB} = \max(PL_{LOS} _{dB}, PL_A _{dB})$ $PL_A _{dB} = 161.94 - 7.1 \log_{10} \left(\frac{w_{street}}{1 \text{ m}} \right) + 7.5 \log_{10} \left(\frac{\bar{h}_{building}}{1 \text{ m}} \right) - \left(24.37 - 3.7 \left(\frac{\bar{h}_{building}}{h_{BS}} \right)^2 \right) \log_{10} \left(\frac{h_{BS}}{1 \text{ m}} \right) + \left(43.42 - 3.1 \log_{10} \left(\frac{h_{BS}}{1 \text{ m}} \right) \right) \left(\log_{10} \left(\frac{d_{3D}}{1 \text{ m}} \right) - 3 \right) + 20 \log_{10} \left(\frac{f_c}{1 \text{ GHz}} \right) - 0.6 \left(\frac{h_{UE}}{1 \text{ m}} \right)$ <p>with w_{street} being the street width, and $\bar{h}_{building}$ being the average building height.</p> <p>Shadow fading std in [dB] is assumed to be $\sigma_{SF} = 6$ according to [3GPP10-36814]</p>	Applicability range $10 \text{ m} < d_{2D} < 5 \text{ km}$ $10 \text{ m} \leq h_{BS} \leq 150 \text{ m}$ $1.5 \text{ m} \leq h_{UE} \leq 22.5 \text{ m}$ $5 \text{ m} \leq w_{street} \leq 50 \text{ m}$ $5 \text{ m} \leq \bar{h}_{building} \leq 50 \text{ m}$ default values $w_{street} = 20 \text{ m}$ $\bar{h}_{building} = 20 \text{ m}$ $h_{BS} = 25 \text{ m}$
$PL_{O2I} _{dB} = PL_{LOS/NLOS} _{dB}(d_{3D-out} + d_{3D-in}) + 20 + 0.5 \left(\frac{d_{2D-in}}{1 \text{ m}} \right)$ <p>d_{2D-in} is assumed to be uniformly distributed between 0 and 25 m.</p> <p>Shadow fading std in [dB] is assumed to be $\sigma_{SF} = 7$ according to [3GPP10-36814]</p>	Applicability range $10 \text{ m} < d_{2D-out} + d_{2D-in} < 1 \text{ km}$ $0 \text{ m} < d_{2D-in} < 25 \text{ m}$ default antenna heights $h_{BS} = 25 \text{ m}$

7.3.20 Parameterisation (based on measurement / literature)

The parameterisation is going to be checked against METIS measurements and older measurements as well as by raytracing simulations.

Table 7-13: Parameterisation [3GPP14-36873]

Scenarios	3D-UMi			3D-UMa		
	LOS	NLOS	O-to-I	LOS	NLOS	O-to-I
Delay spread (μ_{DS}) in [$\log_{10}(\text{s})$]	μ_{DS}	-7.19	-6.89	-6.62	-7.03	-6.44
	ϵ_{DS}	0.40	0.54	0.32	0.66	0.39
AoD spread (σ_{ASD}) in [$\log_{10}(\text{deg})$]	μ_{ASD}	1.20	1.41	1.25	1.15	1.41
	ϵ_{ASD}	0.43	0.17	0.42	0.28	0.28
AoA spread (σ_{ASA}) in [$\log_{10}(\text{deg})$]	μ_{ASA}	1.75	1.84	1.76	1.81	1.87
	ϵ_{ASA}	0.19	0.15	0.16	0.20	0.11
ZoA spread (σ_{ZSA}) in [$\log_{10}(\text{deg})$ ²⁾	μ_{ZSA}	0.60	0.88	1.01	0.95	1.26
	ϵ_{ZSA}	0.16	0.16	0.43	0.16	0.16
Shadow fading (σ_{SF}) [dB]	σ_{SF}	3	4	7	4	6
Ricean K-factor (K) [dB]	μ_{KF}	9	N/A	N/A	9	N/A
	σ_{KF}	5	N/A	N/A	3.5	N/A
Cross-Correlations	ASD vs DS	0.5	0	0.4	0.4	0.4
	ASA vs DS	0.8	0.4	0.4	0.8	0.6
	ASA vs SF	-0.4	-0.4	0	-0.5	0
	ASD vs SF	-0.5	0	0.2	-0.5	-0.6
	DS vs SF	-0.4	-0.7	-0.5	-0.4	-0.5
	ASD vs ASA	0.4	0	0	0	0
	ASD vs K	-0.2	N/A	N/A	0	N/A
	ASA vs K	-0.3	N/A	N/A	-0.2	N/A
	DS vs K	-0.7	N/A	N/A	-0.4	N/A
	SF vs K	0.5	N/A	N/A	0	N/A
Cross-Correlations ¹⁾	ZSD vs SF	0	0	0	0	0
	ZSA vs SF	0	0	0	-0.8	-0.4
	ZSD vs K	0	N/A	N/A	0	N/A
	ZSA vs K	0	N/A	N/A	0	N/A
	ZSD vs DS	0	-0.5	-0.6	-0.2	-0.5
	ZSA vs DS	0.2	0	-0.2	0	-0.2
	ZSD vs ASD	0.5	0.5	-0.2	0.5	0.5
	ZSA vs ASD	0.3	0.5	0	0	-0.1
	ZSD vs ASA	0	0	0	-0.3	0
	ZSA vs ASA	0	0.2	0.5	0.4	0
Delay distribution	ZSD vs ZSA	0	0	0.5	0	0.5
		Exp	Exp	Exp	Exp	Exp
	AoD and AoA distribution	Wrapped Gaussian			Wrapped Gaussian	
	ZoD and ZoA distribution	Laplacian			Laplacian	
	Delay scaling parameter r_r	3.2	3	2.2	2.5	2.3
	XPR [dB]	μ_{XPR}	9	8.0	9	8
		σ_{XPR}	3	3	11	4
Number of clusters					3	11
	Number of rays per cluster	12	19	12	12	20
	Cluster ASD in [deg] σ_{CASD}	20	20	20	20	20
	Cluster ASA in [deg] σ_{CASA}	3	10	5	5	2
	Cluster ZSA ²⁾ in [deg] σ_{CZSA}	17	22	8	11	15
	Per cluster shadowing std ζ [dB]	7	7	3	7	3
		3	3	4	3	4
Decorrelation distance d_{cor} in the horizontal plane [m] ³⁾	DS	7	10	10	30	40
	ASD	8	10	11	18	50
	ASA	8	9	17	15	50
	SF	10	13	7	37	50
	K	15	N/A	N/A	12	N/A
	ZSA	12	10	25	15	50
	ZSD	12	10	25	15	50

7.4 Output

METIS initial channel model output is either 1) the path loss L between TX and RX location or specifically path loss L_{uv} between TX and RX antenna element pair uv in the case of very large arrays, or 2) MIMO impulse response matrices $\mathbf{H}(\tau) \in \mathbb{C}^{U \times V}$ or 3) MIMO transfer matrices $\mathbf{H}(f) \in \mathbb{C}^{U \times V}$, where U and V are the number of antenna elements at receiver and transmitter. When the transceivers or the environment are in motion the outputs are time and location dependent.



8 Conclusion and future work

This deliverable introduced 5G requirements, METIS propagation scenarios, measurement results, channel model approaches, as well as the Initial METIS Channel Models. More specifically, the scenarios and test cases that have been identified in an early stage of the METIS project from the end user perspective were analysed and mapped to the METIS propagation scenarios. Those scenarios have been investigated by searching the literature, conducting measurement campaigns, and exploring several modelling approaches. Several channel modelling approaches are promising to fulfil the 5G requirements. The Initial METIS Channel Models encompass two model approaches, i.e. a geometry-based stochastic and a map-based model. The results of the measurement campaigns conducted by the METIS partners have been provided; although it is still due to include them into the parameterisation of the channel models.

The propagation group of the METIS project will continue investigations on different channel model approaches, namely visibility-region based, grid-based GSCM, and map-based models. Also extensive validation of the proposed channel models, with computer simulations and comparison to literature and measurement results, is still to be done. Additionally, the propagation group plans to do complementary propagation measurements. The aim of the measurements is to get an improved understanding of the frequency dependent propagation parameters, clustering in stochastic models, as well as several phenomena (specular vs. diffuse scattering, diffraction, outdoor-to-indoor case etc.) of deterministic map-based models. Moreover, complexity issues and simplification methods of different channel model approaches will be investigated.

The final METIS channel models will be published in D1.4 in February 2015.

Appendix A Propagation scenarios sets

METIS work is specified in five generic scenarios each describing the specific challenge of the coming 5G mobile systems [MET13-D11]. The scenarios and the corresponding challenges are:

- Scenario 1: Amazingly fast to reflect the very high data rate challenge
- Scenario 2: Great service in a crowd to address the challenge of very dense crowds of users
- Scenario 3: Ubiquitous things communicating to represent very low energy, cost, and a massive number of devices challenge
- Scenario 4: Best experience follows you to address the mobility challenge
- Scenario 5: Super real-time and reliable connections to set the very low latency challenge

Furthermore, twelve TCs are defined to cover the practical applications of 5G system and simulation needs in METIS for the coming 5G system [MET13-D11]. A TC may belong to different scenarios, which may affect the details of the TCs but preserve the main content of the TCs. TCs are listed in Table A-1 below:

Table A-1: METIS test cases

TC#	METIS Test Case
1	Virtual Reality Office
2	Dense Urban Information Society
3	Shopping Mall
4	Stadium
5	Teleprotection in smart grid network
6	Traffic Jam
7	Blind Spots
8	Real-Time Remote Computing for Mobile Terminals
9	Open Air Festival
10	Emergency Communications
11	Massive Deployment of Sensors and Actuators
12	Traffic Efficiency and Safety

The mapping of the five scenarios to twelve test cases is detailed in [METISD11].

A.1 Virtual reality office propagation scenario set (for TC1)

TC1 the virtual reality office, is an indoor test case where very high data rates are investigated targeting also implementations at a reasonable cost. A realistic office environmental model for this test case is attained by explicitly considering walls, screens, desks, chairs and people. One single backhaul fibre connection is assumed for one AP. Applying multiple access points requires to use in-band wireless backhaul. The TC1 reference environment is shown in Figure A-1. The detailed definition of the TC1 can be found in [MET13-D61].

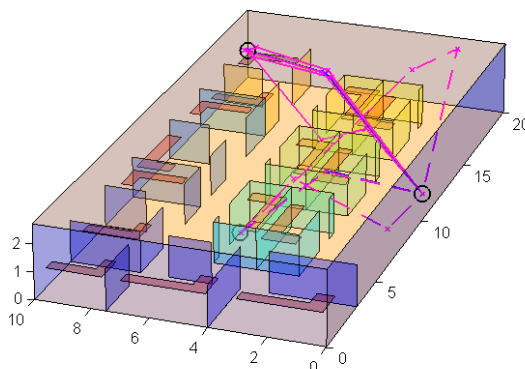


Figure A-1: Virtual reality office environmental reference model.

A.1.1 Basic propagation environment and link topology

Main propagation link type is the Base Station to Mobile Station (BS-UE) link and the propagation link topology is I2I (indoor to indoor). Furthermore, D2D links can be considered for the big volume data sharing between users in the same office room. Line-of-Sight (LOS) links can be assumed to dominate, but also reflected waves need to be taken into account due to shadowing effects. For this scenario blocking by humans may have a severe impact, particularly in the high frequency range.

It is assumed that the used frequencies can vary from 2 - 6 GHz to the millimetre waves.

A.2 Dense urban propagation scenario set (for TC2)

These propagation scenarios are derived for the “Dense Urban Information Society” test case (TC2). In this test case a strongly densified macro/micro and small (pico/femto) cell deployment (and with a larger availability of spectrum) is envisaged. Moreover, novel multi-antenna (e.g., massive MIMO) [MET13-D31], multi-node, network-level and spectrum usage concepts as well as D2D communication are envisaged. The deployment may be ultra-dense, both indoor and outdoor, with minimum Inter-Site Distances (ISDs) of tens of meters or below outdoor and one or more BS(s) (or APs) per room indoor. Bandwidths above 6 GHz (e.g., mmW) can be used to support extreme data rates in LOS cases indoor and outdoor. Also for the backhaul for indoor and outdoor dense networks, mmWs may be used. In order to improve the spectral efficiency, multi-hop relaying, coordinated multipoint and massive antenna solutions may be used [MET13-D31]. The densified nodes/antennas may be located on lamp posts, walls, ceiling, etc.

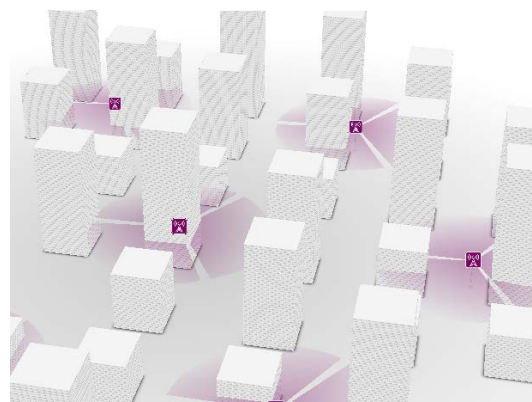


Figure A-2: Conceptual image of TC2 environment.

The preferred frequency bands for this test case are IMT (450 MHz to 6 GHz) and ISM (e.g., 2.45, 5.25 GHz). Frequency band depends on the propagation scenario (urban, indoor), mmW

bands are considered for extreme data rates in case of LOS propagation as well as for wireless LOS backhaul. Regarding propagation modelling novel aspects have to be accounted for such as:

- Mobility of both Tx and Rx (D2D)
- Due to the fact that both users and access points are distributed in 3D space (considering tall buildings) the propagation needs to be modelled in 3D and not, as traditionally done, in 2D

The propagation scenario set is divided into three sub-scenarios. We assume that communication takes place using links between base stations (BSs), relay stations (RSs) and user equipment of multiple users (UEs). The frequency, bandwidth and power level are adjustable and rely on the configuration at the RS/BS side. We assume that RSs, BSs and UEs are either located outside (e.g., in urban environments like street canyons or university campus areas) or indoors (e.g., in office buildings with a large number of connected devices).

A.2.1 Basic propagation environment and link topology

The dense urban environment is assumed, e.g., as given in Figure A-3 [MET13-D61]. For this test case all of the basic propagation link types: BS-UE, backhaul (RS-BS) and D2D are taken into account. Note that D2D communication is not envisioned for millimetre wave frequencies. Furthermore most of the basic link topologies are considered, i.e., O2O, O2I, and I2I.

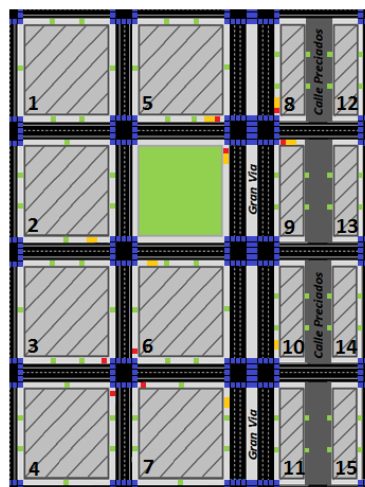


Figure A-3: Overview on the Madrid grid model.

A.2.2 Link topology specific characteristics

Backhaul (O2O):

RSs are used for wireless point-to-point backhauls to densely deployed cells. The RS height may be typically 5-30 m and we assume that antennas in RSs are very directive and that a condition similar to LOS exists. The RSs are assumed to be located on lamp posts, walls, roofs etc. The RS-BS distance is assumed to be in the order of 70-1000 m, ranging from the minimum block length to longer distances, e.g. in campus areas.

BS-UE (O2O):

This is the standard urban outdoor cellular propagation scenario. For the mmW range however, the propagation characteristics such as delay spread are assumed to be quite different due to the higher carrier frequency and broader bandwidth. UEs are mobile with a velocity of 0-50 km/h and heights of 0.5-2 m, i.e., in the hand of the user.

BS-UE (O2I):

This is the standard urban indoor cellular propagation scenario. It is particularly important as most of the users are located indoors. Moreover, the users are distributed in 3D wherefore 3D channel modelling is required. This scenario most likely does not apply to the millimetre wavelengths due to heavy building penetration loss.

D2D (O2I):

This scenario is similar to BS-UE (O2I) except that also the outdoor end of the link may be mobile (0-50 km/h) and located at low heights of about 1.5 m. Same/similar model may be applied with appropriate parameter settings. This might be a difficult propagation scenario, because of the high attenuation on the street and through walls.

D2D (O2O):

This scenario is similar to BS-UE (O2O) except that both ends of the link may be mobile (0-50 km/h) and located at low heights of about 1.5 m.

For frequencies below 6 GHz the available standard propagation modelling covers this test case to a large extent. There are some well-established models for the cellular scenarios (BS-UE and RS-UE), like in [WIN08-D112], [WIN10-D53] and [DC99]. Also for the D2D scenarios there are available models, e.g., [AE13a] and [AE13b]. However, there are still some issues which might not be accounted for in available propagation modelling:

- Cellular 3D Modelling: 3GPP has recently created the 3D channel models for the UMi and UMa environment. E.g. rural models do not exist.
- D2D modelling: There is an ongoing work in 3GPP. D2D modelling has similarities to cellular scenarios. However, the antenna height is low in both ends and both ends may be moving. LOS probability, Doppler and large scale parameter correlations are to a large extent unknown.

The updated propagation model taking into account the above aspects will be given in deliverable D1.4.

A.2.3 Frequency regions

The propagation scenario set of the dense urban test case (TC2) can concern the lower frequency region of 2 to 6 GHz and also the mmW region.

A.3 Shopping mall propagation scenario set (for TC3)

The Shopping Mall test case (TC3), according to the description in [MET13-D11], has a typical setting for a future extended rich communication environment that involves both “traditional” radio networks as well as wireless sensor networks. Customers are strongly interested in getting access to mobile broadband communication services in the heterogeneous indoor environment of the mall. In addition they will be directly addressed by generalized and/or personalized location-based services of the shopping environment, e.g., via augmented reality, multimedia objects, or holographic applications.

Besides customer oriented services, more general commercial as well as operational services are going to be provided by a fixed wireless communication infrastructure.

A.3.1 Basic propagation environment and link topology

For the shopping mall propagation scenario mainly I2I (both LOS and NLOS) link topology is assumed. Furthermore, co-channel usage between indoors and outdoors of the shopping mall is assumed (in particular for lower cellular frequency bands, e.g., the lower IMT bands). According to the test case description, the indoor radio propagation encompasses both open spaces such as walking space (white), catering space (brown) and galleries, and closed spaces such as shops (yellow), see Figure A-4.

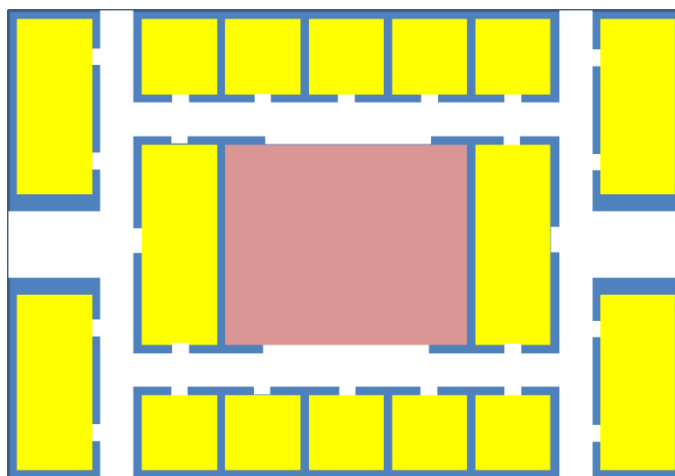


Figure A-4: Plan of the reference shopping mall [MET13-D61].

As for the indoor radio network, the radio links Base Stations (BSs), Relay Stations (RSs), BS, RS and (UEs) (including Sensor Nodes (SN)) should be considered. More specifically, Backhaul (I2I) (BS-RS), D2D (I2I) (UE-UE), BS-UE (I2I) are considered as propagation scenario set.

A.3.2 Propagation scenarios

BS-UE (I2I):

Indoor BS heights are typically about 3-4 m, and indoor hotspot propagation model (e.g., ITU-R model [ITU09-2135]) can be utilized for LOS/NLOS model especially in case of lower frequency bands, although the model should allow higher frequency bands up to the mmW region. The UE height is assumed to be 1.5 m, and the velocity of the UE is assumed to be in the range of 0-3 km/h. The penetration loss due to walls may need to be considered for the communication between BSs and UEs on different floors and in different shops/areas. As for the carrier frequency, the licensed or dedicated band, e.g., 2.6 GHz and 3.5 GHz as well as unlicensed bands (ISM bands) should be considered at least. In addition, unlicensed bands and shared spectrum bands need to be considered. The transmission bandwidth may be in the range of 10-100 MHz, therefore, multipath should be taken into account.

Backhaul (I2I):

A BS is connected to another BS (or RS) via wireless backhaul. BS height is typically around 3-4 m. In case of NLOS backhaul connection, the penetration loss due to walls may need to be considered in case of the backhaul communication between BSs on different floors or in different shops/areas.

D2D (I2I):

Direct D2D radio links between different UEs may be used. The UE height is modelled around 1.5 m. In case of NLOS, the penetration loss due to walls needs to be considered for the communication between UEs on different floors or in different shops/areas.

A.3.3 Frequency ranges

The main features that distinguish the shopping mall from other indoor propagation scenarios in METIS are large open spaces as well as high user densities. At mmWs, LOS is typically needed due to high attenuation of shadowing objects. MIMO and beam steering can be utilized to receive signals from reflected paths, for example, in case of human body shadowing. Indoor BSs are placed on elevated structures (above 2 m) in the shopping mall in order to increase LOS probability. The height of the UE is about 1.5 m and the distance between BS and UE is typically 1-10 m. Since the BS-UE distance is limited, a large number of BSs is needed to cover, for example the catering areas. In addition, it is assumed that a high number of UEs is communicating with the closest BS under LOS condition.

It seems that the cellular type propagation is more beneficial to be implemented with frequencies below 6 GHz, although high capacity requirements would favour mmW. However, e.g the backhaul links could be implemented with mmW connections, because a high probability of LOS links, stationary devices and high-gain antennas would make this a tempting alternative.

It is recommended in [MET13-D61] that ray-tracing type models would be created for the TC3, at least for the higher frequencies.

A.4 Stadium propagation scenario set (for TC4)

According to TC4 description, the stadium test case refers to a dense user crowd scenario with a high throughput demand [MET13-D21]. The reference stadium specified in [MET13-D61] contains elevated roof-type structures which can be used for mounting advanced antenna constellations. Thus it is possible to install for example large antenna arrays at positions which offer good LOS propagation conditions to all spectators. In this propagation scenario the RF communication can occur between elevated small Tx power base station antenna arrays and a large number of handsets. It is also probable that spectators communicate with each other by exchanging multi-media content. Therefore, the Stadium TC can include in principle also D2D propagation scenarios.

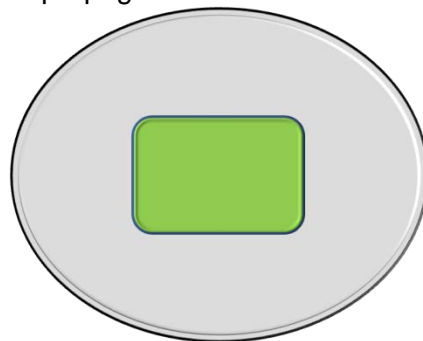


Figure A-5: Reference stadium environment [METISD61].

A.4.1 Basic propagation environment and link topology

The location of the stadium is not very crucial, but we assume it is located in an urban environment. It is assumed that the focus is in providing wireless services inside a large stadium using carrier frequencies greater than 2 GHz. Hence it is assumed that the main propagation link type is from a number of micro BSs to a large number of UEs. BS antennas are attached on stadium roof structures so that the main propagation condition is LOS. In addition to the micro BS-UE (O2O) scenario D2D (O2O) communication is possible. The backhaul to the base stations is assumed to be provided via optical fibre.

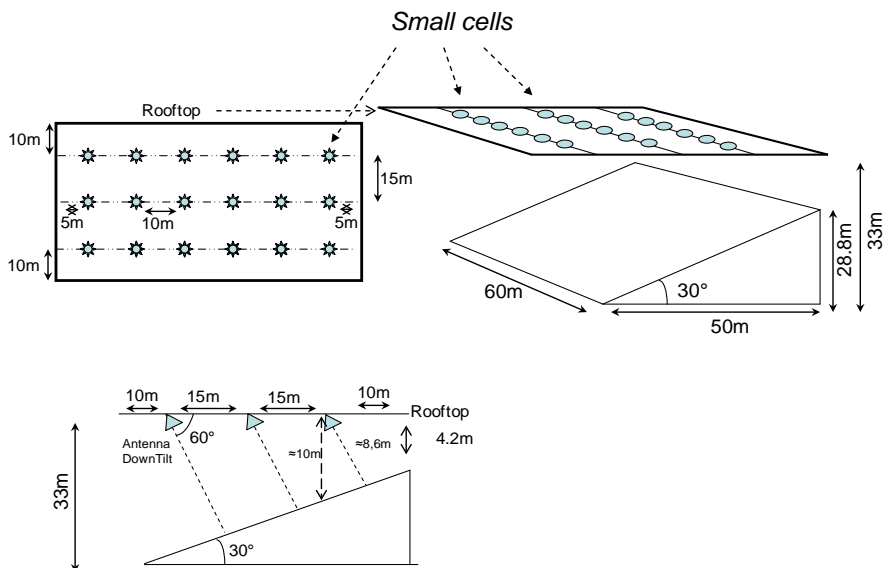


Figure A-6: An example of stadium sector as an elementary block of the test case.

A.4.2 Frequency ranges

It is obvious that large bandwidths are needed to fulfil the prospective system capacity needs. As an example, large antenna arrays could be deployed for small cell base stations operating at some available 2-6 GHz frequency range with enough bandwidth. The entire stadium could be covered by a number of antenna arrays which have tens of antenna elements. As regards the propagation, 60 GHz links could be possibly deployed also for micro BS-UE and possibly also for D2D links if large bandwidths are required. The reason is the short propagation distances from BS to UE.

A.4.3 Propagation scenarios

BS-UE (O2O):

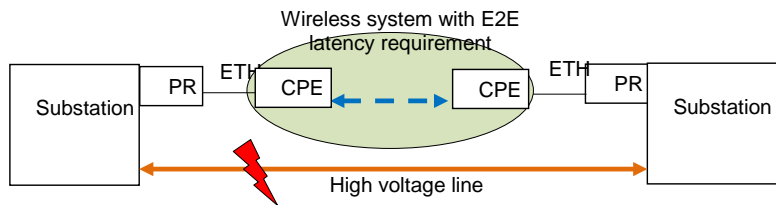
UEs are connected to Micro BSs (MBSs). MBS heights are typically less than 30 m, and Urban Micro scenario can be utilized with the consideration of the dense population of human bodies. Because the geometry of the stadium is well specified, a map-based 3D model can be applied, possibly a special case of the new model for the TC2.

D2D (O2O):

D2D considers a radio link between different UEs. UE heights are assumed to be around 0.5-1.0 m above the stadium seats. In case of D2D communication absorption loss due to human bodies should be taken into account, although it depends quite heavily on the locations of the respective UEs.

A.5 Smart energy distribution grid propagation scenario set (for TC5)

Teleprotection for smart energy distribution grids (SG) is essential to prevent a local energy blackout from escalating to the entire grid. In the case of a malfunction in an energy distribution network error messages must be sent between substations of the electricity network (SSs) within a latency of less than 10 ms.



PR: Protective Relay

CPE: Customer Premises Equipment

ETH: Ethernet

Figure A-7: Overview of smart energy distribution grid.

Radio communication between fixed BSs and SSs can be organized utilizing normal cellular BS antennas and directive SS antennas at lower frequencies. Alternatively, highly directive antennas for BSs and SSs can be utilized if higher frequencies (e.g. 6-20 GHz) are deployed for composing fixed radio links. The TC is described in more detail in [MET13-D61].

A.5.1 Propagation scenarios

Possible carrier frequencies include the sub 6 GHz IMT bands as well as unlicensed bands (e.g., at 2.4-2.5 GHz, 5.15-5.35 GHz and 5.725-5.875 GHz). The SS antennas can be assumed as high gain fixed antennas with limited multi-paths.

BS-SS (O2O):

Macro BSs are connected to substations (SSs). BS height is typically about 10-30 m, and Dense Urban, Urban and Rural environments are assumed to be simulated in METIS. System simulation may be conducted with the UMi and UMa channel models in the urban environments. Rural Macro (RMa) model can be used in the rural environment.

SS-SS (O2O):

Substations are connected to each other. The possible propagation environments cover Urban, Suburban, and Rural macro cell types. Assuming relatively high SS antenna heights LOS (or obstructed LOS) channel models, e.g., UMi-LOS, UMa-LOS, SMa-LOS, and RMa-LOS models of IMT-Advanced [ITU09-2135] can be applied depending on the propagation environment.

A.6 Traffic jam propagation scenario set (for TC6)

In a traffic jam, the throughput demand is expected to grow substantially, due to the consumption of network based infotainment services. The traffic jam scenario may occur anywhere due to, e.g., traffic accidents or extreme weather conditions. However, in METIS outdoor dense urban, urban and highway environments are simulated.



Figure A-8: Conceptual overview of traffic jam test case environment.

A.6.1 Propagation scenarios

There are basically two possible propagation scenarios which need to be modelled, i.e. radio propagation from the BS or network infrastructure to the UE inside a vehicle and from the BS to the external antennas of the vehicle. The BS antenna heights are expected to range from 10 to 25 m, the network infrastructure on the road is at a height of around 10 m, and the user device / vehicle antennas at 1.5-1.8 m height for passenger cars. The vehicle velocity is assumed to be very slow, i.e. 0-30 km/h.

BS-Vehicle (O2O):

BSs are connected to vehicles and user devices inside those vehicles. BSs are the same that are used in the environment in question, although some additional BSs can be used [MET13-D61]. PSs to be covered are UMa and UMi scenarios as well as Highway PS.

The transmission from a relay to the interior of the vehicle can be amplified and should allow good connections.

BS-UE (O2I):

In-vehicle users experience additional penetration loss from outdoor to indoor that should be taken into account.

A.7 Blind spots propagation scenario set (for TC7)

Wireless service quality might be significantly degraded in blind spots or coverage holes. The vehicle may be shadowed, e.g., by large buildings. To overcome the above problem stationary vehicles can be used for providing better coverage so that the radios in the vehicle communicate with the base station and with the nearby UEs acting as relays. It is assumed that the car can have a greater antenna height and a better antenna system than ordinary UEs.

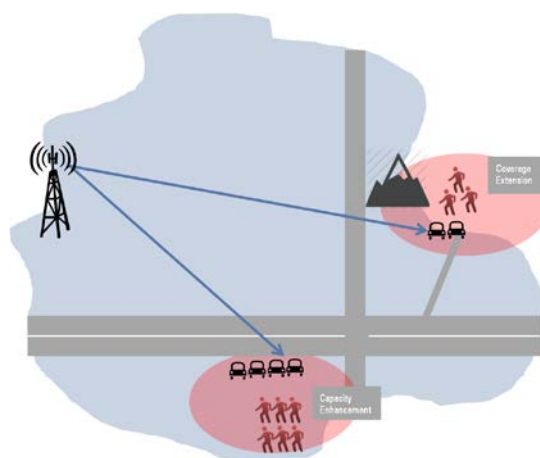


Figure A-9: Propagation scenarios for TC7 Blind Spots. Two conditions shown: The vehicle out of the ordinary coverage area (upper) and the vehicle in the ordinary coverage area (lower) of the BS.

A.7.1 Propagation scenarios

There are two propagation scenarios which are relevant, i.e. rural macro cell and urban macro cell. In both propagation scenarios a channel model from elevated BS antennas to the antennas of vehicles is needed. The network coverage area can be extended by letting the vehicle relay the signal to the user devices outside the vehicle. The BSs are assumed to be at their normal heights in rural and urban environments. The vehicle antennas are assumed to be at a height of 1-3 m and the user devices at a height of 1-2 m. The vehicles are furthermore assumed to be stationary.

BS-Vehicle (O2O):

BSs are connected to the vehicle relay via outdoor antennas. The connection to the outdoor users near the vehicle is formed through the vehicle relay. Same BSs are used for these connections as for other types of connections in the environments in question. PSs to be covered are UMa and RMa scenarios.

Vehicle-UE (O2O):

Vehicle roof top antennas are connected to the pedestrian outdoor users. D2D rural and urban micro cell PSs are specified for this connection type. In [MET13-D61] it is specified that the UEs are located within a 50 m radius around the vehicles.

A.8 Remote computing propagation scenario set (for TC8)

In TC8 real-time access is provided for remote computing for highly mobile terminals. High data rates and low latency are offered in the presence of high mobility. The increased capacity is provided by using a mobile relay together with advanced antenna solutions inside of the vehicle. This test case provides an extra aspect to TC2, the dense urban information society, since the focus is only on terminals with mobility. As a result, the environment, propagation, traffic, mobility and deployment models assumed for TC2 can all be reused for TC8. More detailed specification is given in [MET13-D61].

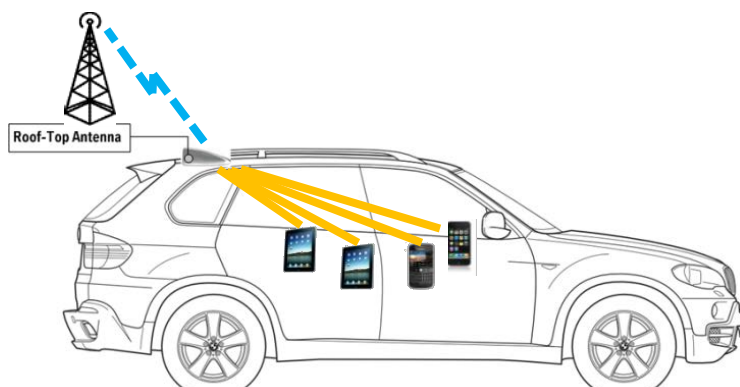


Figure A-10: Propagation scenario for TC8 [MET13-D11].

This test case is investigating the method to exploit external relays as wireless gateways to overcome the high vehicle penetration attenuation (up to 20 dB), as shown in Figure A-10. The propagation model should support high velocities of cars and high-speed trains. The I2I link from the gateway to UE inside the vehicle may be assumed quite stationary and due to short propagation distance, this link may be of less importance than the O2O link from BS to RS. In order to achieve high reliability, the BS-RS link is much more vulnerable due to the varying propagation channel.

A.8.1 Propagation scenarios

The used BSs are the same as in the ordinary PSs, i.e. cases where connections are formed without a relay in the vehicle, in the same environment in both propagation scenarios below. Urban environment is assumed for the TC8 [MET13-D61].

BS-UE (O2I):

BSs are connected to in-vehicle UEs without relays. UE antenna height is assumed to be around 1-2 m in cars. In buses and other greater vehicles UE antenna heights are assumed to be 2 – 2.5 m or even 3.5 m in a double decker.

BS-RS (O2O):

BSs are connected to the in-vehicle UEs with relays. This scenario is similar to the BS-UE (O2O) scenario, except that the location of the RS antenna is assumed to be outside of the vehicle (e.g. on the roof or in the window). RS heights are assumed to be around 1.5-3 m on the outside of the vehicles. Buses and other greater vehicles may have antenna heights of 2.5-4.5 m. If buses will be simulated, the upper limit for the height should be 4.5 m.

The relays are moving with velocities of up to 250 km/h or more, which needs to be taken into account in the channel models.

RS-UE (I2I):

It is assumed that the placement of the RS is outside of the vehicle, but there are means to convey the signal through the shell of the vehicle so that no loss needs to be considered (e.g. by cables) and the signal is regenerated in the interior part of the relay. This means that the RS-UE link is an I2I link with very small distances from the RS to the UEs in the car, and relatively small distances, e.g. in buses and other big vehicles. The RS antenna height inside the vehicles is assumed to be 1-1.5 m in cars and 2-2.5 m in buses and rail cars, assuming the location of the RS inner part is near the ceiling.

A.9 Open air festival propagation scenario set (for TC9)

The open air festival test case is related to the outdoor open space propagation scenarios in a rural environment. Except the festival event, only few people live in the area, and the existing telephone connections have too low capacity for the festival visitors so that almost all connections for the festival are arranged by temporary base stations in the festival area. In the simulations the festival place is modelled as a square field, with an area of 1 km by 1 km. The

number of the festival visitors is assumed to be 100,000, there are 10 stages for the entertainers and the communication network consists of five, nine or 25 base stations.

The BS antennas are assumed to be 10 m high, and in addition to human users (antenna height 1-2 m) there are sensor UEs and corresponding with antenna heights ranging from 1 to 5 m. More details can be found in [MET13-D61].

An efficient backhaul link accommodation via wireless is assumed, as indicated in [MET13-D11]. It is also assumed that the high-capacity wireless external connection is only seen as a source/sink of information.

A dense deployment by high-capacity small cells is assumed, bandwidths 20-100 MHz, as well as the reuse of 3D MIMO channel model for TC2 with the shadowing feature adapted for this test case. In TC9 an extremely important feature is to model shadowing and scattering by human bodies in a dense crowd. This is especially important for the D2D link type.

A.9.1 Frequency ranges

The default frequency range is between 2 and 6 GHz.

In addition also higher frequencies can be considered:

- Ku/K bands (12-28 GHz) may be feasible mainly in small cells, sensor and wireless backhaul. Due to poor link budget mmW frequencies are not assumed to be used for macro cells.
- Millimetre waves (60 GHz and beyond) have the possibility to enable highly resolved spatial multiplexing and large bandwidth for high capacity, in particular for wireless backhaul of small cells.

A.9.2 Propagation scenarios

BS-UE (O2O):

In this PS UEs are directly connected to the BSs. UE heights are assumed to be in the range of 1-5 m. Below we propose three modelling approaches with two channel models.

Option 1: 5 BSs

If the coverage is planned with five BSs, the usage of macro cells is recommended. BS heights are assumed to be 20-30 m. Ordinary UEs are assumed to be located at a height of 1-2 m, the antenna heights for the sensors and comparable equipment range from 1 to 5 m. Rural ITU-R model [ITU09-2135] is proposed for the channel model.

Option 2: 25 BSs

If the coverage is planned with 25 BSs, using of micro cells is recommended. The BS antenna heights are assumed to be around 10 m. The antenna heights are the same as in Option 1. For Option 2 the channel model of TC2 is recommended. Shadowing and scattering by human bodies in a dense crowd needs to be modelled.

Option 3: 9 BSs

If the coverage is planned with nine BSs, either the model of Option 1 or Option 2 is possible. Even a combination could be considered.

D2D (O2O):

UE heights are assumed to be around 1.5 m above the ground. As regards the sensors and comparable equipment, the antenna heights are in the range of 1-5 m. The absorption loss due to human body shadowing should be taken into account. Again, the channel model for TC2 is proposed to be reused.

Backhaul (O2O):

For wireless backhaul, standard LOS channel models might be applicable. For small cells highly resolved spatial multiplexing is possible, particularly for the highest frequency range by means of “pencil beam-forming”. For this purpose highly elevated access points are assumed

in order to achieve high LOS probability to the users. For this case also point-to-point microwave link channel models might be usable for initial channel models. However, in this case human body shadowing and UE mobility have to be taken into account. It is assumed that the final channel models for mmW range need to be three dimensional.



Figure A-11: Conceptual overview of TC9 Open Air Festival.

A.10 Emergency propagation scenario set (for TC10)

This propagation scenario assumes that the legacy Base Station network is partially or completely collapsed. UEs are operating in a battery save mode providing low data rate services (voice & SMS and terminal localization) at least for one week. UEs compose a meshed network serving as UE relay stations (URs) when needed. In terms of propagation there is no difference between UE and UR, therefore these are used interchangeably in this section. Emergency Base Stations (EBSs) are deployed to enable a connection to legacy networks. Links from EBSs to the legacy network are assumed to be mostly in LOS condition. The propagation environments are urban and rural areas with collapsed buildings and structures. UEs/URs are assumed to be stationary at a height of either about 1.5 m above ground or buried in the rubble. Routed communication from basement rooms is possible via UE-UR mesh. EBSs are mobile (height 1-3 m with speed of 4-40 km/h), hovering (height 3-100 m) or flying (height 3-100 m with speed of 10-100 km/h).

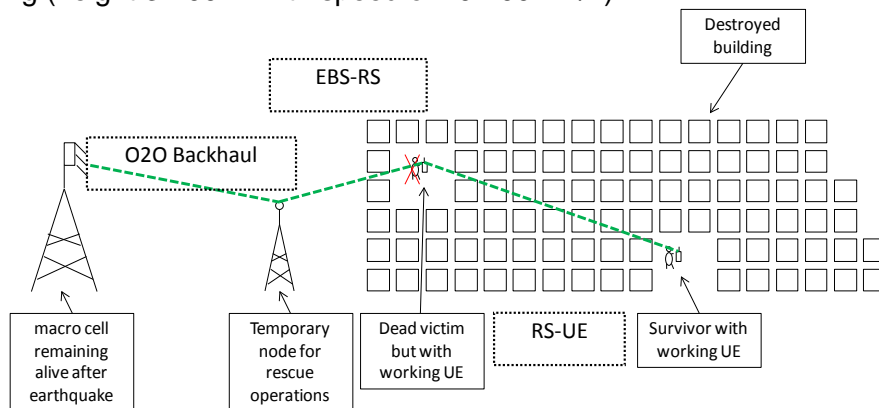


Figure A-12: Overview of TC environment and NW deployment / user distribution.

There are several link types categorized by link environment. The same link type can include a range of EBS heights and velocities.

A.10.1 Propagation scenarios

EBS-UR (O2O) with dominant LOS:

UEs and corner URs are connected to EBSs or to survived legacy BSs. Initially, ITU-R M.2135 (RMa) [ITU09-2135] can be used to model this connection.

EBS-UR (O2I) LOS/NLOS through walls, openings & windows:

UEs and corner URs are connected to EBSs. Initially, ITU-R M.2135 (UMi) can be used to model this connection. Note that the conventional losses due to walls and windows can possibly be eased due to broken structures. Signal penetration to partially ruined buildings needs further studies.

EBS-UR (O2R) LOS/NLOS through rubble:

UEs and the corner URs are directly connected to EBSs. LOS is most often obscured, propagation through collapsed structures (rubble). Initially, ITU-R M.2135 (UMi LOS/NLOS) added with a rubble attenuation can be used to model this connection. Little propagation studies have been done on this situation [HKG+08] and most likely new measurement data is needed to specify the rubble attenuation.

UR-UE (O2O) with dominant LOS:

UEs are connected to URs in a meshed network. This propagation scenario is similar to D2D (O2O) with stationary or nomadic devices. The channels between UE and UR are assumed to be reciprocal.

UR-UE (O2I) LOS/NLOS through openings & windows:

UEs are connected to URs in a meshed network. This propagation scenario can be modeled by wall penetration models, similar to UMi O2I in [ITU09-2135].

UR-UE (I2I) LOS/NLOS indoor:

UEs are connected to URs in a meshed network. UE and UR can reside in different buildings. This propagation scenario is similar to D2D I2I.

UR-UE (R2R) LOS/NLOS through rubble:

UEs are connected to URs in a meshed network. LOS is most often blocked/obscured, propagation through collapsed structures (rubble). This case also contains propagation from buried UE to an indoor UE (i.e. indoor structures that are not collapsed). Few propagation studies have been done on this situation [CLR10], [HKG+05], [HKG+08], [HZC+11], and most likely new measurement data is needed.

A.11 Massive sensor and actuator propagation scenario set (for TC11)

This TC consists of vast amounts of low-power sensors and actuators (see [MET13-D11] for details). Several sensors are transmitting to a device collecting the data from sensors and transmitting it further e.g. to a cellular network. The data collecting device should be located in the vicinity of sensors. The link between the data collecting device and network can be modelled with current cellular propagation models, but it is out of scope in this analysis, which concentrates on the link between the sensors and the data collecting device.

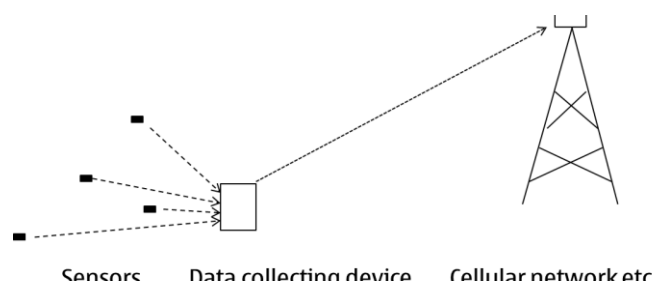


Figure A-13: Data from several sensors is received by a data collecting device, which transmits it further to the network.

In most applications both sensors and the data collecting device are at low height. Their connections can be regarded as D2D links.

Typically sensors have only one Tx antenna, though polarization diversity might be feasible. The receiving device can have several antennas for better sensitivity. An antenna array also makes it possible to locate the transmitter. Therefore the channel type is assumed to be SIMO. The receiving devices are assumed to be stationary. The sensors and actuators are assumed to be stationary or moving as vehicles. The environments considered in the simulations are urban microcell (TC2) and urban macrocell.

A.11.1 Propagation scenarios

BS and UE are typically stationary or moving. If moving, the movement is similar as in the corresponding UMi or UMa case. In an urban environment sensors can be attached to various objects, which need to be monitored.

D2D, Urban macrocell (O2O):

Sensors can be distributed in the macro-cellular environment as specified in [MET13-D61]. The urban macro-cellular channel model is recommended with the reduced antenna height of the data collecting unit compared to the original model.

D2D, Urban microcell (O2O):

Sensors can be distributed in the microcellular Madrid grid environment as specified in [MET13-D61]. In this scenario the 3D microcellular model or the corresponding D2D model is recommended, depending on the height of the sensors and the receiver.

A.12 Traffic safety propagation scenario set (for TC12)

The main focus of this test case is on traffic safety and vulnerable road users, e.g. where drivers are warned of dangerous situations and automatic braking or steering is activated if the driver is unable to avoid an accident. Another example is the highly automated driving.

It is also assumed that some road infrastructure (road signs, traffic lights, etc.) is equipped with communication modules, with antenna heights of 2 – 5 m, that communicate with the vehicle modules. In order to meet very high real time requirements, D2D communication is assumed. However, for coordination and management the cellular network can be used.

A.12.1 General requirements for the TC12 D2D channel models

The antennas are mounted on the roof of the vehicles which are 1-2 m high for passenger cars, and between 2.5 – 4.5 m for buses and trucks, depending on the vehicle type. For the case of vulnerable road users (VRU) like pedestrians, the number and type of antennas is assumed to be those of regular UEs (e.g. smartphones). Furthermore antenna heights of 1-1.5 m are assumed. Frequency range below 6 GHz is preferable due to the smaller losses by obstructions, like buildings and vehicles, than compared to the losses at higher frequencies.

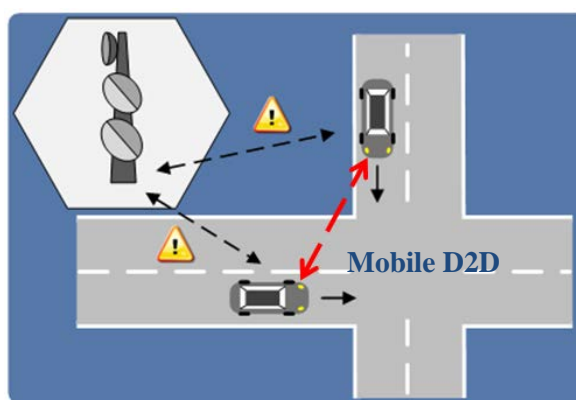


Figure A-14: Overview of TC12 traffic safety environment.



A.12.2 Propagation scenarios

The mobility models, device densities and other details can be found in [MET13-D61].

D2D, Urban (O2O):

Urban D2D model is proposed for this scenario taking into account the movement of both link ends and environment. The maximum coverage distance is 300 m and environment is the same as in TC2, i.e. Madrid grid.

D2D, Highway (O2O):

Rural cellular model is proposed to be reused adjusting the BS antenna height and taking into account the movement of both link ends and environment.

D2D, Rural (O2O):

Rural cellular model is proposed to be reused adjusting BS antenna height and taking into account the movement of both link ends and environment.

V2I, Urban (O2O):

Urban vehicle to infrastructure channel can be modelled by the TC2 3D model by adjusting the antenna heights appropriately.

Appendix B Detailed measurement reports

This section provides the detailed technical descriptions of the measurement campaigns conducted by the METIS partners. The brief summary of the measurement campaigns are explained in Section 4. Table 5-1 summarizes and lists the conducted measurements.

B.1 Channel measurements at 2.3 GHz and 5.25 GHz in Oulu downtown

The measurements have been executed in the Oulu downtown area. Five measurement environments (ME) were covered for METIS Dense Urban Test Case 2 (TC 2):

- ME1: Urban Vehicle to Vehicle (V2V), SIMO
- ME2: Urban Macrocell Outdoor (O2O), SIMO and MIMO
- ME3: Urban Macrocell Outdoor to Indoor (O2I), MIMO
- ME4: Urban Microcell Outdoor to Indoor (O2I), MIMO
- ME5: Urban Microcell Outdoor (O2O), MIMO

The measurement environments are summarized in Table B-1.

Table B-1: The summary of the measurement environments at 2.3 and 5.25 GHz in Oulu downtown

Measurement environment	ME1	ME2	ME3	ME4	ME5
Link topology	UE-UE	BS-UE	BS-UE	BS-UE	BS-UE
Propagation Scenario	Urban V2V	UMa O2O	UMa O2I	UMi O2I	UMi O2O
Center Frequencies	2.3 GHz and 5.25 GHz	2.3 GHz and 5.25 GHz	2.3 GHz	2.3 GHz and 5.25 GHz	2.3 GHz and 5.25 GHz
Polarizations	TX Vertical, RX dual pol (45deg)	TX: Vertical (dipole) /dual pol ±45 deg (antenna array), RX dual pol (45deg)	Dual pol (±45 deg)	Dual pol (45 deg)	Dual pol (45 deg)
TX location / velocity	Oulu downtown, 0-30 km/h	One stationary location	2 Stationary locations, on the roof of building	2 Stationary locations	One Stationary location
TX height above ground level	1.6 m	18 m	17.45 m	5 m, 10 m, 15 m (only for corridor measurements)	5 m, 10 m
RX location / velocity	Oulu downtown, 0-30 km/h	Oulu downtown, 0-30 km/h	Stationary, a) Hotel room :5 spots/TX location //floor b) Hotel corridor: 17 spots/floor	Hotel corridor: 7 spots/floor, Hotel room: 5 spots/floor	Oulu downtown, Stationary (vehicle stops for measurement)
RX height above ground level	2.5 m	2.5 m	1.6 m+ floor height	1.6 m+ floor height	2.5 m, RX on the rooftop of car
TX-RX distance	20-150 m	20-150 m	40-100 m	15-50 m	30-200 m
Antenna beamwidth, Azimuth / Elevation	RX az ±180 deg, TX Omnidirectional, RX el -70 -- +90 deg, TX ±80 deg	RX az ±180 deg, TX Omnidirectional, RX el -70 -- +90 deg, TX ±80 deg	RX az ±180 deg, TX az -70 -- +70 deg, RX vertical -70 -- +90 deg, TX vertical -70 -- +90 deg	RX az ±180 deg, TX az -70 -- +70 deg, RX vertical -70 -- +90 deg, TX vertical -70 -- +90 deg	RX az ±180 deg, TX az -70 -- +70 deg, RX vertical -70 -- +90 deg, TX vertical -70 -- +90 deg

			70 -- +90 deg		
Number of measurements, Channel sampling rate	Several long measurements covering streets and street corners 2.3 GHz: 583.567 Hz (SIMO), 192.99 Hz (MIMO) 5.25 GHz: 978.847 Hz (SIMO),	Several long measurements covering streets and street corners 2.3 GHz: 583.567 Hz (SIMO), 192.99 Hz (MIMO) 5.25 GHz: 978.847 Hz (SIMO),	27 / floor	~ 30 / floor / frequency	> 50 / frequency
Remarks	TX and RX move simultaneously	2.3 GHz measurements for SIMO (1 x 56) and MIMO (30 x 16) setup, 5.25 GHz measurements only for SIMO (1 x 50) setup	UE in several spots in different floors, varying link length	UE in several spots in different floors, varying link length	30 x 16 (2.3 GHz), 30 x 18 (5.25 GHz), Limited MIMO configuration due to moving scatterers
Campaign duration	2 days	2 days	2 days	2 days	2 days
Amount of data stored	89.9 GB	43.78 GB	43.67 GB	94.4 GB	4.41 GB

B.1.1 Measurement equipment and antennas

The measurements were conducted by EB PropSound channel sounder [Ele04]. The measurement device consists of two separate units: transmitter (TX) and receiver (RX) units. The both units use the same intermediate frequency (IF) of 1.45 GHz and have replaceable RF units for different RF frequency bands. The architecture of PropSound system is presented in Figure B-1.

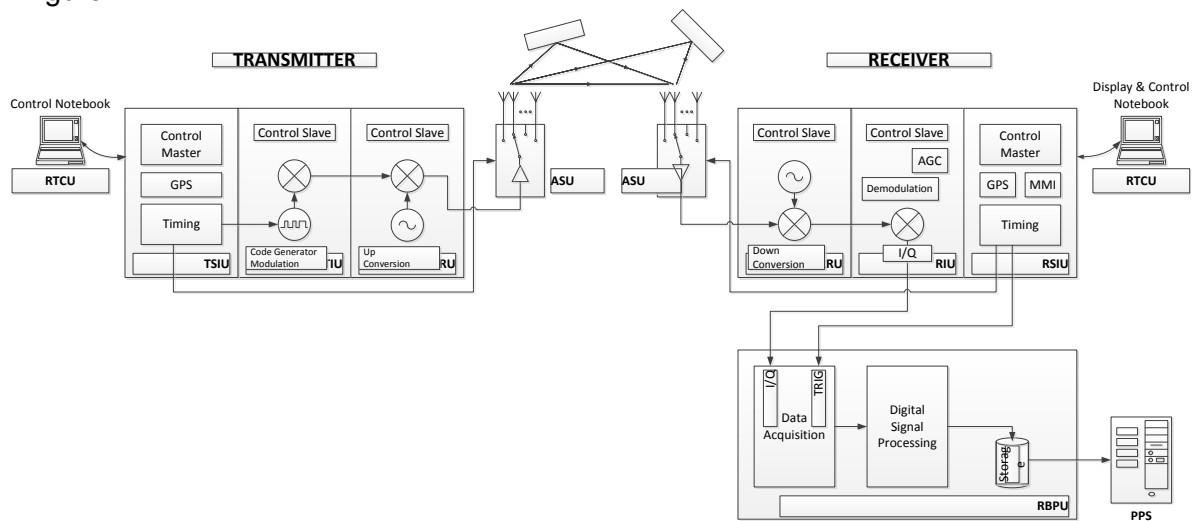


Figure B-1: PropSound system architecture.

PropSound uses direct sequence spread spectrum technique and BPSK modulation for channel sounding. Impulse responses of channel samples are obtained by correlating the received signal with the same spreading code as was used in the transmission. Sounding in the spatial domain is employed by switching through multiple antennas in the time domain. The antenna elements are switched almost instantaneously so that the channel response remains constant within antenna switching period.

B.1.1.1 Antennas

Dipole antennas were used as TX antenna in ME1 and ME2 scenarios and its properties are presented in Table B-2.

Table B-2: TX antenna properties

Antenna designation	Dipole_2G45	Dipole_5G25 (Modified 5G version of AV1433 WLAN antenna)
Frequency / Bandwidth	2.25 -2.55 GHz	5.2—5.3 GHz
Radiation	±180° az, 70° el (3 dB beam width)	
Antenna type		Coaxial dipole
Gain		1 dBi
Polarization		Vertical

Uniformly spaced linear antenna arrays (ULAs) illustrated in Figure B-2 were used as TX antennas in ME3, ME4 and ME5.

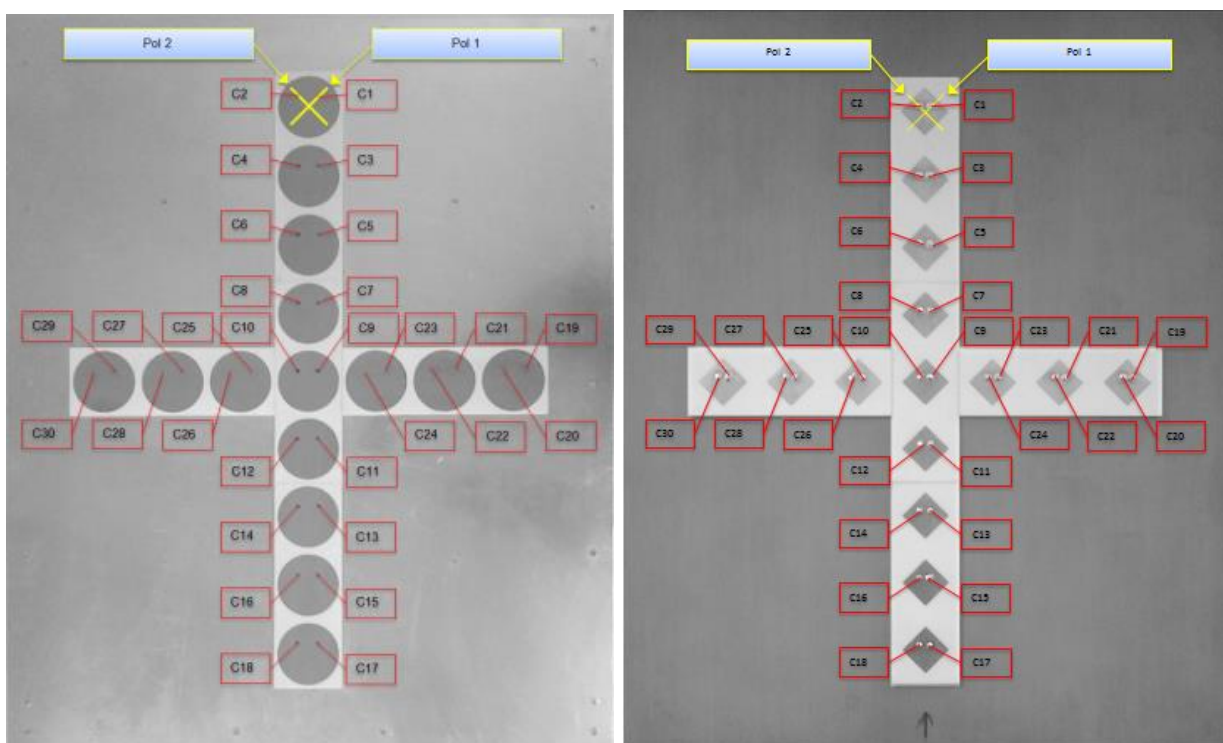


Figure B-2: TX ULA antenna for ME3, ME4 and ME5 scenarios at 2.3 GHz (left) and 5.25 GHz (right).

Omnidirectional antenna arrays were used as receiver antennas in all measurement scenarios and their properties are presented in Table B-3.

Table B-3: RX antenna properties

Antenna designation	3x8ODA_2G45_T1	2x9ODA_5G25_T1
Number of antenna elements	28	25
Type of element	Patch	
Polarization	Dual (± 45 degrees)	

Radiation	360° az, -70° -- + 90° el (HPBW)	
Gain of element	6 dBi	
Arrangement of elements	3 x 8 + 4 Dual-polarized elements	2 x 9 + 6 +1 Dual-polarized elements

The RX antennas for 2.3 GHz and 5.25 GHz are presented in Figure B-3 and Figure B-4, respectively.

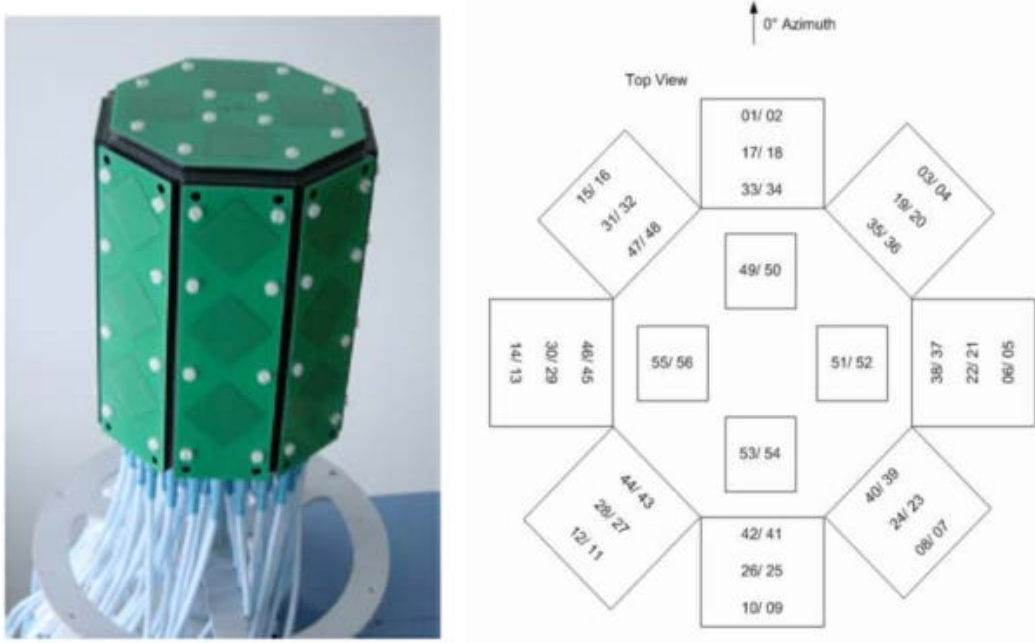


Figure B-3: RX antenna for 2.3 GHz.

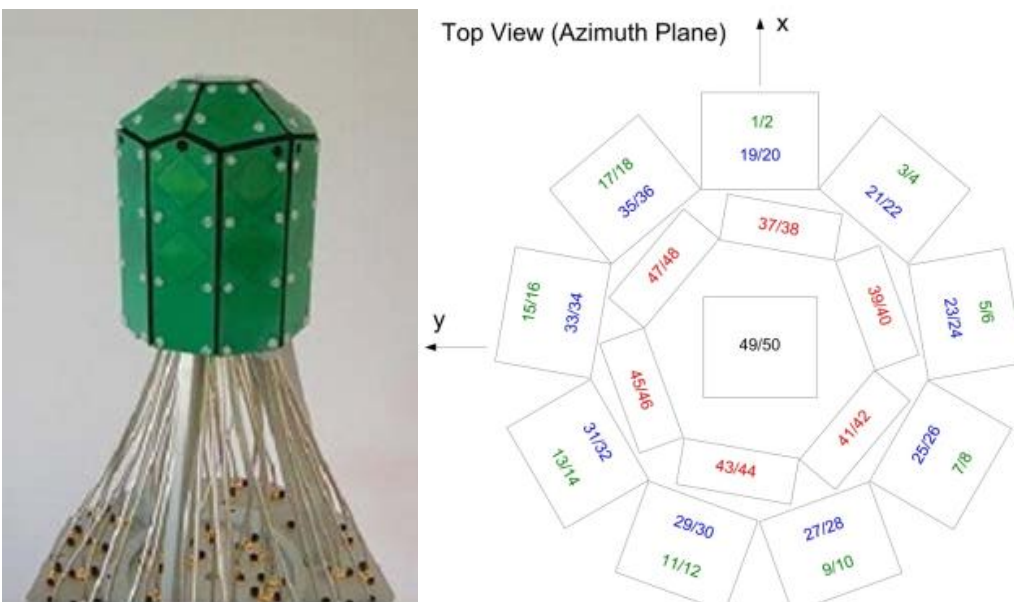


Figure B-4: RX antenna for 5.25 GHz.

B.1.1.2 Settings definition

The settings for all measurement scenarios for 2.3 GHz and 5.25 GHz are given in Table B-4 and Table B-5, respectively. The bandwidth and the code length effect on many important

features of the measurement. The code length affects directly on dynamic range by giving 3 dB more gain when doubled. The code length must also be chosen to have longer duration than the longest propagation delay to be measured. Increasing the code length deteriorates the ability of following the Doppler effects and requires a higher data storage rate. The bandwidth is directly defined by the chip frequency. The chip frequency has an influence on code duration thus it also has an influence on Doppler tolerance and the minimum code length. The dynamic range of a measurement can be increased by 3 dB by halving the bandwidth. The most important feature of bandwidth selection is its influence on the delay resolution of the measurement. Therefore the bandwidth should be kept as wide as possible.

Table B-4: Settings for measurements at 2.3 GHz

Basic Parameters						Remarks
Center frequency [GHz]	2.3					Radio license for 2.25-2.35 GHz
Transmit power [dBm]	+23					ALC / AGC enabled, Front-end attenuator 0 dB (as a default)
Bandwidth [MHz]	100					null-to-null, bandwidth based on radio license
Chip rate [Mchip/s]	50					BW/2
Chip sampling rate [samples/chip]	2					
Sampling rate [MHz]	100					Chip rate · Chip sampling rate → Delay resolution = 1 / Sampling rate
Measurement distance	ME1	ME2*	ME3	ME4	ME5	Remarks
Code length [chips]	255	255 / 127	511	511	127	
Measurable excess delay [μs]	5.11	5.11 / 2.55	10.22	10.22	2.55	Code length / Chip rate
Measurable excess distance [m]	~1500	~1500 / 750	~3000	~3000	750	Measurable excess delay · speed of light
Spatial resolution parameters	ME1	ME2*	ME3	ME4	ME5	Remarks
Number of TX antenna elements	1	1 / 30	30	30	30	Dipole or ULA
Number of RX antenna elements	56	56 / 16**	56	56	16**	ODA_2GHz
Number of channels	56	56 / 480	1680	1680	480	
Fast switching	Not used					Guard time according to code length, e.g. 255 chips. If fast switching is used, guard time between TX antenna elements switching can be decreased and thus array scan time can be decreased.
Array scan time [μs]	571.2	571.2 / 2590.8	34952	34952	2590.8	Array scan time should be shorter than channel coherence time
IR resolution parameters	ME1	ME2*	ME3	ME4	ME5	Remarks
Channel sample rate (trigger rate) [Hz]	583.567	583.567 / 192.99	7.153	7.153	192.99	
samples per wavelength	3.425	3.425 / 3.761	-	-	3.02	
TX relative speed [km/h]	0-20	-	-	-	-	TX is moving to the same direction as the RX with



						the same speed or TX is moving away or towards the RX
RX relative speed [km/h]	0-20	0-20 / -	-	-	-	RX is moving to the same direction as the TX with the same speed or RX is moving away or towards the TX
Max. scatter speed [km/h]	20	20	-	-	15	Assumption for max. scatter speed
Max. Doppler shift [Hz]	170.37	170.37 / 63.894	-	-	63.889	
Channel coherence time [μs]	~1050	~1050 / 2802	-	-	2802	9/(16·π·Max. Doppler shift)
Data storage parameters	ME1	ME2*	ME3	ME4	ME5	Remarks
Burst mode	Yes				Burst mode is used to decrease the storage data rate.	
Burst length [Cycles]	8	8 / 8	4	4	8	Number of cycles, which are acquired during one burst period.
Burst period [Cycles]	20	20 / 16	8	8	16	
Burst rate [Hz]	29.178	29.178 / 12.062	0.894	0.894	12.062	
Movement during burst [m]	0.381	0.381 / 0	-	-	-	
Storage data rate [MB/s]	12.716	12.716/ 23.842	11.922	11.922	23.842	
Storage duration [min]	~182	~182 / ~97	~195	~195	~97	Hard disk size 136 GB
Data recorded / measurement spot [Cycles]***	-	- / 80	80	80	80	

* Two configurations were used for ME2,

1. SIMO, RX moves during the measurement, recording was stopped after every measurement route
2. MIMO, RX stationary during the data recording, the fixed number of cycles were recorded

** The lowest ring of ODA elements was used (see Figure B-3)

*** The fixed number of cycles was recorded in ME3, ME4 and ME5 scenarios.

Table B-5: Settings for measurements at 5.2 GHz

Basic Parameters		Remarks
Center frequency [GHz]	5.25	Radio license for 5.15-5.35 GHz
Transmit power [dBm]	+23	ALC / AGC enabled, Front-end attenuator 0 dB (as a default)
Bandwidth [MHz]	200	null-to-null, bandwidth based on radio license
Chip rate [Mchip/s]	100	BW/2



Chip sampling rate [samples/chip]	2				
Sampling rate [MHz]	200				Chip rate · Chip sampling rate → Delay resolution = 1/ Sampling rate
Measurement distance	ME1	ME2	ME4	ME5	Remarks
Code length [chips]	511	511	511	127	
Measurable excess delay [μ s]	5.11	5.11	5.11	1.27	Code length/ Chip rate
Measurable excess distance [m]	~1500	~1500	~1500	~380	Measurable excess delay · speed of light
Spatial resolution parameters	ME1	ME2	ME4	ME5	Remarks
Number of TX antenna elements	1	1	30	30	Dipole or ULA
Number of RX antenna elements	50	50	50	18*	ODA_5GHz
Number of channels	50	50	1500	540	
Fast switching	Not used				Guard time according to code length, i.e. 255 chips. If fast switching is used, guard time between TX antenna elements switching can be decreased and thus array scan time can be also decreased.
Array scan time [μ s]	511	511	15636.6	1447.8	Array scan time should be shorter than channel coherence time
IR resolution parameters	ME1	ME2	ME4	ME5	Remarks
Channel sample rate (trigger rate) [Hz]	978.474	978.474	7.106	345.352	
Samples per wavelength	3.354	3.354	-	-	
TX relative speed [km/h]	0-20	-	-	-	0 km/h [TX is moving to the same direction as the RX with the same speed], 20 km/h [TX is moving away or towards the RX]
RX relative speed [km/h]	0-20	0-20 / -	-	-	0 km/h [RX is moving to the same direction as the TX with the same speed], 20 km/h [RX is moving away or towards the TX]
Max. scatter speed [km/h]	20	20	-	10	Assumption for max. scatter speed
Max. Doppler shift [Hz]	291.69	291.69	-	97.22	
Channel coherence time [μ s]	~613.83	~613.83	-	1841.6	9/(16· π ·Max. Doppler shift)
Data storage parameters	ME1	ME2	ME4	ME5	Remarks
Burst mode	Yes				Burst mode is used to decrease the storage data rate.
Burst length [Cycles]	8	8	4	8	Number of cycles, which are acquired during one burst period.
Burst period [Cycles]	32	32	8	32	
Burst rate [Hz]	30.577	30.577	0.888	10.792	

Movement during burst [m]	0.182	0.182	-	-	
Storage data rate [MB/s]	23.8	23.8	10.597	23.842	
Storage duration [min]	~97	~97	~219	~97	Hard disk size 136 GB
Data recorded / measurement spot [Cycles] **	-	-	80	80	

* The lowest ring of ODA elements was used (see Figure B-4)

** Recording was stopped after every measurement route In ME1 and ME2 scenarios whereas the fixed number of cycles were recorded in ME4 and ME5 scenarios.

B.1.2 Measurement scenarios

B.1.2.1 ME1: Urban Vehicle to Vehicle (SIMO)

In ME1, the measurements were performed using two moving vehicles. One vehicle was carrying the TX unit while the other was equipped with the RX unit. Cars moved in different directions and distances, and at varying velocities within Oulu city centre area. The measurement parameters were selected carefully to allow Doppler induced by typical scatter velocities in urban environment. The TX antenna and the RX antenna height was 1.6 m and 2.5 m, respectively.

The setup for the vehicle-to-vehicle (V2V) measurement scenario is depicted in Figure B-5.

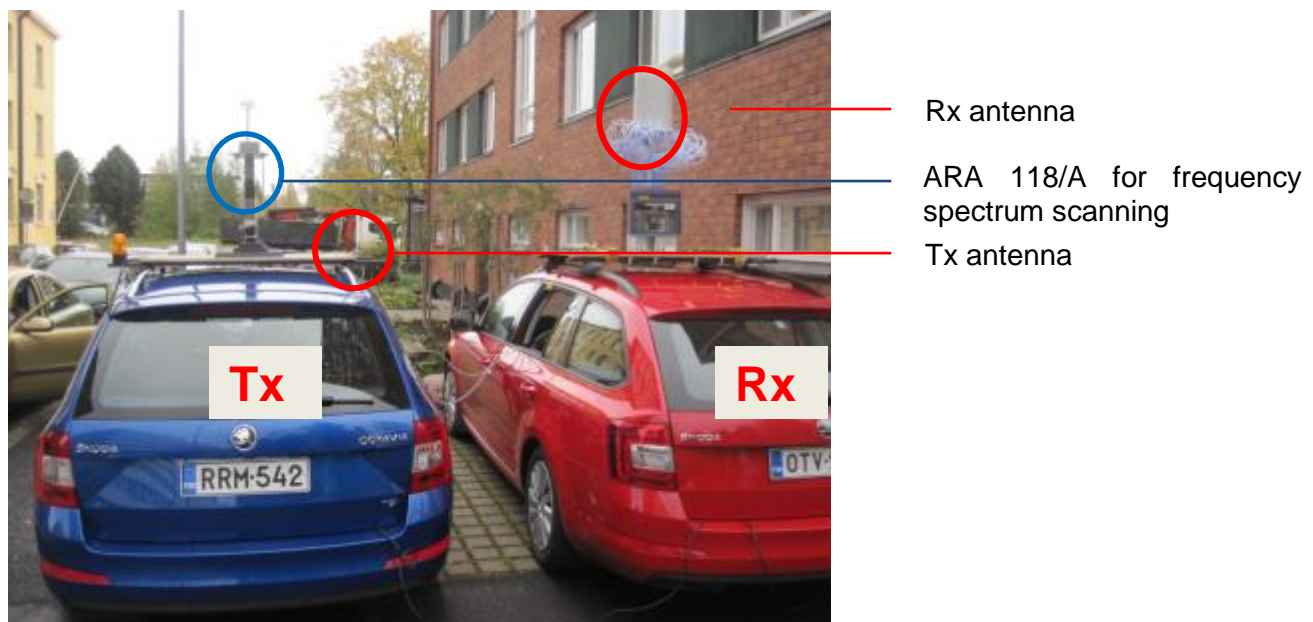


Figure B-5: Measurement setup for ME1.

B.1.2.1.1 Measurement routes

The measurements consisted of seven measurement routes illustrated in Figure B-6 to Figure B-9. Vehicles were moving in the same direction in the first three measurements (Figure A-6 and Figure A-7) whereas vehicles were moving in opposite directions in 4th and 5th measurement (Figure B-8). During the last two measurements one of the vehicles (either RX or TX) was stationary and other vehicle was moving on the cross street (Figure B-9).



Figure B-6: TX leading and RX follows, vehicles move in the same directions.

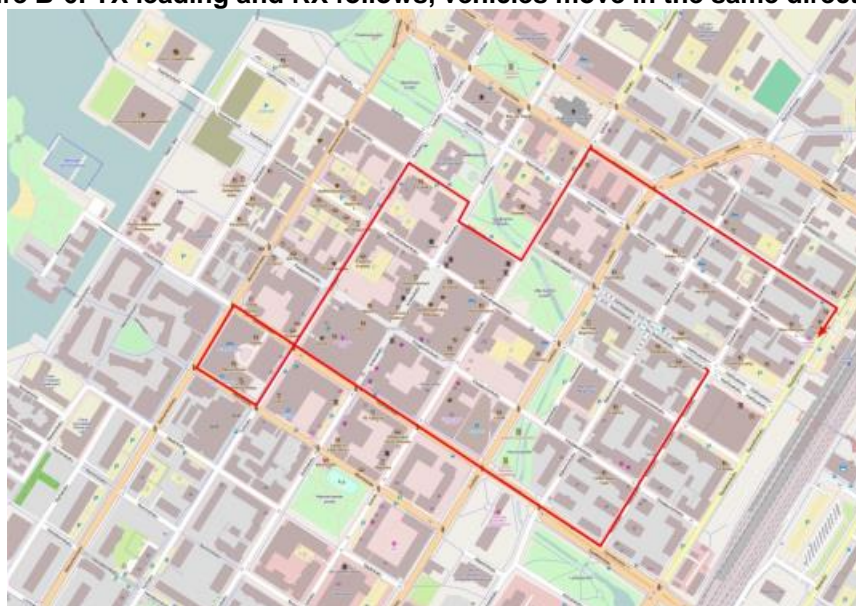


Figure B-7: RX leading and TX follows, vehicles move to the same directions.

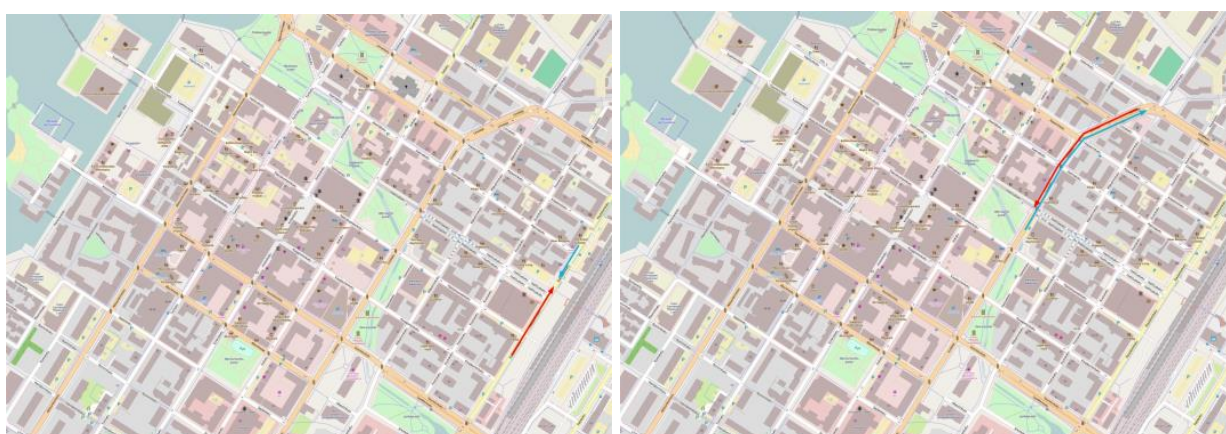


Figure B-8: TX (blue line) and RX (red line) routes moves to the opposite directions.



Figure B-9: TX/RX (blue/red dot) stationary position and RX/TX (red/blue line) moves on the cross street.

B.1.2.2 ME2: Urban Macrocell Outdoor

In ME2, the measurements were performed for SIMO and MIMO antenna setup. RX antenna was placed on top of car (height 2.5 m above street level) and TX antenna was located at around 18 m height by a building wall as depicted in Figure B-10. The RX setup is similar to ME1. RX moved close to TX location gathering path loss information along the street and around the street corners. The measurement parameters were selected to allow moderate scatter velocities. The data was recorded continuously during the SIMO measurements whereas the RX was stationary during the data recording in MIMO measurements.



Figure B-10: TX antennas: 5.25 GHz dipole (SIMO) and 2.3 GHz ULA (MIMO).

B.1.2.2.1 Measurement routes

TX antenna location ($65^{\circ} 0.647'$ LAT, $25^{\circ} 28.987'$ LON, blue circle) and RX routes (red line) are presented in Figure B-11 to Figure B-14.



Figure B-11: RX measurement routes 1 and 2.



Figure B-12: RX measurement routes 3 and 4.



Figure B-13: RX measurement routes 5 and 6.



Figure B-14: RX (red line) measurement route 7.

B.1.2.3 ME3: Urban Macrocell Outdoor to Indoor (MIMO)

The RX antenna was located at the inside of the Scandic hotel ($65^{\circ} 0.714'$ LAT, $25^{\circ} 27.919'$ LON), which has six floors. The TX antenna was located ($65^{\circ} 0.715'$ LAT, $25^{\circ} 28.175'$ LON) on a balcony of a neighbouring building at 17.45 m from ground and 1.30 m from the exterior wall (Figure B-15). The height of the TX antenna in relation to the target building was 16 m above the ground floor.



Figure B-15: TX antenna on the top of building.

B.1.2.3.1 Measurement spots

The RX was stationary during the data recording. The RX location was either in the hotel room or in the corridor of the hotel. The measurement spots in the hotel room are presented as red dots in Figure B-16. Five measurement spots were selected in the hotel room with two different TX positions on the roof of a neighbouring building. The measurements were repeated in the same vertically aligned rooms on floors 2 to 5.

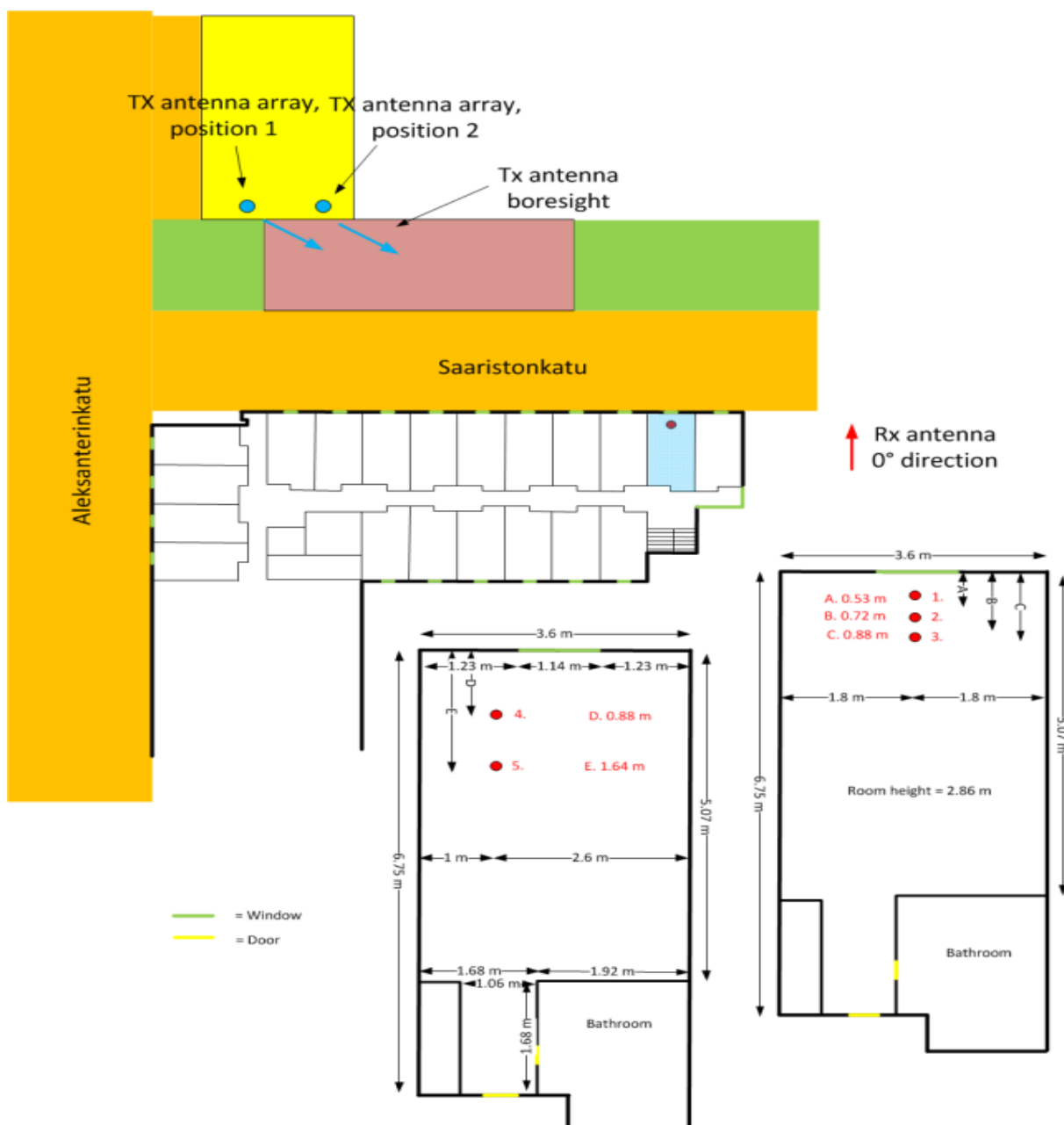


Figure B-16: Measurement spots inside the hotel room for ME3 scenario.

17 spots were measured on the hotel corridor on floors 2 to 5. In addition, 9 spots were measured on the 6th floor. The layout of the hotel corridor is similar for the 3rd, 4th and 5th floor. Figure B-17 presents the measured spots in the corridor of these floors.

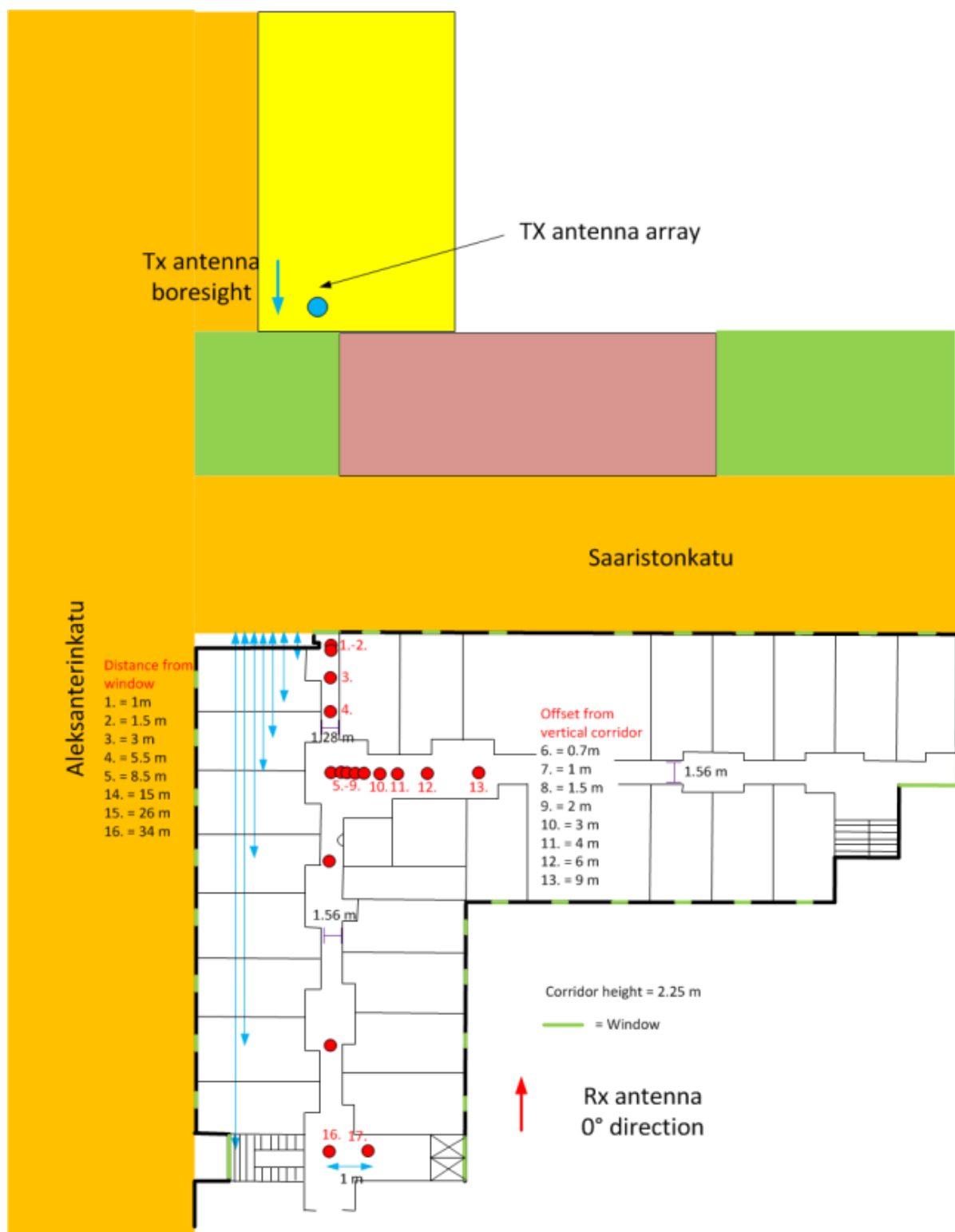


Figure B-17: The floorplan of the hotel with measurement spots in the corridors on floors 3 to 5.

Figure B-18 shows the detailed distance information of the corridor and Figure B-19 shows the example of the measurements on the 8th measurement spot (cf. Figure B-17) on the 5th floor. Figure B-20 presents the view from the TX location. Figure B-21 and Figure B-22 show the layout and collected distance information on the 2nd floor and 6th floor, respectively.

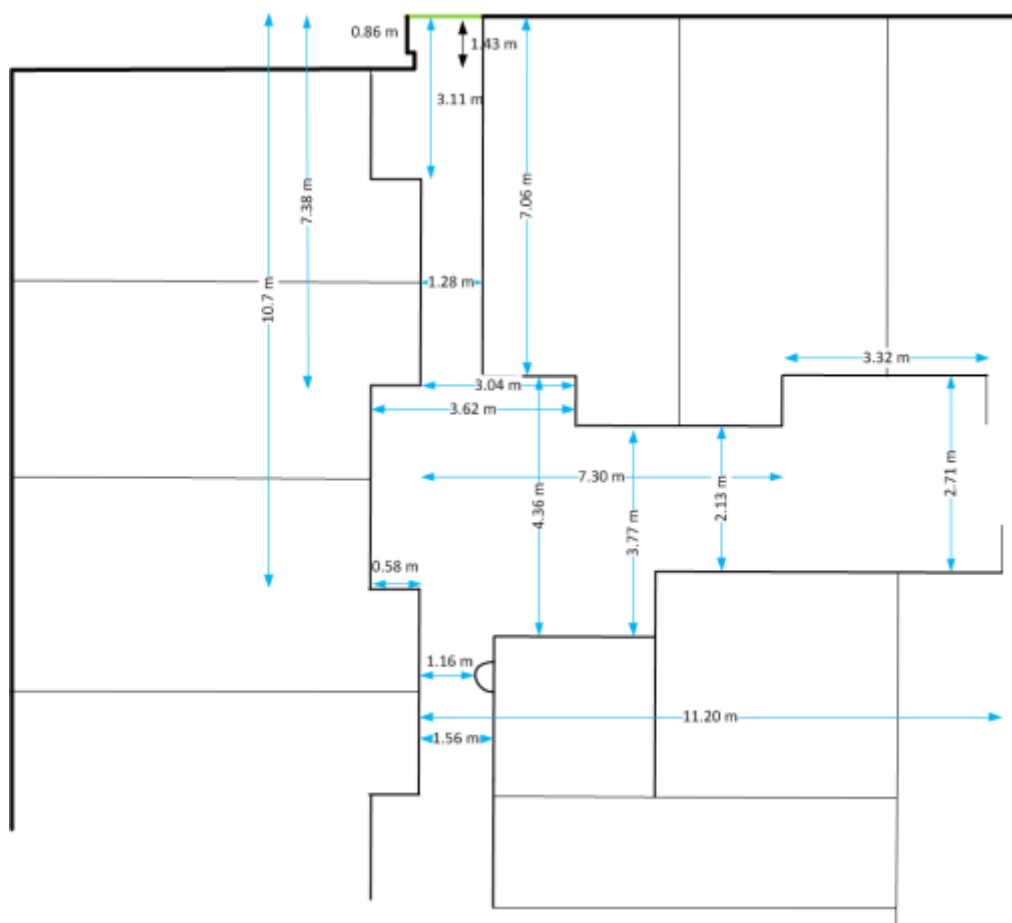


Figure B-18: Magnified floorplan of the hotel corridors on floors 3 to 5.



Figure B-19: Measurement example, TX was located on the roof of neighbouring building.



**Figure B-20: Views from the TX site towards the target building
Left: from position 2, Right: From position 1.**

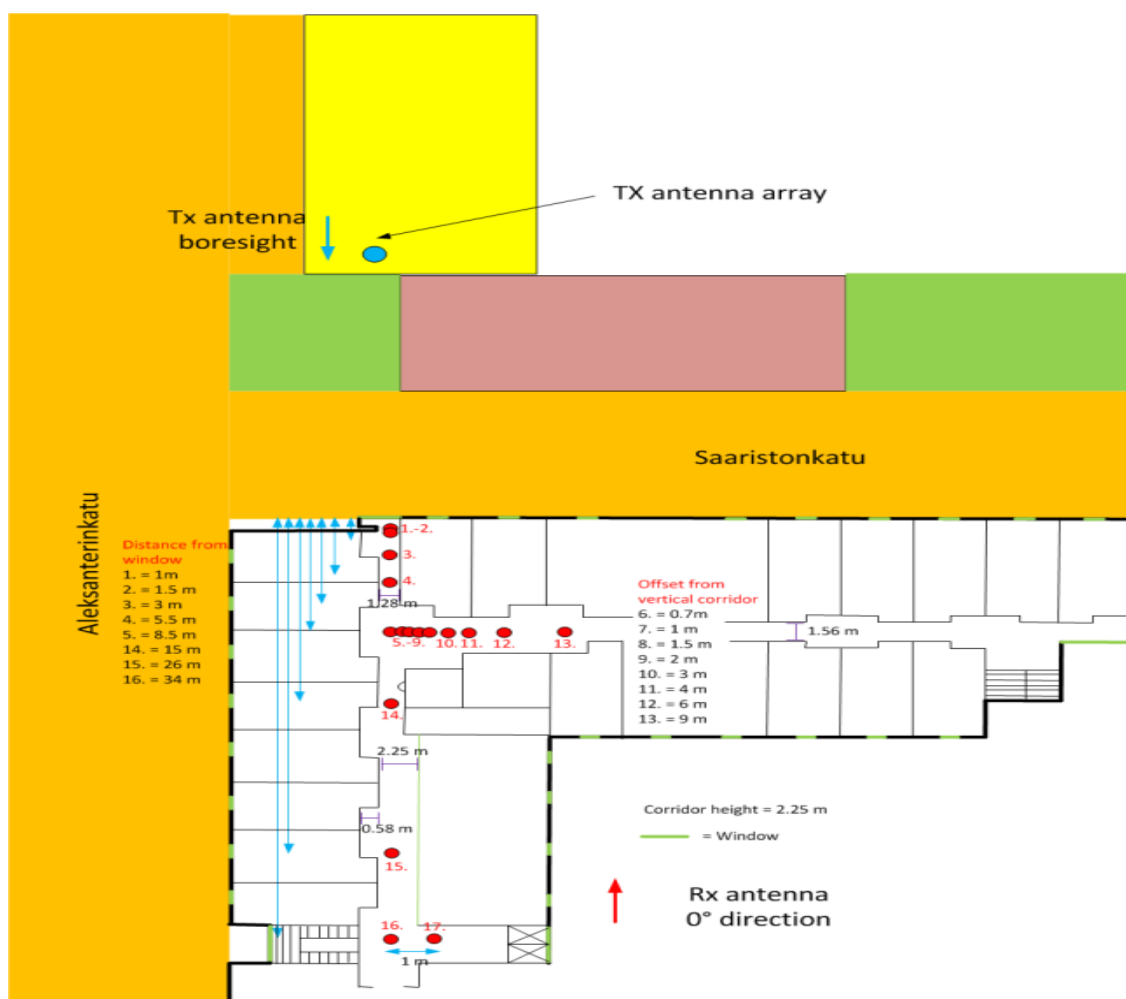


Figure B-21: The hotel layout and measurement spots on the corridor of 2nd floor.

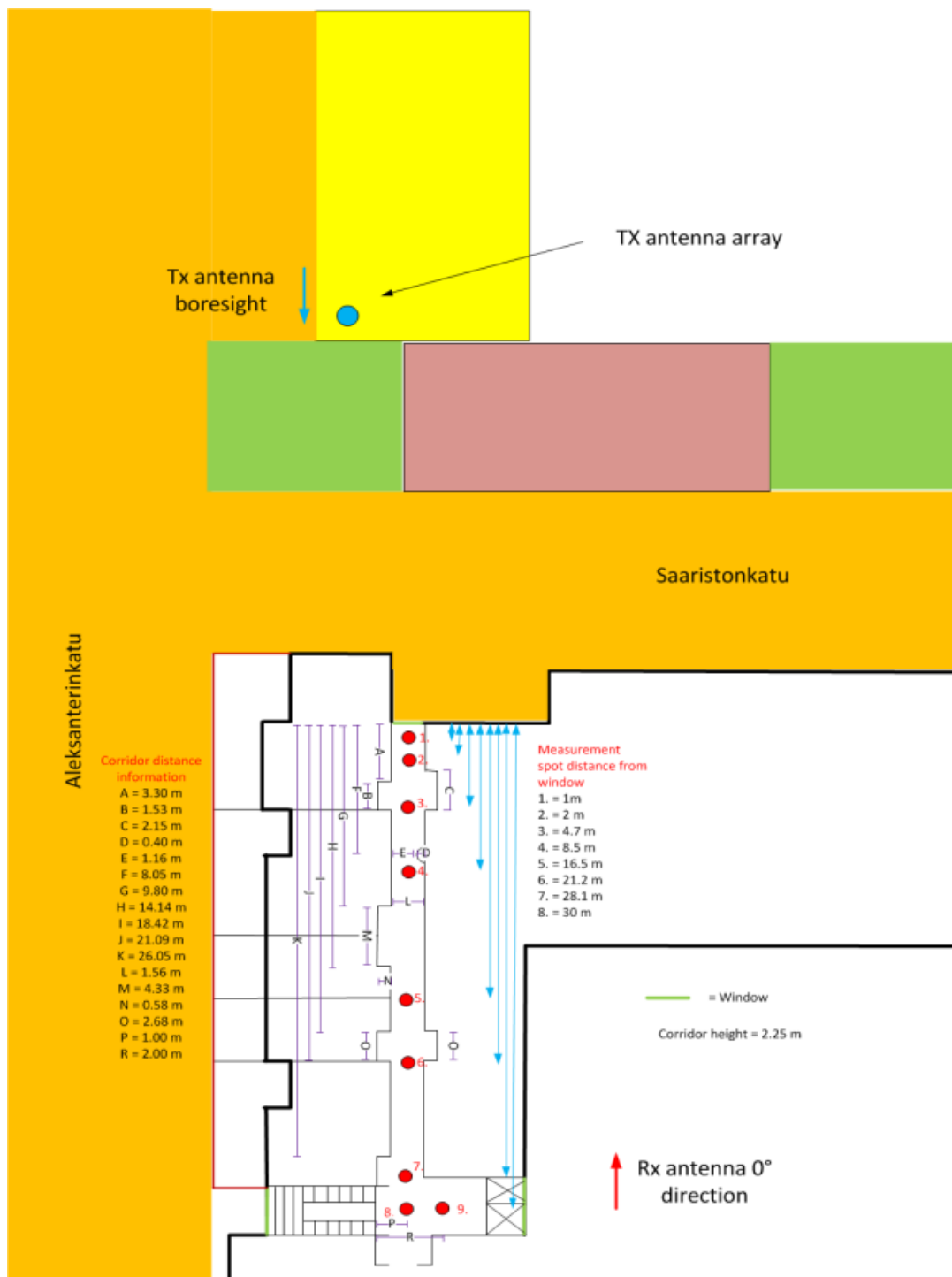


Figure B-22: The hotel layout and measurement spots in the corridor of 6th floor.

B.1.2.4 ME4: Urban microcell outdoor-to-indoor (MIMO)

The measurements were performed within a multi-storey building in the same manner as in ME3. The RX location was either the hotel room or the corridor of hotel. The TX unit and antenna were located on an articulated crane. The TX and the RX were stationary during the recordings. Emphasis was on collecting data for TX elevation angle spread analysis.

B.1.2.4.1 Measurement spots

Five measurement spots were selected in the hotel room and one measurement spot in the end of the corridor facing to Saaristonkatu. The measurements were repeated in the same spots on floors 2 to 5 in the corresponding rooms (room numbers 258, 358, 458 and 558,

Figure B-23). The height of the TX antenna was 5 m and 10 m and the distance in relation to the reference corners of the target building is depicted in Figure B-24.

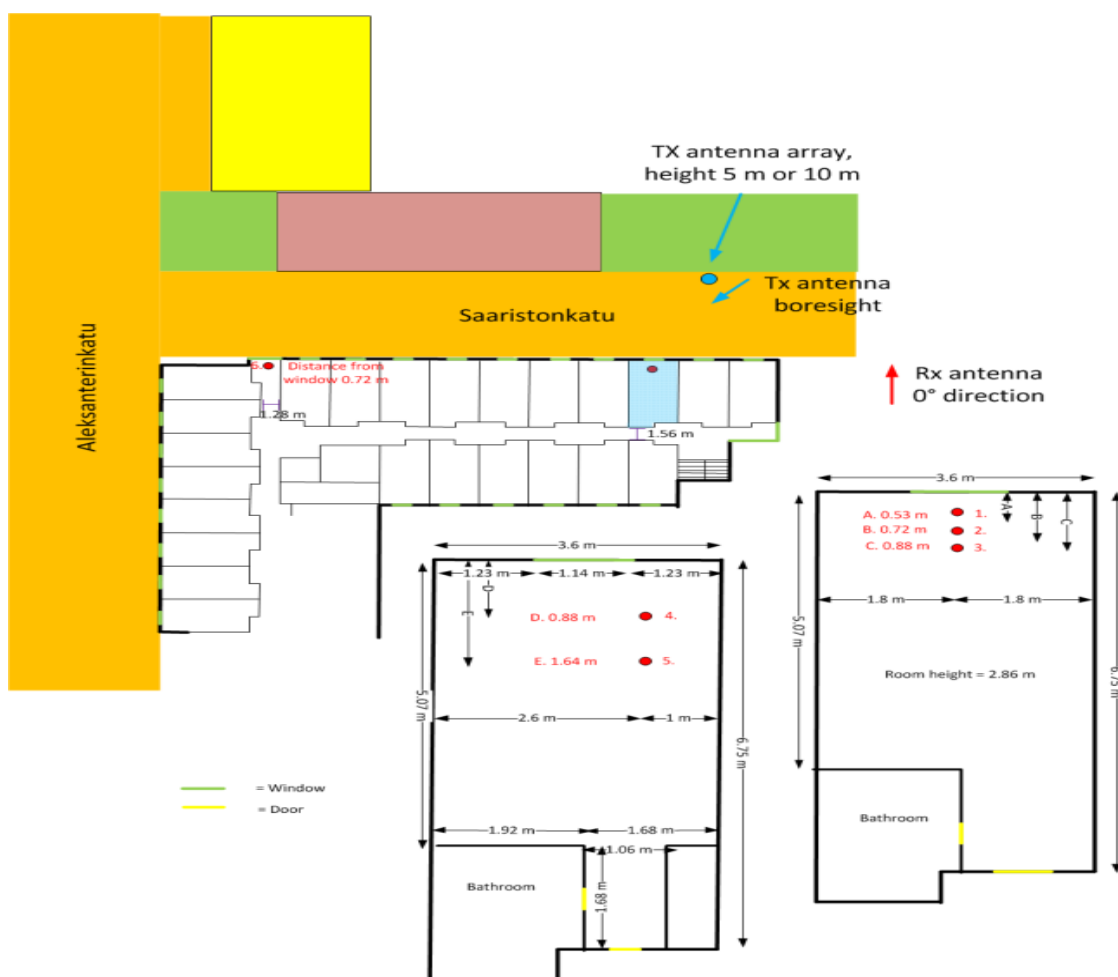


Figure B-23: Measurement spots in the hotel room and in the end of corridor at 2.3 GHz and 5.25 GHz.



Figure B-24: TX antenna distances at different heights in room measurements.

In the second part of the ME4 measurements, 6 spots were measured in the hotel corridor on floors 2 to 5. Furthermore, one measurement was executed in the elevator, having the TX directed towards the elevator. The measurements were performed with TX heights of 5 m, 10 m and 15 m (Figure B-25). It should be noted that the 6th measurement spot was skipped in

5.25 GHz measurements due to lack of signal. Figure B-27 presents the distance information collected from these measurements. Notice that the image orientation of Figure B-27 is rotated 90 degrees CCW with respect to the previous indoor sketches.



Figure B-25: The TX mounted on an articulated crane at a height of 5 m (left) and 15 m (right).



Figure B-26: TX antenna distances at different heights in corridor measurements.

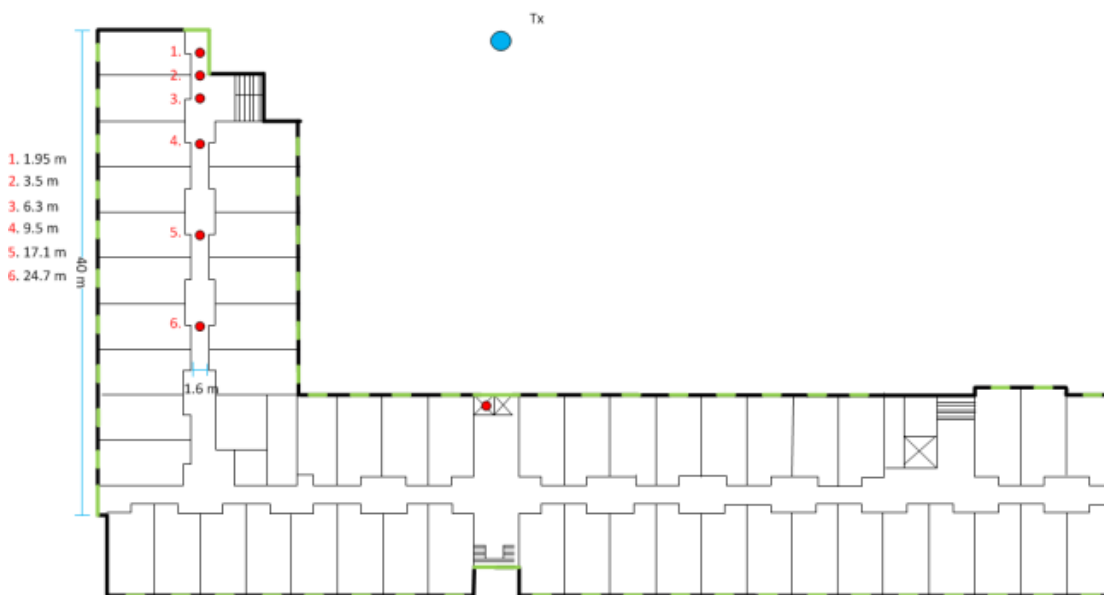


Figure B-27: Measurement spots on the hotel corridor for ME4 at 2.3 GHz and 5.25 GHz.

B.1.2.5 ME5: Urban microcell outdoor (MIMO)

In ME5, the measurements were performed using a single RX vehicle in the same manner as in ME2. The TX unit and antenna were located on an articulated crane at 5 and 10 m above the ground. The RX setup is similar as in ME1. The RX is moving close to the TX location gathering path loss information along the street and around the street corners. The measurement parameters are selected balancing between moderate scatter velocities and

maximum MIMO array size. Emphasis was on collecting data for TX elevation angle spread analysis. The measurement routes are presented in Figure B-28. The TX position is marked as a blue dot. Eight to twenty measurement spots, i.e., vehicle stops for data recording, were recorded on the three different measurement routes.

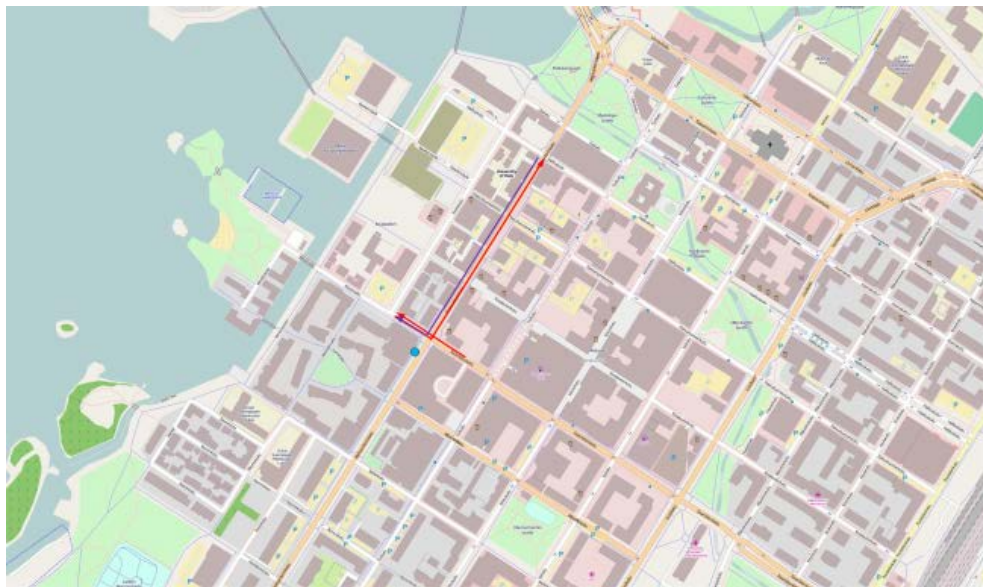


Figure B-28: Measurement routes for ME5 at 2.3 GHz and 5.25 GHz.

B.1.3 Measurement results

This section reports the measurement results that have been obtained so far. The ISIS post-processing is still ongoing and it is complete for 20 % of data at 2.3 GHz. Therefore, the preliminary angular statistics are presented only for 2.3 GHz data.

B.1.3.1 V2V

The preliminary results of V2V IR analysis is shown in Table B-6.

Table B-6: V2V measurement results (ME1)

Parameter	Statistics	2.3 GHz		5.25 GHz	
		SD LT	OD HT	SD LT	OD HT
Path loss	exponent	1.95	2.18	2.02	2.13
	intercept	48.0	45.5	45.2	49.8
Delay spread [ns]	μ_{DS}	30.7	33.3	24.1	28.3
	σ_{DS}	17.8	18.7	15.6	23.0
Max excess delay [ns]	μ_{MED}	203.0	234.8	147.3	228.0
	σ_{MED}	115.8	121.8	88.3	174.6
SF [dB]	σ_{SF}	4	4	3	4
K-factor [dB]	μ_{KF}	14.9	10.2	14.6	15.9
	σ_{KF}	4.8	5.7	8.0	6.4
Decorrelation distance [m]	δ_{DS}	6.6	5.7	7.9	6.8
	δ_{SF}	9.4	6.5	9.7	9.0
	δ_{KF}	7.4	4.4	8.4	10.3



SD = Same Direction, OD = Opposite Direction, LT = Low Traffic, HT = High Traffic,
 DS = Delay Spread, SF = Slow Fading

B.1.3.2 Spatial results for O2I scenarios

The results for O2I are summarized in Table B-7, Table B-8 and Table B-9.

Table B-7: The summary of UMi O2I room results at 2.3 GHz (ME4)

Parameter	Stat	UMi O2I Room, 2.3 GHz								
		2nd Floor		3rd Floor		4th Floor		5th Floor		
		TX 5 m	TX 10 m	TX 5 m	TX 10 m	TX 5 m	TX 10 m	TX 5 m	TX 10 m	All
ESD [log10(deg)]	μ_{ESD}	0.88	0.69	0.97	0.66	1.03	0.65	0.83	0.66	0.89
	σ_{ESD}	0.14	0.3	0.34	0.41	0.43	0.29	0.49	0.34	0.41
ESA [log10(deg)]	μ_{ESA}	1.49	1.4	1.48	1.41	1.47	1.49	1.48	1.48	1.44
	σ_{ESA}	0.09	0.14	0.08	0.15	0.12	0.09	0.16	0.09	0.13
ASD [log10(deg)]	μ_{ASD}	0.63	0.9	0.89	1.05	0.87	0.74	0.99	0.82	0.97
	σ_{ASD}	0.3	0.54	0.55	0.57	0.59	0.55	0.59	0.53	0.58
ASA [log10(deg)]	μ_{ASA}	1.74	1.73	1.72	1.67	1.65	1.66	1.72	1.73	1.69
	σ_{ASA}	0.12	0.17	0.12	0.21	0.11	0.14	0.21	0.14	0.16
Cross-Correlations	ESD vs ASD	0.31	0.71	0.61	0.74	0.83	0.62	0.78	0.67	0.67
	ESD vs ASA	-0.21	-0.55	-0.54	-0.59	-0.8	-0.39	-0.81	-0.49	-0.54
	ESD vs ESA	-0.52	-0.44	-0.45	-0.52	-0.71	-0.38	-0.72	-0.5	-0.52
	ESA vs ASA	0.83	0.76	0.43	0.86	0.79	0.84	0.89	0.85	0.73
	ESA vs ASD	-0.37	-0.7	-0.49	-0.8	-0.88	-0.6	-0.83	-0.52	-0.69
	ASD vs ASA	-0.36	-0.7	-0.6	-0.81	-0.78	-0.54	-0.8	-0.42	-0.64
	ASD vs DS	-0.51	-0.73	-0.71	-0.79	-0.85	-0.31	-0.83	-0.66	-0.16
	ESD vs DS	-0.43	-0.42	-0.32	-0.58	-0.75	-0.12	-0.8	-0.36	0
	ASA vs DS	0.82	0.92	0.73	0.97	0.88	0.63	0.98	0.33	0.35
	ESA vs DS	0.76	0.69	0.24	0.84	0.84	0.32	0.89	0.15	0.08
ESD = Elevation Spread, Departure; ESA = Elevation Spread, Arrival ASD = Azimuth Spread, Departure; ASA = Azimuth Spread, Arrival										

Table B-8: The summary of UMi O2I corridor results at 2.3 GHz (ME4)

Parameter	Stat	UMi O2I Corridor, 2.3 GHz											
		2nd Floor			3rd Floor			4th Floor			5th Floor		
		TX 5 m	TX 10 m	TX 15 m	TX 5 m	TX 10 m	TX 15 m	TX 5 m	TX 10 m	TX 15 m	TX 5 m	TX 10 m	TX 15 m
													All



ESD [log10(deg)]	μ_{ESD}	0.72	0.78	0.8	1	0.75	0.98	1.14	1.07	0.89	1.14	1.03	0.56	0.9
	σ_{ESD}	0.45	0.22	0.21	0.23	0.41	0.14	0.17	0.15	0.17	0.23	0.35	0.44	0.33
ESA [log10(deg)]	μ_{ESA}	1.2	1.36	1.37	1.36	1.37	1.42	1.38	1.3	1.32	1.41	1.46	1.37	1.36
	σ_{ESA}	0.34	0.22	0.17	0.11	0.13	0.07	0.17	0.15	0.11	0.19	0.14	0.18	0.19
ASD [log10(deg)]	μ_{ASD}	1.36	1.09	0.81	1.31	1.04	0.91	1.32	1.06	0.99	0.8	0.95	1.07	1.06
	σ_{ASD}	0.27	0.28	0.45	0.28	0.24	0.42	0.21	0.43	0.39	0.36	0.5	0.43	0.41
ASA [log10(deg)]	μ_{ASA}	1.62	1.63	1.58	1.63	1.71	1.67	1.63	1.64	1.65	1.63	1.68	1.65	1.64
	σ_{ASA}	0.15	0.13	0.16	0.12	0.09	0.06	0.2	0.13	0.09	0.13	0.12	0.16	0.13
Cross-Correlations	ESD vs ASD	0.33	-0.53	0.82	0.36	0.5	0.28	0.33	0.27	0.6	0.26	0.37	0.62	0.33
	ESD vs ASA	-0.02	0.14	0.09	-0.08	-0.11	0.09	-0.13	-0.19	-0.11	-0.11	-0.46	0.14	-0.05
	ESD vs ESA	0.63	0.51	0.46	0.08	0.23	0.21	-0.1	0.01	-0.21	0.23	-0.08	0.48	0.26
	ESA vs ASA	0.38	0.71	0.84	0.62	0.77	0.06	0.88	0.28	0.61	0.78	0.66	0.82	0.64
	ESA vs ASD	0.11	-0.68	0.01	-0.29	-0.13	0.14	-0.29	0.11	-0.35	-0.31	0	0.41	-0.09
	ASD vs ASA	-0.21	-0.62	-0.3	-0.42	-0.36	-0.07	-0.17	-0.35	-0.62	-0.22	0.04	0.05	-0.2
	ASD vs DS	-0.08	0.15	0.13	-0.25	-0.04	-0.06	-0.25	-0.47	-0.47	0.2	-0.18	-0.22	-0.08
	ESD vs DS	0.03	-0.14	-0.27	-0.09	0.24	0.15	-0.14	0.22	-0.56	0.29	0.36	-0.48	-0.04
	ASA vs DS	-0.11	-0.31	-0.37	-0.13	-0.64	0.55	-0.65	0.2	-0.1	-0.67	-0.67	-0.69	-0.21
	ESA vs DS	-0.06	-0.26	-0.55	-0.25	-0.68	-0.61	-0.63	-0.45	-0.08	-0.65	-0.64	-0.79	-0.24
ESD = Elevation Spread, Departure; ESA = Elevation Spread, Arrival ASD = Azimuth Spread, Departure; ASA = Azimuth Spread, Arrival														

Table B-9: The summary of UMa O2I corridor results at 2.3 GHz (ME3)

Parameter	Stat	UMa O2I Corridor, 2.3 GHz					
		2nd Floor	3rd Floor	4th Floor	5th Floor	6th floor	All
ESD [log10(deg)]	μ_{ESD}	0.94	0.92	0.94	1.06	0.92	0.96
	σ_{ESD}	0.27	0.13	0.22	0.24	0.05	0.21
ESA [log10(deg)]	μ_{ESA}	1.35	1.38	1.39	1.27	1.29	1.34
	σ_{ESA}	0.17	0.15	0.18	0.25	0.2	0.2
ASD [log10(deg)]	μ_{ASD}	1	0.9	1.02	1.05	0.17	0.84
	σ_{ASD}	0.61	0.51	0.43	0.58	0.31	0.6
ASA [log10(deg)]	μ_{ASA}	1.57	1.61	1.68	1.54	1.56	1.59
	σ_{ASA}	0.15	0.17	0.2	0.27	0.28	0.22
Cross-correlations	ESD vs ASD	0.82	0.62	0.8	0.79	-0.36	0.77
	ESD vs ASA	-0.27	-0.38	-0.61	-0.56	0.33	-0.39
	ESD vs ESA	-0.46	-0.33	-0.66	-0.57	0.39	-0.45
	ESA vs ASA	0.72	0.87	0.91	0.93	0.84	0.86
	ESA vs ASD	-0.58	-0.4	-0.68	-0.6	0.08	-0.46

	ASD vs ASA	-0.4	-0.47	-0.59	-0.58	0.1	-0.41
	ASD vs DS	-0.09	-0.41	-0.65	-0.44	0.19	-0.15
	ESD vs DS	-0.26	-0.15	-0.57	-0.15	-0.07	-0.22
	ASA vs DS	-0.13	-0.24	0.29	-0.21	0.59	0.03
	ESA vs DS	-0.07	-0.32	0.34	-0.14	0.32	0.09
ESD = Elevation Spread, Departure; ESA = Elevation Spread, Arrival ASD = Azimuth Spread, Departure; ASA = Azimuth Spread, Arrival							

B.1.3.3 Spatial results for O2O scenarios

Table B-10 summarizes the results for the outdoor measurements.

Table B-10: The summary of O2O results at 2.3 GHz

Parameter	Stat	UMa O2O (ME2)	UMi O2O (ME5)				
			TX 5 m, LOS	TX 10 m, LOS	TX 5 m, NLOS	TX 10 m, NLOS	All
ESD [log10(deg)]	μ_{ESD}	0.5	0.71	0.79	0.91	0.89	0.59
	σ_{ESD}	0.36	0.59	0.55	0.35	0.36	0.55
ESA [log10(deg)]	μ_{ESA}	1.04	0.91	0.94	0.97	1.03	0.92
	σ_{ESA}	0.38	0.32	0.36	0.3	0.25	0.38
ASD [log10(deg)]	μ_{ASD}	1.23	1.38	1.47	1.61	1.71	1.42
	σ_{ASD}	0.35	0.34	0.36	0.26	0.13	0.38
ASA [log10(deg)]	μ_{ASA}	1.27	1.1	1	1.11	1.15	1.03
	σ_{ASA}	0.43	0.4	0.32	0.27	0.33	0.34
Cross-Correlations	ESD vs ASD	0.6	0.57	0.52	0.2	0.23	0.61
	ESD vs ASA	-0.07	-0.23	0.1	-0.24	-0.3	0.04
	ESD vs ESA	0.08	0.19	0.08	0.01	0.12	0.08
	ESA vs ASA	0.23	0.46	0.31	0.13	0.14	0.3
	ESA vs ASD	-0.14	0	0	0.07	0.26	0.09
	ASD vs ASA	-0.16	-0.25	0.21	0.11	0.11	0.18
	ASD vs DS	-0.16	-0.04	0.23	-0.2	0.3	0.41
	ESD vs DS	-0.09	-0.16	-0.02	-0.21	-0.23	0.09
	ASA vs DS	0.49	0.76	0.62	0.53	0.41	0.56
	ESA vs DS	0.05	0.38	0.04	0.13	0.06	0.11
	ASD vs SF	-0.22	-0.09	-0.04	-0.42	0.3	0.14
	ESD vs SF	-0.36	-0.34	-0.3	-0.26	-0.18	-0.2
	ASA vs SF	0.17	0.46	0.04	-0.05	0.23	0.09
	ESA vs SF	-0.08	0.06	-0.09	0.15	0	0.01
ESD = Elevation Spread, Departure; ESA = Elevation Spread, Arrival ASD = Azimuth Spread, Departure; ASA = Azimuth Spread, Arrival							

B.2 Channel measurement in crowded areas

B.2.1 Measurement system

The measurements were conducted by using the DOCOMO channel sounder [KSO+09] at 2.225 GHz centre frequency for UMi and D2D scenarios. The pictures of the transmitter (Tx) and the receiver (Rx) are shown in Figure B-29 and the measurement parameters are shown in Table B-11. The UE antenna height was set to 1.45 m and the BS antenna heights for UMi and D2D scenarios were set to 2.9 and 1.45 m, respectively. A sleeve antenna and a slotted cylinder antenna were used to transmit vertically and horizontally polarized waves, respectively. The signal was received by a cylindrical array antenna, which has 96 dual-polarized patch antenna elements.

In the measurements, the received power, the delay profiles, the azimuth arrival angle profile, and the elevation arrival angle profiles were measured. In UMi scenario, the downstream measurement and the upstream measurement was carried out by reversing the Tx and the Rx to obtain the angle profiles of both the BS side and UE side. In D2D scenario, only UE side angle profiles were measured since the BS and UE antenna heights were equal and the BS side angle profiles were assumed to correspond to the UE side profiles.

To obtain the MIMO channel model parameters, we estimated the paths' propagation parameters using the SAGE algorithm [FH94]. In the SAGE algorithm, maximum path number was 40, and the maximum iteration number was 20. To obtain the intra-cluster propagation parameter spreads, we classified the paths into 10 clusters by the K-Power-Means based clustering algorithm [SKI+12]. In the clustering algorithm, the normalization parameters of Multipath-Component-Distance calculation were $\rho_{ToA} = 1.0 \mu\text{s}$ and $\rho_{AoA} (\rho_{AoD}) = 360 \text{ deg}$.



Figure B-29: Measurement equipment: transmitter (left) and receiver (right).

Table B-11: Measurement parameters.

Measurement parameters		SAGE algorithm	
Frequency	2.225 GHz	Max num. of paths	40
Bandwidth	50 MHz	Max num. of iterations	20
Tx antenna	Sleeve/slot	K-power Means Algorithm	

Rx antenna	UCA (96 dual polarized patch antenna element)	Num. of clusters	10
BS antenna height (h_b)	UMi: 2.9 m, D2D: 1.45 m	Normalization parameter	$\rho_{ToA} = 1.0 \mu s$ $\rho_{AoA}(\rho_{AoD}) = 360 \text{ deg}$
UE antenna height (h_m)	1.45 m		
Tx power	8.7 dBm		
Delay window length	1000 m		
Measurement interval	1 s		

B.2.2 Measurement environment

The measurements were carried out on the square in front of Shibuya station that is a typical urban railway station in Tokyo. The measurement routes and the figures of the square are shown in Figure B-30. To clarify the impact of pedestrians on the MIMO channel properties, the measurements were carried out during day- and night-time. While there were several hundred pedestrians on the square during the day, there were only several pedestrians during the night.

In UMi scenario, BS was mounted on the measurement car that was located at P1, across the street from the plaza. In D2D scenario, BS was mounted on the carriage that was located at P2, at the corner of the plaza. All measurement courses were in LOS condition. The UE was mounted on the carriage and the channel was measured continuously every 1 second while UE moved along the courses at about 1 m/s that is the typical walking speed.

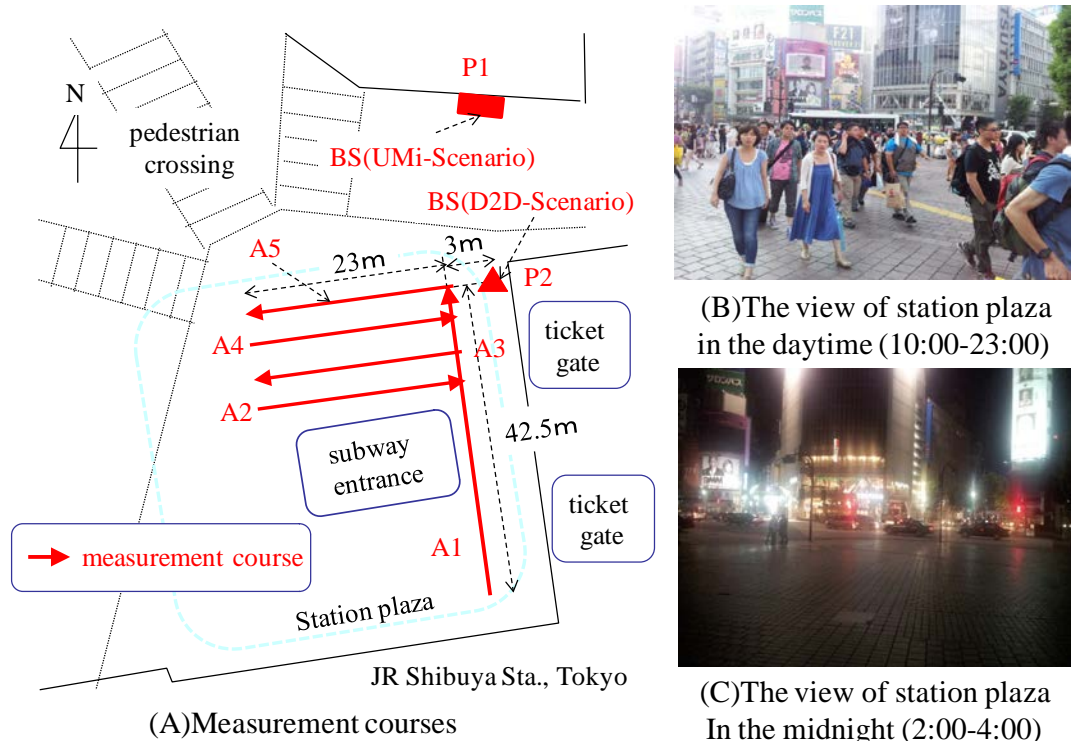


Figure B-30: Measurement environment in front of Shibuya station.

B.2.3 Measurement results

The CDFs of a number of propagation parameters based on the measured data of day- and the night-time for both scenarios are shown in Figure B-31. Here, Tx and Rx polarizations are vertical. CDFs of ASD and ESD in D2D scenario are reproduced from the estimation results of AoA spread since we assume the BS side angle profiles correspond to the UE side profiles.

In Figure B-31(A), it can be observed that in the daytime the received power decreased compared to night-time in both scenarios. The decreases in the median received power were 5 dB in UMi scenario and 4 dB in D2D scenario, respectively.

In Figure B-31(B), the median delay spreads decreased in the daytime. The reason for the observation above is that the delayed waves, whose propagation distances are longer, tend to be blocked by the pedestrians more severely.

In Figure B-31(C), there are no significant differences in the ASAs between the day- and night-time.

In Figure B-31(D), the ESAs tend to decrease in the night. One reason for the difference in the ESAs between day and night is the following. Since during the day, there were many pedestrians around the UE, there were more diffracted rays that propagated over the pedestrians, which caused an increase of the ESA.

In Figure B-31(E) and (F), the differences in the angular spreads between day and night at the TX are similar to those observed at the RX, i.e. during the day the ESDs tend to increase.

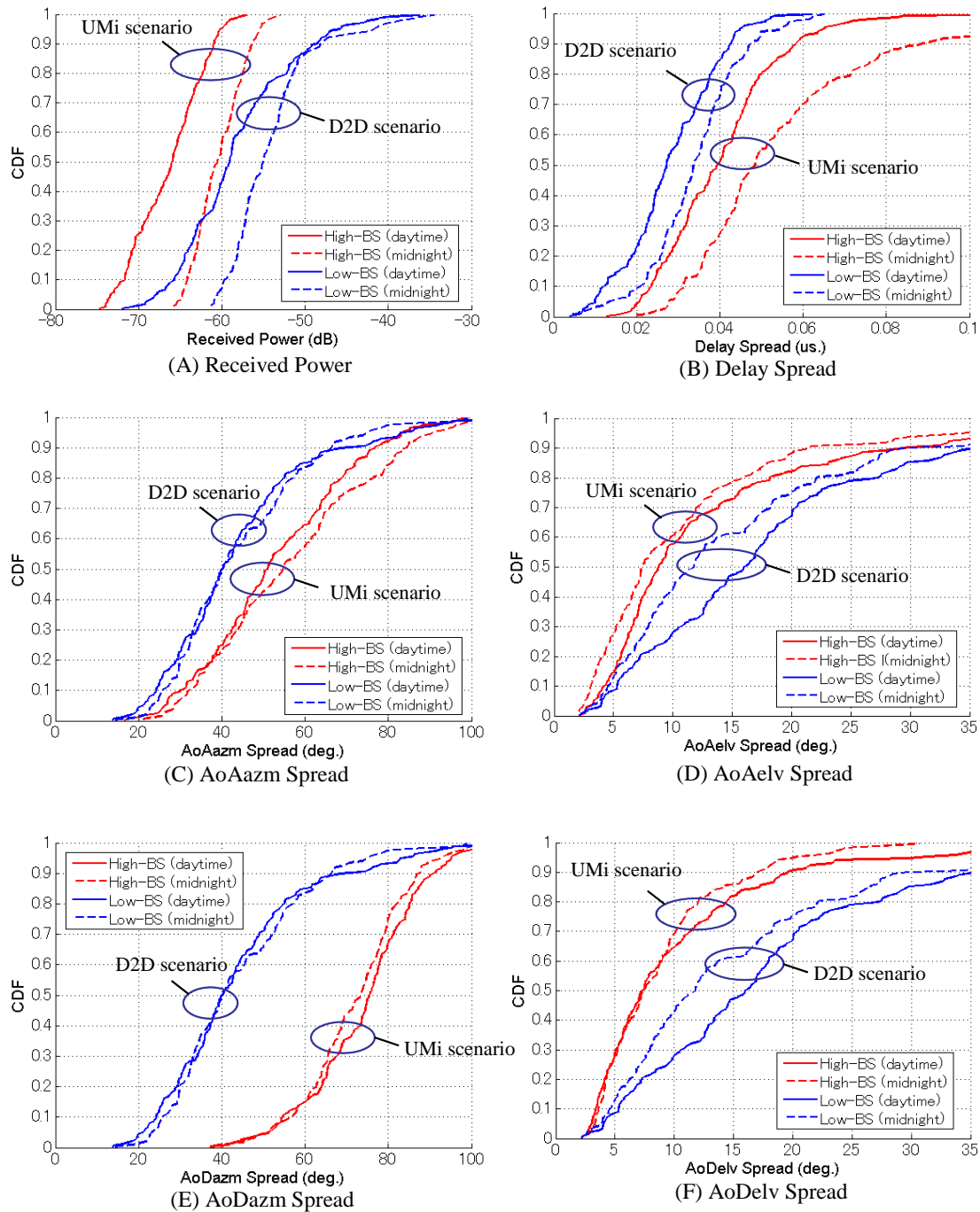


Figure B-31: Measurement results

The spreads of the propagation parameters in all the measurement conditions are summarized in Table B-12. For reference, the large scale parameters of urban micro cell scenario of ITU-R M.2135 channel model are also shown. Although the spreads of propagation parameters almost corresponded to the parameters of ITU-R M.2135 channel model, the delay spreads are smaller and the ASDs are larger than the spreads of the channel model. In UMi scenario in the daytime, there was no significant difference between VV-polarized channel and HH-polarized channel in regard to the received power, ASA, ESA, ASD, and ESD. The median XPR from V-pol. to H-pol. was 8 dB, and the median XPR from H-pol. to V-pol. was 5 dB.

Table B-12: Large scale parameters of measured data

Scenario		ITU-R M2135 UMi (LoS)	SmallCell (LoS, Daytime)	SmallCell (LoS, Midnight)	D2D (LoS, Daytime)	D2D (LoS, Midnight)
Polarization			V-V	H-H	V-V	V-V
Delay spread (DS) log10(sec)	μ_{DS}	-7.19	-7.42	-7.24	-7.29	-7.59
	σ_{DS}	0.4	0.18	0.41	0.17	0.21
AoD azimuth spread (ASD) log10(deg)	μ_{ASD}	1.2	1.86	1.86	1.85	
	σ_{ASD}	0.43	0.08	0.08	0.08	
AoD elevation spread (ESD) log10(deg)	μ_{ESD}		0.90	0.90	0.88	
	σ_{ESD}		0.30	0.22	0.25	
AoA azimuth spread (ASA) log10(deg)	μ_{ASA}	1.75	1.70	1.65	1.73	1.61
	σ_{ASA}	0.19	0.16	0.16	0.16	0.17
AoA elevation spread (ESA) log10(deg)	μ_{ESA}		1.00	1.02	0.91	1.16
	σ_{ESA}		0.31	0.28	0.32	0.31
Cross correlation	ASD vs DS	0.5	0.07	0.23	0.27	
	ASA vs DS	0.8	0.21	0.52	0.46	0.41
Cluster ASD		3	5.56	5.14	5.99	
Cluster ESD			3.64	3.53	3.42	
Cluster ASA		17	5.91	6.63	6.04	5.26
Cluster ESA			4.50	4.57	3.72	6.08
						4.85

B.3 26 GHz band path loss measurement in urban area

B.3.1 Measurement system

Figure B-32 shows the block diagram of path loss measurement system at 26 GHz bands, which contained the transmitter, the receiver and a personal computer (PC). At transmitter side, a continuous wave at 1.29 GHz was mixed with a 25.1 GHz local signal and gave a RF signal at 26.4 GHz. The RF signal was amplified and transmitted by a sleeve antenna. At receiver side, a sleeve antenna was used to receive the RF signal. The RF signal was down-converted to 1.29 GHz signal by using a down converter module. The 1.29 GHz signal was sampled and stored by a data recorder, and was sent to the PC to analyse. The transmission power was 40 W. For investigating the effect of the antenna height to the path loss, the height of the transmit antenna was set to be 1.5 m, 6 m, and 10 m whereas that of the receiver antenna was set to be 2.5 m and 1.5 m.

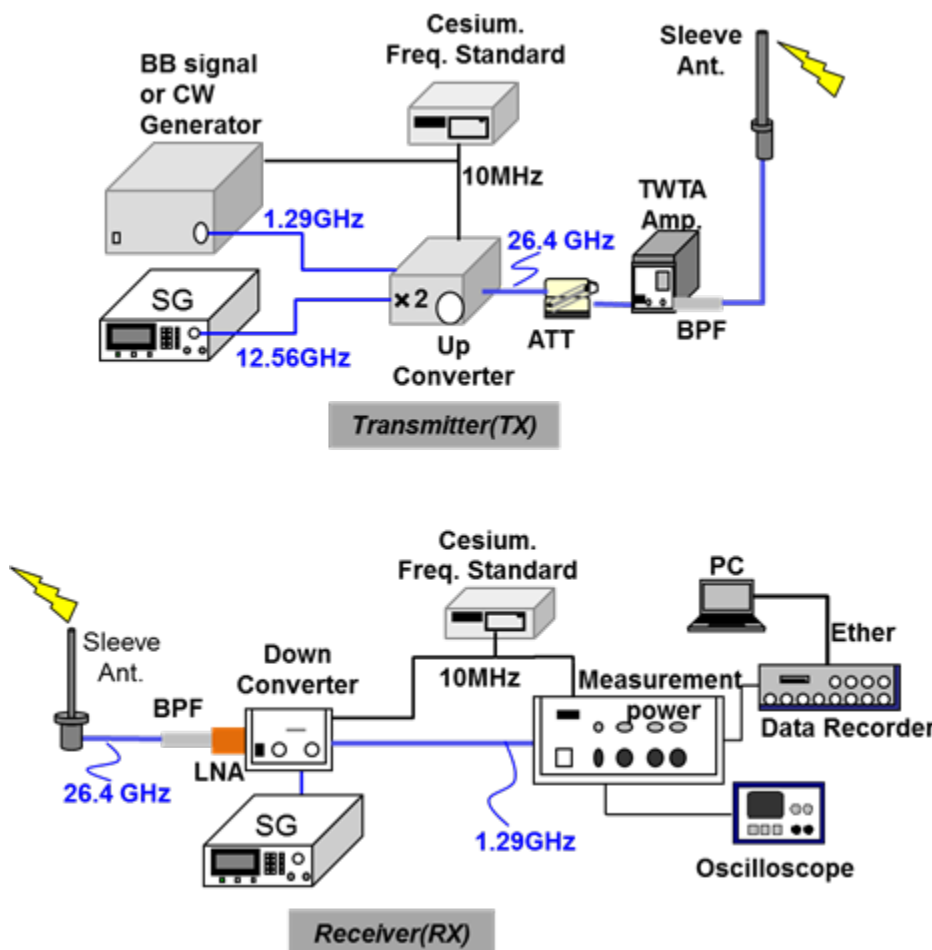


Figure B-32: Path loss measurement system at 26.35 GHz.

To investigate the frequency dependence of path loss, the measurement system at 4.7 GHz bands and 2.2 GHz bands with the same composition, were also built.

B.3.2 Measurement environment

To compare the results with the UMi path loss model in [ITU09-2135], the measurement environment is supposed to be a Manhattan-like grid layout. Figure B-33 shows the map of the chosen measurement area in Nihonbashi, Tokyo. The transmitters were set at the circle mark in the figure. The receivers were set in a car or on trolleys and moved along the 4

targeted routes: 1 LOS route and 3 NLOS routes. The widths of the routes were listed in Table B-13.



Figure B-33: Map of Nihonbashi in Tokyo (typical Manhattan grid layout environment).

Table B-13: Street widths of the routes

Route name	Width [m]
LOS route	33
NLOS route 1	33
NLOS route 2	15
NLOS route 3	33

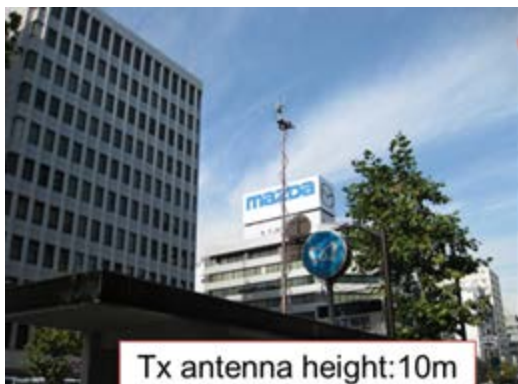


Figure B-34: Photographs of the measurement environment

B.3.3 Measurement results

Figure B-35 shows the frequency dependencies of the path loss. The solid lines are calculated path loss values using the path loss model of UMi scenario in [ITU09-2135]. The asterisk marks indicate the measured path loss values, which were obtained by taking the median value of the instantaneous path loss values in the range of 10 m with moving. From Figure B-35, it is found that, when the higher frequency is used, the larger differences between calculated path loss values and the measured path loss values increase. By taking the median values, standard deviation values, RMS values of the differences are shown in Table B-14, it is verified that in case of using 26.35 GHz, the median and RMS of the differences are over 10 dB larger than those at 2.2 GHz or 4.7 GHz.

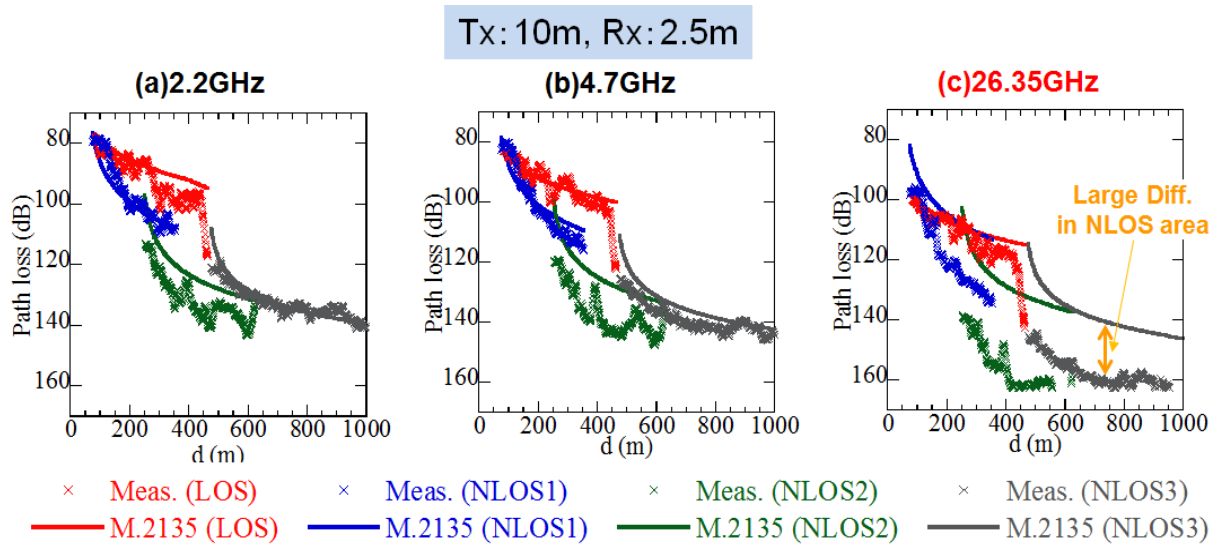


Figure B-35: The frequency dependence of the path loss; (a) Path loss at 2.2 GHz (b) Path loss at 4.7 GHz (c) Path loss at 26.35 GHz.

Table B-14: The median, standard deviation and RMS of the differences due to the frequency

Frequency	Median [dB]	Standard deviation [dB]	RMS [dB]
2.2 GHz	1.1	4.9	5.4
4.7 GHz	3.0	5.4	6.6
26.4 GHz	17.0	9.0	17.9

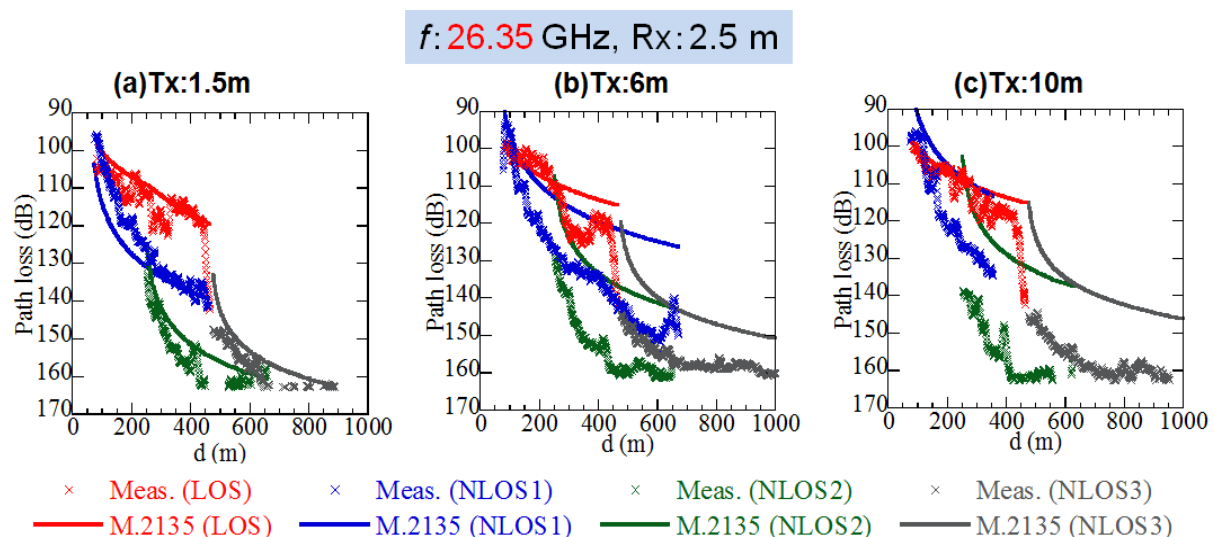


Figure B-36: TX antenna height dependency of the path loss. (a) TX antenna height is 1.5 m. (b) TX antenna height is 6 m. (c) TX antenna height is 10 m.

Table B-15: The median, standard deviation and RMS of the differences due to the frequency

Tx antenna height [m]	Median [dB]	Standard deviation [dB]	RMS [dB]
1.5	2.1	5.4	5.5

6	12.6	7.1	14.4
10	17.0	9.0	17.9

Figure B-36 and Table B-15 illustrate the transmission antenna height dependencies of the path loss at 26.35 GHz. It is verified that the differences between calculated path loss values and the measured path loss values increase rapidly due to the antenna height.

The equations below show the outcome of the measurements obtained by using all results with Tx heights of 1.5, 6, 10 m and Rx heights of 1.5, 2.5 m, and frequencies of 2.2, 4.7, 26.35 GHz. Here, the median value is 0 dB, and the standard deviation, RMS values were 6.6 dB. From the analysis results, for both cases of LOS and NLOS, the coefficients of distances d_1 and frequencies f_c are larger than those of path loss model in [ITU09-2135]. On the other hand, the coefficients of antenna heights are smaller than those of path loss model in [ITU09-2135].

$$PL_{\text{LOS}} = \begin{cases} 34.5 \log_{10} \frac{d_1}{[m]} + 1.7 + 23.4 \log_{10} \frac{f_c}{[\text{GHz}]} & \text{for } d_1 \leq d'_{BP} \\ 42.1 \log_{10} \frac{d_1}{[m]} - 6.8 - 7.6 \left(\log_{10} \frac{h'_{BS}}{[m]} + \log_{10} \frac{h'_{UE}}{[m]} \right) + 15.8 \log_{10} \frac{f_c}{[\text{GHz}]} & \text{else} \end{cases}$$

$$PL_{\text{NLOS}}(d_1, d_2) = PL_{\text{LOS}}(d_1) + 1.1 - 13.7 n_j + 11.5 n_j \log_{10} \frac{d_2}{[m]} + 6.1 \log_{10} \frac{f_c}{[\text{GHz}]}$$

B.4 60 GHz indoor office measurements

This section reports the measurement results for METIS propagation scenario indoor office (TC1) at the 57.68-59.68 GHz band performed by Ericsson Research.

B.4.1 Overview

The measurements campaign overview and description of antennas are given in Table B-16 and Table B-17.

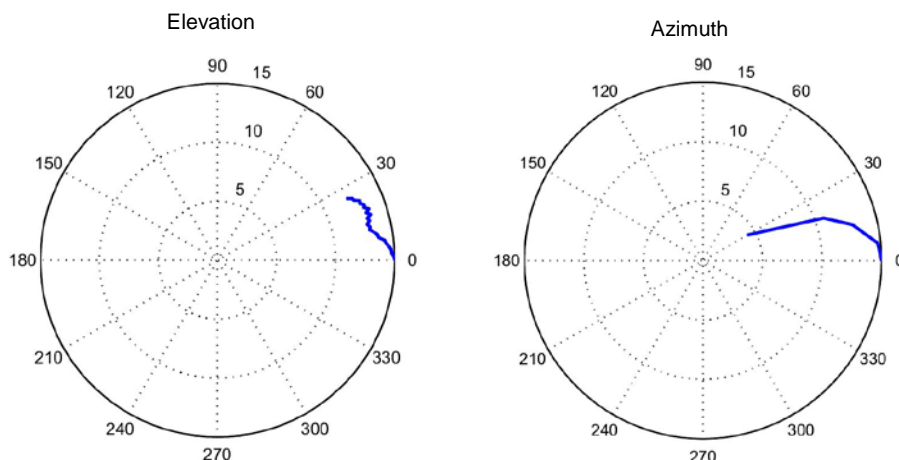
Table B-16: Measurement campaign overview

Test case	TC1
Link topology	BS-UE, UE-UE
Propagation scenario	Indoor office
Carrier frequency range	57.68 - 59.68 GHz
Polarisation	co-polarisation
Tx location	27 test locations
Tx velocity	Stationary

Tx height above ground level	1 m
Rx location	3 test locations
Rx velocity	Stationary
Rx height above ground level	1 m
Tx-Rx distance	2 - 80 m
Campaign duration	2 days

Table B-17: Tx and Rx antennas

Tx/Rx antenna gain	10 dBi
Tx/Rx antenna beam-width	60° in elevation plane (E-plane) and 30° in azimuth plane (H-plane)


Figure B-37: Measurement antenna patterns.

B.4.2 Measurement setup

The measurement setup was based on a vector network analyser (VNA). However, in order to allow long range measurements an optical fibre extension of the transmit RF cable was used. The RF signal of the VNA was in the range 2-4 GHz. This signal was up-converted at the transmitter end and down-converted at the receiver end. Further the local oscillator was also distributed to both converters using optical fibres.

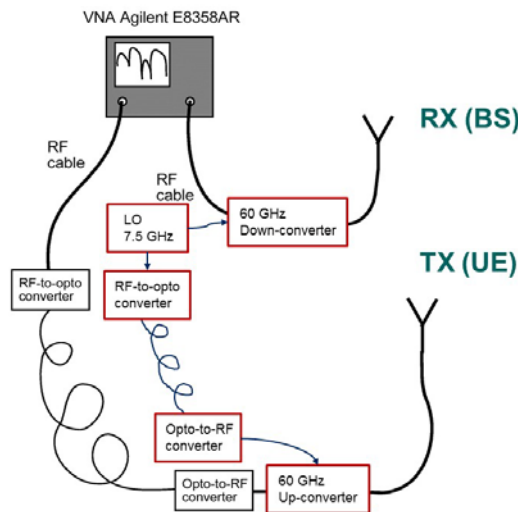


Figure B-38: Measurement Set-Up.

B.4.3 Body blocking scenario

A LOS link of 3.7 m distance was measured when a person walked back and forth between TX and RX blocking the link. The measurement shows that the METIS body blocking model is accurate. The assumed width of the corresponding screen is 30 cm.

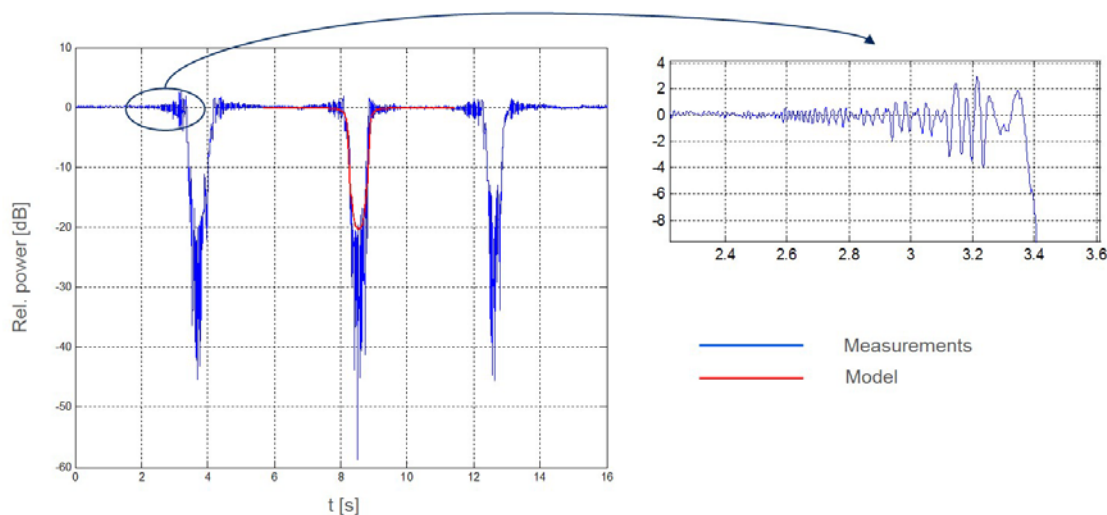


Figure B-39: Human body shadowing: Measurements vs. model at 60 GHz.

B.4.4 Office medium range measurements

A set of measurements for ranges between 2 and 20 m were performed in order to determine wall, window and door attenuation. Moreover, NLOS loss for corridor-to-room and room-to-room was measured, as seen from Figure B-40.



Figure B-40: Measurement locations for medium range measurement.

The measured wall, window and door losses were 7.5, 1.0 and 11.5 dB respectively as indicated by Figure B-41. The loss in excess of free space loss for the case corridor-to-room (TX location 1) and room-to-room (TX location 2) was 29 dB and 48 dB which is double the loss at 2.4 GHz in dB units.

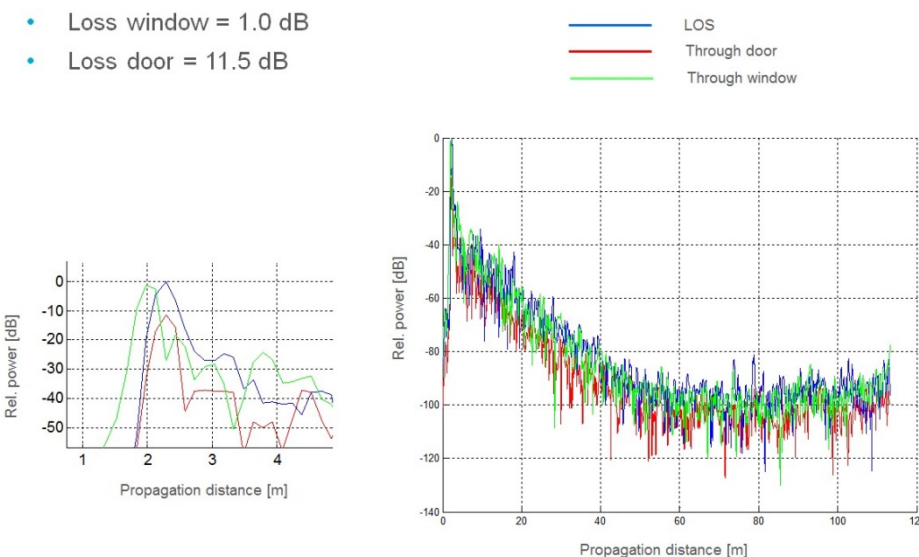


Figure B-41: Measured loss through door and window.

B.4.5 Office corridor long range measurements

A measurement campaign was performed in a long corridor of the office environment. The first 75 m was LOS and additionally 25 m around the corner was NLOS. The corresponding signal strength was used to fit the Berg recursive model [Ber95]. As depicted in Figure B-43, the model fits the measurements very well.

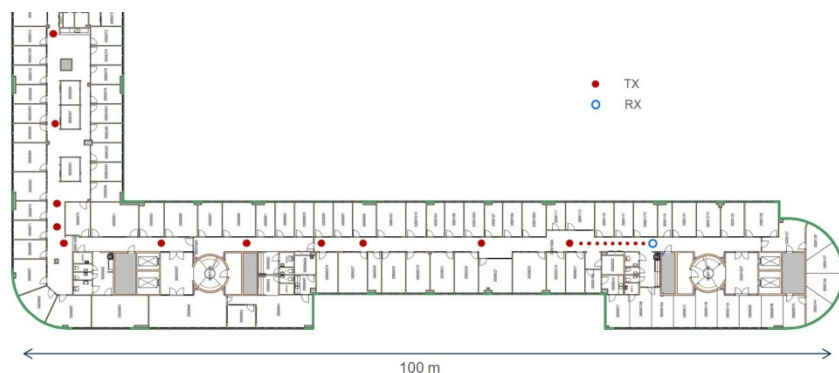


Figure B-42: Measurement locations for long range corridor measurement.

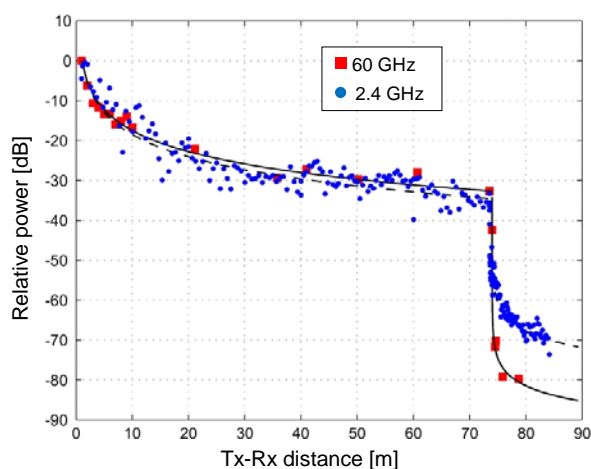


Figure B-43: Relative RX power measured and modelled at 2.4 GHz and 60 GHz for the long range corridor measurement.

B.5 60 GHz channel measurements in a shopping mall

This chapter reports the measurement results for METIS Propagation scenario shopping mall (TC3) at the 61 - 65 GHz band performed by Aalto University. It includes a description of the measurement scenario, sounder configuration, post-processing and analysis of the results.

B.5.1 Overview

The measurement campaign overview and the description of antennas are given in Table B-18 and Table B-19.

Table B-18: Measurement campaign overview

Test case	TC3
Link topology	BS-UE
Propagation scenario	Indoor shopping mall
Carrier frequency range	61 - 65 GHz
Polarisation	co-polarisation
Tx location	41 test locations
Tx velocity	Stationary
Tx height above ground level	2 m
Rx location	3 test locations
Rx velocity	Stationary
Rx height above ground level	2 m
Tx-Rx distance	1.5 - 16 m
Angular scanning	Tx rotated in azimuth 0 - 360° with 3° steps
Number of measurements	55
Remarks	41 LOS and 14 NLOS measurements
Campaign duration	2 days
Amount of data stored	2 GB

Table B-19: Tx and Rx antennas

Tx antenna	standard gain horn
Tx antenna gain	20 dBi
Tx antenna beam-width	19° in elevation plane (E-plane) and 17° in azimuth plane (H-plane)
Rx antenna	Biconical horn

Rx antenna gain	5 dBi
Rx antenna beam-width	11° in elevation plane (E-plane) and omnidirectional in azimuth plane (H-plane)

B.5.2 Measurement system and sounder configuration

The RF part of the used measurement system is illustrated in Figure B-44. The system is based on using a vector network analyser (VNA) with an intermediate frequency (IF) of 5 – 9 GHz. The RF frequencies 61 – 65 GHz are generated with up and down converters and a LO operating at 14 GHz. Both Tx and Rx sides are connected by cables to the VNA.

The up converter and the Tx antenna are on a rotator. A 20 dBi standard gain horn is used as the Tx antenna. An omnidirectional biconical horn antenna is used as the Rx antenna. A photograph of the antennas is presented in Figure B-45. The Tx antenna is rotated in the azimuth direction from 0° to 360° with 3° steps. Three samples of the amplitude and phase are measured at each direction with 2001 frequency points. The 4 GHz IF band width leads to a 0.25 ns delay resolution and the maximum delay is 500 ns. A direct connection back-to-back calibration is used to compensate the transfer function of the measurement system. Both, Tx and Rx antennas have relatively narrow elevation plane radiation patterns which limits the measurements to the azimuth plane. Both antennas are vertically polarised and only the co-polarisation measurements are done.

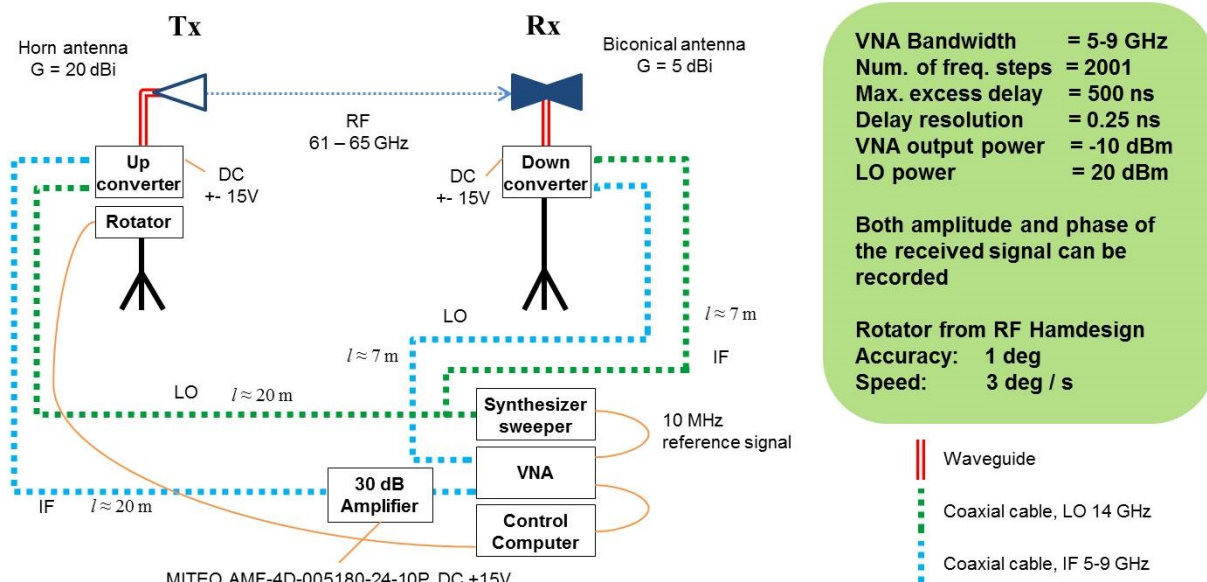


Figure B-44: Measurement system and sounder configuration.

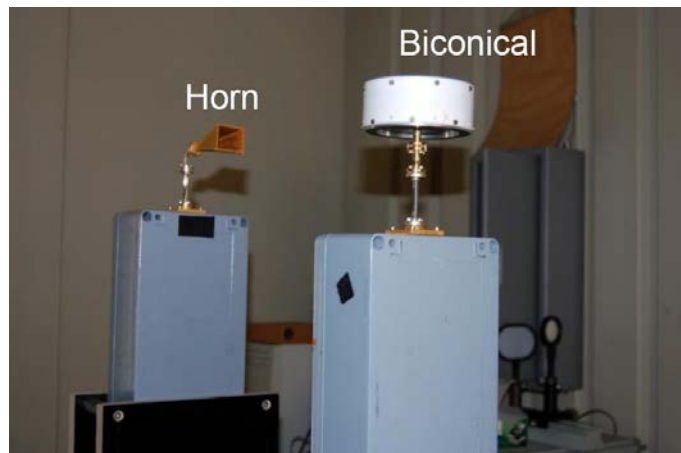


Figure B-45: Tx (left) and Rx (right) antennas.

B.5.3 Measurement scenario

These measurements are conducted in an indoor shopping mall Sello (Leppävaarankatu 3-9, Espoo, Finland). The measurements are done on the first and on the third floor. Photographs of the measurement locations are in Figure B-46 and the floor maps with the Tx and Rx locations are presented in Figure B-47 and Figure B-48.

In total 55 measurements are done, 41 of them are LOS and 14 NLOS measurements. In the NLOS measurements the Rx antenna is located behind a wide pillar (see Figure B-46). The Tx-to-Rx distances are between 1.5 m and 16 m. The number of measurements as a function of the Tx-Rx distance is presented in Figure B-49.



Figure B-46: Photographs of the measurement sites of the 60 GHz channel measurements at the first and third floors of the Sello shopping mall.

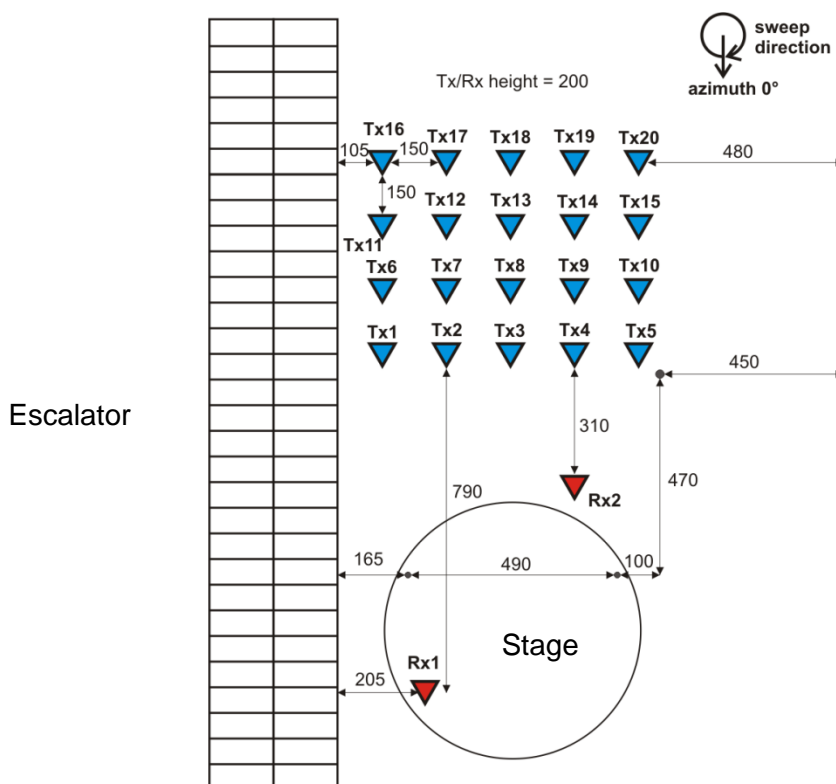


Figure B-47: Floor plan of the 1st floor of the Sello shopping mall with Tx and Rx locations.

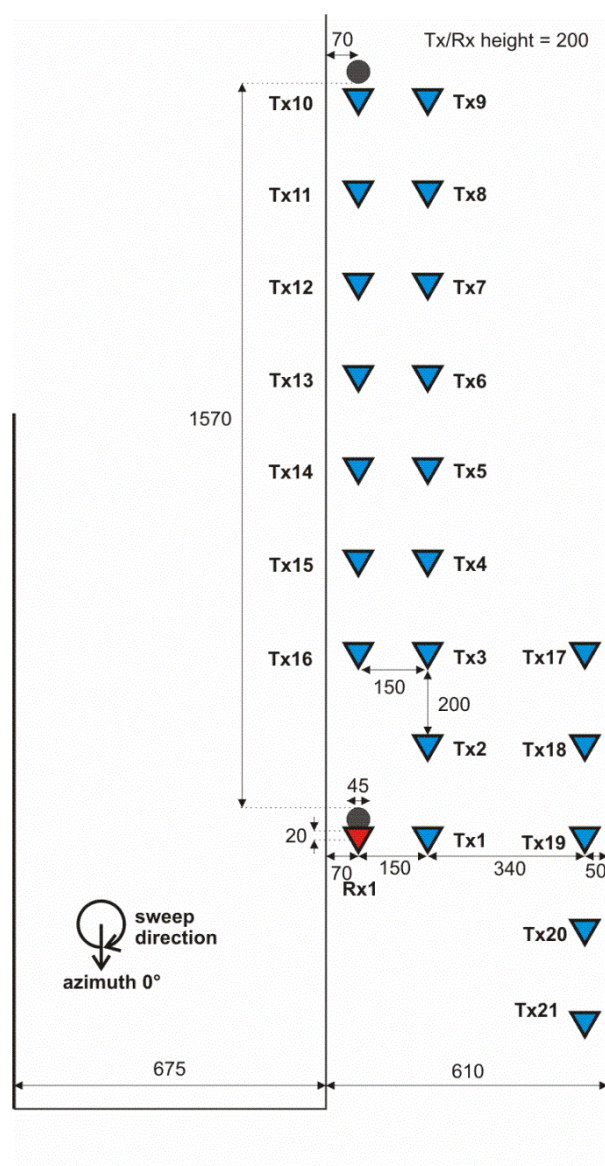


Figure B-48: Floor plan of the 3rd floor of the Sello shopping mall with Tx and Rx locations.

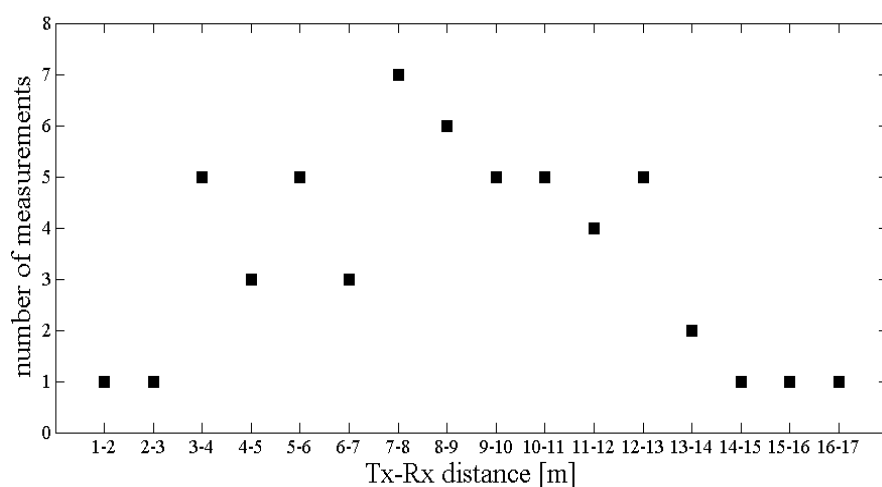


Figure B-49: Number of measurements as a function of the Tx-Rx distance.

B.5.4 Post-processing and results

Post-processing and results are explained in Sections B.5.4.1 – B.5.4.4. The table summarizing the measured parameters is given in Section B.5.4.5.

B.5.4.1 Path loss and shadow fading

Two different path loss and shadow fading estimates are derived; first for the case when the directive Tx horn antenna is aligned to the direction that gives the highest received power, and secondly for the case corresponding to the whole 360° rotation of the Tx.

The total received power as a function of the rotation angle is

$$P_{tot}(\phi) = \frac{1}{2001} \sum_f |H(\phi, f)|^2, \quad (\text{B-1})$$

where H is the average of the three complex samples measured at the azimuth rotation angle ϕ and f is the frequency. Path loss and shadow fading, when the Tx is aligned for maximum received power, can be derived by using the maximum of $P_{tot}(\phi)$. In LOS case this naturally corresponds to the LOS directions and in NLOS case it corresponds to the direction of the strongest reflection. The total transmitter and receiver antenna gain is 25 dB at the centre frequency. The linear fit to the path loss and standard deviation of shadow fading are:

$$\text{LOS: } PL = 71.82 + 19.42 \cdot \log(d)$$

$$\text{LOS: } \sigma_{SF} = 1.44 \text{ dB}$$

$$\text{NLOS: } PL = 96.68 + 5.15 \cdot \log(d)$$

$$\text{NLOS: } \sigma_{SF} = 1.58 \text{ dB}$$

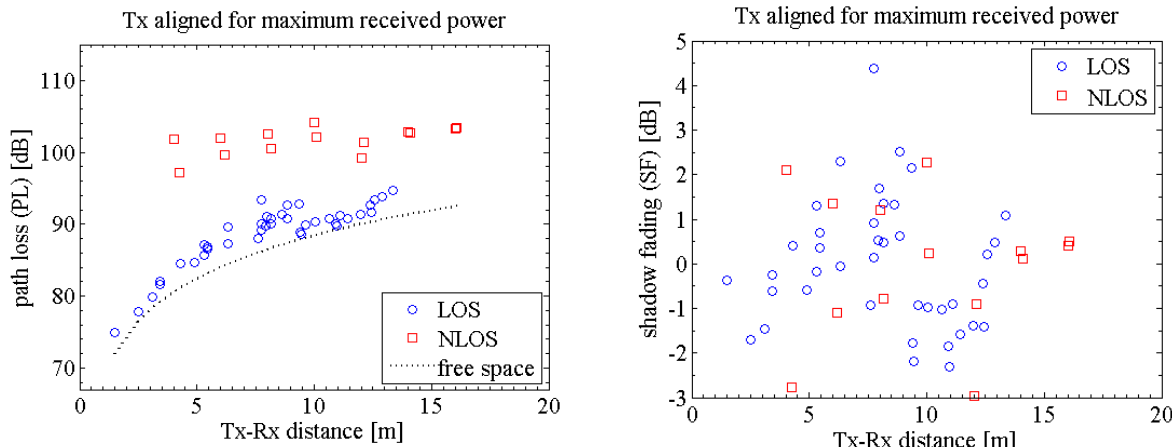


Figure B-50: Path loss and shadow fading when the Tx is aligned for maximum received power.

When the whole 360° rotation of the Tx is considered the total received power is

$$P_{tot} = \frac{1}{120} \frac{1}{2001} \sum_{\phi} \sum_f |H(\phi, f)|^2 \quad (\text{B-2})$$

The linear fit to the path loss and standard deviation of shadow fading are now:

$$\text{LOS: } PL = 85.83 + 15.73 \cdot \log(d)$$

LOS: $\sigma_{SF} = 1.15 \text{ dB}$

NLOS: $PL = 107.15 + 0.92 \cdot \log(d)$

NLOS: $\sigma_{SF} = 0.35 \text{ dB}$

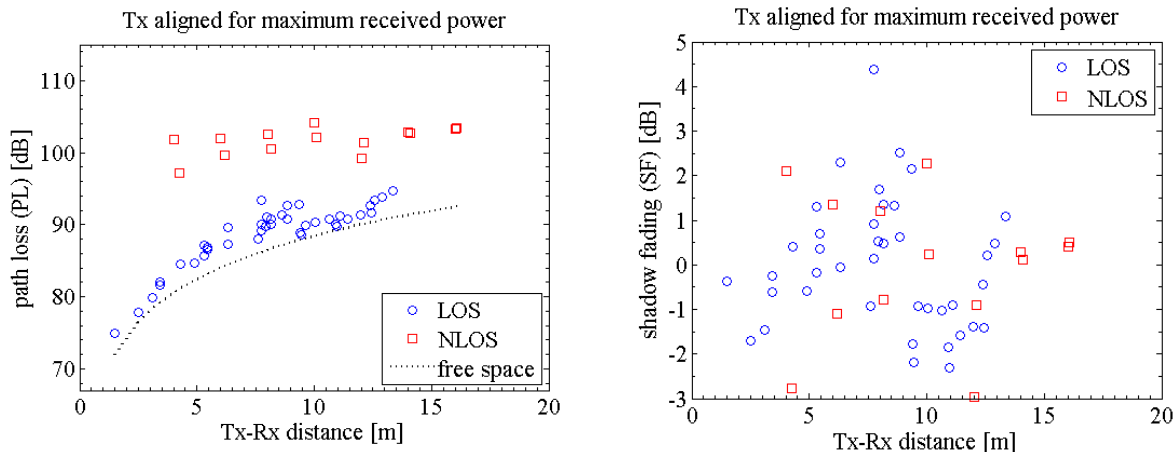


Figure B-51: Path loss and shadow fading with the 360° rotation of the Tx.

B.5.4.2 PADP and angular spread

Power angular delay profile (PADP) is calculated via Fourier transform from the average of the three complex samples measured at each azimuth angle. Examples of PADPs are presented in Figure B-52. Angular spread is calculated from PADP and presented in Figure B-53.

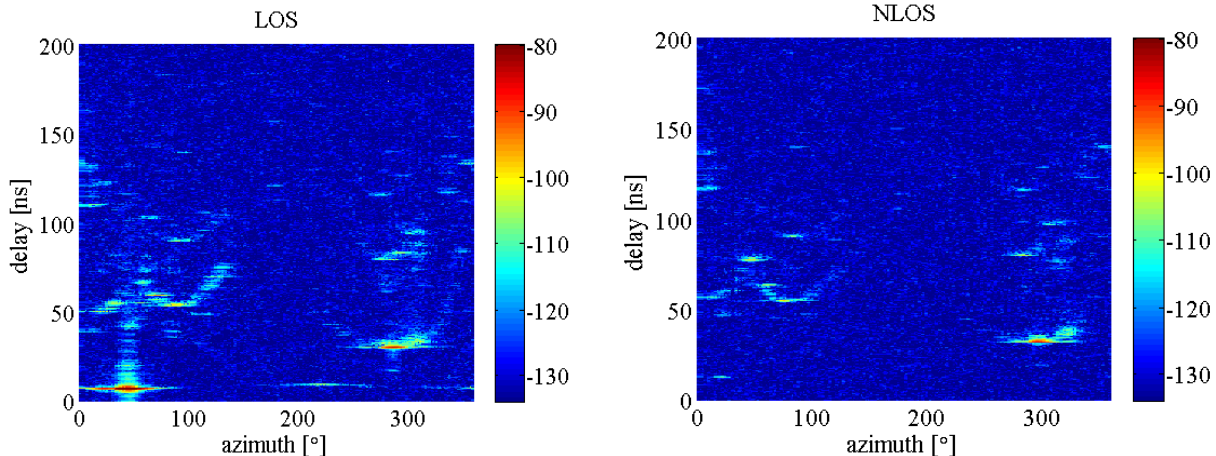


Figure B-52: Examples of LOS and NLOS PADP's: third floor measurement locations Rx1Tx2 and Rx1Tx3.

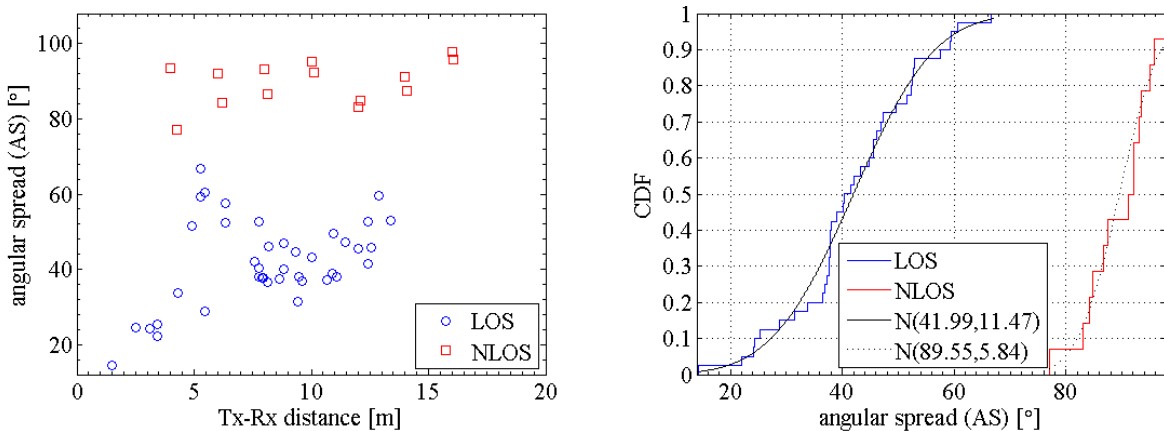


Figure B-53: Angular spread as a function of the Tx-Rx distance and cumulative distribution functions with fitted normal distributions $N(\mu, \sigma^2)$.

B.5.4.3 PDP and delay spread

The power delay profile (PDP) is derived by the integral of PADP over the angles

$$P(\tau) = \frac{1}{I} \sum_{i=1}^I P_i(\tau), \quad (\text{B-3})$$

where i is the azimuth rotation angle and P is the channel impulse response for that angle. Examples of PDPs are presented in Figure B-54.

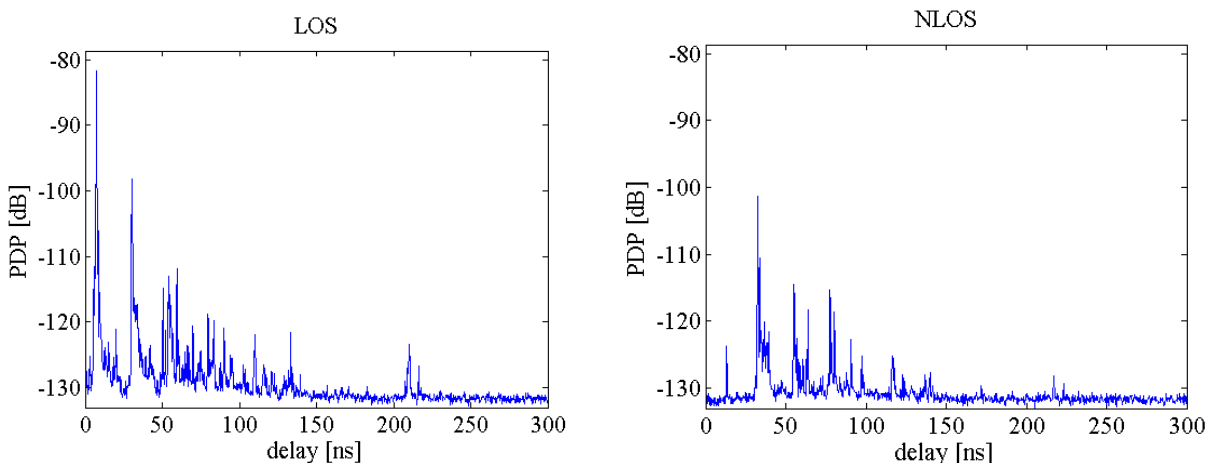


Figure B-54: Examples of LOS and NLOS PDP's: third floor measurement locations Rx1Tx2 and Rx1Tx3.

Delay spread is calculated from PDP with 20 dB threshold level, i.e. upper 20 dB of PDP. Delay spread results are presented in Figure B-55.

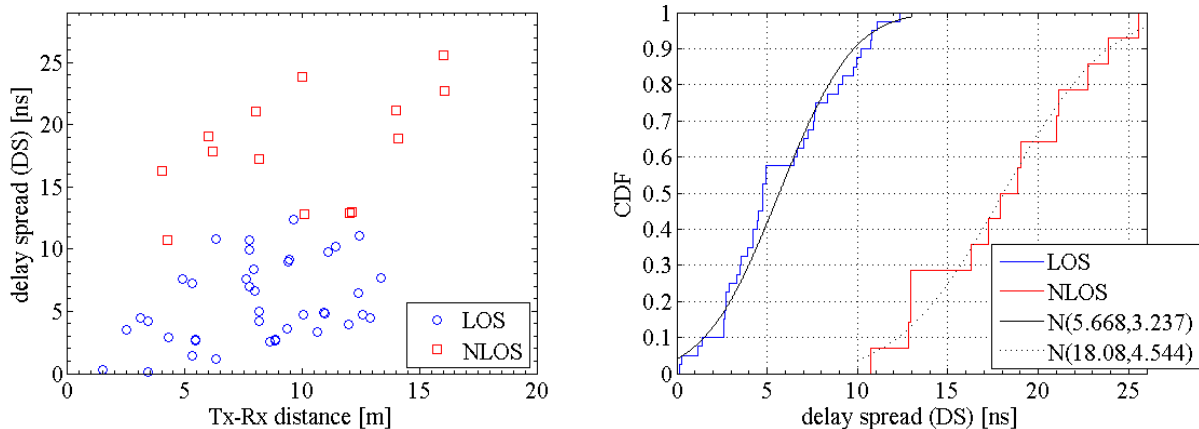


Figure B-55: Delay spread as a function of the Tx-Rx distance and cumulative distribution functions with fitted normal distributions $N(\mu, \sigma^2)$.

B.5.4.4 Peak detection and K-factor

Multipath components are identified from PDP. Multipath components are local maxima peaks in the PDP. Point on the PDP curve $P(\tau)$ is a peak if

$$P(\tau) > \frac{1}{\Delta} \int_{\tau-\Delta/2}^{\tau+\Delta/2} P(t) dt, \quad (\text{B-4})$$

$$P(\tau - \Delta\tau) < P(\tau) < P(\tau + \Delta\tau), \quad (\text{B-5})$$

$$P(\tau) > \text{noise level} + 3dB, \quad (\text{B-6})$$

and

$$\tau \geq d / c_0, \quad (\text{B-7})$$

where $\Delta = 2.0$ ns is the length of sliding window over delays, $\Delta\tau = 0.25$ ns is the delay resolution, d is the distance from Tx to Rx, and c_0 is the speed of light. The length of the sliding window, compared to the delay resolution, needs to be selected carefully in order to detect all the peaks. An example of PDPs with the detected peaks is presented in Figure B-56. CDF of all the detected peaks and CDF of detected strong peaks (upper 20 dB of PDP, i.e., with the additional condition $P(\tau) > \max(P(\tau))/100$) are presented in Figure B-57.

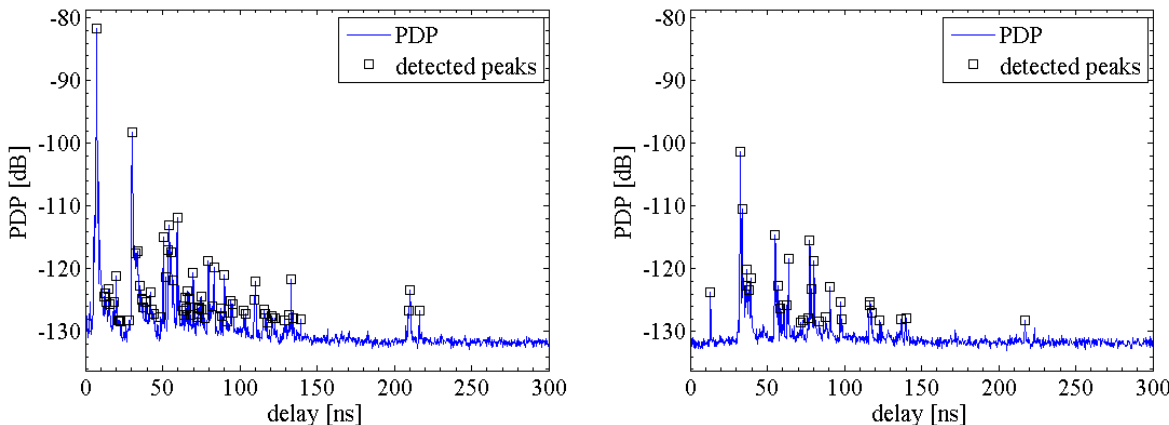


Figure B-56: Examples of LOS and NLOS PDP's with the detected peaks: third floor measurement locations Rx1Tx2 and Rx1Tx3.

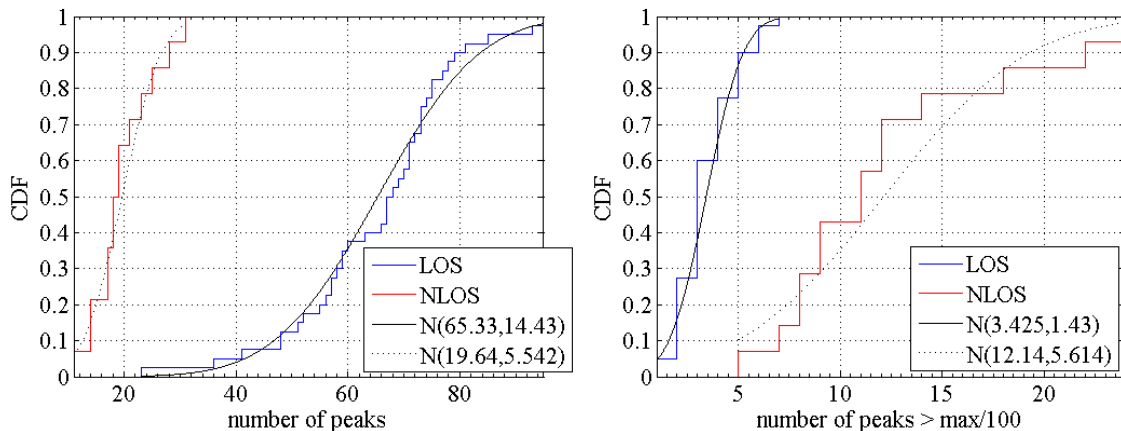


Figure B-57: CDF of the number of detected peaks 3 dB or more above noise level and of the number of relatively strong peaks (upper 20 dB of PDP).

The narrowband Ricean K-factor is estimated starting from a complex, zero mean random time variation in channel response. The time-varying response $v(t)$ approximates the signal in the vicinity of the measurement location. We calculate $v(t)$ as

$$v(t) = \sum_{l=1}^L \alpha_l e^{j\theta_l}, \quad (\text{B-8})$$

where α_l is the amplitude of the l^{th} peak, L is the number of peaks, and θ_l is a statistically independent random phase for each peak with uniform distribution $[0 \ 2\pi]$. The narrowband Ricean K-factor is estimated from moments of $v(t)$. 10^5 random realisations are calculated for each measurement localisation for the K-factor estimation.

The linear fit to the narrowband Ricean K-factor is:

$$\text{LOS: } K[\text{dB}] = 13.11 - 0.72 \cdot d[\text{m}]$$

$$\text{NLOS: } K[\text{dB}] = 3.36 - 0.03 \cdot d[\text{m}]$$

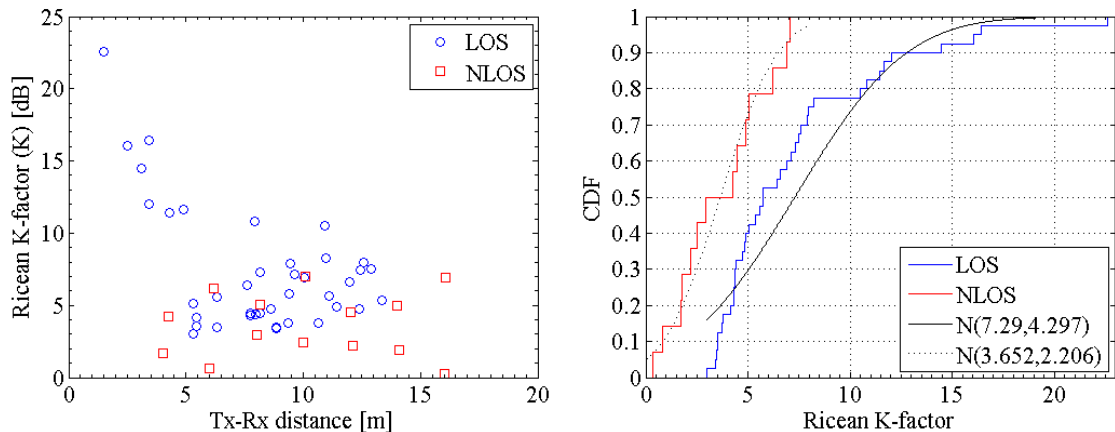


Figure B-58: Narrowband Ricean K-factor as a function of the Tx-Rx distance and cumulative distribution functions with fitted normal distributions $N(\mu, \sigma^2)$.

B.5.4.5 Parameter table

Table B-20: Parameters

		Shopping mall	
		LOS	NLOS**
Delay spread (DS) $\log_{10}([\text{s}])$	μ_{DS}	0.8	1.3
	σ_{DS}	0.5	0.7
Angular spread of departure (ASD) $\log_{10}([\text{s}])$	μ	1.6	2.0
	σ	1.1	0.8
Path loss* (PL) $PL = A \log_{10}(d[\text{m}]) + B$	A	19	5.1
	B	78	103
Shadow fading* (SF) [dB]	σ	1.4	1.6
Ricean K-factor (K) [dB] $K = C + D \cdot d [\text{m}]$	C	13	3.4
	D	-0.7	0.03
Correlation coefficients	DS [s] vs AS [°]	0.2	0.8
	DS [s] vs K [dB]	-0.3	-0.2
	AS [°] vs K [dB]	-0.6	-0.2

* 20 dB standard gain horn aligned for maximum received power by omnidirectional antenna

** blocked-LOS, omnidirectional receiver behind a wide pillar



Appendix C Early simulation channel models

The early channel models for METIS simulations in the beginning of the project are listed in Table C-1. The models have been defined in the starting phase of the project to be used in the early simulations conducted before the actual METIS channel models were created.

Table C-1: Early simulation channel models for METIS project

PS#	Link Type	Propagation Scenario	Path Loss Model	Fading Channel Model
1	BS-UE	UMi O2O	WINNER+ B1, Manhattan layout [WIN10-D53]	IMT-Advanced UMi-O2O [ITU09-2135]
2		UMi O2I	WINNER+ B4, Manhattan layout [WIN10-D53]	IMT-Advanced UMi-O2I [ITU09-2135]
3		UMa O2O	WINNER+ C2 O2O [WIN10-D53]	WINNER II C2 O2O [WIN08-D112]
4		UMa O2I	WINNER+ C4 O2lb [WIN10-D53]	WINNER II C4 [WIN08-D112]
5		Rural O2O	IMT-Advanced-RMa [ITU09-2135]	IMT-Advanced-RMa [ITU09-2135]
6		Rural O2I	IMT-Advanced RMa-O2I [ITU09-2135] -Outdoor PL from O2O-R	IMT-Advanced RMa-O2I [ITU09-2135] Angle spreads: BS: O2O-RMa, UE: O2I-UMa
7		Indoor Office	WINNER II -A1-rr (room-to-room) [WIN08-D112]	WINNER II -A1-rr [WIN08-D112]
8		Indoor Shopping mall	WINNER II -A1-cc (corridor-to-corridor) WINNER II -A1-cr (corridor-to-room) WINNER II -A1-rr [WIN08-D112]	WINNER II -A1-cc WINNER II -A1-cr WINNER II -A1-rr [WIN08-D112]
9	D2D	D2D-O2O-U (also V2V)	WINNER+ B1, Manhattan layout with 10 dB extra loss, page 74-75, Table 4-1 [WIN10-D53]	IMT-Advanced-UMi [ITU09-2135] Angle params at BS: - Update to UE params.
10		D2D-O2I-U	WINNER+ B4, Manhattan layout with 10 dB extra loss, page 74-75, Table 4-1 [WIN10-D53]	IMT-Advanced-UMi(O2I) [ITU09-2135]. Angle params at BS: Update to O2O UE params.
11		D2D-O2O-R	WINNER+ C2 [WIN10-D53] (hBS =1.5 m, hUE=1.5 m)	WINNER+ C2 [WIN10-D53] Angle params at BS: Update to UE params.
12		D2D-O2I-R	WINNER+ C4 [WIN10-D53], page 75, Table 4-1	IMT-Advanced-UMa (O2I) [ITU09-2135]
13		D2D-Indoor Office	Dual strip model of [3GPP10-36814]	WINNER II -A1-rr [WIN08-D112] , Angle params at BS: Update to UE params.
14		D2D-Indoor Shopping mall	WINNER II -A1-cc WINNER II -A1-cr WINNER II -A1-rr [WIN08-D112]	WINNER II -A1-cc WINNER II -A1-cr WINNER II -A1-rr [WIN08-D112]
15		D2D-O2O-H (V2V)	Karedal [KTC+09]	Karedal [KTC+09]
16	RS-UE	D2D-O2O-UMi (TC7)	WINNER+ B4, Manhattan layout with -10 dB offset, [WIN08-D112] (hBS =1.5 m, hUE=1.5 m)	IMT-Advanced UMi [WIN10-D53]
17		I2I-Car (TC8-car)	IMT-Advanced-InH [ITU09-2135] (hBS =1.5 m, hUE=0.5-1.5 m),	IMT-Advanced-InH [ITU09-2135]
18	RS-UE	I2I-Train (TC8-train)	WINNER II -A1 (cc) [WIN08-D112]	WINNER II -A1 (cc) [WIN08-D112]
19	BS-RS	O2O-H (TC8-car)	WINNER II D1 [WIN08-D112]	WINNER II D1 [WIN08-D112]
20		D2D-O2O-R (TC8-car)	WINNER+UMi [WIN10-D53] (hBS =1.5 m, hUE=1.5 m)	WINNER+ UMi [WIN10-D53]
21	Backhaul	UMa O2O	IMT-Advanced UMa [ITU09-2135] (hBS =25 m, hUE=10 m)	IMT-Advanced UMa [ITU09-2135]
22a		RMa O2O	IMT-Advanced RMa [ITU09-2135]	IMT-Advanced RMa [ITU09-2135]
22b		RMa O2O (TC8-train)	WINNER II -D2 (bad) [WIN08-D112] IMT-Advanced RMa (good) [ITU09-2135]	WINNER II -D2 (bad) [WIN08-D112] IMT-Advanced RMa (good) [ITU09-2135]

*

Appendix D Details of METIS initial model

D.1 LOS path antenna rotations

In the following we describe step-by-step instructions on how to determine the LOS component given the antenna radiation field patterns at transmitter and receiver, the antenna orientations, as well as the position vectors of the antennas.

1. Choose appropriate antenna element radiation field patterns of the UE and BS $\mathbf{F}_{LCS,rx}$, $\mathbf{F}_{LCS,tx}$ which are generally defined in LCS. Note: For untilted directive antennas the LCS boresight should always point in direction of the x-axis.
2. Set the rotation matrices \mathbf{R}_{rx} , \mathbf{R}_{tx} according to the orientation of the antennas. Note: Whereas the BS's azimuthal orientation is given by the hexagonal grid layout, the orientation in elevation direction is defined by the mechanical downtilt angle. In addition it has to be noted that the orientation of the UE needs to be explicitly modelled, especially in case of multiple antenna elements.
3. Calculate the unit vector $\hat{\mathbf{r}}_{Tx \rightarrow Rx, GCS}$ and $\hat{\mathbf{r}}_{Rx \rightarrow Tx, GCS}$ pointing from BS to UE and vice versa based on their respective locations.
4. Transform these vectors into the LCS of Tx and Rx respectively using the previously defined rotation matrices.

$$\hat{\mathbf{r}}_{Tx \rightarrow Rx, LCS} = \mathbf{R}_{tx}^T \hat{\mathbf{r}}_{Tx \rightarrow Rx, GCS} \quad (\text{D-1})$$

$$\hat{\mathbf{r}}_{Rx \rightarrow Tx, LCS} = \mathbf{R}_{rx}^T \hat{\mathbf{r}}_{Rx \rightarrow Tx, GCS} \quad (\text{D-2})$$

5. Calculate the departure angles at the Tx in LCS.

$$\theta'^d = \arccos \left\{ \begin{pmatrix} 0 \\ 0 \\ 1 \end{pmatrix}^T \hat{\mathbf{r}}_{Tx \rightarrow Rx, LCS} \right\} \quad (\text{D-3})$$

$$\phi'^d = \arg \left\{ \begin{pmatrix} 1 \\ j \\ 0 \end{pmatrix}^T \hat{\mathbf{r}}_{Tx \rightarrow Rx, LCS} \right\} \quad (\text{D-4})$$

And respectively the arrival angles at the Rx in LCS.

$$\theta'^a = \arccos \left\{ \begin{pmatrix} 0 \\ 0 \\ 1 \end{pmatrix}^T \hat{\mathbf{r}}_{Rx \rightarrow Tx, LCS} \right\} \quad (\text{D-5})$$

$$\phi'^a = \arg \left\{ \begin{pmatrix} 1 \\ j \\ 0 \end{pmatrix}^T \hat{\mathbf{r}}_{Rx \rightarrow Tx, LCS} \right\} \quad (\text{D-6})$$

6. Calculate the amplitude of the radiation field patterns at Rx and Tx with the respective angles, i.e. $\mathbf{F}_{LCS,rx}(\theta'^a, \phi'^a)$, $\mathbf{F}_{LCS,tx}(\theta'^d, \phi'^d)$.
7. Calculate $\cos(\psi)$ and $\sin(\psi)$, which are needed for the vector field rotation from LCS to GCS

$$\cos(\psi_{tx}) = \mathbf{e}_{\theta, GCS}(\theta^d, \phi^d)^T \mathbf{R}_{tx} \mathbf{e}_{\theta, LCS}(\theta'^d, \phi'^d) \quad (\text{D-7})$$



$$\sin(\psi_{tx}) = \mathbf{e}_{\theta,GCS}(\theta^d, \phi^d)^T \mathbf{R}_{tx} \mathbf{e}_{\theta,LCS}(\theta'^d, \phi'^d) \quad (\text{D-8})$$

$$\cos(\psi_{rx}) = \mathbf{e}_{\theta,GCS}(\theta^a, \phi^a)^T \mathbf{R}_{rx} \mathbf{e}_{\theta,LCS}(\theta'^a, \phi'^a) \quad (\text{D-9})$$

$$\sin(\psi_{rx}) = \mathbf{e}_{\theta,GCS}(\theta^a, \phi^a)^T \mathbf{R}_{rx} \mathbf{e}_{\theta,LCS}(\theta'^a, \phi'^a) \quad (\text{D-10})$$

8. Calculate the radiation field in the GCS

$$\mathbf{F}_{GCS,rx}(\theta^a, \phi^a) = \begin{pmatrix} \cos \psi_{rx} & -\sin \psi_{rx} \\ \sin \psi_{rx} & \cos \psi_{rx} \end{pmatrix} \mathbf{F}_{LCS,rx}(\theta'^a, \phi'^a) \quad (\text{D-11})$$

$$\mathbf{F}_{GCS,tx}(\theta^d, \phi^d) = \begin{pmatrix} \cos \psi_{tx} & -\sin \psi_{tx} \\ \sin \psi_{tx} & \cos \psi_{tx} \end{pmatrix} \mathbf{F}_{LCS,tx}(\theta'^d, \phi'^d) \quad (\text{D-12})$$

Calculate the channel coefficient with (7-16).

References

- [3GPP03-25996] 3GPP TR 25.996, "Spatial channel model for multiple input multiple output (MIMO) simulations", V6.1.0 (2003-09).
- [3GPP10-36814] 3GPP TR 36.814, "Further advancements for E-UTRA physical layer aspects", V9.0.0 (2010-03).
- [3GPP14-36873] 3GPP R1-141062, "Study on 3D channel model for LTE", draft TR 36.873 V1.3.0, 2014-02.
- [AE13a] Anite, Elektrobit, "Technical considerations about D2D channel models", 3GPP R1-132621, RAN1#73, Fukuoka, Japan, May 2013.
- [AE13b] Anite, Elektrobit, "Proposal for modification of IMT-A channel model for D2D", 3GPP R1-132622, RAN1#73, Fukuoka, Japan, May 2013.
- [AP09] P. Agrawal and N. Patwari, "Correlated link shadow fading in multihop wireless networks", IEEE Trans. Wireless Commun., vol. 8, no. 8, pp. 4024–4036, Aug. 2009.
- [Bal89] C. A. Balanis, "Advanced Engineering Electromagnetics", John Wiley & Sons, New York, 1989.
- [Ber95] Berg, J. E., "A recursive method for street microcell path loss calculations", In Personal, Indoor and Mobile Radio Communications, PIMRC'95, September, 1995.
- [CLR10] L. Chen, M. Loschonsky, L. M. Reindl, "Large-scale fading model for mobile communications in disaster and salvage scenarios", in Proc. Int. Conf. on Wireless Communications and Signal Processing (WCSP), 2010.
- [DC99] E. Damosso, L. M. Correia, "Digital Mobile Radio Towards Future Generation Systems", COST Action 231, European Commission, 1999.
- [DGM+04] Degli-Esposti, V., Guiducci, D., de'Marsi, A., Azzi, P., & Fuschini, F., "An advanced field prediction model including diffuse scattering" in IEEE Transactions on Antennas and Propagation, 52(7), 1717-1728, 2004.
- [Ele04] Elektrobit Ltd, "Propsound - multi-dimensional radio channel sounder. System specifications document. concept and specifications. Technical report." 2004.
- [FE08] F. P. Fontan, P. M. Espineira, Modeling the wireless propagation channel, John Wiley & Sons, 2008.
- [FH94] J. A. Fessler, A. O. Hero, "Space-alternating generalized expectation - maximization algorithm," IEEE Trans. Signal Processing, vol. 42, no. 10, pp. 2664-2677, Oct. 1994.
- [FR45] H. T. Friis, "Friis transmission equation," 1945, Online reference at http://en.wikipedia.org/wiki/Friis_transmission_equation.
- [HKC+05] C. L. Holloway, G. Koepke, D. Camell, K. A. Remley, D. F. Williams, S. A. Schima, S. Canales, D. T. Tamura, "Propagation and Detection of Radio Signals Before, During, and After the Implosion of a 13-Story Apartment Building", NIST Technical Note 1540, 2005.
- [HKC+08] C. L. Holloway, G. Koepke, D. Camell, K. A. Remley, " Radio Propagation Measurements Before, During, and After the Collapse of Three Large Building Structures," Proceedings of the General Assembly of the International Union of Radio Science (Union Radio Scientifique Internationale-URSI), 2008.

- [HZC+11] Q. Hamp, R. Zhang, L. Chen, O. Gorgis, T. Ostertag, J. Pavlina, "Results from German research project I-LOV", In Proc. the 1st International Conference on Wireless Technologies for Humanitarian Relief, ACM, pp. 249-258, 2011.
- [ITU09-2135] ITU-R M.2135-1, "Guidelines for evaluation of radio interface technologies for IMT-Advanced", International telecommunication union (ITU), Geneva, Switzerland, Technical Report, December 2009.
- [ITU12-1238] ITU-R P.1238-7, "Propagation data and prediction methods for the planning of indoor radiocommunication systems and radio local area networks in the frequency range 900 MHz to 100 GHz", International Telecommunication Union (ITU), Geneva, Switzerland, Technical Recommendation, February 2012.
- [ITU12-1410] ITU-R P.1410-5, "Propagation data and prediction methods required for the design of terrestrial broadband radio access systems operating in a frequency range from 3 to 60 GHz", International Telecommunication Union (ITU), Geneva, Switzerland, Technical Recommendation, February 2012.
- [ITU12-1411] ITU-R P.1411-6, "Propagation data and prediction methods for the planning of short-range outdoor radiocommunication systems and radio local area networks in the frequency range 300 MHz to 100 GHz", International Telecommunication Union (ITU), Geneva, Switzerland, Technical Recommendation, February 2012.
- [ITU13-676] ITU-R P.676-10, "Attenuation by atmospheric gases", International Telecommunication Union (ITU), Geneva, Switzerland, Technical Recommendation, September 2013.
- [JAC08] E. Jacobsen, "Frequency Dependence in Free Space Propagation", May 14, 2008. Online at <http://www.dsprelated.com/showarticle/62.php> (24th March 2014).
- [JRB+14a] S. Jaeckel, L. Raschkowski, K. Börner, L. Thiele, F. Burkhardt and E. Eberlein, "QuaDRiGa- Quasi Deterministic Radio Channel Generator, User Manual and Documentation", Fraunhofer Heinrich Hertz Institute, Tech. Rep. v1.2.0-283, 2014.
- [JRB+14b] Jaeckel, S.; Raschkowski, L.; Börner, K.; Thiele, L., "QuaDRiGa: A 3-D Multicell Channel Model with Time Evolution for Enabling Virtual Field Trials," IEEE Transactions on Antennas and Propagation, 2014
- [KP74] R. G. Kouyoumjian, P. H. Pathak, "A Uniform Geometrical Theory of Diffraction for an Edge in a Perfectly Conducting Surface," Proc. IEEE, Vol. 62, pp. 1448-1461, Nov. 1974.
- [KSO+09] K. Kitao, K. Saito, Y. Okano, T. Imai, J. Hagiwara, "Basic study on spatio-temporal dynamic channel properties based on channel sounder measurements," in APMC 2009. Asia Pacific, pp.1064--1067, Dec. 2009.
- [KTC+09] J. Karedal, F. Tufvesson, N. Czink, A. Paier, C. Dumard, T. Zemen, C. F. Mecklenbräuker, and A. F. Molisch, "A Geometry-Based Stochastic MIMO Model for Vehicle-to-Vehicle Communications," IEEE Trans. Wireless Comm., Vol. 8, No. 7, July 2009.
- [Lue84] R. J. Luebbers, "Finite Conductivity Uniform GTD Versus Knife Edge Diffraction in Prediction of Propagation Path Loss," IEEE Trans. AP, Vol. AP-32, No. 1, pp. 70-76, Jan. 1984.

- [MAB+12] J. Medbo, et al., "Directional channel characteristics in elevation and azimuth at an urban macrocell base station", in Proc. of the 6th European Conference on Antennas and Propagation (EuCAP 2012), Prague, Czech Republic, March 2012.
- [MBH+14] J. Medbo, et al., "Channel modelling for the fifth generation mobile communications", in Proc. of the 8th European Conference on Antennas and Propagation (EuCAP 2014), Hague, Netherlands, April 2014.
- [MEP10] A. Maltsev, V. Erceg, and E. Perahia, "Channel models for 60 GHz WLAN systems", IEEE Document (2010):802-11.
- [MET12] METIS, Mobile and wireless communications Enablers for the Twenty-twenty Information Society, EU 7th Framework Programme, [<http://www.metis2020.com>].
- [MET13-D11] "Future radio access scenarios, requirements and KPIs", M. Fallgren, B. Timus (Editors), Deliverable D1.1, V1.0, ICT-317669, METIS project, May 2013, [<http://www.metis2020.com>].
- [MET13-D31] "Positioning of multi-node/multi-antenna transmission technologies", E. de Carvalho, P. Popovski and H. Thomsen (Editors), Deliverable D3.1, V1.0, ICT-317669, METIS project, July 2013, [<http://www.metis2020.com>].
- [MET13-D51] "Intermediate description of the spectrum needs and usage principles", H. D. Schotten, M. A. Uusitalo (Editors), Deliverable D5.1, V1.0, ICT-317669, METIS project, August 2013, [<http://www.metis2020.com>].
- [MET13-D61] "Simulation guidelines", J. F. Monserrat, M. Fallgren (Editors), Deliverable D6.1, V1.0, ICT-317669, METIS project, October 2013, [<http://www.metis2020.com>].
- [MH13] Medbo, J., & Harrysson, F., "Channel modeling for the stationary UE scenario" in Proc. the 7th European Conference on Antennas and Propagation (EuCAP 2013), (pp. 2811-2815), April, 2013.
- [MSK+09] Medbo, J., Siomina, I., Kangas, A., & Furuskog, J. "Propagation channel impact on LTE positioning accuracy: A study based on real measurements of observed time difference of arrival" in Proc. the 20th International Symposium on Personal, Indoor and Mobile Radio Communications (PIMRC 2009), (pp. 2213-2217), September 2009.
- [OBB+14] "Scenarios for the 5G mobiles and wireless communications: the vision of the METIS project", A. Osseiran et al., accepted for publication in IEEE Communications Magazine; Feature topic on 5G wireless communication systems: prospects and challenges.
- [QC13] Qualcomm Incorporated, "Remaining issues of EoD/EoA modeling", 3GPP R1-135895, RAN1#75, San Francisco, USA, Nov 2013.
- [SJ03] A. Stucki and P. Jourdan, "MIMO radio channel parameter estimation using the initialization and search improved SAGE (ISIS) algorithm," in The 13th Virginia Tech/MPRG Symposium on Wireless Personal Communications, Blacksburg, Virginia, USA, Jun. 4–6 2003.
- [SKI+12] K. Saito, K. Kitao, T. Imai, S. Miura, "Human-body shadowing modeling for indoor quasi-static MIMO channels", in Proc. 10th Int. Symposium on Antennas, Propagation & EM Theory (ISAPE), pp. 608--611, 2012.
- [VA03] R. Vaughan and J. B. Andersen, "Channels, Propagation and Antennas for Mobile Communications" The IEE, London, UK, 2003.



Document: FP7-ICT-317669-METIS/D1.2

Date: 29/04/2014

Security: Public

Status: Final

Version: 1.0

- [VZ12] R. Verdone, A. Zanella, "Pervasive mobile and ambient wireless communications," COST Action 2100, Springer, 2012.
- [WIN08-D112] "WINNER II channel models", P. Kyösti, et al., IST-4-027756 WINNER II Deliverable D1.1.2, V1.2.4.2, 2008, online available at [<http://www.ist-winner.org/deliverables.html>].
- [WIN10-D53] "WINNER+ final channel models", P. Heino, et al., CELTIC CP5-026 WINNER+ project, Deliverable D5.3, V1.0, June 2010, [http://projects.celtic-initiative.org/winner+/deliverables_winnerplus.html].